

NORTHWESTERN UNIVERSITY

Graphene Inks with Cellulosic Dispersants:  
Development and Applications for Printed Electronics

A DISSERTATION

SUBMITTED TO THE GRADUATE SCHOOL  
IN PARTIAL FULFILLMENT OF THE REQUIREMENTS

for the degree

DOCTOR OF PHILOSOPHY

Field of Materials Science and Engineering

By

Ethan Benjamin Secor

EVANSTON, ILLINOIS

September 2017

© Copyright by Ethan Benjamin Secor 2017  
All Rights Reserved

## ABSTRACT

Graphene Inks with Cellulosic Dispersants:  
Development and Applications for Printed Electronics

Ethan Benjamin Secor

Graphene offers promising opportunities for applications in printed and flexible electronic devices due to its high electrical and thermal conductivity, mechanical flexibility and strength, and chemical and environmental stability. However, scalable production and processing of graphene presents a critical technological challenge preventing the application of graphene for flexible electronic interconnects, electrochemical energy storage, and chemically robust electrical contacts. In this thesis, a promising and versatile platform for the production, patterning, and application of graphene inks is presented based on cellulosic dispersants. Graphene is produced from flake graphite using scalable liquid-phase exfoliation methods, using the polymers ethyl cellulose and nitrocellulose as multifunctional dispersing agents. These cellulose derivatives offer high colloidal stability and broadly tunable rheology for graphene dispersions, providing an effective and tunable platform for graphene ink development. Thermal or photonic annealing decomposes the polymer dispersant to yield high conductivity, flexible graphene patterns for various electronics applications. In particular, the chemical stability of graphene enables robust electrical contacts for ceramic, metallic, organic and electrolytic materials, validating the diverse applicability of graphene in printed electronics. Overall, the strategy for graphene ink design presented here offers a simple, efficient, and versatile method for integrating graphene in a wide range of printed devices and systems, providing both fundamental insight for nanomaterial ink development and realistic opportunities for practical applications.

## ACKNOWLEDGEMENTS

I would first like to acknowledge my advisor, Professor Mark C. Hersam, for supporting me and my research over the past five years. Mark provided critical guidance and high-level direction, while also giving me the autonomy and flexibility to tailor the work to my interests. His confidence in the research, investment in time and resources, and unwavering support were invaluable in getting this work to its present stage. His active promotion of the work led to numerous collaborations and continuing research directed towards commercialization, which made for an interesting and engaging graduate school experience. He was the best mentor I could hope for, challenging me to produce my best, motivating and leading by example, offering encouragement and feedback, and providing many opportunities for growth. I was and continue to be deeply grateful for the opportunity to join the Hersam group and work with Mark.

I would also like to thank Prof. Tobin J. Marks, Prof. Ramille N. Shah, and Prof. Kenneth R. Shull for their time and effort in serving on the committee for my qualifying examination and thesis defense. They provided helpful guidance and suggestions and, on several occasions, opportunities for collaboration.

I would next like to thank the members of the Hersam group over the years, for making graduate school such an enjoyable experience and establishing a fun, collegial, and motivating atmosphere. I would especially like to acknowledge Prof. Karl Putz, Dr. Joshua Wood, Dr. Deep Jariwala, Dr. Pradyumna Prabhumirashi, Dr. Michael Geier, Dr. Kan-Sheng Chen, Dr. Jian Zhu, Dr. Kyle Luck, Dr. Nikhita Mansukhani, Sarah Clark, and Shay Wallace. I also had the opportunity to work with two excellent undergraduate researchers, Theodore Gao and Manuel Dos Santos,



whose hard work and loyalty is greatly appreciated, and who made my graduate school experience much richer.

I benefited from many collaborations with researchers external to Northwestern, which contributed substantially to my thesis research and professional development. I would especially like to acknowledge the following: at the University of Minnesota, Prof. Lorraine F. Francis, Prof. C. Daniel Frisbie, Dr. Sooman Lim, Dr. Woo Jin Hyun, Dr. Ankit Mahajan, and Dr. Donghoon Song, whose hard work and creativity led to productive research over the past several years; at the Air Force Research Laboratory, Dr. Benji Maruyama, Dr. Christopher Tabor, Dr. Alexander Cook, Dr. Ahmad Islam, and Dr. Rahul Rao, especially for their time and energy spent hosting me at AFRL for research; and at Harvard University, Prof. Jennifer A. Lewis and Dr. Bok Yeop Ahn, from whom I learned valuable lessons regarding organization and communication for successful collaborative research.

I would like to acknowledge support from the National Defense Science and Engineering Graduate Fellowship, the Ryan Fellowship, and the Cabell Terminal Year Fellowship, along with the outstanding shared research facilities at Northwestern University which made this all possible.

I am very thankful to my friends at Northwestern, particularly Jeffrey Cain, Dr. Logan Ward, Dr. Andrew Bobel, Dr. Ashley Paz y Puente, and Vuk Brajuskovic, for adopting me into the group, as well as Michael Knudson and Do Soon Kim for welcoming me to the Triathlon Club. In addition, I am grateful to Essene Waters and Jackson Harris for their steadfast friendship over the years.

I would also like to thank my many teachers, coaches, and mentors over the years for preparing me for graduate school and life, especially Doug and Jean Rydeen, Rich Keller, and

Matt Oswald. I would have been unprepared for graduate school without a community of support at Drake University, including the Department of Chemistry and Department of Physics, and especially Prof. Maria Bohorquez and Prof. Klaus Bartschat. For their role in mentoring me through undergraduate research projects external to Drake, I would like to also thank Dr. Vilas Pol and Dr. P. Randall Schunk.

And of course, I cannot begin to thank my family enough – my mom and dad, Helen and Robert Secor; my siblings, Isaac, Duncan, Laura and Andy; and the rest of the clan – especially Karen Secor, Linda Mehoke, and Mary Anne and Bret Kelley, for adopting me while I lived in Chicago. And finally, I am grateful to my girlfriend Samantha Haas, whose encouragement, inspiration, and friendship while writing this thesis kept me full of energy, laughter, hope, and joy.

**LIST OF ABBREVIATIONS**

AFM	Atomic Force Microscopy
AJP	Aerosol Jet Printing
DIW	Direct Ink Writing
DSC	Differential Scanning Calorimetry
EC	Ethyl Cellulose
EGT	Electrolyte-Gated Transistor
FTIR	Fourier Transform Infrared (Spectroscopy)
IPL	Intense Pulsed Light (Annealing)
LPE	Liquid Phase Exfoliation
MSC	Microsupercapacitor
NC	Nitrocellulose
(O)TFT	(Organic) Thin Film Transistor
PEN	Polyethylene Naphthalate
PET	Polyethylene terephthalate
PI	Polyimide
(R)GO	(Reduced) Graphene Oxide
SEM	Scanning Electron Microscopy
TGA	Thermogravimetric Analysis
TMDC	Transition Metal Dichalcogenide
UV-VIS	Ultraviolet-Visible (Absorption Spectroscopy)
XPS	X-ray Photoelectron Spectroscopy

*For my family*

# Table of Contents

ABSTRACT.....	3
ACKNOWLEDGEMENTS.....	4
LIST OF ABBREVIATIONS.....	7
LIST OF FIGURES .....	13
<b>Chapter 1. Introduction and Background.....</b>	<b>27</b>
1.1. Motivation and Thesis Statement.....	28
1.2. Introduction to Printed Electronics .....	29
1.3. Technical Background for Printed Electronics .....	34
<i>1.3.1. Technologies and Processes for Printed Electronics .....</i>	<i>34</i>
<i>1.3.2. Materials for Printed Electronics .....</i>	<i>40</i>
1.4. Introduction to Graphene .....	43
<i>1.4.1. Structure and Properties of Graphene.....</i>	<i>43</i>
<i>1.4.2. Liquid-Phase Exfoliation of Graphene .....</i>	<i>44</i>
1.5. Graphene Inks .....	46
<i>1.5.1. Motivation for Graphene Inks.....</i>	<i>46</i>
<i>1.5.2. Literature Overview .....</i>	<i>47</i>
1.6. Recent Progress in Printed Electronics .....	53
<i>1.6.1. Materials: Post-Graphene 2D Nanomaterial Inks .....</i>	<i>54</i>
<i>1.6.2. Methods: Resolution, Registration, and Direct-Write .....</i>	<i>56</i>
<i>1.6.3. Devices and Applications: Bio-Interfaced and Hybrid Electronics .....</i>	<i>58</i>
1.7. Thesis Organization .....	60
<b>Chapter 2. Inkjet Printing of Graphene/Ethyl Cellulose .....</b>	<b>64</b>
2.1. Introduction to Inkjet Printing of Graphene.....	65
2.2. Liquid Phase Exfoliation of Graphene with Ethyl Cellulose.....	66
2.3. Ink Formulation and Inkjet Printing of Graphene/EC .....	69

	10
2.4. Functional Characterization of Graphene/EC Patterns .....	72
2.5. Summary for Graphene/EC Inkjet Printing .....	77
<b>Chapter 3. Gravure Printing of Graphene/Ethyl Cellulose.....</b>	<b>78</b>
3.1. Introduction to Gravure Printing of Graphene.....	79
3.2. Graphene/EC Ink Formulation for Gravure Printing.....	80
3.3. Print Characterization of Gravure-Printed Graphene/EC .....	84
3.4. Functional Characterization of Gravure-Printed Graphene/EC.....	87
3.5. Summary for Graphene/EC Gravure Printing.....	91
<b>Chapter 4. Screen Printing of Graphene/Ethyl Cellulose .....</b>	<b>92</b>
4.1. Introduction to Screen Printing of Graphene .....	93
4.2. Graphene/EC Ink Formulation and Screen Printing Method Development .....	95
4.3. Screen Printing Optimization and Characterization .....	101
4.4. Functional Properties and Application of Screen-Printed Graphene/EC.....	105
4.5. Summary for Graphene/EC Screen Printing.....	110
<b>Chapter 5. Photonic Annealing of Graphene/Ethyl Cellulose .....</b>	<b>111</b>
5.1. Introduction to Photonic Annealing of Graphene.....	112
5.2. Graphene Exfoliation and Process Overview .....	113
5.3. Effect of Graphene Film Composition on Annealing Effectiveness .....	115
5.4. Process Generalization and Optimization.....	119
5.5. Revisiting Inkjet Ink Formulation with Improved Process Control .....	121
5.6. Film Morphology and Mechanical Properties .....	127
5.7. Summary for Graphene/EC Photonic Annealing.....	131
<b>Chapter 6. Graphene Inks with a Nitrocellulose Dispersant.....</b>	<b>132</b>
6.1. Nitrocellulose as an Alternative Graphene Dispersant .....	133

	11
6.2. Graphene Exfoliation and Ink Development .....	134
6.3. Chemical and Structural Analysis.....	138
6.4. Characterization of Functional Properties .....	146
6.5. Summary for Graphene/NC Ink Development .....	151
<b>Chapter 7. Combustion-Assisted Photonic Annealing of Graphene Inks .....</b>	<b>152</b>
7.1. Introduction to Combustion-Assisted Photonic Annealing .....	153
7.2. Proof-of-Concept Combustion-Assisted Photonic Annealing .....	154
7.3. Functional Characterization of Photonic Annealed Graphene/NC .....	159
7.4. Application of Porous Graphene Thin Films for Printed Microsupercapacitors .....	162
7.5. Summary for Graphene/NC Photonic Annealing .....	165
<b>Chapter 8. Chemically Stable Electrodes for Printed InGaZnO Transistors.....</b>	<b>166</b>
8.1. Introduction to Printed InGaZnO Transistors .....	167
8.2. Demonstration of Stable Graphene Electrodes for InGaZnO .....	169
8.3. Study and Optimization of Device Geometry.....	172
8.4. Detailed Transistor and Contact Characterization .....	175
8.5. Stability Assessment for Inkjet-Printed InGaZnO Transistors .....	181
8.6. Summary of Graphene Electrodes for Chemically Stable InGaZnO Electrodes .....	185
<b>Chapter 9. Stable Graphene Contacts for Liquid Metal.....</b>	<b>187</b>
9.1. Introduction to Stable Graphene Contacts for Liquid Metal .....	188
9.2. Process Integration of Graphene with Liquid Metal.....	189
9.3. Electrical Characteristics and Stability of Graphene Interfaces .....	193
9.4. Summary of Stable Graphene Electrodes for Liquid Metal Electronics.....	196
<b>Chapter 10. Interfacing Graphene with Organic Semiconductors and Electrolytes .....</b>	<b>197</b>
10.1. Introduction to Graphene Interfaces with Organic and Electrolytic Materials .....	198

	12
10.2. Templating C <sub>60</sub> Devices with a Graphene Ink Interlayer.....	199
10.3. Graphene Electrodes for Printed, Flexible Electrolyte-Gated Transistors.....	201
10.4. Printed, Flexible Graphene Microsupercapacitors.....	204
10.5. Summary of Graphene Applications with Organic and Electrolytic Materials .....	205
<b>Chapter 11. Opportunities for Future Research .....</b>	<b>207</b>
11.1. Introduction to Future Work .....	208
11.2. Translating Concepts to Other Nanomaterials .....	208
11.3. Expanded Processing Beyond Printed Electronics .....	211
11.4. Fundamental Investigation Utilizing Versatile Process Control.....	214
11.5. Summary of Future Work .....	217
<b>Chapter 12. Summary and Outlook.....</b>	<b>218</b>
12.1. Summary of Thesis Research.....	219
12.2. Outlook for Practical Applications .....	223
REFERENCES .....	225
Curriculum Vitae for Ethan B. Secor.....	253



## LIST OF FIGURES

Figure 1.1. Schematic illustration of various printed electronics technologies. The combination of information collection, processing, and transmission in a common process framework underlies the potential of printed electronics to impact and enable emerging technologies, such as the Internet of Things. ....	30
Figure 1.2. General comparison of metrics for printed electronics (green) and conventional silicon electronics (red), showing tradeoffs in cost, performance, functionality, and processing. ....	31
Figure 1.3. Selected target applications for printed electronics. (a) Illustration showing integration of multiple operations in a single product to build up more complex functionality. (b) Images of target applications, including (clockwise from top-left) sensor tags, photovoltaics, RFID chips, and displays. ....	33
Figure 1.4. Process metrics for several common printing techniques. (a) Typical resolution and throughput for several printing methods. (b) Required viscosity of different printing methods plotted against typical throughput, showing target viscosities spanning five orders of magnitude. Data taken in part from Ref. 14. ....	35
Figure 1.5. Schematic illustration of a hybrid manufacturing process for transistor fabrication, indicating multiple deposition techniques being used for particular materials, adapted from Ref. 15. ....	37
Figure 1.6. Fundamentals of inkjet printing. (a) Schematic illustration of piezoelectric inkjet printing, which uses an electronically-driven actuator to eject droplets of ink onto the substrate for drop-on-demand patterning. (b) Phase space for ink design and printing in terms of dimensionless fluid dynamics parameters, namely the Weber number, the Reynolds number, and the inverse Ohnesorge number. Figures adapted from Ref. 17. ....	39
Figure 1.7. Wetting and drying processes in inkjet printing. (a) Typical line shapes with varying drop spacing and wetting properties, ranging from coalesced droplets to bulging lines; adapted from Ref. 17. (b) Influence of solvent mixture on printing morphology, showing enhanced uniformity following the addition of 10% high boiling cosolvent; adapted from Ref. 23. ....	40
Figure 1.8. Qualitative comparison of the primary classes of conductive inks, including (a) metals, (b) polymers, and (c) carbon materials. ....	41
Figure 1.9. Introduction to liquid-phase exfoliation (LPE) of graphene. (a) Schematic diagram describing the exfoliation of graphite to produce graphene in pure organic solvents (top) and with surfactants or stabilizers (bottom), adapted from Ref. 54. (b) Transmission electron microscopy image of a single-layer graphene flake produced by LPE of graphene in N-methyl pyrrolidone, taken from Ref. 52. (c) AFM image of single-layer graphene flakes produced by LPE of graphene with the aqueous surfactant sodium cholate and isolated from multi-layer flakes by density gradient ultracentrifugation, taken from Ref. 61. ....	45

- Figure 1.10. Breadth of applications for graphene. From center to edge, the structure, key attributes, and corresponding possible application areas are delineated..... 47
- Figure 1.11. Pristine graphene inks for printed electronics. (a-b) Illustration of two different chemistries for pristine graphene inks, specifically direct dispersion in select organic solvents and polymer-stabilized dispersion using ethyl cellulose for (a) and (b), respectively. (c) Target plot illustrating the tradeoffs between the ink chemistries for a range of desirable attributes, highlighting the room for improvement through alternative ink chemistries or further development of existing methods..... 48
- Figure 1.12. Inkjet printing of graphene. (a) Dark-field optical microscopy image of an inkjet-printed drop of graphene from NMP on a treated glass slide. (b) Schematic of a TFT with inkjet-printed graphene as the channel and (c) transfer characteristics of the inkjet-printed graphene TFT, showing a current on-off ratio of  $\sim 10$  and a mobility of  $\sim 95 \text{ cm}^2/\text{V}\cdot\text{s}$ . (a-c) adapted from Ref. 68. (d) SEM image of inkjet-printed graphene using EC, ethanol and terpineol, following annealing. (e) Optical image of a microsupercapacitor (MSC) based on inkjet-printed graphene and (f) current-voltage characteristics of the MSC structure. (d-f) adapted from Ref. 71. .... 50
- Figure 1.13. Printed devices based on reduced graphene oxide (RGO). (a) Schematic (left) and transfer curves (right) of a pentacene OTFT with inkjet-printed electrodes based on RGO, with similar devices using gold and PEDOT:PSS contacts for comparison, adapted from Ref. 94. (b) Response of a RGO vapor sensor exposed to  $\text{Cl}_2$  vapor at varying concentrations (left) and to various gases ( $\text{NH}_3$ ,  $\text{Cl}_2$ ,  $\text{NO}_3$  at 100 ppm) (right), adapted from Ref. 88. (c) Temperature sensing capability of an RGO film, including resistance plotted against temperature (left) and the resistance response due to tapping with a finger (right), adapted from Ref. 91. (d) Function of RGO thin film as an acoustic actuator electrode, including speaker system design (left) and frequency response (right), adapted from Ref. 92..... 52
- Figure 1.14. Post-carbon nanomaterial inks. (a) Schematic structure of a  $\text{MoS}_2$  nanosheet, which is a prototypical TMDC. (b) Illustration of a h-BN nanosheet with atomic thickness and honeycomb structure similar to graphene. (c) Vials of liquid-phase exfoliated 2D nanosheets of  $\text{WS}_2$ , h-BN, and graphene (left) as well as inkjet printing schematic and inkjet-printed patterns on Si/SiO<sub>2</sub> (right); adapted from Ref. 110..... 56
- Figure 2.1. Characterization of graphene flakes. (a) Representative AFM scan of the graphene flakes that was used to obtain particle statistics. Histograms of (b) flake thickness and (c) flake area for 355 and 216 flakes, respectively. .... 67
- Figure 2.2. Thermal gravimetric analysis of pure EC (black) and graphene/EC composite powder (red), showing (a) mass as a function of temperature and (b) the differential mass loss. For the composite powder, the decomposition peaks of EC in (b) are shifted to different temperatures due to the presence of graphene. A heating rate of  $5 \text{ }^\circ\text{C}/\text{minute}$  in air was used for this measurement. .... 67
- Figure 2.3. Schematic illustration of the ink preparation method. (a) Graphene is exfoliated from graphite powder in ethanol/EC by probe ultrasonication. A graphene/EC powder is

then isolated following (b) centrifugation-based sedimentation to remove residual large graphite flakes and (c) salt-induced flocculation of graphene/EC. (d) An ink for inkjet printing is prepared by dispersion of the graphene/EC powder in 85:15 cyclohexanone:terpineol. (e) Vial of the prepared graphene ink and (f) drop formation sequence for inkjet printing, with spherical drops forming after  $\sim 300 \mu\text{m}$ . ..... 69

Figure 2.4. Shear viscosity of the graphene ink over a shear rate range of  $10\text{-}1000 \text{ s}^{-1}$  at temperatures of 25, 30, 35 and  $40 \text{ }^\circ\text{C}$ . ..... 70

Figure 2.5. Morphology of inkjet-printed graphene features on HMDS-treated Si/SiO<sub>2</sub>. Scanning electron micrographs of (a) multiple printed lines and (b) a single printed line and drop (inset, scale bar corresponds to  $40 \mu\text{m}$ ) illustrate the uniformity of the printed features. (c) An AFM image of a single line following 10 printing passes that shows no coffee ring features. (d) Averaged cross-sectional profiles of printed lines after 1, 3, and 10 printing passes, demonstrating the reliable increase in thickness obtained after multiple printing passes. The cross-sectional profiles are obtained from the averaged AFM height profile over  $\sim 20 \mu\text{m}$  as indicated by the boxed region in (c). ..... 72

Figure 2.6. Electrical characterization of graphene features. (a) Electrical resistivity of blade-coated films plotted against annealing temperature for a fixed annealing time of 30 minutes, showing effective binder decomposition at  $250 \text{ }^\circ\text{C}$  and increased resistivity due to graphene oxidation above  $400 \text{ }^\circ\text{C}$ . (b) Dependence of electrical resistivity on annealing time for a fixed annealing temperature of  $250 \text{ }^\circ\text{C}$ , showing that low resistivity is achieved following annealing for 20 minutes. (c) Thickness of inkjet-printed graphene lines on HMDS-treated Si/SiO<sub>2</sub> for increasing numbers of printing passes. (d) Electrical resistivity of the printed features for increasing numbers of printing passes, showing relatively stable performance after only 3 printing passes. ..... 73

Figure 2.7. SEM images of printed lines annealed to (a,c)  $250 \text{ }^\circ\text{C}$  and (b,d)  $450 \text{ }^\circ\text{C}$ . (c) and (d) are higher magnification SEM images of the highlighted area (yellow box) from images (a) and (b), respectively. Following  $450 \text{ }^\circ\text{C}$  annealing, the EC residue is removed, leading to a sparse graphene network. This observation suggests the importance of EC decomposition products in maintaining electrical and mechanical integrity of the printed features. .... 75

Figure 2.8. Flexibility assessment of printed graphene lines on Kapton® substrates. (a) Resistance of graphene lines folded to a radius of curvature of  $0.9 \text{ mm}$  (blue) and  $3.4 \text{ mm}$  (red) normalized to the resistance prior to bending. (b) Normalized resistance of graphene lines measured in a flexed state for various degrees of bending, showing reliable retention of electrical conductivity across all measured flex states. (c) Normalized resistance of graphene lines while measured in a folded state, showing a small and irreversible increase in resistance following folding. Images of the sample in the (d) original and (e) folded state. .... 76

Figure 3.1. Development of the graphene ink for gravure printing. (a) Schematic of the ink, showing a graphene sheet stabilized by ethyl cellulose in terpineol. (b) Photograph of the formulated ink. (c-e) Illustration of the gravure printing method decomposed into three steps: (c) flooding of the gravure cells; (d) doctor blading; (e) printing. .... 82

Figure 3.2. Optimization of graphene inks for gravure printing. (a) Shear viscosity for the three different ink formulations. (b) Size of printed dots for each ink using a gravure cell of 50 $\mu\text{m}$ . (c-e) Optical images of the printed dots for each ink. (f-h) Optical images showing line formation as the cell spacing is reduced, corresponding to 50, 25 and 5 $\mu\text{m}$ spacing for a cell size of 50 $\mu\text{m}$ . .....	84
Figure 3.3. Line width measurements for lines printed with different cell spacing. The printing ratio (PR) defines the ratio of cell spacing to cell width. The similar width of lines printed at different printing ratios suggests that the additional ink contributes to the line uniformity and thickness rather than increased ink spreading. ....	85
Figure 3.4. Optical microscopy images of printed graphene lines using cell sizes of 15, 20, 25, 30, 35 and 50 $\mu\text{m}$ for (a-f), respectively. Lines printed without the specified cell size are shaded gray in each case. ....	86
Figure 3.5. Characterization of gravure-printed graphene lines. (a) Line width and (b) line thickness for varying cell size. (c) Large-area scanning electron micrograph of printed lines. (d) Line height profiles measured by optical profilometry. ....	87
Figure 3.6. A scanning electron micrograph of graphene lines indicates a dense and continuous network of flakes. ....	89
Figure 3.7. Characterization of gravure-printed graphene for electronics. (a) Line resistance for the varying cavity size. (b) Thickness contraction during annealing for the graphene/EC composite. (c) AFM images of a printed line, illustrating that the printed lines are considerably thinner than the substrate surface roughness. (d) Normalized resistance of printed lines over 500 bending cycles at a radius of curvature of 2 mm, or 3.1% strain. (e) Printed crossbar array. (f) Photograph of large-area patterns. ....	90
Figure 4.1. (a) Fabrication steps for a thin silicon stencil using conventional lithography techniques. (b) Schematic process of screen printing using the silicon stencil and a pristine graphene ink. (c) Cross-sectional illustration of the screen printing method with the flexible silicon stencil during printing. ....	96
Figure 4.2. Schematic diagram of screen printing with a silicon stencil in a cross-sectional view. (a) The graphene ink is placed on the silicon stencil. (b) The squeegee moves the ink and presses the stencil at the same time, which makes contact between the stencil and the substrate. (c) As the squeegee passes the openings, the ink is printed on the substrate. (d) When the squeegee is removed from the stencil, the stencil separates from the substrate, leaving the ink on the substrate. ....	96
Figure 4.3. (a) Optical microscopy (OM) image of a thin silicon stencil showing line openings with different widths ( $w_{\text{screen}}$ ) of 20 (top), 30 (middle), and 40 $\mu\text{m}$ (bottom) in a silicon stencil. (b, c) High-resolution OM images for line openings with $w_{\text{screen}}$ of 20 and 5 $\mu\text{m}$ , respectively. (d) OM images of graphene lines printed on polyimide films through line openings with $w_{\text{screen}}$ of 20 (top), 30 (middle), and 40 $\mu\text{m}$ (bottom). The printing was accomplished from two inks of different viscosities (Ink 1 and 2), in two different printing directions (A and B). (e) Measured shear viscosity for Ink 1 and 2. (f) Width ( $w_{\text{printed}}$ ) of	

screen-printed graphene lines measured by OM on polyimide substrates with different inks and printing directions for varying  $w_{\text{screen}}$ ..... 98

Figure 4.4. AFM characterization of graphene flakes. (a) Representative AFM image of graphene flakes dropcast on  $\text{SiO}_2$ . Distributions of (b) flake thickness and (c) flake area for 715 particles, indicating typical flake dimensions of  $\sim 2$  nm thickness and  $\sim 70$  nm  $\times$  70 nm area. .... 101

Figure 4.5. (a) OM images of a screen-printed graphene line with  $w_{\text{printed}}$  of 40  $\mu\text{m}$  and (b-e) graphene lines (dark double stripes) with different spacing of 30, 50, 70, and 90  $\mu\text{m}$  on polyimide films. (f) Thickness of screen-printed graphene lines for different inks and printing directions. (g) Comparison of the aspect ratio (thickness/width) and  $w_{\text{printed}}$  of the printed graphene lines through a 20  $\mu\text{m}$  wide line opening with respect to the ink viscosity and the printing direction. .... 103

Figure 4.6. Surface profile of screen-printed graphene lines through 20  $\mu\text{m}$  wide line opening, from (a) Ink 1 in Direction A and B and (b) Ink 2 in Direction A and B.  $w_{\text{printed}}$  was measured from one side to the other side of printed graphene lines and thickness was obtained from average thickness between sides of printed graphene lines. .... 104

Figure 4.7. Aspect ratio (thickness/width) of the screen-printed graphene lines for different inks and printing directions..... 104

Figure 4.8. OM image of screen-printed graphene to measure electrical properties of the graphene lines for different lengths and  $w_{\text{printed}}$ . (b) SEM image of the graphene following annealing. (c) Resistance per unit length of the graphene as a function of  $w_{\text{printed}}$ . (d) Relative resistance of the screen-printed graphene lines on flexible substrates with two different thicknesses over 1000 bending cycles at a bending radius of 4 mm, corresponding to 1.0% tensile strain..... 106

Figure 4.9. Thickness of the printed graphene lines after annealing at a temperature of 300  $^{\circ}\text{C}$  for 30 min. .... 106

Figure 4.10. (a) OM image of screen-printed graphene source and drain electrodes on a polyimide substrate for EGTs ( $W/L = 900\mu\text{m}/90\mu\text{m}$ ). (b) Schematic illustration for the EGT architecture fabricated on the graphene electrodes. (c) Transfer and (d) output characteristics of the printed EGTs. The voltage sweep rate was 50  $\text{mV s}^{-1}$ . e) Stability of charge carrier mobility ( $\mu$ ) and threshold voltage ( $V_{\text{th}}$ ) for the EGTs during repeated bending cycles with a bending radius of 4 mm, corresponding to 1.0% strain. .... 109

Figure 5.1. Inkjet printing and intense pulsed light (IPL) annealing of graphene. (a) AFM image of graphene flakes; inset: image of graphene ink vial. (b) Schematic illustration of inkjet printing of graphene. (c) Schematic illustration of IPL annealing applied to graphene patterns..... 114

Figure 5.2. Characterization of solvent-exfoliated graphene comprising the inks. (a) Flake area distribution for the graphene sample, indicating both number-weighted and volume-weighted distributions. (b) Flake thickness distribution showing both number-weighted and volume-weighted histograms. .... 114

- Figure 5.3. (a) Graphene yield as a function of EC loading for sonication and shear mixing-based exfoliation. (b) TGA curves of graphene/EC powders prepared with different initial EC concentrations, illustrating the ability to broadly tune the final graphene/EC ratio. (c) Graphene content as a percentage by weight of total solids for different batches, both prior to and following the flocculation step..... 116
- Figure 5.4. Dependence of annealing on graphene:polymer ratio of the films. (a) Sheet resistance as a function of processing conditions for a film containing 25% wt. graphene for thermal (left) and IPL (right) annealing. (b) Corresponding sheet resistance as a function of annealing conditions for a film containing 50% wt. graphene, showing improved effectiveness of IPL annealing. .... 118
- Figure 5.5. Raman spectroscopy of graphene films. (a,b) Evolution of the Raman D-to-G band intensity ratio for films containing 25% wt. graphene following thermal and photonic annealing, respectively. (c) Representative spectra for films containing 25% wt. graphene prior to and following annealing with the most energetic thermal and IPL annealing conditions. (d-f) Corresponding data for films containing 50% wt. graphene. Raman spectra were collected using a 532 nm laser. .... 119
- Figure 5.6. Versatility of IPL annealing for graphene patterns. (a) Sheet resistance of graphene films as a function of annealing voltage, for different substrates (PET, PEN, PI, and glass). (b) Optical microscopy images of lines on five different surfaces with a drop spacing of 35  $\mu\text{m}$ , showing high-fidelity, uniform pattern definition. (c) Resolution of inkjet-printed lines on the five surfaces as a function of drop spacing..... 120
- Figure 5.7. Characterization of inkjet-printed graphene patterns. Optical images of printed lines with different drop spacing on various substrates, including untreated glass, HMDS-treated glass, PI, PEN, and PET. (bottom right) Printed drop array on untreated glass, showing stable and reproducible jetting and wetting performance. The direction of printing is oriented vertically in this image. .... 121
- Figure 5.8. Rheological properties of graphene inks. (a) Viscosity as a function of shear rate for high graphene content inks at temperatures relevant for inkjet printing. (b) Corresponding viscosity vs. shear rate plots for an ink with the same solids content, but lower graphene:EC ratio, showing a viscosity too high for optimal inkjet printing. .... 123
- Figure 5.9. Characterization of high concentration graphene inks. (a) Thickness as a function of printing passes for graphene/ethyl cellulose films as-printed and following thermal annealing. Dashed lines indicate the least squares linear fit to the thickness data, indicating a thickness per pass of 190 nm following thermal annealing. (b) Sheet resistance of graphene films at various thicknesses following thermal and IPL annealing, illustrating the suitability of IPL annealing over a broad range of film thickness. (c) Map of ink concentration and conductivity for reported non-metal conductive inkjet-printable inks, including inks based on graphene, RGO, CNTs, and PEDOT:PSS. The product of conductivity ( $\sigma$ ) and concentration ( $c$ ) is an indicator of the conductance achieved per printing pass, a key figure of merit for inkjet-printed conductors. Isolines for this metric are drawn as dashed lines to aid the eye. .... 124

- Figure 5.10. Film morphology changes as a function of annealing conditions, showing dark field optical microscopy images of films on PI following thermal and IPL annealing. As the pulse energy is increased, bubbles and other defects begin to form..... 128
- Figure 5.11. Film morphology as a function of film thickness for IPL annealing at 18.9 J/cm<sup>2</sup>. Thicker films exhibit features with a larger length-scale than thin films. .... 129
- Figure 5.12. Effectiveness of IPL annealing for films of different thicknesses. (a) Sheet resistance as a function of IPL annealing energy for films of varying thicknesses using a single light pulse. (b) Effect of multiple light pulses for films with one and eight printed layers, showing sheet resistance for a single 1-ms pulse and five 1-ms pulses spaced by 5 s. .... 129
- Figure 5.13. (a) Large-area inkjet-printed graphene patterns on PI. (b,c) Resistance measured over cyclic bending cycles of graphene lines on PEN following IPL annealing at 5.6 and 7.8 J/cm<sup>2</sup>, with bending radii of curvature of 8.1 and 1.3 mm, respectively (tensile strain of 0.0031 and 0.019, respectively). .... 130
- Figure 6.1. Process overview and ink characterization. (a) Schematic illustration of the preparation and utilization of nitrocellulose-based graphene inks, including the NC chemical structure (top left) and representative AFM image of graphene flakes (top right). (b,c) Graphene flake thickness and area distributions, respectively, showing both number-weighted and volume-weighted statistics from AFM measurements (number of flakes > 600). (d) Shear viscosity of graphene inks tailored to blade coating, inkjet printing, and spray coating. .... 136
- Figure 6.2. Liquid-phase exfoliation of graphene/NC by high shear mixing. (a) UV-Vis spectra following different exfoliation times, collected on diluted samples and rescaled. (b) Calculated graphene concentration as a function of exfoliation time, following a power-law relation..... 136
- Figure 6.3. Inkjet printing of the graphene/NC ink. (a) Drop formation sequence using a piezoelectric inkjet printer. (b) Printed drop array on glass showing high reproducibility and uniformity. (c) Height profile of an individual printed drop, showing suppression of coffee ring formation. (d) Printed line array, showing smooth coalescence of drops to form connected lines, along with inset height profile. (e) Photograph of flexible inkjet-printed graphene/NC patterns over a large area. .... 138
- Figure 6.4. TGA and in situ Raman characterization of graphene/NC. (a) TGA curves showing mass and mass derivative for graphene/NC (top) and pure nitrocellulose (bottom), indicating primary nitrocellulose decomposition at 200 °C with noticeable residue. (b) Raman spectra of graphene/NC films during in situ heating in an oxidizing environment, taken at ~75 °C increments. (c) Representative Raman spectrum with peak fitting taken at 350 °C, revealing the presence of peaks in addition to the original graphene. (d) Peak area relative to the G band, plotted as a function of temperature during in situ heating. .... 140
- Figure 6.5. Raman spectra for graphene/NC films as cast and following annealing, including (a) the full measured range and zoomed in regions showing (b) D and G peaks and (c) the 2D peak. Annealing is accompanied by a reduction in the D/G intensity ratio, a

slight decrease in the 2D peak, and the emergence of a distinct peak near the G band, associated with the polymer residue. .... 142

Figure 6.6. Chemical characterization of graphene/EC films. (a) Raman spectrum following thermal annealing with peak fitting, showing no evidence of amorphous carbon residue. (b) In situ Raman spectroscopy of graphene/EC films during thermal annealing. (c,d) FTIR spectra and XPS C1s spectra, respectively, for graphene/EC films as cast and following thermal annealing. .... 142

Figure 6.7. IR and XPS characterization of graphene/NC. (a) IR reflectance spectra collected from graphene/NC during in situ heating with 25 °C increments, showing characteristic changes resulting from polymer decomposition. (b) Intensity of a characteristic nitrate group peak at 1670 cm<sup>-1</sup> as a function of temperature. (c) Ex situ FTIR spectra before and after annealing at 350 °C. (d) XPS spectra of as-cast and annealed graphene/NC films showing the three constituent elements. (e) Atomic composition of as-cast and annealed graphene/NC films as determined by XPS. (f) High-resolution XPS spectra for as-cast and annealed graphene/NC showing the changes in the C1s peaks..... 144

Figure 6.8. Direct comparison of chemical characterization for graphene/NC and graphene/EC films, including in situ Raman spectroscopy, XPS, and FTIR spectroscopy..... 146

Figure 6.9. Morphology and electrical characterization of graphene films. (a) Plan-view (top) and cross-section (bottom) SEM images of a graphene film, showing a dense, compact microstructure with significant flake alignment. (b) Conductivity of graphene/NC films following annealing in air over the range 150-450 °C. (c) Relative resistance of graphene/NC lines following cyclic bending tests at a radius of curvature of 1.3 mm (bending strain ~4.8%)..... 147

Figure 6.10. Schematic of the Scotch™ tape test applied to graphene films with EC and NC..... 148

Figure 6.11. Mechanical and environmental stability of graphene processed with NC. (a) Images during (top) and after (bottom) the Scotch™ tape test for graphene patterns printed on polyimide. The dashed black lines indicate the outline of the tape, while the text 'graphene' is printed with graphene/EC (left) and graphene/NC (right). (b) Change in electrical resistance for graphene/EC and graphene/NC films following the Scotch™ tape test, with PI and glass substrates. (c) Series of images showing the water sonication test results for graphene/EC and graphene/NC. (d) Change in electrical resistance following the damp heat test, 312 h at 85 °C and 85% relative humidity, for graphene/EC and graphene/NC films on PI and glass..... 149

Figure 6.12. Water sonication test results for graphene/EC and graphene/NC, showing percentage of film remaining as a function of time during ultrasonication in deionized water. The graphene films are coated onto a glass slide and annealed prior to the test. .... 150

Figure 7.1. (a) Differential scanning calorimetry of graphene/NC showing large exothermic reaction of nitrocellulose at ~200 °C. (b) Corresponding data for graphene/EC showing endothermic decomposition for ethyl cellulose. Measurement is taken under nitrogen to more closely mimic rapid photonic annealing..... 155



- Figure 7.2. Schematic illustration and cross sectional SEM image showing assisted photonic annealing, with a self-fueled reaction yielding a porous graphene microstructure. Photonic annealing on a Si substrate is not typically possible due to the substrate's effective heat sink properties, but the reactive binder enables annealing through nearly the entire film, resulting in a porous microstructure..... 156
- Figure 7.3. Microstructural characterization of graphene films. (a,b) Cross sectional SEM images of graphene/EC films before and after exposure to pulsed light annealing, respectively, showing little change in microstructure suggesting ineffective annealing. (c,d) Corresponding images for graphene/NC films, showing evolution from a dense, polymer-rich microstructure to a porous, annealed film. .... 156
- Figure 7.4. Chemical characterization of photonic annealed graphene/NC films. (a) FTIR spectra for graphene/NC films following different annealing conditions. (b) Evolution of FTIR peak intensity with pulse energy showing a sharp threshold for annealing. (c) Elemental composition determined by XPS for the films. .... 157
- Figure 7.5. Chemical characterization of graphene/NC annealing. (a) XPS C1s spectra for graphene/NC films following different post-treatment conditions. (b) Representative Raman spectra for different annealing conditions. (c)  $I_D/I_G$  ratio following annealing on various substrates, showing a consistent reduction following photonic annealing for different substrates. .... 158
- Figure 7.6. Electrical characterization of photonic annealed graphene/NC films. (a) Sheet resistance relative to thermally annealed samples for graphene/NC and graphene/EC, showing an abrupt threshold for nitrocellulose decomposition and minimum resistance on par with thermal annealing. (b) Normalized sheet resistance relative to thermal annealing for graphene/NC films on various substrates. (c) Sheet resistance for graphene/NC films as a function of thickness following thermal and photonic annealing. Note that the thickness corresponds to thickness prior to annealing (photonic annealing leads to thicker films with the same amount of material due to porosity)..... 160
- Figure 7.7. Printed graphene/NC microsupercapacitors. (a) Photograph of the extrusion printing head during device fabrication, with inset photograph of printed interdigitated electrodes. (b) Optical profilometry data showing the height map of the device active area. (c) Cyclic voltammetry for devices following thermal and photonic annealing. (d) Device capacitance as a function of current for MSCs from galvanostatic charge/discharge cycling. .... 163
- Figure 7.8. Characterization of graphene MSCs. (a) Thickness and (b) capacitance of printed graphene/NC MSCs as a function of printed layer number, showing a consistent linear increase in both values. (c) Capacitance for graphene/EC MSCs with different thicknesses, showing saturation of the performance. (d) Capacitance retention of graphene/NC MSC over 1000 cycles..... 164
- Figure 8.1. Process flow and comparison of IGZO TFTs with silver and graphene contacts. (a) Schematic illustration of the fabrication of inkjet-printed IGZO TFTs with silver and graphene source/drain electrodes. (b,c) Representative saturation transfer characteristics

for IGZO TFTs with silver and graphene contacts, respectively (channel length $\sim 200 \mu\text{m}$ ). .....	170
Figure 8.2. Annealing optimization for IGZO TFTs with silver contacts. (a) Box plots of mobility for IGZO with silver contacts fabricated with processing temperatures from 150-250 °C ( $n = 31$ , 5 min annealing in ambient at the specified temperature in each case). (b,c) Representative transfer curves and corresponding gate leakage, respectively, for IGZO TFTs with silver contacts.....	171
Figure 8.3. Effect of device architecture on IGZO TFTs with graphene contacts. (a-c) Representative output characteristics of IGZO TFTs with graphene source/drain electrodes in a top contact, bottom contact, and middle contact configuration, respectively (channel length $\sim 200 \mu\text{m}$ ). Inset diagrams illustrate cross-sections of the device structure in each case.....	172
Figure 8.4. Representative output curves for non-optimal IGZO devices. (a) Output characteristics for an IGZO TFT with silver source/drain contacts, following optimal annealing at 200 °C. (b,c) Output characteristics for IGZO TFTs with graphene bottom and top contacts, respectively. Note the low drain current for the case of (b), and the nonlinearity at low bias for (c).....	173
Figure 8.5. Atomic force microscopy characterization of an IGZO TFT with graphene contacts. (a,b) AFM topography images at the channel-electrode interface and at the center of the electrode, respectively. (c,d) Height histograms for regions on the IGZO film and on the graphene electrode, respectively.....	174
Figure 8.6. (a) Optical microscopy image of IGZO TFTs with graphene contacts inkjet-printed on Si/SiO <sub>2</sub> . (b) Thickness profile across an inkjet-printed IGZO film following five printing passes, showing an average thickness of 15 nm.....	174
Figure 8.7. Measured mobility ( $\mu_{\text{SAT}}$ ) for top, bottom, and middle contact devices as a function of channel length ( $n = 40, 25, 122$ for TC, BC, and MC, respectively).....	175
Figure 8.8. Electrical characteristics of MC IGZO TFTs with graphene contacts. (a,b) Current on/off ratio ( $I_{\text{ON}}/I_{\text{OFF}}$ ) and threshold voltage ( $V_{\text{TH}}$ ), respectively, plotted against channel length ( $n = 122$ ). .....	176
Figure 8.9. Electrical characterization of IGZO TFTs with graphene middle contacts. (a) Measured mobility for devices as a function of channel length ( $n = 122$ ). (b) Total resistance plotted against channel length, which allows for the extraction of contact resistance by the transmission line method. (c) Contact resistance plotted as a function of gate voltage.....	178
Figure 8.10. Contact resistance measurements for IGZO TFTs with graphene contacts. (a,b) Total resistance plotted against channel length for top contact and bottom contact devices, respectively. (c,d) Contact resistance plotted against gate bias for top contact and bottom contact devices, respectively. ....	179
Figure 8.11. Characterization of hysteresis for MC IGZO TFTs with graphene contacts. (a) Threshold voltage hysteresis from the forward and reverse sweeps of the transfer	

characteristics. (b) Difference in calculated mobility based on the forward and reverse voltage sweeps. (c) Calculated mobility plotted against channel length using the average mobility calculated from the forward and reverse voltage sweeps. Number of devices, $n = 122$ .....	181
Figure 8.12. Electrical performance of MC graphene/IGZO TFTs during aging in ambient conditions. (a-c) Transfer characteristics for a single device measured nine times over the course of 365 days, with different axes scaling. ....	182
Figure 8.13. Stability of graphene/IGZO TFTs against ambient aging. (a) Mobility, (b) $I_{ON}/I_{OFF}$ , and (c) $V_{TH}$ , measured at various times over 365 days ( $n = 22$ ). ....	182
Figure 8.14. Stability of graphene/IGZO TFTs against high temperatures. (a) Mobility, (b) $I_{ON}/I_{OFF}$ , and (c) $V_{TH}$ , measured following post-fabrication thermal treatment to 100-400 °C in air ( $n = 30$ ). ....	183
Figure 8.15. Connection of graphene/IGZO TFTs with silver interconnects. (a) Schematic illustration showing TFT fabrication process with silver inserted into standard MC graphene/IGZO TFTs. (b) Optical micrograph showing the printed devices, with the different materials indicated. (c) Representative transfer curve for the TFTs.....	185
Figure 9.1. Proof of concept demonstration of graphene as a stable interfacial material for eGaIn. (a) Schematic of test setup, showing eGaIn printed over exposed and graphene-covered silver lines, with alloy formation occurring for the eGaIn-silver interface. (b) Optical microscopy image showing formation of the silver-eGaIn alloy resulting in large defects. (c) Optical microscopy image showing a graphene-passivated junction with a silver-graphene-eGaIn configuration, with no alloy formation evident. ....	190
Figure 9.2. Optical profilometry images of the samples shown in Figure 9.1b-c, confirming the alloy formation and severe instability of the silver-eGaIn junction (a) and passivated junction with graphene (b). ....	191
Figure 9.3. Process development for the integration of eGaIn with graphene. (a) Optical microscopy images showing printed tracks of eGaIn (horizontal lines) across a bare glass-graphene film boundary (left: glass; right: graphene), resulting in changes in line morphology. Following annealing of the graphene films at 250-350 °C, stable wetting of the eGaIn was achieved to print continuous lines. (b) Summary of aspect ratio for printed eGaIn lines on glass and graphene, showing a systematic trend of decreasing aspect ratio, associated with improved wetting, for graphene films annealed at higher temperatures. ....	192
Figure 9.4. Electrical characterization of graphene interfaces. (a) Contact resistance measurement for a graphene-eGaIn junction using the transmission line method. (b) Summary of contact resistances for three junction configurations, namely silver-graphene, eGaIn-graphene, and silver-graphene-eGaIn. The reduced contact resistance in the silver-graphene-eGaIn configuration is likely a result of current crowding for the individual silver-graphene and graphene-eGaIn junctions. (c) Normalized electrical resistance of silver-graphene-eGaIn junctions following thermal treatment, showing stable performance up to at least 300 °C. ....	194

- Figure 9.5. Mechanical testing of graphene contacts for liquid metal. (a) Normalized resistance of silver-graphene-eGaIn structures over 250 bending cycles, with the resistance change subdivided into contact resistance associated with the eGaIn and total resistance including the silver-graphene lines. (b) Normalized resistance of graphene-eGaIn junction as a function of bending angle, showing a small and reversible change in resistance likely due to deformation of the eGaIn patterns. (c) Normalized resistance of graphene-eGaIn junctions over 100 bending cycles, showing stable performance. .... 196
- Figure 10.1. Templating C<sub>60</sub> deposition with a graphene film. (a,b) GIXD data and SEM image, respectively, for a C<sub>60</sub> film deposited on ITO. (c,d) Corresponding data for a C<sub>60</sub> film deposited on graphene at 150 °C, showing improved crystallinity. (e) Schematic of device design and (f) electrical characterization, showing greatly improved current density for films deposited on graphene (the inset labels indicate the graphene ink concentration, and correlate with film thickness). .... 200
- Figure 10.2. Foldable organic transistors on paper using graphene electrodes. (a) Change in conductance of graphene lines as a function of folding cycles, showing retention of performance following extreme mechanical deformation. (b,c) SEM images of graphene lines on glassine paper before and after folding, respectively. (d) Photograph of printed graphene electrodes on paper for EGT fabrication. (e) Transfer curves and (f) mobility and threshold voltage for transistors over 100 folding cycles. .... 202
- Figure 10.3. High resolution graphene printing for organic transistors. (a) SEM image showing a 3.2 μm wide graphene line on PET, with a pitch of 6 μm. (b) Macroscopic photograph and (c) microscope image of fabricated EGTs using graphene electrodes. (d,e) Transistor performance for devices based on clean silver electrodes and graphene electrodes, showing superior stability with graphene. .... 203
- Figure 10.4. Printed graphene microsupercapacitors. (a) Schematic structure of a printed graphene MSC on polyimide. (b) Cyclic voltammetry data for the MSC at various scan rates, showing suitable operation as an electrolytic double layer capacitor. (c) Capacitance as a function of current density, collected from galvanostatic charge/discharge measurements. (d-f) Stability of device performance upon extended cycling, operation while under strain, and repeated bending, respectively. Red data points in (e) and (f) correspond to a MSC, while black points correspond to a sandwich-structure supercapacitor. .... 205
- Figure 11.1. Processing conductive nanomaterials with ethyl cellulose. (a) Thermal gravimetric analysis data for a silver nanoparticl/EC composite, showing ~20% wt. silver nanoparticles with minimal EC residue. (b) SEM image of a composite silver nanoparticle/MWCNT film following annealing, showing homogeneous dispersion of the materials enabled by a common polymer dispersant, EC. .... 209
- Figure 11.2. Extending processing methods to post-graphene 2D nanomaterials. (a) Photograph of a spray coated thin film of hBN held in front of the ink vial. (b) Photograph of an exfoliated MoS<sub>2</sub> dispersion with EC. (c,d) TGA data for hBN/EC powders, including the mass curve and mass derivative, respectively. .... 210

Figure 11.3. Phase inversion for morphology control. (a) Schematic explanation of the phase inversion process based on a ternary phase diagram, adapted from Ref. 287. (b) SEM images of graphene/EC films cast using a phase inversion process to induce porosity. .... 213

Figure 12.1. Scaling production of graphene inks for large-area flexible electronics. (a) Photograph of a closed-loop system for graphene exfoliation based on high shear mixing. (b) Photograph of large area inkjet-printed graphene patterns. .... 224

**LIST OF TABLES**

Table 1.1. Summary of typical process metrics for common printing techniques, adapted from Ref. 14. ....	36
Table 1.2. Summary of pristine graphene inks developed for various printing methods. ....	51
Table 5.1. Comparison of non-metal ink characteristics from the recent literature (plotted in Figure 5.9c). ....	126
Table 8.1. Device metrics for IGZO TFTs having different contact geometries. ....	176

# **CHAPTER ONE**

Introduction and Background

## 1.1. Motivation and Thesis Statement

Manufacturing is a core component in technological development, constituting the linchpin between scientific discoveries, practical applications, and realization on a broader societal scale. Connecting scientific discovery to practical implementation is a key challenge in accelerating technological progress, with broad significance across many facets of society. For electronics, conventional materials and manufacturing platforms have unleashed unprecedented opportunities, ushering in the information age. However, despite their incredible success, the scope of electronics technologies has certain limitations. Notably, high temperature processing with intrinsically brittle and rigid materials limits the possibility for flexible devices and low-cost, high-throughput production.

Printed electronics is an emerging manufacturing paradigm for electronic devices, leveraging liquid-phase patterning capabilities coupled with compatible electronically functional materials. While there remain limitations in process complexity, resolution, and performance, as will be discussed in detail later, the ability to print a diverse array of electronic materials and devices would offer a compelling foundation for research and development for a wide range of electronic systems. A key requirement for this vision is the ability to process high performance electronic materials in a liquid phase. This presents a clear challenge for materials science – to broaden the palette of electronically functional liquid inks.

This thesis is focused on graphene, which offers a suite of properties highly desirable for applications in printed electronics. However, the two-dimensional nature of graphene imparts a tendency to aggregate in a colloidal phase, limiting its compatibility and performance for integration in printed electronics. Here, this dispersion stability is directly addressed using a



stabilizing cellulose derivative. This offers a high-performance system with excellent versatility, enabling the integration of graphene in printed electronics for a wide range of applications. This thesis will examine the materials, processing, and properties relationships for this material system, while also highlighting several practical applications. The rest of this chapter will detail the background information and context to frame the remainder of the thesis.

## **1.2. Introduction to Printed Electronics**

Printed electronics describes a manufacturing paradigm that leverages liquid-phase, additive printing methods for the fabrication of electronic devices and circuits. This platform offers numerous benefits for commercial applications, but for more widespread impact it requires significant technological development and research spanning materials, patterning methods, devices, and systems. Printed electronics is built on materials and methods distinct from conventional silicon-based electronics to enable complementary functionality and applications.<sup>1</sup> The field leverages high-throughput, solution-phase processing methods originally developed for graphic arts printing such as inkjet, gravure, and screen printing, and is therefore well-suited for large-area applications.<sup>2</sup> Moreover, low-temperature, solution-phase processing circumvents substrate limitations present in traditional electronics manufacturing, enabling functional devices on flexible, low-cost, plastic or paper substrates.<sup>3</sup> These characteristics of printed electronics position it competitively for inexpensive, large-area and flexible systems with a range of functionality. By integrating electronically responsive components, such as chemical, biological, mechanical, and optical sensors,<sup>4-6</sup> with signal processing and data storage elements, such as logic and memory circuits,<sup>7</sup> overall system functionality is enhanced. Combining this with information

communication devices, such as displays and wireless radio frequency transmission antennae,<sup>8-10</sup> along with power management strategies, such as batteries and solar cells,<sup>11,12</sup> enables a fully functional system with a diverse spectrum of possible applications,<sup>13</sup> as illustrated in Figure 1.1. The promise of printed electronics is to enable this system in a large-area, flexible format at low cost.

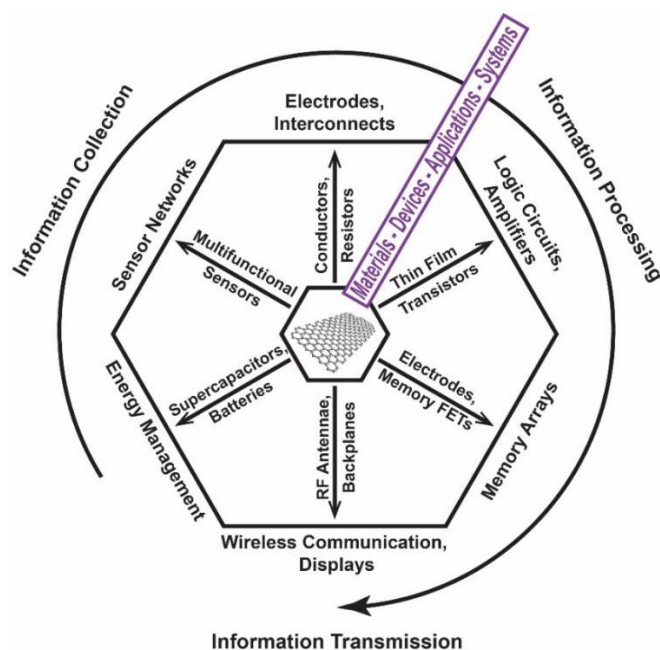


**Figure 1.1.** Schematic illustration of various printed electronics technologies. The combination of information collection, processing, and transmission in a common process framework underlies the potential of printed electronics to impact and enable emerging technologies, such as the Internet of Things.

Printed electronics is in many ways complementary to conventional silicon-based electronics, as shown in Figure 1.2. For end-use applications, the flexibility afforded by printing onto plastic and paper substrates offers a key advantage for robust and bendable products. In terms of manufacturing, liquid-phase printing methods scale to large areas and high throughput production very efficiently. Moreover, the simplified process flow of an additive method offers more straightforward design of processes and more environmentally benign production. Low-

temperature methods broaden the scope of compatible materials, opening design space not accessible for silicon-based circuits. Ultimately, the low cost, versatile production, and novel functionality of printed electronics presents a compelling justification for sustained research and development. It is worth noting that the performance, integration density, and reliability of printed electronics will not match that of conventional circuits, due to limitations in patterning resolution and intrinsic materials properties. As a result, there is widespread belief that many of the first advanced, commercial implementations of printed electronics will be in hybrid systems, interfaced with conventional circuits to handle the demanding data processing functions. Whether as a standalone product, or in combination with silicon chips, printed electronics is a growing commercial sector with initial products appearing and broader market penetration expected.

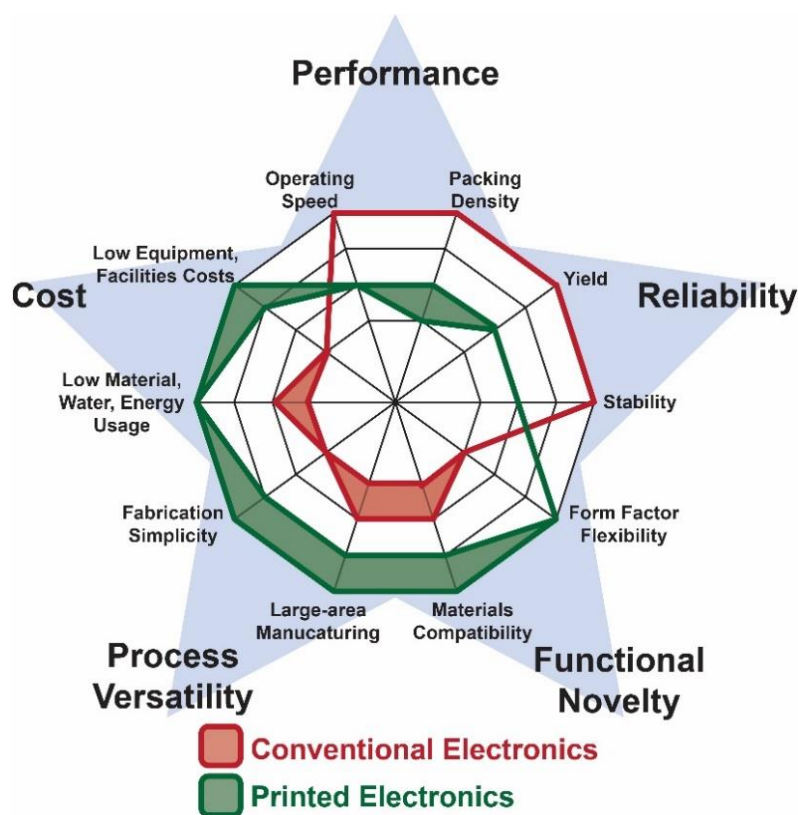


**Figure 1.2.** General comparison of metrics for printed electronics (green) and conventional silicon electronics (red), showing tradeoffs in cost, performance, functionality, and processing.

The targeted applications for printed electronics offer insight into the practical benefits of this technology and realistic areas of use. Several examples highlight the potential for this to be a disruptive technology with broad impacts in everyday life, as shown in Figure 1.3. Radio frequency identification (RFID) tags printed at low cost could transform inventory and logistics. Rather than a barcode, a wireless RFID tag could track parts or products, either through the manufacturing process or through retail. Customers could walk through a grocery store, filling their cart with the desired items, and walk out the door without standing in line at the checkout, with each item in the cart identified and charged for automatically. An application such as this depends critically on driving down the cost of components, a key prospect for printed electronics. The Internet of Things constitutes another concept for which printed electronics could provide significant foundational capability. The widespread deployment of distributed sensors will require not only the sensors, but associated logic circuits, power management, and data communication functionalities. Being able to deliver all components in a cost-effective manner would fuel the impending emergence of the Internet of Things. A third application area for which printed electronics is likely to have significant impact is large-area optoelectronic devices. The scalability of liquid-phase patterning methods makes them particularly suitable for these devices, such as large-screen displays, lighting, and photovoltaics. Finally, the mechanical flexibility afforded by this process technology allows improved interfacing of electronic devices with humans, suggesting biomedical applications and wearable devices.

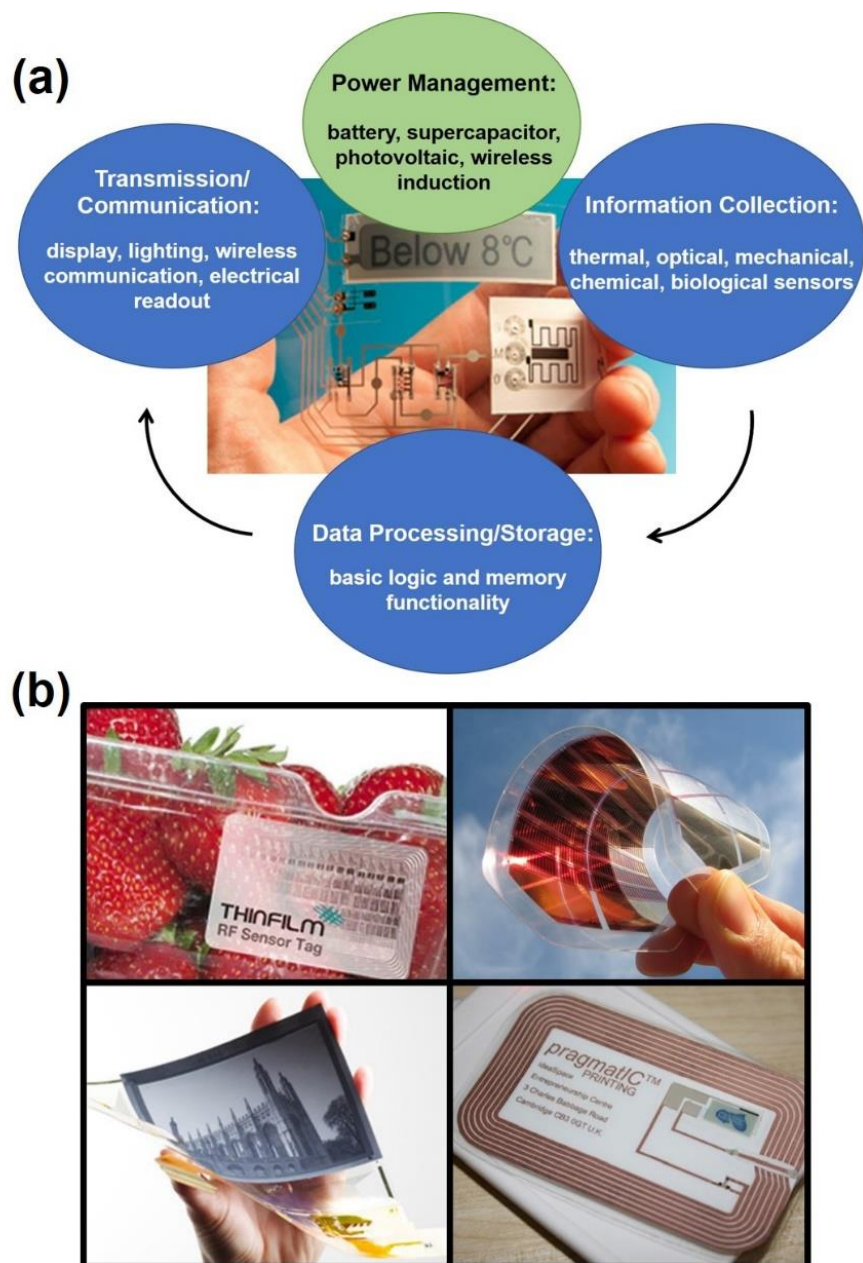


**Figure 1.3.** Selected target applications for printed electronics. (a) Illustration showing integration of multiple operations in a single product to build up more complex functionality. (b) Images of target applications, including (clockwise from top-left) sensor tags, photovoltaics, RFID chips, and displays.

### **1.3. Technical Background for Printed Electronics**

#### *1.3.1. Technologies and Processes for Printed Electronics*

The field of printed electronics leverages mature liquid-phase patterning technologies originally developed for graphic arts printing. The variety of methods available can be classified into digital and master-based techniques, and span a range of process metrics as shown in Figure 1.4 and summarized in Table 1.1. Digital printing methods, exemplified by inkjet and direct-write printing, use computer-controlled motion systems to define the printed patterns. In inkjet printing, microscale (~10-20 micron) droplets of ink are deposited individually onto a substrate to precisely define functional patterns. This is commonly known as drop-on-demand printing, and the digital nature of patterning is particularly well-suited to rapid prototyping and custom fabrication, in that parts can be modified on the fly. Master-based techniques, such as gravure and screen printing, require up-front time to machine a master containing the pattern. Screen printing involves pushing a paste through a stencil screen using a squeegee to reproduce the stencil pattern on the substrate, and is widely used industrially due to its simple and robust nature. Gravure, offset, and flexographic printing are roll-to-roll processes that use machined cylinders with the defined patterns as positive or negative features to transfer ink onto the substrate similar to a stamp. Following the initial investment to create the pattern masters, these methods can achieve very high printing speeds up to ~1000 m/min, establishing their utility for high-throughput, mass production of large-area components. By offering a low-cost route to either custom fabrication or high-throughput production, printed electronics has broad utility in manufacturing. Some methods, such as inkjet printing, offer favorable characteristics for both digital and high-speed patterning due to advances in parallelization, making them particularly attractive.

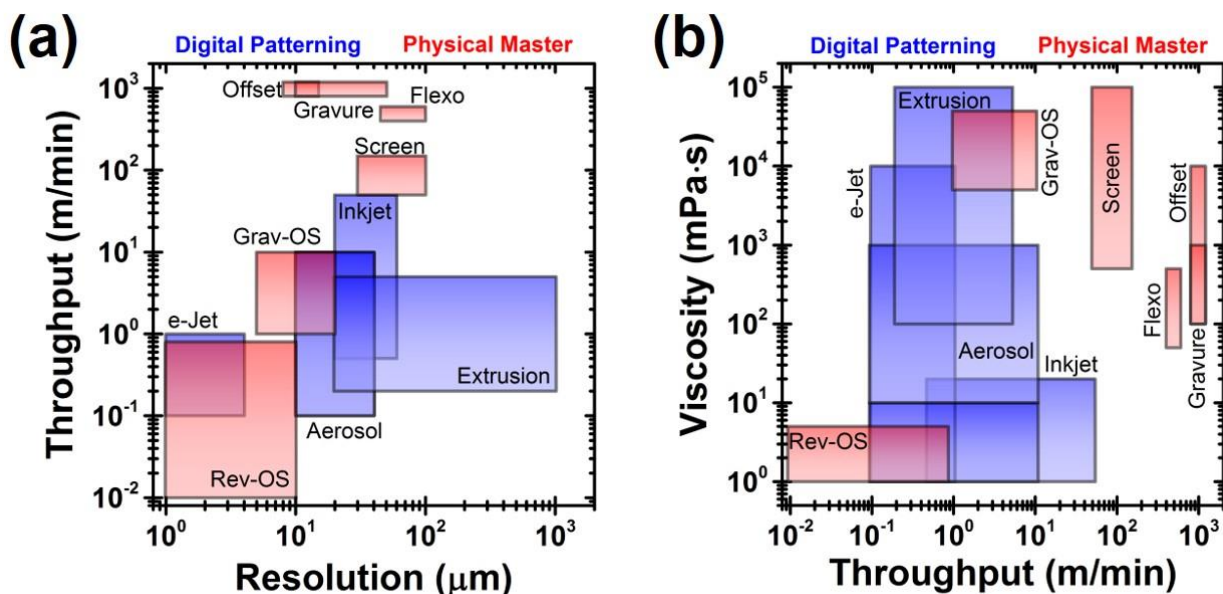


**Figure 1.4.** Process metrics for several common printing techniques. (a) Typical resolution and throughput for several printing methods. (b) Required viscosity of different printing methods plotted against typical throughput, showing target viscosities spanning five orders of magnitude. Data taken in part from Ref. 14.

While process throughput is an important determinant of production cost, the resolution and thickness attained by different printing techniques is critical for device performance. Printing methods commonly achieve printing resolution in the 10-100 μm length scale, with pattern thicknesses ranging from tens of nanometers to tens of microns. While high resolution is commonly beneficial for device performance, as will be discussed later, the desired thickness is application-dependent. For example, conductive lines require thicker deposits for lower resistance, while gate dielectrics require thin, uniform films for improved capacitance. Moreover, multilayer configurations require careful consideration in design to prevent defects resulting from printing on a nonuniform surface.

Method	Ink Viscosity (mPa·s)	Resolution (μm)	Line Thickness (μm)	Process Speed (m/min)
<b>Digital</b>				
Inkjet	1-20	20-60	0.1-1	1-500
E-Jet	1-10 <sup>4</sup>	1-4	0.001-0.1	<1
Aerosol Jet	1-10 (UA) 10-10 <sup>3</sup> (PN)	10-40	0.1-1 0.1-100	1-10
Extrusion	10 <sup>3</sup> -10 <sup>5</sup>	20-1000	10-100	0.1-2
<b>Physical Master</b>				
Offset	10 <sup>2</sup> -10 <sup>4</sup>	8-15	1-10	~1000
Gravure	10 <sup>2</sup> -10 <sup>3</sup>	10-50	0.1-1	~1000
Flexo	50-500	45-100	<1	~500
Screen	5 <sup>2</sup> -10 <sup>5</sup>	30-100	5-100	50-150
Grav-OS	5 <sup>3</sup> -5 <sup>4</sup>	5-20	1-3	1-10
Rev-OS	1-5	1-10	0.05-1	0.01-1
<b>Other</b>				
Transfer	--	0.1-5	~1	Slow
Nanoimprint	--	0.01-1	~0.1	Slow

**Table 1.1.** Summary of typical process metrics for common printing techniques, adapted from Ref. 14.

UA = ultrasonic; PN = pneumatic; OS = offset

In addition to different factors affecting production (digital/physical master, throughput) and performance metrics (resolution, thickness), the various printing methods have disparate requirements for compatible inks. The fluid viscosity is a critical parameter for designing inks for a printing method. As a function of ink composition and concentration, the viscosity can limit the range of printing methods for which a given ink or material is compatible. Solubility or dispersion stability limitations can prevent the development of high viscosity pastes, while low viscosity inks may require reduced solids loading, and thus deposition thickness, to maintain process compatibility. A general illustration of the target viscosity for different printing methods is given



in Figure 1.4b. As is evident from this plot, for a given viscosity range only a subset of printing techniques is realizable. As such, the ability to tailor the viscosity over a broad range is important in generalizing a given material or ink chemistry.

Given the diversity of printing techniques with differing requirements (fluid viscosity), performance (resolution/thickness), and cost (throughput, pattern definition mode), hybrid manufacturing combining multiple deposition methods is considered for complex device integration (Figure 1.5). This further reinforces the demand to formulate inks based on a material for a suite of printing methods. Effective ink development requires careful tuning of ink characteristics, such as viscosity, surface tension, and drying characteristics. Due to its versatility and commercial relevance, inkjet printing is widely used for laboratory experimentation. With digital pattern generation, broad materials compatibility, additive processing, and substrate versatility due to the non-contact printing mechanism, this technique is well-suited for rapid prototyping. As such, due to its relevance for this work, inkjet printing is discussed here in greater detail.

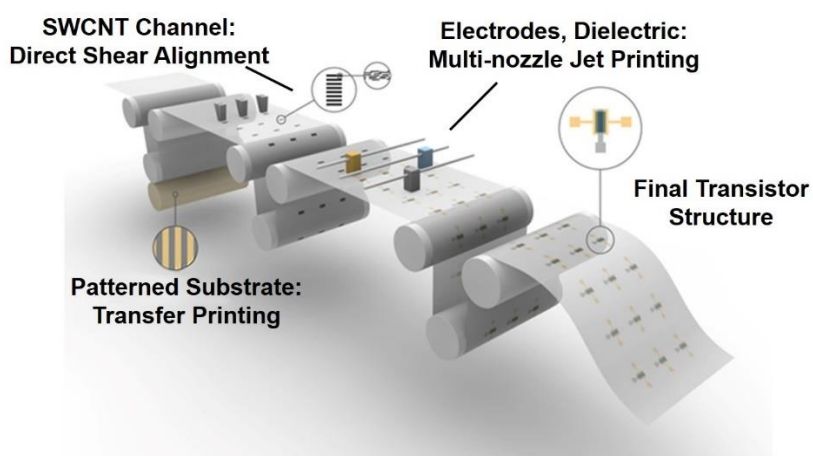


**Figure 1.5.** Schematic illustration of a hybrid manufacturing process for transistor fabrication, indicating multiple deposition techniques being used for particular materials, adapted from Ref. 15.

As discussed above, inkjet printing is well-suited to laboratory-scale experimentation. As a digital printing technique, it enables rapid prototyping and on the fly pattern variation. Due to its additive nature and precise application, it offers efficient materials usage. In addition, the non-contact nature of printing maintains compatibility with a broad range of substrates. The characteristics of suitable fluids for inkjet printing have been extensively studied, and are important for three key physical processes: jetting, wetting, and drying. Jetting behavior has been correlated with the inverse of the Ohnesorge number, defined as  $Z$ , a dimensionless grouping of parameters defined by

$$Z = \frac{\sqrt{\rho\sigma a}}{\eta} \quad (1.1)$$

in which  $\rho$  is the density,  $\sigma$  the surface tension,  $\eta$  viscosity, and 'a' denotes the characteristic length scale, in this case the inkjet nozzle diameter. A value of  $1 < Z < 10$  or  $1 < Z < 14$  is considered suitable for inkjet printing; inks exceeding this range often exhibit satellite drop formation, while inks with a lower  $Z$  value are often not ejected from the nozzle (Figure 1.6).<sup>16,17</sup> Moreover, particle-based inks are susceptible to nozzle clogging; this can be caused by ink drying at the nozzle plate due to improper design of the evaporation kinetics, or to trapped air bubbles which nucleate at large particles.<sup>18</sup>

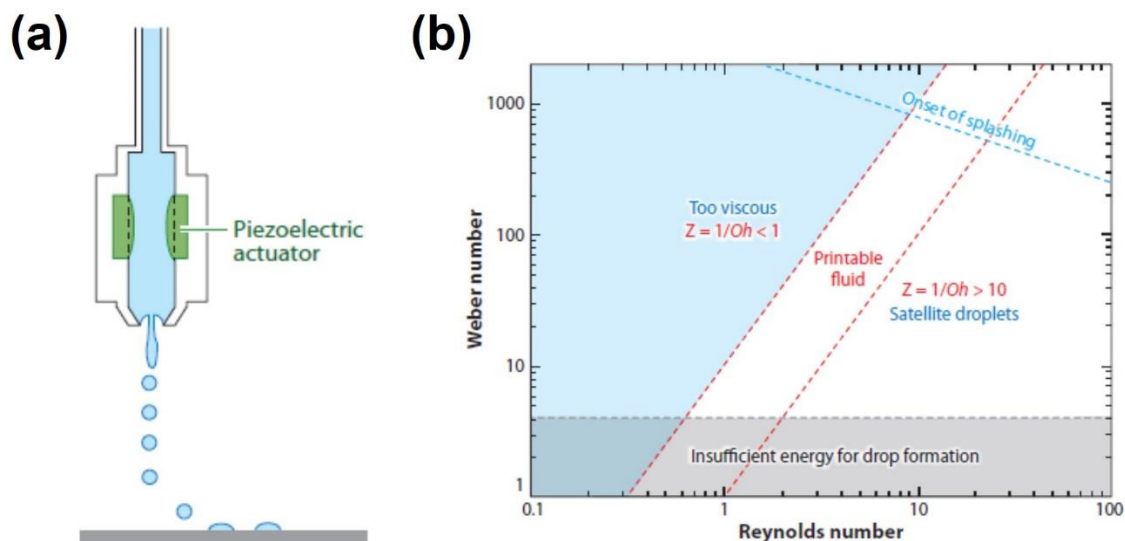


**Figure 1.6.** Fundamentals of inkjet printing. (a) Schematic illustration of piezoelectric inkjet printing, which uses an electronically-driven actuator to eject droplets of ink onto the substrate for drop-on-demand patterning. (b) Phase space for ink design and printing in terms of dimensionless fluid dynamics parameters, namely the Weber number, the Reynolds number, and the inverse Ohnesorge number. Figures adapted from Ref. 17.

In addition to proper jetting behavior, inks must wet the substrate in a controlled manner. This depends on the ink surface tension, the substrate surface energy and topography, and the unique interaction between the substrate and the ink. Drops on the substrate must coalesce to form continuous lines and films; if the drops break apart due to a Rayleigh instability, the continuity and uniformity of the resulting film are limited (Figure 1.7a).<sup>19</sup> The final physical process involved for inkjet printing is the ink solidification, typically by solvent evaporation. Pinning of the contact line at the ink-substrate-air boundary is commonly observed, and complex patterns cannot be formed without this phenomenon.<sup>20</sup> However, this often leads to the coffee ring effect; accelerated evaporation at this contact line drives fluid flow from the center of the pattern to the edge, resulting in enhanced material deposition at the contact line. A common strategy to mitigate this effect is to

add high boiling solvents to suppress evaporation (Figure 1.7b). In addition, the solvent system can be tailored to produce a surface tension gradient during drying, leading to a Marangoni flow which counteracts the fluid flow toward the contact line.<sup>21,22</sup>

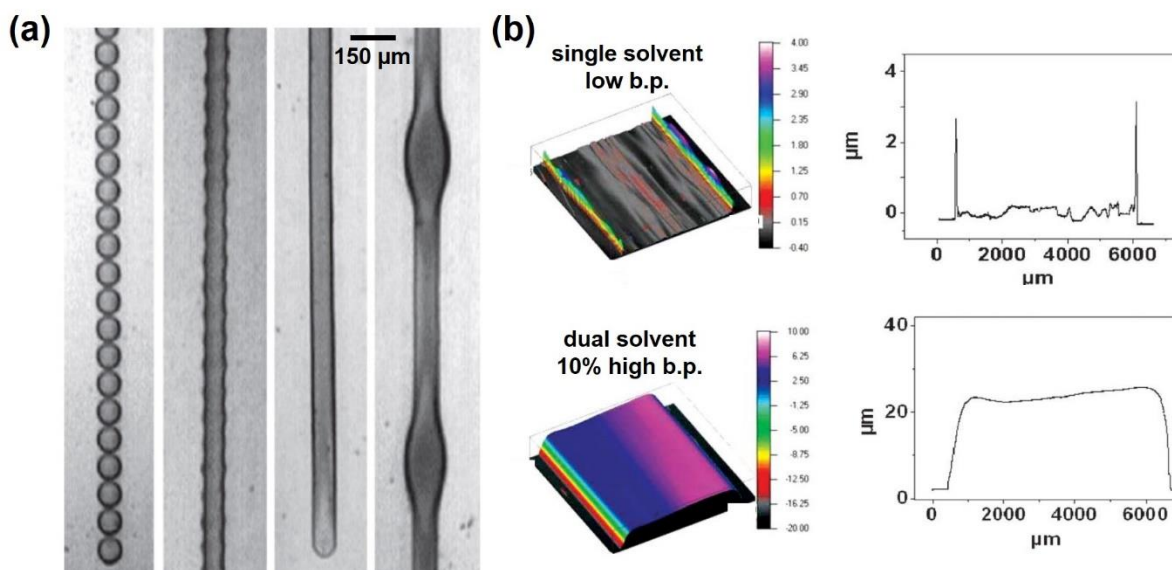


**Figure 1.7.** Wetting and drying processes in inkjet printing. (a) Typical line shapes with varying drop spacing and wetting properties, ranging from coalesced droplets to bulging lines; adapted from Ref. 17. (b) Influence of solvent mixture on printing morphology, showing enhanced uniformity following the addition of 10% high boiling cosolvent; adapted from Ref. 23.

### 1.3.2. Materials for Printed Electronics

The materials generally employed in printed electronics can be classified based on electronic band structure as conductors, dielectrics and semiconductors. Common conductive inks are based on metal nanomaterials, most commonly silver, copper and gold; select conductive polymers such as PEDOT:PSS; and carbon nanomaterials, including carbon nanotubes and graphene.<sup>24</sup> Printable dielectric materials include insulating polymers, certain metal oxides, and electrolytes,<sup>25</sup> while semiconductors include conjugated polymers, aromatic molecules,

semiconducting single walled carbon nanotubes (s-SWCNTs) and amorphous metal oxide semiconductors.<sup>14,26–28</sup> Each of these materials offers distinct characteristics in terms of performance, ease of processing, and stability; in addition, the unique interactions between materials can dominate the properties of devices. Due to their relevance to this work, conductive inks will be discussed in greater detail here (Figure 1.8).

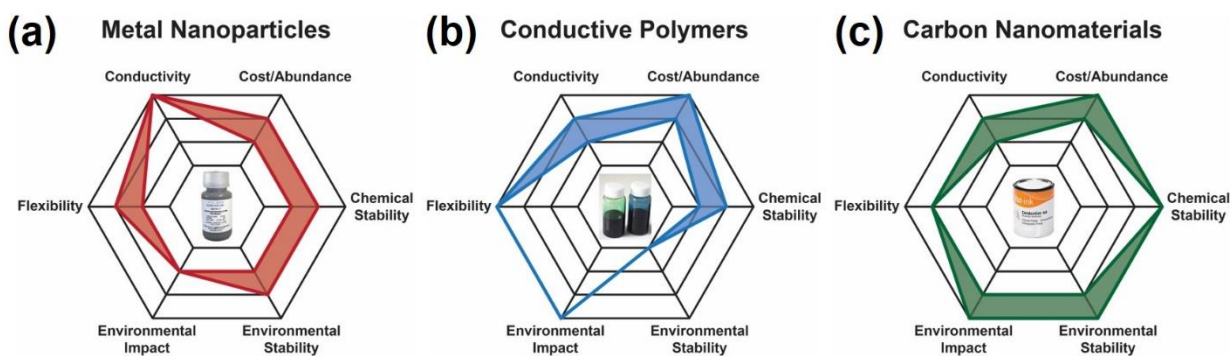


**Figure 1.8.** Qualitative comparison of the primary classes of conductive inks, including (a) metals, (b) polymers, and (c) carbon materials.

Metal-based inks offer the highest conductivity among printed conductors. Silver is the most prevalent conductive ink due to its high conductivity and resistance to oxidation. For inkjet printing, silver nanoparticles offer good colloidal stability, and can be formulated in either aqueous or solvent-based inks with appropriate ligands.<sup>24,29</sup> Alternatively, reactive silver inks based on silver precursor salts with built-in reducing agents have recently been demonstrated, offering a particle-free alternative similar to molecular silver inks for select printing methods.<sup>30</sup> For applications demanding excellent oxidation stability or materials compatibility (i.e., bioelectronics and OTFTs), gold-based inks have also been employed.<sup>31</sup> Due to its low cost, there is significant interest in developing inks based on copper. The primary technical challenge facing this is the

tendency of copper particles to oxidize, which has driven advances in post-processing methods such as pulsed light annealing.<sup>32–35</sup>

Conductive polymers offer a low-cost, highly flexible alternative to metal-based inks for applications in which conductivity is not critical. Poly(3,4-ethylenedioxythiophene):polystyrene sulfonate, or PEDOT:PSS, is a prototypical conductive polymer consisting of a polythiophene conjugated polymer and a sulfonated polystyrene. PEDOT:PSS is widely used as a transparent conductor in applications such as organic light-emitting diodes (OLEDs) and organic photovoltaics (OPVs).<sup>36,37</sup> Despite its favorable characteristics including low cost, mechanical flexibility, good conductivity, and transparency in thin films, the chemical and environmental stability of this material restricts its application space.

For applications requiring robust stability, carbon-based materials constitute the third class of conductive inks. Conventional carbon-based inks used commercially are based on carbon black and graphite. While carbon black is used primarily as a material for resistors, graphite offers improved conductivity. Although the electrical performance is still lower than conductive polymers, and several orders of magnitude lower than metal-based inks, these inks are used for certain applications such as glucose test strips. More recently, carbon nanomaterials including carbon nanotubes and graphene have attracted interest for conductive inks.<sup>24,38,39</sup> These materials based on sp<sup>2</sup>-bonded carbon offer improved conductivity, and can be compatible with high resolution liquid-phase patterning methods. The high surface area of these nanomaterials is also beneficial for select applications, such as energy storage and sensing. Moreover, the excellent mechanical, chemical, electrochemical, thermal, and environmental stability of carbon-based materials is desirable for many applications in printed electronics.

## 1.4. Introduction to Graphene

### 1.4.1. Structure and Properties of Graphene

Graphene, the two-dimensional,  $sp^2$ -bonded allotrope of carbon, has been the focus of widespread research in recent years.<sup>40,41</sup> The electronic,<sup>42</sup> thermal,<sup>43</sup> and mechanical<sup>44</sup> properties of graphene make it an attractive material for a variety of applications, including high-speed electronics,<sup>45</sup> energy storage devices,<sup>46</sup> sensors,<sup>47</sup> and composites.<sup>48</sup> Some important attributes of graphene include its linear dispersion relation, excellent thermal conductivity and strength, and high surface area. A range of different graphene production methods exist, each producing a distinct grade of material. While initial studies of fundamental graphene physics employed micromechanical exfoliation of graphene crystals with very high quality, practical applications of this material require more directed, high throughput techniques. Epitaxial growth of graphene on SiC by Si sublimation is one such technique, and is particularly suitable for electronics applications.<sup>49</sup> Growth of graphene on select metals by chemical vapor deposition (CVD) is widely studied, and offers a promising route toward large-area single- and multi-layer graphene films, which can be transferred onto various substrates for electronic devices and transparent conductive films.<sup>50</sup> In addition, solution-phase techniques have been developed based on chemical synthesis,<sup>51</sup> exfoliation of pristine graphite,<sup>52</sup> and the exfoliation and subsequent reduction of graphite oxide.<sup>53</sup> Due to their compatibility with liquid-based printing processes, these solution-phase graphenes are suitable for printed electronics.

### 1.4.2. Liquid-Phase Exfoliation of Graphene

For printed electronics applications, liquid-phase manipulation of graphene is necessary. Top-down approaches to exfoliate graphene sheets from graphite precursors fall into two categories: exfoliation of pristine graphene and exfoliation of graphene oxide followed by reduction.<sup>53,54</sup> Given the persistent structural and electronic degradation resulting from oxidation and reduction, the use of pristine graphene is desirable.<sup>55,56</sup> Coleman and coworkers first demonstrated the liquid-phase exfoliation (LPE) of graphene by ultrasonication, a process schematically illustrated in Figure 1.9.<sup>52</sup> They found that select solvents, such as N-methyl pyrrolidone (NMP) and dimethyl formamide (DMF), present a surface tension suitable for stabilizing graphene flakes against aggregation, while sonication-induced cavitation provides sufficient force to exfoliate graphite. In other work following this initial demonstration, Coleman and coworkers extensively characterize process parameters, correlating graphene stability with solvent solubility parameters,<sup>57</sup> identifying centrifugation methods for crude particle size selection,<sup>58</sup> and developing strategies for producing highly concentrated samples.<sup>59</sup> While these methods rely on the solvent alone to ensure the stable dispersion of graphene, alternative procedures utilize various surfactant chemistries. Lotya, et al. report using the aromatic surfactant sodium dodecylbenzene sulfonate to exfoliate and disperse graphene in aqueous solutions, with exfoliation of small graphene flakes at a concentration of up to 50  $\mu\text{g/mL}$ .<sup>60</sup> Green and Hersam employ the planar surfactant sodium cholate to disperse graphene at a concentration of up to 90  $\mu\text{g/mL}$  with good stability, enabling sorting of the flakes by layer number using density gradient ultracentrifugation.<sup>61</sup> Liang and Hersam use the cellulose derivative ethyl cellulose (EC) in ethanol to exfoliate and disperse graphene at a concentration of 122  $\mu\text{g/mL}$ , and use this material to



produce conductive thin films and composites.<sup>62</sup> Numerous stabilizing molecules, particularly polycyclic aromatic molecules such as pyrenes, have also been investigated, as well as many polymers.<sup>54</sup> One disadvantage to exfoliation based on ultrasonication is damage to graphene flakes. Using detailed Raman analysis, Bracamonte, et al. show the formation of topological defects such as pentagon-heptagon pairs in graphene flakes following sonication for longer than 2 hours.<sup>63</sup>

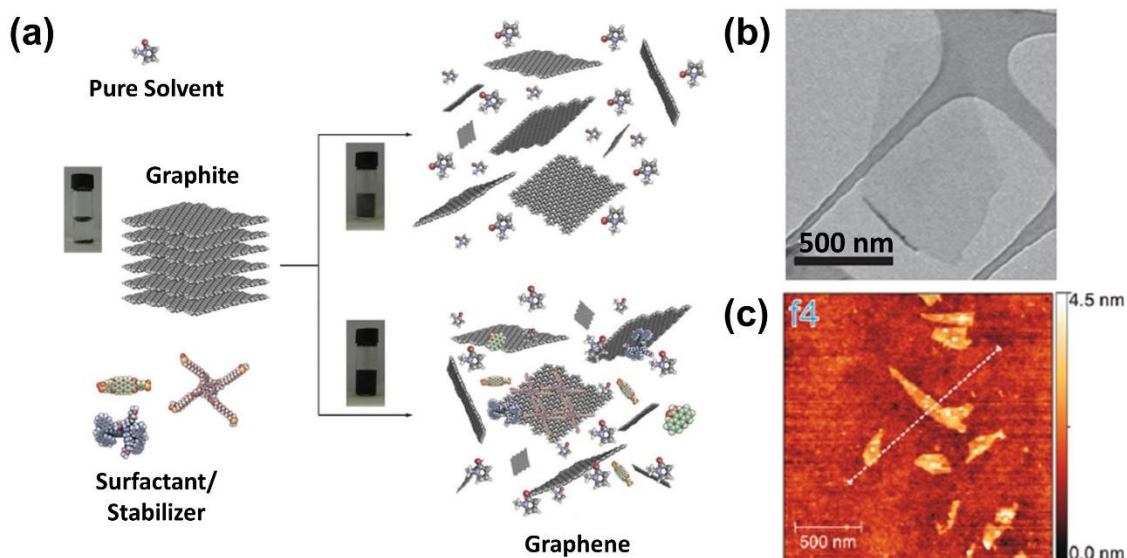


**Figure 1.9.** Introduction to liquid-phase exfoliation (LPE) of graphene. (a) Schematic diagram describing the exfoliation of graphite to produce graphene in pure organic solvents (top) and with surfactants or stabilizers (bottom), adapted from Ref. 54. (b) Transmission electron microscopy image of a single-layer graphene flake produced by LPE of graphene in N-methyl pyrrolidone, taken from Ref. 52. (c) AFM image of single-layer graphene flakes produced by LPE of graphene with the aqueous surfactant sodium cholate and isolated from multi-layer flakes by density gradient ultracentrifugation, taken from Ref. 61.

While ultrasonication is widely used to produce graphene for academic research, alternative techniques have been developed. Knieke, et al. demonstrate a mechanical milling technique to produce predominantly few-layer graphene in a scalable and efficient process, with concentrations up to 25 mg/mL.<sup>64</sup> In addition, Li and coworkers report an electrochemical

exfoliation technique capable of producing uniformly thin graphene flakes with a lateral size up to 30  $\mu\text{m}$ , which show excellent transparent conductivity metrics of  $\sim 210 \Omega/\square$  at 96% transmittance.<sup>65</sup> Paton, et al. establish high shear mixing for the scalable and efficient exfoliation of graphene using both NMP and aqueous surfactants, showing a high production rate along with good material quality free of oxidation.<sup>66</sup> High shear mixing using a rotor-stator configuration is a scalable technique widely used industrially, and therefore is a promising method for graphene production. In a recent study, Karagiannidis, et al. establish microfluidization of graphite for centrifugation-free, 100% yield of dispersed few-layer graphene in an aqueous medium, overcoming the severe yield limitations of preceding demonstrations.<sup>67</sup> By forcing graphite flakes through microchannels under high pressure, efficient and uniform size reduction is realized. While the high pressure and cooling requirements imposed by this method are not ideal, the high yield makes this a compelling possibility for commercial application.

## **1.5. Graphene Inks**

### *1.5.1. Motivation for Graphene Inks*

With the aforementioned excellent properties, and compatibility with solution-phase processing, graphene presents promising advantages for printed electronics. In many cases, it is the unique combination of properties offered by graphene that establishes it as a leading candidate for applications. Figure 1.10 illustrates general properties of graphene, along with application areas in which these properties could be desirable. The ability of graphene to bridge application areas with its suite of characteristics motivates the development of graphene-based technologies. Printed

electronics is one such field in which graphene presents numerous advantages and opportunities for practical impact.

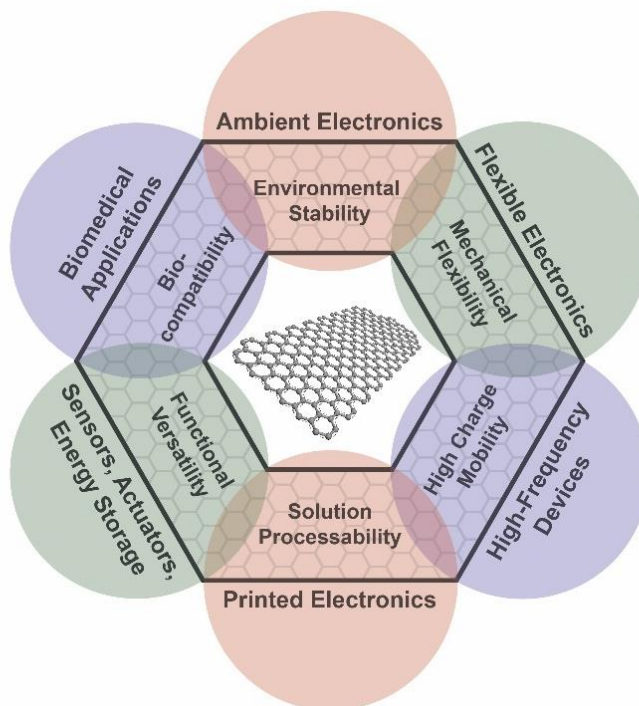


**Figure 1.10.** Breadth of applications for graphene. From center to edge, the structure, key attributes, and corresponding possible application areas are delineated.

### 1.5.2. Literature Overview

Two general strategies have been demonstrated for inkjet printing, shown schematically in Figure 1.11a-b. Graphene can be exfoliated directly in NMP and subsequently printed onto select substrates, as demonstrated for TFTs and electrodes.<sup>68,69</sup> Alternatively, graphene can be stabilized in a broader range of organic solvents using the polymer ethyl cellulose (EC) or similar polymer dispersants.<sup>70-72</sup> Figure 1.11c shows a general comparison of the benefits and disadvantages of each strategy.

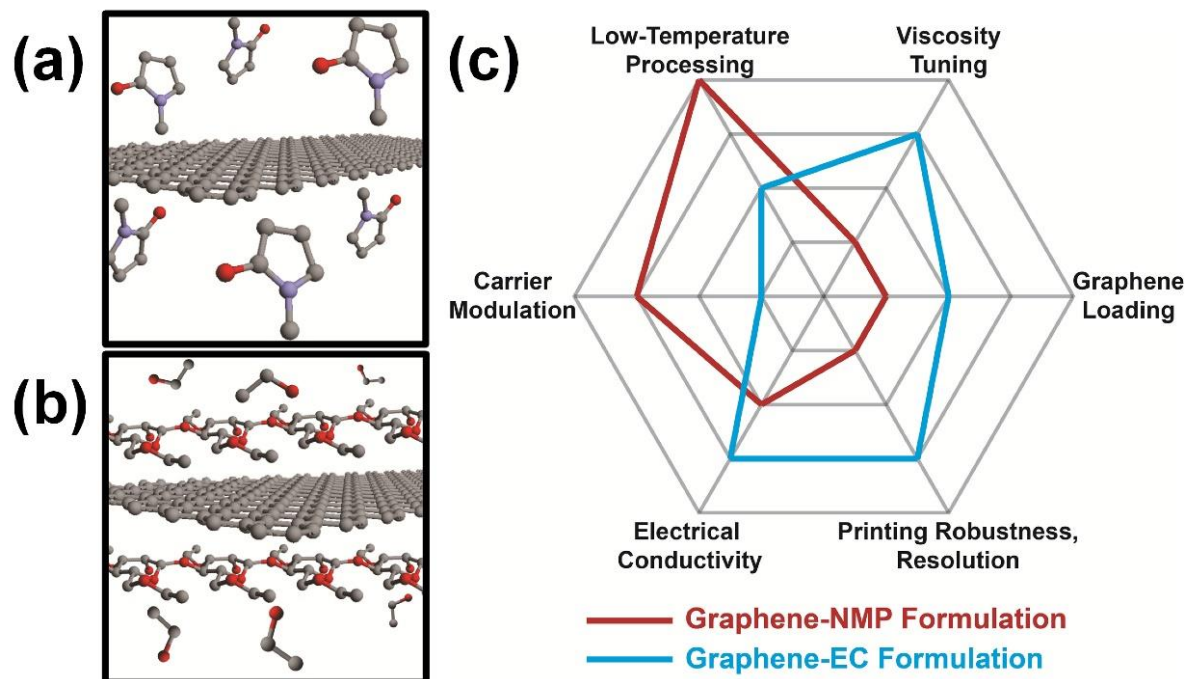


**Figure 1.11.** Pristine graphene inks for printed electronics. (a-b) Illustration of two different chemistries for pristine graphene inks, specifically direct dispersion in select organic solvents and polymer-stabilized dispersion using ethyl cellulose for (a) and (b), respectively. (c) Target plot illustrating the tradeoffs between the ink chemistries for a range of desirable attributes, highlighting the room for improvement through alternative ink chemistries or further development of existing methods.

Using NMP to exfoliate and disperse graphene, Ferrari and coworkers print graphene on HMDS-treated Si/SiO<sub>2</sub> and glass substrates for transparent conductors and thin film transistors.<sup>68</sup> With a large flake size of 300-1000 nm, limited bulk disorder, and high content of single-layer flakes, a mobility of ~95 cm<sup>2</sup>/V·s and current on-off ratio of ~10 is realized (Figure 1.12a-c). Finn, et al. also employ NMP for inkjet printing of graphene.<sup>69</sup> Using redispersion methods to tailor the graphene concentration and flake size, an optimized ink containing ~1.6 mg/mL graphene with a mean lateral size of ~170 nm is printed on coated polyethylene terephthalate (PET) substrates. The conductivity with no post-annealing treatment is measured to be 3000 S/m, and saturates for films

>160 nm thick. An alternative method to disperse graphene, used by Li, et al., uses the polymer EC to stabilize graphene in ethanol and terpineol.<sup>71</sup> Following exfoliation in DMF, graphene is transferred to an EC/terpineol solution by rotary evaporation, after which ethanol is added to tune the fluid properties. While offering good printing behavior and line morphology, this strategy necessitates thermal annealing at 375 °C to yield a conductivity of 3400 S/m. Microsupercapacitors (MSCs), narrow-line resistors, and TFTs are demonstrated based on this ink (Figure 1.12d-f). Hersam and coworkers also use EC to stabilize graphene dispersions, using a solvent system of cyclohexanone and terpineol. A conductivity of ~25000 S/m is achieved following annealing of printed patterns at 250 °C.<sup>70</sup> The favorable process and functional properties resulting from EC have led to broader adoption of this chemistry.<sup>72,73</sup> In addition, alternative cellulose derivatives, including nitrocellulose,<sup>74</sup> carboxymethyl cellulose,<sup>67</sup> and hydroxypropyl methylcellulose,<sup>75</sup> have all been shown to offer similar benefits. In addition to generalizing the methods to alternative polymers, the high colloidal stability and tunable viscosity enables translation to alternative printing methods, such as gravure and screen printing, as will be discussed in greater detail below.<sup>76-78</sup> This scope of the graphene ink literature is summarized in Table 1.2, which lists the composition and key metrics for pristine graphene inks.

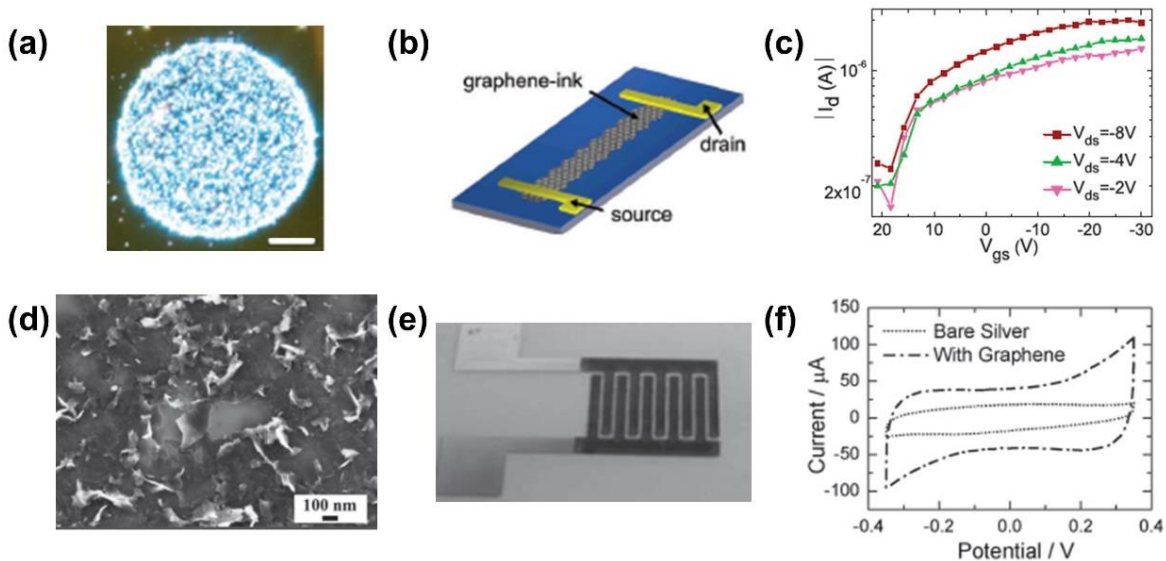


**Figure 1.12.** Inkjet printing of graphene. (a) Dark-field optical microscopy image of an inkjet-printed drop of graphene from NMP on a treated glass slide. (b) Schematic of a TFT with inkjet-printed graphene as the channel and (c) transfer characteristics of the inkjet-printed graphene TFT, showing a current on-off ratio of  $\sim 10$  and a mobility of  $\sim 95 \text{ cm}^2/\text{V}\cdot\text{s}$ . (a-c) adapted from Ref. 68. (d) SEM image of inkjet-printed graphene using EC, ethanol and terpineol, following annealing. (e) Optical image of a microsupercapacitor (MSC) based on inkjet-printed graphene and (f) current-voltage characteristics of the MSC structure. (d-f) adapted from Ref. 71.

Printing Method	Dispersant	Solvent	Loading (mg/mL)	Annealing Temp. ( $^{\circ}\text{C}$ )	Conductivity (S/m)	Ref.
Aerosol	EC	CHO/TpOH	3.1	250	8300	78
Inkjet	--	NMP	0.1	100	100	68
Inkjet	--	NMP	6.0	70	3000	69
Inkjet	EC	CHO/TpOH	3.4	250	25000	70
Inkjet	EC	EtOH/TpOH	1.2	375	3400	71
Inkjet	EC	CHO/TpOH	1	300	9240	72
Inkjet	EC	NMP/EG	3.2	350	40000	73
Inkjet	EC	CHO/TpOH	20	Phot.	--	79
Inkjet	HPMC	H <sub>2</sub> O/BD	8.5	250	24000	75
Inkjet	NC	EL/OA/EGDA	10	350	40500	74
Inkjet	Pyr-SA	H <sub>2</sub> O/PG	8	300	12500	80
Inkjet	EC	EtOH/TpOH	1-2	400	--	81
Inkjet	EC	CHO/TpOH/ DEGME	15	350	--	82
Gravure	EC	TpOH	20	250	10000	76

Screen	PVP/PVAc	DPGME	3-26	100	1300	83
Screen	PVP/PVAc	DPGME	~25	Phot./Comp.	29000	84
Screen	PVP/PVAc	DPGME	~25	Phot./Comp.	25000	85
Screen	unknown	unknown	unknown	100/Comp.	43000	86
Screen	EC	TpOH	80	300	18600	77
Screen	EC	TpOH	80	Phot.	--	87
Screen	CMC	Water	100	300	20000	67

**Table 1.2.** Summary of pristine graphene inks developed for various printing methods.

Dispersants: EC = ethyl cellulose; HPMC = hydroxypropyl methylcellulose; NC = nitrocellulose; Pyr-SA = pyrene-sulfonic acid derivative; PVP/PVAc = copolymer polyvinylpyrrolidone-polyvinylacetate; CMC = sodium carboxymethylcellulose

Solvents: CHO = cyclohexanone; TpOH = terpineol; NMP = N-methyl pyrrolidone; EtOH = ethanol; EG = ethylene glycol; H<sub>2</sub>O = water; BD = 2,3-butanediol; EL = ethyl lactate; OA = octyl acetate; EGDA = ethylene glycol diacetate; PG = propylene glycol; DEGME = di(ethylene glycol) methyl ether; DPGME = di(propylene glycol) methyl ether

Misc.: Phot. = photonic annealing; Comp. = compression; loading is graphene loading only

Due to its low cost and ready availability, reduced graphene oxide (RGO) is commonly used for inkjet-printed electronics, demonstrating a range of potential applications for printed graphene. This overview is not intended to offer a comprehensive summary of inkjet-printed RGO, but to highlight select publications which demonstrate unique applications of graphene materials. Dua, et al. demonstrate inkjet-printed vapor sensors based on RGO, with a baseline conductivity of 1500 S/m and an electrical response to various molecules, including NO<sub>2</sub>, NH<sub>3</sub>, Cl<sub>2</sub> and CH<sub>3</sub>OH.<sup>88</sup> Huang, et al. print graphene oxide (GO), with subsequent thermal reduction, to demonstrate H<sub>2</sub>O<sub>2</sub> sensors and interconnects with a conductivity of 900 S/m.<sup>89</sup> Lee and coworkers also print GO, with subsequent thermal reduction, to demonstrate flexible MSCs and temperature sensors.<sup>90,91</sup> Jang and coworkers pattern GO using inkjet printing, and employ a hydrazine or vacuum annealing treatment to demonstrate dipole antennae and acoustic actuators.<sup>92,93</sup> Lim, et al. prepare an ink based on RGO and PVA to print electrodes for pentacene-based OTFTs, with superior performance compared to gold and PEDOT:PSS electrodes demonstrated.<sup>94</sup> Su, et al., also

use inkjet-printed RGO for TFT electrodes. Using weakly-reduced GO, with chemical vapor reduction following printing, they demonstrate patterns with an electrical conductivity as high as 42000 S/m, and use the material as source, drain and gate electrodes for SWCNT TFTs.<sup>95</sup> Select applications of inkjet-printed RGO are illustrated in Figure 1.13.

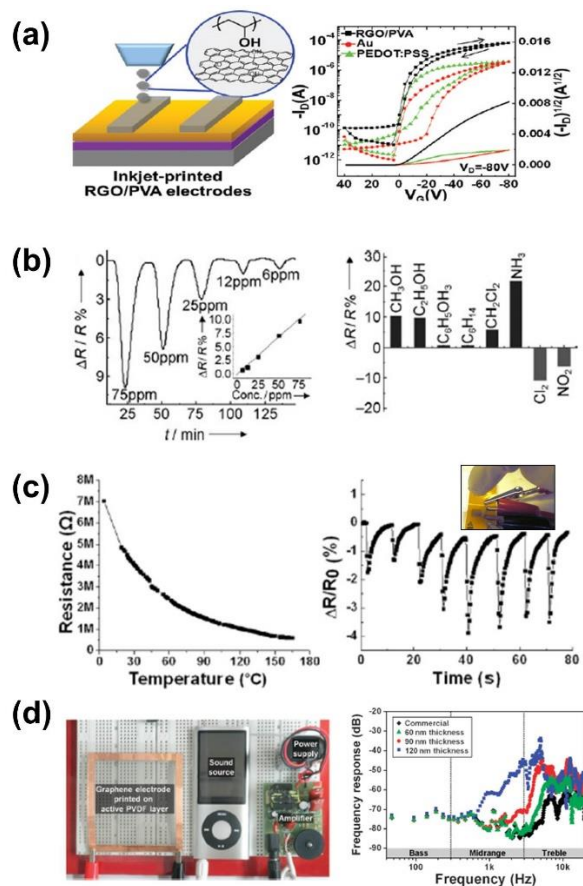


**Figure 1.13.** Printed devices based on reduced graphene oxide (RGO). (a) Schematic (left) and transfer curves (right) of a pentacene OTFT with inkjet-printed electrodes based on RGO, with similar devices using gold and PEDOT:PSS contacts for comparison, adapted from Ref. 94. (b) Response of a RGO vapor sensor exposed to  $\text{Cl}_2$  vapor at varying concentrations (left) and to various gases ( $\text{NH}_3$ ,  $\text{Cl}_2$ ,  $\text{NO}_3$  at 100 ppm) (right), adapted from Ref. 88. (c) Temperature sensing capability of an RGO film, including resistance plotted against temperature (left) and the resistance response due to tapping with a finger (right), adapted from Ref. 91. (d) Function of RGO thin film as an acoustic actuator electrode, including speaker system design (left) and frequency response (right), adapted from Ref. 92.



While inkjet printing constitutes the primary method used in academic labs, other printing methods have also been demonstrated. Huang, et al. develop a wireless strain sensor based on gravure-printed GO following thermal reduction, as well as a sulfonated-RGO flexible chemical sensor for the detection of NO<sub>2</sub>.<sup>96,97</sup> Hersam and coworkers demonstrate gravure printing of pristine graphene, using EC-stabilized graphene in terpineol along with a modified flooding-doctoring-printing method to produce patterns with a conductivity of ~10000 S/m following annealing at 250 °C.<sup>76</sup> This strategy was also employed to design inks for screen printing graphene, using thinned silicon stencils to screen print high resolution patterns with a conductivity of 18600 S/m.<sup>77</sup> Qian, et al. demonstrate screen printing of RGO using EC and terpineol for electron field emission applications.<sup>98</sup> In addition, Mülhaupt and coworkers develop thick dispersions of RGO for 3D microextrusion to produce free-standing films and supercapacitor electrodes,<sup>99,100</sup> and Arapov, et. al present a gelled graphene dispersion method using a copolymer of polyvinylpyrrolidone and polyvinylacetate for screen printing of graphene.<sup>83-85</sup> Recently, Ferrari and coworkers demonstrated a viscous graphene ink for blade-coating using carboxymethyl cellulose as a binder with a straightforward and high-yield microfluidization method.<sup>67</sup> A common trend of graphene inks requiring high viscosity for methods such as screen printing is the use of a polymer dispersant or binder, as this offers broader control over rheology and enables higher concentration dispersion of graphene without aggregation.

## **1.6. Recent Progress in Printed Electronics**

Recent advances in the broader field of printed electronics, not limited to graphene inks, are presented here. Due to the expansive and diverse nature of this field, the discussion here will

focus on select trends and prominent advances rather than a comprehensive overview of the field. This discussion spans research in materials/inks, processing methods, and concepts for devices and applications. Awareness of these broader developments in the field of printed electronics provides important context for the utility of graphene inks and the work presented in this thesis.

### *1.6.1. Materials: Post-Graphene 2D Nanomaterial Inks*

Following the development of graphene-based inks, there has been substantial research into graphene analogues, 2D nanomaterials offering distinct properties. Foremost among these are transition metal dichalcogenides (TMDCs) and hexagonal boron nitride, shown in Figure 1.14a-b.<sup>101</sup> Hexagonal boron nitride (h-BN) is a wide bandgap insulator isoelectronic to graphene, which has attracted interest as an ultrathin dielectric and for thermal management applications due to its high thermal conductivity.<sup>102–105</sup> The family of TMDCs offers a range of electronic properties, encompassing n-type and p-type semiconductors, superconductors, and conductors, and featuring strong optical absorption.<sup>106,107</sup> In many cases, dispersion and printing strategies developed for carbon can be adapted for other 2D nanomaterials, accelerating their development for various applications.<sup>69,108</sup> For example, direct bandgap semiconducting TMDC nanosheets such as single-layer MoS<sub>2</sub> and WS<sub>2</sub> offer promising properties for optoelectronic and sensing applications. Liquid-phase exfoliation and printing of these materials has been shown, as illustrated in Figure 1.14c, with photodetectors demonstrated for both MoS<sub>2</sub> and WS<sub>2</sub>.<sup>69,109,110</sup> In general, the devices based on a network of TMDC nanosheets offer reduced performance relative to single-flake analogues, possibly due in part to electronic inhomogeneity and solvent or dispersant residue separating the flakes.<sup>111</sup> In this sense, recent dispersant-free strategies for exfoliating and

processing these materials are promising for cleaner interfaces.<sup>112,113</sup> An additional benefit of solution-phase processing for post-graphene nanomaterials is the straightforward fabrication of hybrid and composite structures.<sup>114,115</sup> In particular, several recent demonstrations have shown devices composed entirely of nanosheets, spanning conducting, insulating, and semiconducting functionality.<sup>80,110,116</sup> Ultimately the performance of these devices will need to improve for them to be competitive with traditional technologies for realistic applications, but these demonstrations illustrate the technical progress of the field in recent years.

There are many colloidal nanosheets beyond hBN and TMDCs that have received less attention. Conductive materials, such as solution-processed 2D carbides and select IV-VI compounds,<sup>117-119</sup> offer superior electrical performance to graphene. Moreover, given the limitations in controlling morphology and uniformity in thin films of 2D flakes, the relaxed requirements for printed conductors make such materials promising for practical application. For semiconducting characteristics, 2D oxides have received relatively little attention, but have demonstrated good performance in network devices composed of many flakes,<sup>120</sup> and may offer broader process compatibility for ambient annealing compared to chalcogenides.

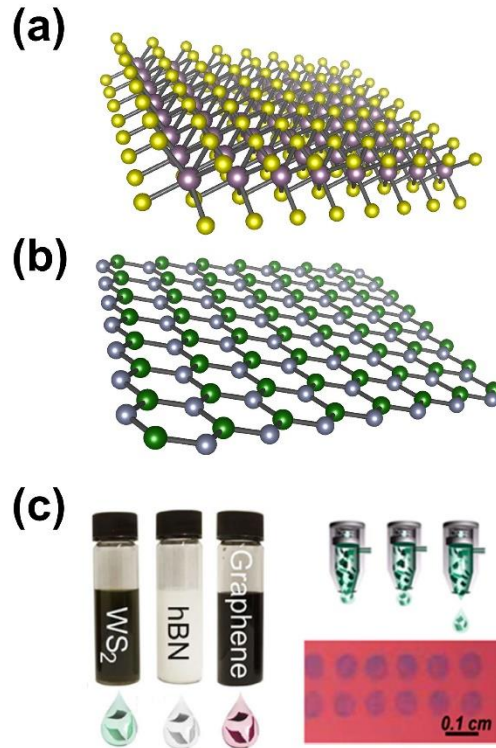


**Figure 1.14.** Post-carbon nanomaterial inks. (a) Schematic structure of a MoS<sub>2</sub> nanosheet, which is a prototypical TMDC. (b) Illustration of a h-BN nanosheet with atomic thickness and honeycomb structure similar to graphene. (c) Vials of liquid-phase exfoliated 2D nanosheets of WS<sub>2</sub>, h-BN, and graphene (left) as well as inkjet printing schematic and inkjet-printed patterns on Si/SiO<sub>2</sub> (right); adapted from Ref. 110.

### 1.6.2. Methods: Resolution, Registration, and Direct-Write

Recent advances in printing methods focus on three key areas, namely resolution, registration, and direct-write methods. High resolution patterning is critical for device performance and integration density, and underlies many of the improvements in silicon-based circuits in recent decades. In particular, operating speed can be described by the cutoff frequency of transistors, approximated as

$$f_T \approx \frac{\mu_{eff}(V_G - V_{TH})}{2\pi L(L + 2L_C)} \quad (1.2)$$

in which  $f_T$  is the cutoff frequency,  $\mu_{\text{eff}}$  the effective mobility,  $V_G$  and  $V_{\text{TH}}$  the gate and threshold voltages,  $L$  the channel length, and  $L_C$  the contact length, which is related to parasitic capacitance. Reducing the channel length provides an effective route to improving speed. This both increases the current through a device, and decreases the capacitance, or total charge required to switch it, while also allowing a higher density of devices per substrate area. There are a number of strategies being pursued to scale down feature size through advanced printing methods. Among digital printing techniques, electrohydrodynamic jet (e-jet) printing offers the highest resolution, with micron-scale line width.<sup>121,122</sup> For higher throughput methods, careful fundamental and computational studies have returned promising results towards scaling the gravure printing process, with feature sizes on the order of several microns.<sup>123,124</sup> In addition, by carefully engineering the capillary forces at play during gravure printing, line width and spacing as small as 1.2 and 1.5  $\mu\text{m}$  were achieved with a model ink.<sup>125</sup> Continuing improvements in scaling these techniques while maintaining throughput are important for the realization of high performance printed devices.

Because transistors and other electronic devices typically require multilayer printing with different materials, improvements in resolution must be accompanied by improvements in registration to maintain proper alignment of the different materials. A general strategy for scaling registration capabilities is to develop materials and processes to engineer self-aligned patterns. Recent advances have employed surface energy patterning and imprinted surface topographic features to exploit capillarity in the alignment of printed patterns. By rationally engineering the wetting characteristics of inks and substrates, devices with minimal drain/gate overlap or reduced channel length can be inkjet printed.<sup>126–128</sup> Additionally, engineering the surface topography to

guide liquid ink migration has been exploited to print electrolyte-gated transistors (EGTs) in a self-aligned process.<sup>129–132</sup> Such bottom-up approaches to printed electronics assembly are highly advantageous for the reliable fabrication of complex, high-resolution circuits.

A third trend in printed electronics is a strong interest in digital, direct-write patterning methods for unique opportunities outside the scope of traditional printed electronics. In particular, integration in a digital manufacturing environment carries the possibility of direct digital feedback in the patterning process and on the fly modifications. Moreover, certain direct-write technologies allow patterning on nonplanar surfaces, with opportunities for straightforward integration of printed components on parts manufactured by other means. Both extrusion-based direct-write printing and aerosol-jet printing have been demonstrated for patterning on nonplanar surfaces in this manner,<sup>133,134</sup> and continued developments in methodologies and supporting computational frameworks for this capability are expected.

### *1.6.3. Devices and Applications: Bio-Interfaced and Hybrid Electronics*

Materials research largely focuses on thin film transistors, owing to their foundational basis for more complex circuits. However, given the diversity of printed electronics applications, and the distinct process and performance specifications of printing methods compared to conventional microelectronics fabrication, it is important to consider novel device architectures and unique application concepts. Hybrid electronics interface conventional silicon circuits with printed components.<sup>135–137</sup> In this way, they leverage the outstanding capability of integrated circuits for logic and memory functionality, while relying on printed elements for wiring, sensors, and power management. In this context, novel fabrication schemes are required,<sup>138,139</sup> and control of the

interface between flexible and rigid electronics is critical, particularly for mechanical durability. Research to support this paradigm is expected to continue, particularly in applied contexts, as initial applications of printed electronics acknowledge the practical merit of continuing to leverage silicon functionality. A second area of active research involving printed electronics is the drive towards bio-interfaced devices. There have been several recent studies detailing wearable sensors and circuits for human performance monitoring.<sup>31,140,141</sup> While these do not exclusively leverage printing methods for fabrication, they share the performance targets and application space for which fabrication by printed electronics would eventually offer substantial benefit. In this context, interfaces with biological materials become important, particularly factors such as biocompatibility, corrosion resistance, toxicity, and biodegradability. This presents a different lens for assessing materials properties beyond baseline electrical performance alone. Finally, the design of novel electronic device architectures is a promising area of research for advances in printed electronics. Vertical devices are one prominent example of this. With the active channel oriented vertically, aggressive scaling can be achieved without corresponding improvements in printing resolution and registration. Several reports have made progress towards this goal, which requires novel designs for conducting or semiconducting materials to enable gating of the source-channel interface directly.<sup>142,143</sup> By working within relaxed constraints for printing resolution and registration, this approach is a promising area for materials development. Graphene inks offer opportunities in the three areas highlighted here. In particular, electrical and mechanical durability of hybrid electronics depends critically on interfaces between rigid and flexible components. Interfaces again play a role in biological applications of electronics, requiring biocompatible materials stable in physiological environments. Moreover, the nanoscale structure of graphene or

electric field permeability of thin films could potentially be exploited for vertical device fabrication. While not directly addressed in the present work, these examples underscore the critical importance of novel materials development in printed electronics.

## **1.7. Thesis Organization**

The present thesis describes the development of a class of graphene inks that employ cellulose derivatives as stabilizing polymers. These polymers, namely ethyl cellulose and nitrocellulose, present several advantages for graphene ink development and application. By sterically stabilizing graphene flakes, they provide excellent colloidal stability and extended process versatility. With this system, graphene/polymer composites can be directly dispersed in organic solvents to prepare inks. This bottom-up ink preparation process marks a departure from conventional methods, and provides excellent control over the ink formulation and resulting properties. In addition to broad process versatility, the cellulosic dispersants impact the functional properties of printed graphene films. Following partial decomposition of the polymer, carbonaceous residue serves to bridge graphene flakes, with the potential to enhance the mechanical and electrical properties of the graphene patterns. The high performance achieved as a result is exploited for several applications in printed electronics. The ensuing chapters trace the development of these graphene inks, and are focused on the topics listed below.

Chapters 2-7 describe a series of materials and processing advances, which broaden the toolbox for working with this system. Chapters 8-10 are focused on applications of the graphene inks in printed electronics, focused on select opportunities for which the combination of properties offered by graphene present a clear benefit. In particular, the chemical stability of graphene is



critical for favorable interfaces with ceramic, metallic, and organic and electrolytic materials. Chapter 11 focuses on opportunities for future work building from this foundation, and Chapter 12 ends with a short summary.

In Chapter 2, the development of a graphene ink for inkjet printing is described. Ethyl cellulose is employed as a graphene exfoliation aide, dispersant, rheology modifier, and fugitive binder to realize high performance graphene inks tailored for inkjet printing. The electrical and mechanical properties of the resulting graphene patterns are studied, with compelling results for applications in printed electronics.

In Chapters 3 and 4, the graphene/EC processing platform is leveraged to design inks for gravure and screen printing, respectively. Broad tunability of the ink loading and viscosity is critical to tailor inks for these printing methods. High resolution patterning is achieved, with functional properties consistent with inkjet-printed patterns. Screen-printed graphene electrodes are further used for highly flexible organic transistors.

Chapter 5 explores replacing the thermal annealing step traditionally used for graphene/EC inks with a pulsed photothermal technique known as photonic annealing. By annealing printed graphene patterns with a light pulse on the order of milliseconds in duration, process compatibility is improved in two ways. The rapid annealing process is well suited for high-throughput roll-to-roll manufacturing, while the short duration and localized nature of the heating process prevent damage to thermally sensitive plastic substrates.

In Chapter 6, the traditional EC dispersant is replaced with an alternative cellulose derivative, nitrocellulose. Due to its disparate decomposition properties, namely the tendency to leave substantial amorphous carbon residue upon charring, nitrocellulose imparts qualitatively

distinct functional properties to the printed graphene patterns. Improved cohesive strength, water tolerance, and environmental stability are observed for graphene films processed with nitrocellulose. The underlying chemical differences leading to these macroscopically distinct properties are studied using advanced in situ spectroscopy techniques.

In Chapter 7, the unique thermochemical properties of nitrocellulose are exploited for combustion-assisted photonic annealing of graphene patterns. As a mild explosive, nitrocellulose decomposes rapidly and exothermically, promising attributes for integration with flash photonic annealing. It is demonstrated that graphene/NC patterns exposed to photonic annealing receive a boost from the built-in energy of the polymer. Moreover, rapid decomposition and volatilization of the polymer lead to a high surface area microstructure, which is leveraged for graphene-based microsupercapacitors.

Chapter 8 explores the use of graphene as an electrode for the amorphous oxide semiconductor InGaZnO. In this context, graphene electrodes provide stable source/drain contacts to printed InGaZnO TFTs. Conventional metal electrodes, such as silver, do not function properly in this capacity due to deleterious interfacial reactions with the oxide semiconductor. Moreover, the excellent thermal and environmental stability afforded by the graphene allows functional InGaZnO devices following high temperature exposure and extended aging, conditions under which devices based on standard metal electrodes deteriorate.

In Chapter 9, the chemical inertness of graphene is again utilized, here to provide stable electrical connections to printed liquid metal. Gallium-based liquid metals offer unique opportunities for stretchable and reconfigurable electronic devices, but aggressive alloying with conventional metals presents a challenge for circuit integration and long-term operation. With its

stable, carbon-based structure, graphene effectively prevents alloy formation, enabling more versatile applications of liquid metal electronics.

Chapter 10 details the application of graphene as a stable, flexible electrode material for organic electronics and electrochemical energy storage devices. Printed graphene electrodes are demonstrated for electrolyte-gated transistors based on the polymer poly(3-hexylthiophene), or P3HT. In this capacity, the graphene provides a stability improvement compared to clean silver electrodes, and the flexibility of graphene can be exploited for highly flexible, and even foldable devices. The suitable interface with organic semiconductors and stability to harsh electrochemical conditions necessary in this context are extended to applications in  $C_{60}$  electron-only devices and microsupercapacitors.

Chapter 11 discusses several opportunities for future work building on the research here. Translating the versatile processing platform developed here to alternative colloidal nanomaterials would provide a broad palette of functional inks with mutual process compatibility, enabling straightforward preparation and printing of functional composites. Utilizing the strong and versatile foundation for graphene production and processing with ethyl cellulose, unique opportunities could be realized by extending methods beyond printed electronics, to include polymer processing techniques more broadly. Finally, the broad control over material parameters offers opportunities for more careful, fundamental characterization of unique aspects of this composite system, with potentially useful outcomes.

Chapter 12 concludes the thesis with a brief summary and general outlook.

## **CHAPTER TWO**

Inkjet Printing of Graphene/Ethyl Cellulose

## 2.1. Introduction to Inkjet Printing of Graphene

Among the diverse printing techniques discussed in Chapter 1, inkjet printing is a promising approach for rapid development and deployment of new material inks. Several key advantages of this technology include digital, additive, and non-contact patterning, reduction in material waste, and compatibility with a variety of substrates with different degrees of mechanical flexibility and form-factor. Various technologically important active components have been inkjet printed<sup>144</sup> including transistors,<sup>145,146</sup> solar cells,<sup>11,147</sup> light-emitting diodes,<sup>9</sup> and sensors.<sup>88,148</sup> Despite these device-level advances, the ability to pattern conductive, stable electrodes with fine resolution remains an important challenge, especially as the field evolves towards highly integrated systems.

In this chapter, a holistic approach is presented for achieving high performance inkjet-printed graphene features that addresses the entire process flow starting with graphene exfoliation and proceeding through ink formulation, printing, and final annealing. Central to this approach is the use of graphene exfoliated in the inexpensive, environmentally benign solvent, ethanol, with the stabilizing polymer ethyl cellulose (EC).<sup>62</sup> By exploiting the solubility of the polymer, a room temperature process is developed to produce a powder of graphene flakes encapsulated by polymer, which is readily redispersed in a variety of organic solvents. In this manner, a graphene ink for inkjet printing can be formulated from the bottom up, offering excellent control, ease of use, and reproducibility. Building on this platform, stable inkjet printing of graphene is demonstrated for the fabrication of high conductivity patterns suitable for flexible electronics.

## 2.2. Liquid Phase Exfoliation of Graphene with Ethyl Cellulose

Graphene inks were produced by the exfoliation of graphite in ethanol and EC, as reported previously.<sup>62</sup> Details of the experimental procedure are as follows. 10.0 g natural graphite flake (Asbury Graphite Mills, 3061 Grade) was dispersed in a solution of 200 mL, 2% w/v EC in ethanol (EC: Aldrich, viscosity 4 cP, 5% in toluene/ethanol 80:20, 48% ethoxy; ethanol: Koptec, 200 proof) in a stainless steel beaker. The dispersion was sonicated using a probe sonication system (Fisher Scientific Sonic Dismembrator Model 500, 13 mm Branson tip) for 90 minutes at 50 W in an ice water bath. The resulting dispersion was centrifuged (Beckman Coulter Avanti® J-26 XPI) at 7500 rpm (~10000 g) for 15 minutes, and the supernatant was collected. To this dispersion, a 0.04 g/mL aqueous solution of NaCl (Sigma-Aldrich, >99.5%) was added in a 1:2 volume ratio. The resulting mixture was centrifuged at 7500 rpm for 8 minutes, after which the supernatant was removed. The resulting graphene/EC solid was dried, dispersed in ethanol, and passed through a 5  $\mu\text{m}$  sieve (Industrial Netting, BS0005-3X1) to remove any large particles that might compromise inkjet printing. The dispersion was then flocculated again, with the same parameters as above. To remove any residual salt, the graphene/EC solid was washed with deionized water and isolated by vacuum filtration (Millipore Nitrocellulose HAWP 0.45  $\mu\text{m}$  filter paper). This isolated graphene/EC was then dried, yielding a fine black powder. This process primarily produces few-layer graphene sheets, with typical thicknesses of ~2 nm and areas of ~50 $\times$ 50 nm<sup>2</sup> (Figure 2.1). The graphene/EC powder in this case has a graphene content of ~15% wt. (Figure 2.2), which is significantly higher than the graphene/EC ratio in the original dispersion.

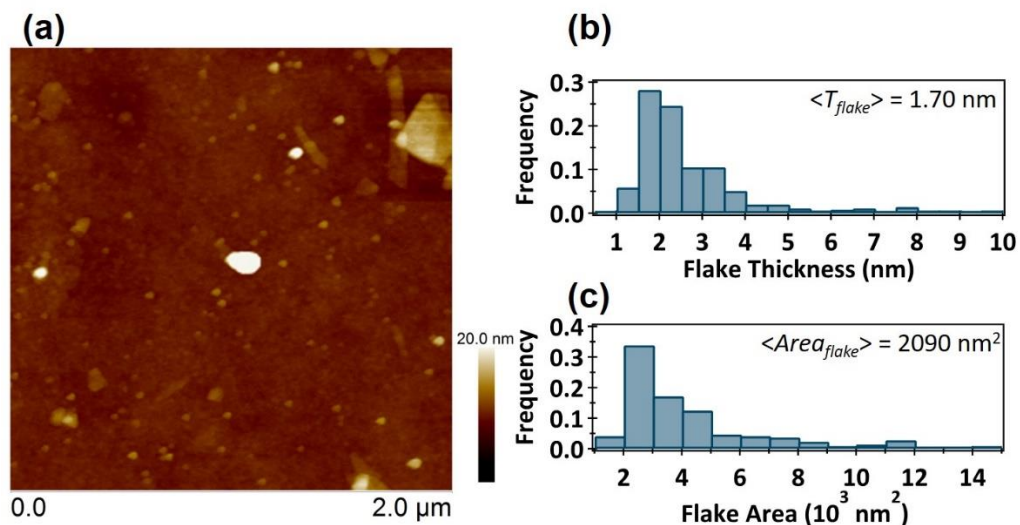


**Figure 2.1.** Characterization of graphene flakes. (a) Representative AFM scan of the graphene flakes that was used to obtain particle statistics. Histograms of (b) flake thickness and (c) flake area for 355 and 216 flakes, respectively.

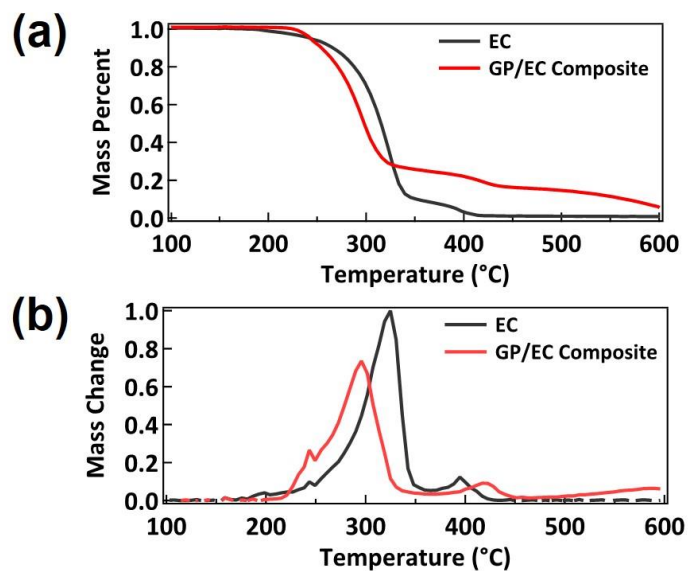


**Figure 2.2.** Thermal gravimetric analysis of pure EC (black) and graphene/EC composite powder (red), showing (a) mass as a function of temperature and (b) the differential mass loss. For the composite powder, the decomposition peaks of EC in (b) are shifted to different temperatures due to the presence of graphene. A heating rate of 5  $^{\circ}\text{C}/\text{minute}$  in air was used for this measurement.

The processing steps are illustrated schematically in Figure 2.3. In particular, excess graphite and EC were used to achieve high yields of suspended graphene ( $> 0.1$  mg/mL). Sedimentation-based centrifugation was employed (Figure 2.3a-b) to remove remaining large graphite flakes, yielding a dispersion of  $\sim 1:100$  graphene:EC in ethanol. To remove excess EC and solvent, a room-temperature method based on the flocculation of graphene/EC was developed. Specifically, upon the addition of  $\text{NaCl}_{(\text{aq})}$ , a solid containing graphene and EC was flocculated and collected following a short centrifugation step (Figure 2.3c). This graphene/EC solid was subsequently washed with water and dried, yielding a black powder with enriched graphene content. Because EC encapsulates graphene flakes in solution, no irreversible aggregation of graphene was observed. The resulting powder is readily dispersed in a variety of solvents, allowing for the tailoring of inks for a range of deposition methods. In particular, dispersion of this material in select organic solvents (Figure 2.3d-e) enables deposition of graphene by inkjet printing (Figure 2.3f).



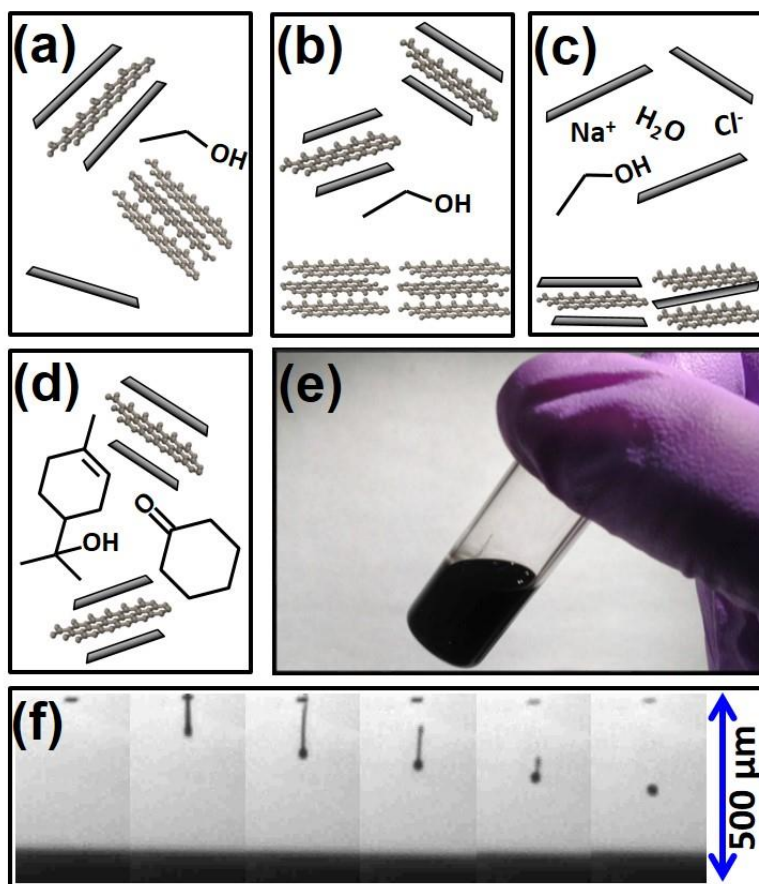


**Figure 2.3.** Schematic illustration of the ink preparation method. (a) Graphene is exfoliated from graphite powder in ethanol/EC by probe ultrasonication. A graphene/EC powder is then isolated following (b) centrifugation-based sedimentation to remove residual large graphite flakes and (c) salt-induced flocculation of graphene/EC. (d) An ink for inkjet printing is prepared by dispersion of the graphene/EC powder in 85:15 cyclohexanone:terpineol. (e) Vial of the prepared graphene ink and (f) drop formation sequence for inkjet printing, with spherical drops forming after  $\sim 300$   $\mu\text{m}$ .

### 2.3. Ink Formulation and Inkjet Printing of Graphene/EC

Inkjet printing requires careful tailoring of the viscosity and surface tension of the ink formulation to achieve stable droplet formation. The wetting and drying properties of the ink must also be tuned to achieve proper morphology of the printed features.<sup>22</sup> Furthermore, inks should not

possess large particles or volatile solvents since these components can lead to clogging of the inkjet printhead. Finally, a high concentration of graphene is desired to reduce the number of necessary printing passes. To achieve these goals, the graphene/EC powder was dispersed in a 85:15 mixture of cyclohexanone:terpineol (Figure 2.3d). At a concentration of 2.4 wt% graphene/EC composite ( $\sim 3.4$  mg/mL graphene), this ink has a surface tension of  $\sim 33$  mN/m and a viscosity of 10-12 mPa·s at 30 °C at a high shear rate (100-1000  $\text{s}^{-1}$ , Figure 2.4). The shear viscosity of the ink was measured using a Physica MCR 300 rheometer equipped with a 50 mm cone and plate geometry at shear rates of 10-1000  $\text{s}^{-1}$ . The temperature was controlled by a Peltier plate for viscosity measurements at 25, 30, 35 and 40 °C to evaluate the optimal printing temperature. The surface tension was estimated by the drop weight method, using calibration solvents of 2-propanol, ethanol, deionized water and ethylene glycol.

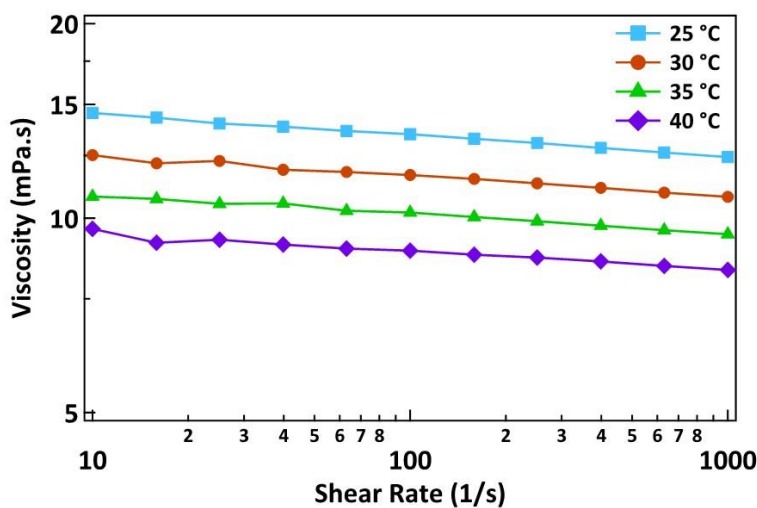


**Figure 2.4.** Shear viscosity of the graphene ink over a shear rate range of 10-1000  $\text{s}^{-1}$  at temperatures of 25, 30, 35 and 40 °C.

The relatively low surface tension of this ink is designed for proper wetting of low surface energy substrates applicable to flexible electronics. To assess the electrical characteristics of the ink, the well-defined substrate of Si/SiO<sub>2</sub> with 300 nm thermally grown oxide was used. For a more suitable model of wetting and drying on low surface energy substrates, the Si/SiO<sub>2</sub> substrate was treated with hexamethyldisilazane (HMDS) to decrease the surface energy. Printing was carried out at 30 °C using a Fujifilm Dimatix Materials Printer (DMP 2800) with a cartridge designed for a 10 pL nominal drop volume (DMC 11610). Drop spacing for all printed features was maintained at 20 μm. Stable printing of graphene lines on HMDS-treated Si/SiO<sub>2</sub> yielded a line width of ~60 μm, as shown in Figure 2.5a-c. The highly uniform dome-shaped cross-sectional profile across the lines provides evidence for successful ink formulation, specifically showing no undesirable coffee ring effects. Importantly, this advantageous cross-sectional profile was maintained after multiple printing passes, as shown in Figure 2.5d. This excellent morphology of the printed features is attributed to the suppression of the coffee ring effect through a Marangoni flow established by the surface tension gradient that develops due to solvent evaporation.<sup>21,144,149–151</sup> This flow homogenizes the droplet composition, resulting in a uniform morphology of the printed features.

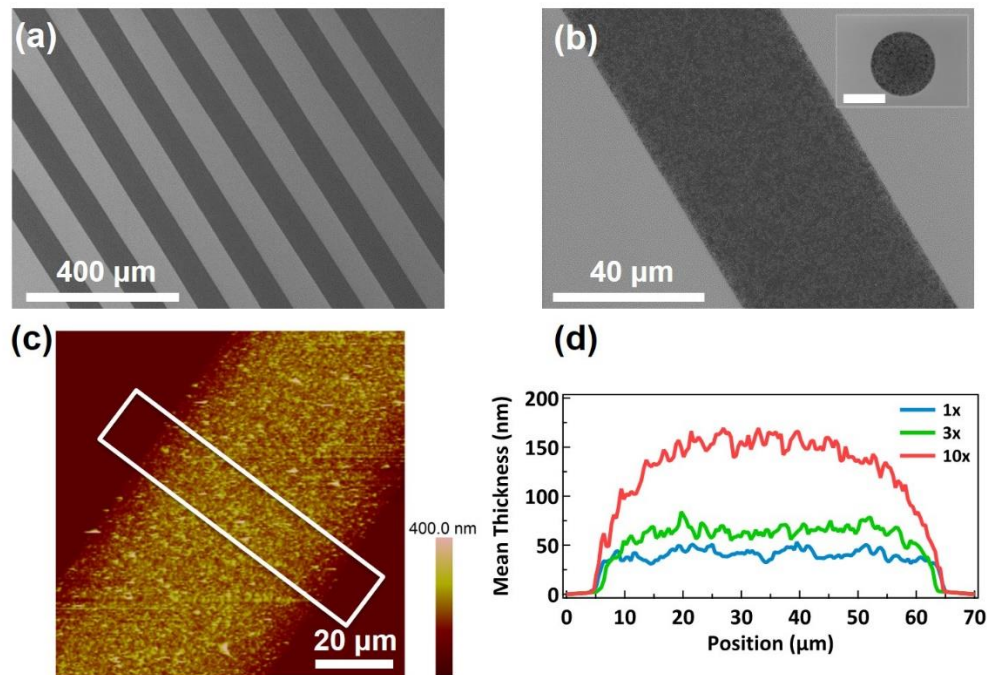


**Figure 2.5.** Morphology of inkjet-printed graphene features on HMDS-treated Si/SiO<sub>2</sub>. Scanning electron micrographs of (a) multiple printed lines and (b) a single printed line and drop (inset, scale bar corresponds to 40 μm) illustrate the uniformity of the printed features. (c) An AFM image of a single line following 10 printing passes that shows no coffee ring features. (d) Averaged cross-sectional profiles of printed lines after 1, 3, and 10 printing passes, demonstrating the reliable increase in thickness obtained after multiple printing passes. The cross-sectional profiles are obtained from the averaged AFM height profile over ~20 μm as indicated by the boxed region in (c).

#### 2.4. Functional Characterization of Graphene/EC Patterns

The polymeric binder EC encapsulates graphene flakes following solvent evaporation, necessitating thermal annealing to obtain highly conductive features. To study the electrical behavior of the composite material as a function of annealing conditions, films were blade coated on glass slides and annealed in an ambient atmosphere with systematic variations in the annealing time and temperature. As shown in Figure 2.6a, a 250-350 °C annealing process for 30 minutes results in high conductivity graphene films. At 250 °C, annealing for as short as 20 minutes was

sufficient to achieve low resistivity (Figure 2.6b). For the remainder of this study, the annealing temperature and time of 250 °C and 30 minutes, respectively, were chosen to enable compatibility with flexible electronics applications.

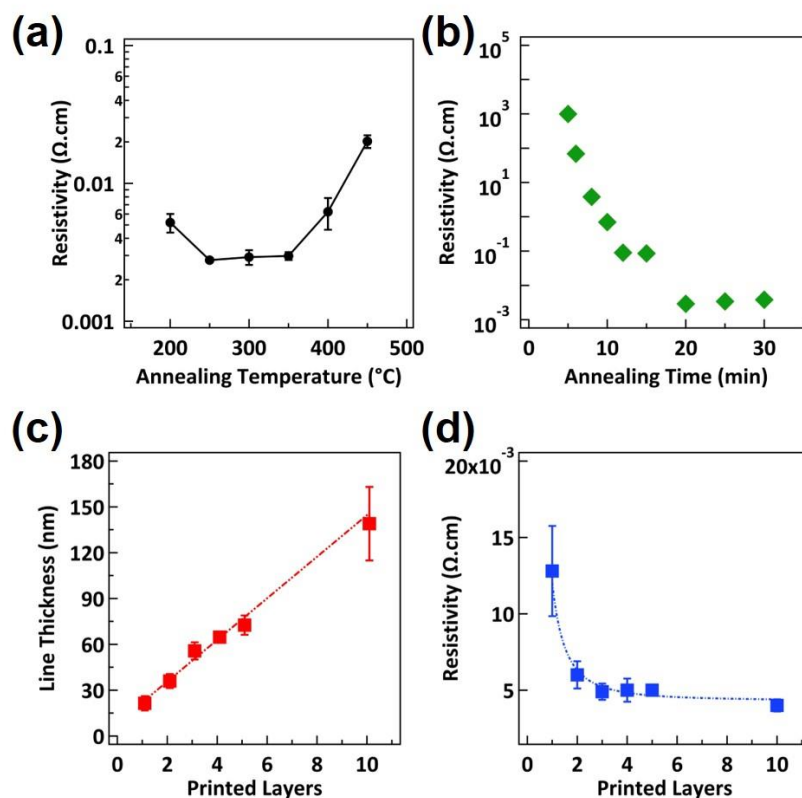


**Figure 2.6.** Electrical characterization of graphene features. (a) Electrical resistivity of blade-coated films plotted against annealing temperature for a fixed annealing time of 30 minutes, showing effective binder decomposition at 250 °C and increased resistivity due to graphene oxidation above 400 °C. (b) Dependence of electrical resistivity on annealing time for a fixed annealing temperature of 250 °C, showing that low resistivity is achieved following annealing for 20 minutes. (c) Thickness of inkjet-printed graphene lines on HMDS-treated Si/SiO<sub>2</sub> for increasing numbers of printing passes. (d) Electrical resistivity of the printed features for increasing numbers of printing passes, showing relatively stable performance after only 3 printing passes.

For a detailed assessment of the electrical performance of the printed features, 4 mm long lines with varying thicknesses were printed on HMDS-treated SiO<sub>2</sub> and annealed at 250 °C for 30 minutes. The line thickness increases linearly with the number of printed layers, with each layer

adding ~14 nm to the thickness (Figure 2.6c). The line resistivity reaches a relatively stable low value after only 3 printing passes, owing to the high concentration of the ink and the excellent morphology of the printed features (Figure 2.6d). The measured conductivity of  $2.5 \times 10^4 \pm 0.2 \times 10^4$  S/m (resistivity of  $4 \times 10^{-3} \pm 0.4 \times 10^{-3}$   $\Omega \cdot \text{cm}$ ) for the printed lines after 10 printing passes is ~250 times higher than previously reported for inkjet-printed graphene.<sup>68</sup> This dramatic improvement indicates the effectiveness of the method presented here, which avoids the graphene degradation that occurs in competing processes based on ultrasonication of graphene in harsh solvents. The evidence of high conductivity films using small flakes indicates the efficiency of flake-to-flake charge transport. This is a result of flake alignment, due to the use of small, pristine graphene flakes, and decomposition of the EC binder.

Thermal gravimetric analysis of the ink indicates that EC decomposition occurs in two stages, with a low temperature charring beginning below 250 °C and volatilization and removal of residue occurring at temperatures above 400 °C (Figure 2.2). This observation coupled with the high electrical conductivity observed after annealing at temperatures of 250-350 °C suggests that the initial decomposition of EC enables efficient charge transport through the graphene network. Because cellulose derivatives can thermally decompose into aromatic species,<sup>152,153</sup> the resulting  $\pi$ - $\pi$  stacking between the residues and the graphene flakes provides relatively efficient charge transport. In addition, the increase in resistivity upon annealing at 400-450 °C correlates well with the removal of residue from the film in the second stage of EC decomposition. Furthermore, the EC residue creates a dense and continuous film, as determined from scanning electron micrographs of printed lines following annealing at 250 °C and 450 °C (Figure 2.7). This film densification

could potentially enhance the mechanical properties of the printed graphene features and enable a robust tolerance for bending stresses in flexible applications.

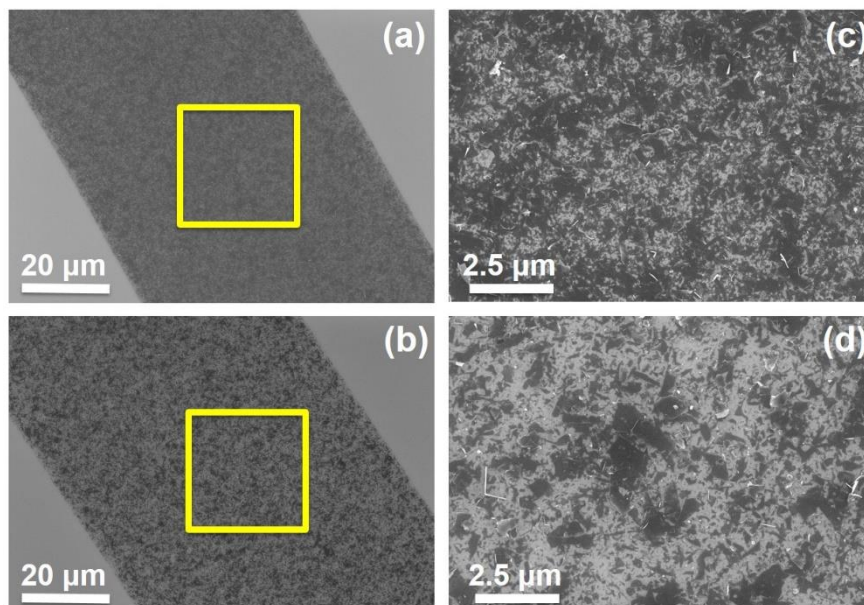


**Figure 2.7.** SEM images of printed lines annealed to (a,c) 250 °C and (b,d) 450 °C. (c) and (d) are higher magnification SEM images of the highlighted area (yellow box) from images (a) and (b), respectively. Following 450 °C annealing, the EC residue is removed, leading to a sparse graphene network. This observation suggests the importance of EC decomposition products in maintaining electrical and mechanical integrity of the printed features.

To assess mechanical properties, lines were printed on polyimide (DuPont Kapton®) substrates and annealed at 250 °C for 30 minutes. Various flexibility tests were employed to characterize these printed graphene lines. For example, to investigate the reliability over many bending cycles, the electrical resistance was measured up to 1000 cycles. As shown in Figure 2.8a, there is no observable degradation in the line conductivity for a bending radius of curvature of 3.4 mm. Even at a radius of 0.9 mm, the resistance remained nearly unchanged after a marginal initial increase. At this radius of curvature, cracking was observed in the substrate, which suggests that the small loss of conductivity is a limitation of the substrate rather than the printed features. The



electrical performance of the printed features was also measured under applied stress for various radii of bending (Figure 2.8b), with no observed loss in conductivity. As a final test, the resistance of the graphene lines was measured in a folded state, as shown in Figure 2.8c-e, again resulting in only a slight decrease in conductivity on the order of 5% that can again be likely attributed to substrate cracking. Overall, these mechanical tests show the utility of these graphene inks in flexible, and possibly even foldable, electronic applications.

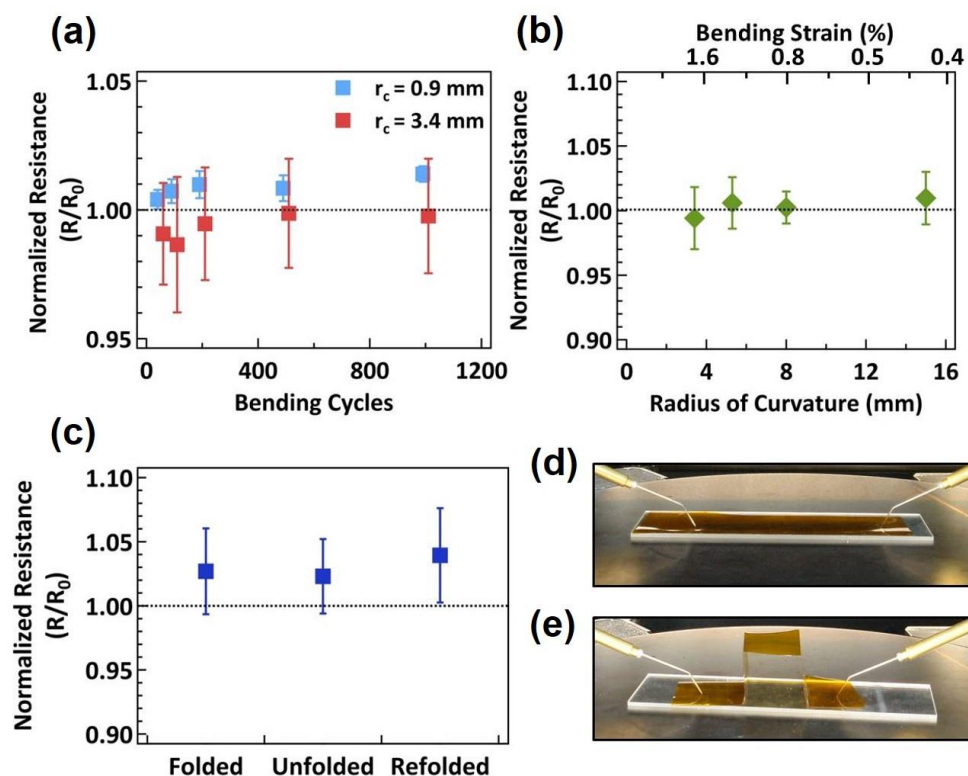


**Figure 2.8.** Flexibility assessment of printed graphene lines on Kapton® substrates. (a) Resistance of graphene lines folded to a radius of curvature of 0.9 mm (blue) and 3.4 mm (red) normalized to the resistance prior to bending. (b) Normalized resistance of graphene lines measured in a flexed state for various degrees of bending, showing reliable retention of electrical conductivity across all measured flex states. (c) Normalized resistance of graphene lines while measured in a folded state, showing a small and irreversible increase in resistance following folding. Images of the sample in the (d) original and (e) folded state.



## **2.5. Summary for Graphene/EC Inkjet Printing**

In summary, this chapter details the development of a novel graphene ink based on a graphene/EC powder that is produced using only room temperature processing methods. The graphene/EC powder allows for careful tuning of the ink to achieve stable inkjet printing of features on a variety of substrates with excellent morphology, and could in principle be applied to other printing techniques in a straightforward manner. In addition, the conductivity of printed features following mild annealing is over two orders of magnitude better than previously reported for inkjet-printed graphene despite a smaller flake size, thus indicating efficient flake-flake charge transport. These results are likely enabled by the synergistic EC binder for graphene exfoliation, which reduces flake-flake junction resistance upon annealing relative to graphene films containing residual solvent or surfactant. Finally, the low processing temperatures enable compatibility with flexible substrates, thereby allowing demonstration of the high tolerance of printed graphene features to bending stresses. With this unique combination of attributes, these graphene-based inks are likely to find utility in a wide range of printed, flexible, and/or foldable electronic applications.

## **CHAPTER THREE**

Gravure Printing of Graphene/Ethyl Cellulose

### 3.1. Introduction to Gravure Printing of Graphene

Recent research, including the previous chapter, has demonstrated inkjet printing of graphene for the fabrication of functional devices such as chemical and thermal sensors,<sup>88,91</sup> acoustic actuators,<sup>92</sup> dipole antennas,<sup>93</sup> and thin film transistors.<sup>68,94</sup> While inkjet printing offers an additive technique that is ideal for rapid prototyping in research laboratories, its limited throughput motivates the development of alternative printing strategies for industrial-scale applications. Gravure printing is a promising option in this regard since it offers high-speed, roll-to-roll deposition of functional materials at high resolution, as discussed in Chapter 1.<sup>2</sup> Gravure printing involves filling an ink into recessed cavities in the master with the aid of a doctor blade, and then transferring ink from these cells onto the substrates upon close contact.

Although several studies have demonstrated the utility of gravure printing for printed electronics,<sup>96,123,154–159</sup> this technique has not yet been demonstrated for pristine graphene. The difficulty in achieving gravure printing of graphene lies in the formulation of suitable inks, since graphene possesses poor dispersion stability in common organic solvents.<sup>57</sup> One strategy that enables graphene dispersions is to oxidatively exfoliate graphite,<sup>160</sup> but this approach typically requires harsh chemical or thermal treatments and results in degradation of electrical properties.<sup>55,68,161</sup> On the other hand, pristine graphene can be dispersed in select solvents such as N-methylpyrrolidone,<sup>69</sup> but this system is unsuitable for gravure printing due to its low viscosity and limited graphene concentration. The research in Chapter 2 demonstrated an alternative approach for producing graphene dispersions using a polymer, ethyl cellulose (EC), to stabilize pristine graphene at high concentrations in common and benign organic solvents such as terpineol.<sup>62,70,71</sup> Moreover, the graphene/EC material system possesses excellent electrical

conductivity and compatibility with flexible substrates, demonstrating retention of electrical properties upon bending and even folding.<sup>70</sup> In addition, the EC/terpineol stabilizer-solvent system has been previously employed for gravure and screen printing.<sup>162</sup> Building on this foundation, the present chapter describes a graphene/EC ink design along with comprehensive printing optimization to demonstrate gravure printing of graphene for high resolution, conductive patterns.

### **3.2. Graphene/EC Ink Formulation for Gravure Printing**

Graphene inks are produced from solvent-exfoliated graphene prepared by a previously described method from Chapter 2.<sup>70</sup> In particular, graphene is exfoliated from graphite in ethanol with the stabilizing polymer EC, which produces a high dispersion yield with minimal processing. After the remaining graphite flakes are removed by centrifugation, a flocculation step is used to remove excess EC from solution, thus isolating graphene/EC as a powder and effectively decoupling the solvents used for exfoliation and printing. This method has been shown to produce predominantly few-layer graphene flakes, with a typical thickness of ~2 nm and lateral size of approximately 50 nm × 50 nm.<sup>70</sup> The use of small graphene flakes is critical for high-resolution gravure printing for which sub-micron particles are needed.<sup>163</sup>

By first producing a graphene/EC powder, the ultimate ink solvent and concentration can be widely varied. In this case, the graphene ink is produced by dispersing the graphene/EC powder in a mixture of ethanol and terpineol, which allows rapid and complete dispersion due to the low viscosity of the solvent system. This step is followed by removal of the ethanol to yield polymer-stabilized graphene in terpineol, as shown in Figure 3.1a-b. Graphene/EC powder (1.0 g) was dispersed in ethanol (~25 mL) and terpineol (10 mL, Aldrich, mixture of isomers, anhydrous) by

bath sonication. This dispersion was passed through a 3.1  $\mu\text{m}$  glass fiber filter membrane (Acrodisc®). The filtered dispersion was heated on a hot plate to remove ethanol, yielding a final ink of 10% w/v solids in terpineol (Ink 1). The medium and low viscosity inks (Inks 2 and 3) were prepared by a similar technique with different concentrations (7.2% w/v and 5% w/v solids, respectively).

For fabrication of the gravure printing pattern, a Si(100) wafer was cleaned by piranha solution (5:1  $\text{H}_2\text{SO}_4$  and  $\text{H}_2\text{O}_2$ ) for 15 minutes at 120 °C, rinsed with deionized water and dried. The wafer was prebaked at 115 °C for 1 minute, after which photoresist (Shipley 1813) was spin-coated onto the wafer at 3000 rpm for 30 seconds. A soft baking step was carried out at 110 °C for 1 minute to drive off solvents and improve adhesion. A mask designed with the gravure cell patterns was aligned with the wafer during a 5 second exposure to UV light (MABA6). The wafer was immersed in developer solution for 1 minute, rinsed with deionized water, and dried. The patterned wafer was then dry etched to the required depth by reactive ion etching (SLR 770 Deep Trench Etcher). The wafer was then washed in acetone, ethanol, and deionized water prior to being used as a gravure pattern.

The prepared graphene inks can be directly applied for gravure printing by employing the flooding-doctoring-printing strategy illustrated in Figure 3.1c-e. This method decouples the critical processes of gravure printing, particularly filling the gravure cells with the ink (flooding), removing excess ink from the surface (doctor blading), and transferring the pattern to the substrate (printing). In this manner, the parameters related to these three distinct steps can be independently optimized, enabling a high degree of control over the printing performance. The graphene inks were printed onto 125  $\mu\text{m}$  thick DuPont Kapton® FPC films purchased from American Durafilm

using a direct gravure printing system. The gravure pattern consisted of square cells from 2 to 50  $\mu\text{m}$  in width and 5  $\mu\text{m}$  in depth. For printing lines, the spacing between cells was varied from 0.1 to  $1 \times$  cell width. During the flooding step, the graphene ink (0.1 g) was flooded onto the gravure plate using the doctor blade at  $70^\circ$  and a typical speed of 5 cm/s. Doctor blading was then performed at  $55^\circ$ , also at a typical speed of 5 cm/s. Finally, the ink in the cells was transferred to the substrate through a nip consisting of a soft and a hard roll at a speed equivalent to the doctoring speed.

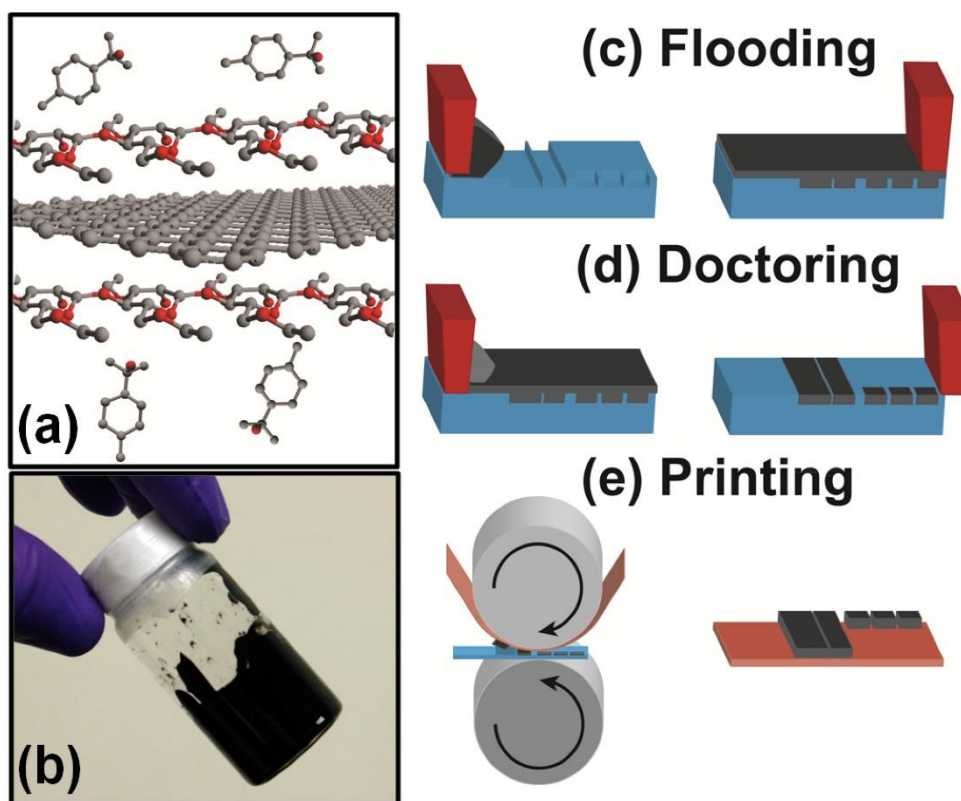


**Figure 3.1.** Development of the graphene ink for gravure printing. (a) Schematic of the ink, showing a graphene sheet stabilized by ethyl cellulose in terpineol. (b) Photograph of the formulated ink. (c-e) Illustration of the gravure printing method decomposed into three steps: (c) flooding of the gravure cells; (d) doctor blading; (e) printing.

The three processes of the gravure printing approach used here are strongly influenced by the ink physical properties, especially the viscosity and surface tension. Because the surface tension is largely determined by the solvent, terpineol, which has previously been shown to be suitable for conductive inks,<sup>164</sup> the viscosity is the most crucial ink parameter to tailor. Towards this end, the three different inks have varying viscosity in the range of 0.2-3 Pa·s (shear rate: 10 s<sup>-1</sup>), shown in Figure 3.2a, corresponding to solids loading of 5-10% by weight. The shear viscosity of the inks was measured using a Physica MCR 300 rheometer equipped with a 25 mm, 2° cone and plate geometry at shear rates of 1-1000 s<sup>-1</sup>, with the temperature controlled by a Peltier plate at 25 °C. The significant printing parameters, including the speed and pressure of flooding and doctoring and the speed of printing, were optimized to print dot patterns of each ink, offering a direct comparison as a function of ink viscosity. As shown in Figure 3.2b, the size of the printed dots increased for the low viscosity inks due to increased spreading on the substrate; for a 50 μm cell, the dots spread to 68 μm and 80 μm for the high and low viscosity inks, respectively. In addition, the lower viscosity inks tended to produce anisotropic dots with an empty center and an extended tail of ink residue along the direction of doctoring, as shown in Figure 3.2c-e. Because the high viscosity ink exhibited superior resolution and pattern fidelity, this ink was used for the remainder of this study.

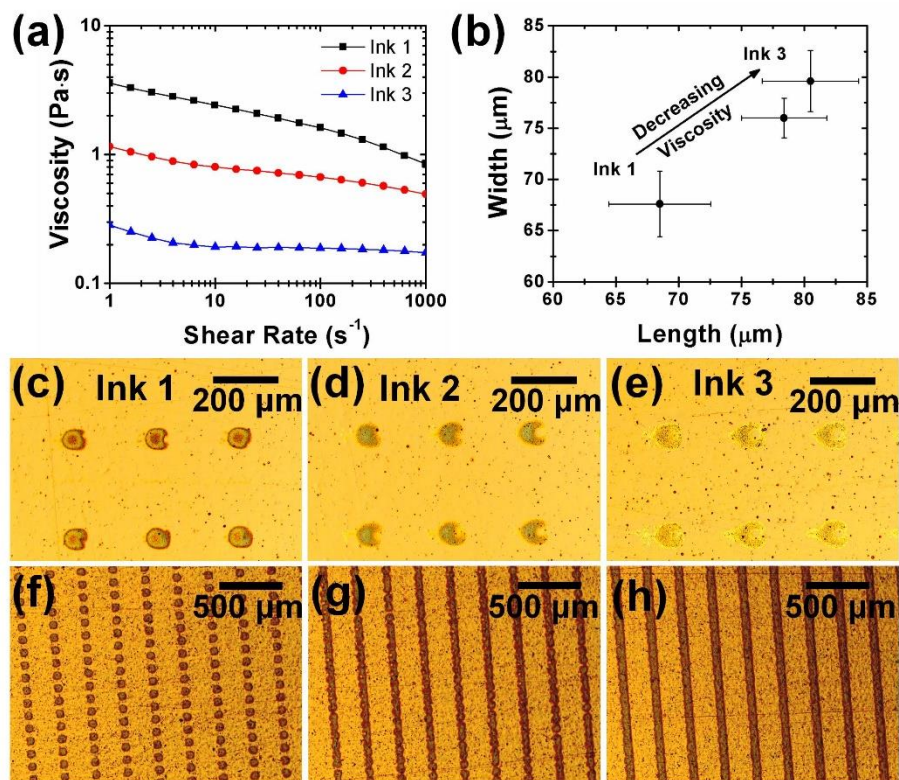


**Figure 3.2.** Optimization of graphene inks for gravure printing. (a) Shear viscosity for the three different ink formulations. (b) Size of printed dots for each ink using a gravure cell of 50  $\mu\text{m}$ . (c-e) Optical images of the printed dots for each ink. (f-h) Optical images showing line formation as the cell spacing is reduced, corresponding to 50, 25 and 5  $\mu\text{m}$  spacing for a cell size of 50  $\mu\text{m}$ .

### 3.3. Print Characterization of Gravure-Printed Graphene/EC

While ink deposition from individual cells is at the core of gravure printing, continuous lines (i.e., wires) are particularly important for electronic applications. Continuous linear printed features require well-behaved spreading and merging of ink from neighboring cells, which depends on the spacing between the cells. Figure 3.2f-h illustrates this issue for 50  $\mu\text{m}$  cells. As the spacing between cells is decreased from 50  $\mu\text{m}$  to 25  $\mu\text{m}$ , the neighboring drops merge to form a discontinuous, rough-edged line. As the spacing is further reduced to 5  $\mu\text{m}$ , the rough edges are



removed, yielding a continuous, uniform line. Importantly, the additional material deposited with decreased cell spacing contributed to the uniformity and thickness of the lines but did not appreciably compromise the resolution (Figure 3.3). Lines printed using this condition, namely the cell spacing to cell size ratio (printing ratio, PR) of 0.1, showed excellent morphology across the range of cell sizes from 15-50  $\mu\text{m}$ , as shown in Figure 3.4.

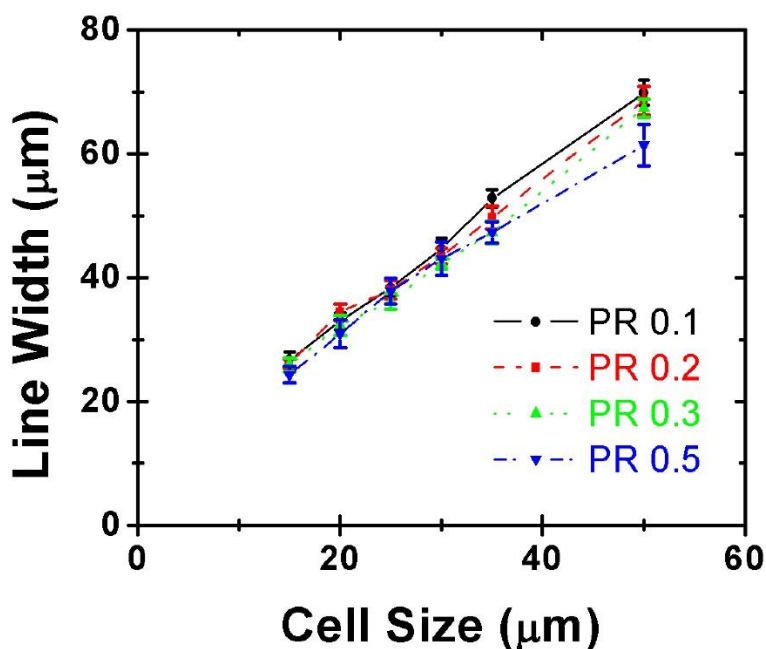


**Figure 3.3.** Line width measurements for lines printed with different cell spacing. The printing ratio (PR) defines the ratio of cell spacing to cell width. The similar width of lines printed at different printing ratios suggests that the additional ink contributes to the line uniformity and thickness rather than increased ink spreading.

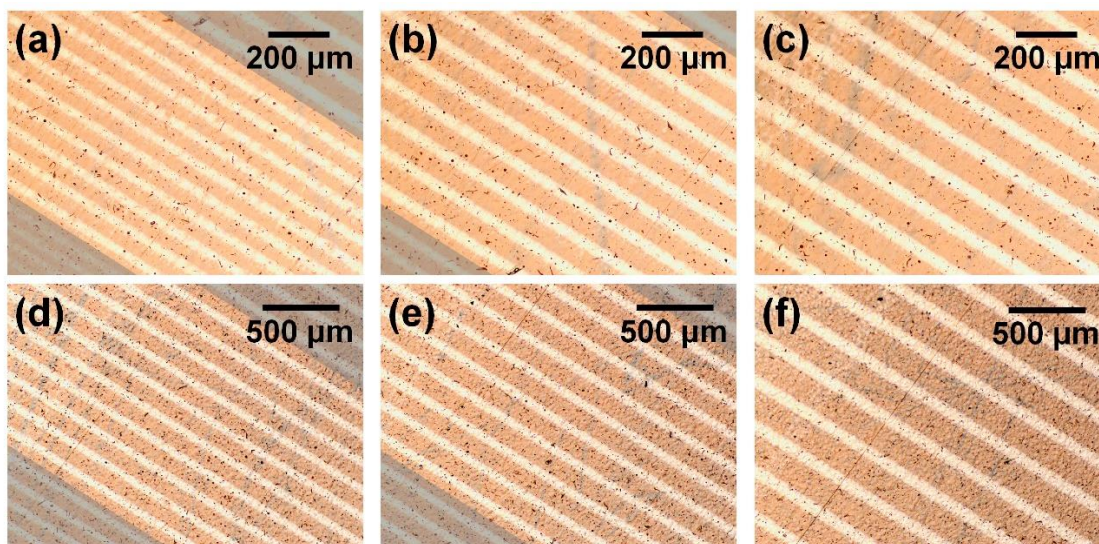


**Figure 3.4.** Optical microscopy images of printed graphene lines using cell sizes of 15, 20, 25, 30, 35 and 50  $\mu\text{m}$  for (a-f), respectively. Lines printed without the specified cell size are shaded gray in each case.

The gravure-printed graphene lines were further characterized to assess their suitability for printed electronics. Measurements of the line width indicate the broad tunability in resolution by varying the cell size, as shown in Figure 3.5a, with 15  $\mu\text{m}$  cells producing lines that are  $\sim 30 \mu\text{m}$  wide. The line thickness was measured prior to annealing by optical profilometry (Figure 3.5b), showing a monotonic increase in thickness that begins to saturate for larger cells, corresponding to the reduced ink spreading relative to the cell size. In addition to well-controlled line dimensions, the optimized printing conditions lead to high quality, uniform printing over large areas, as shown in the scanning electron micrograph in Figure 3.5c and height profiles measured by optical profilometry in Figure 3.5d.

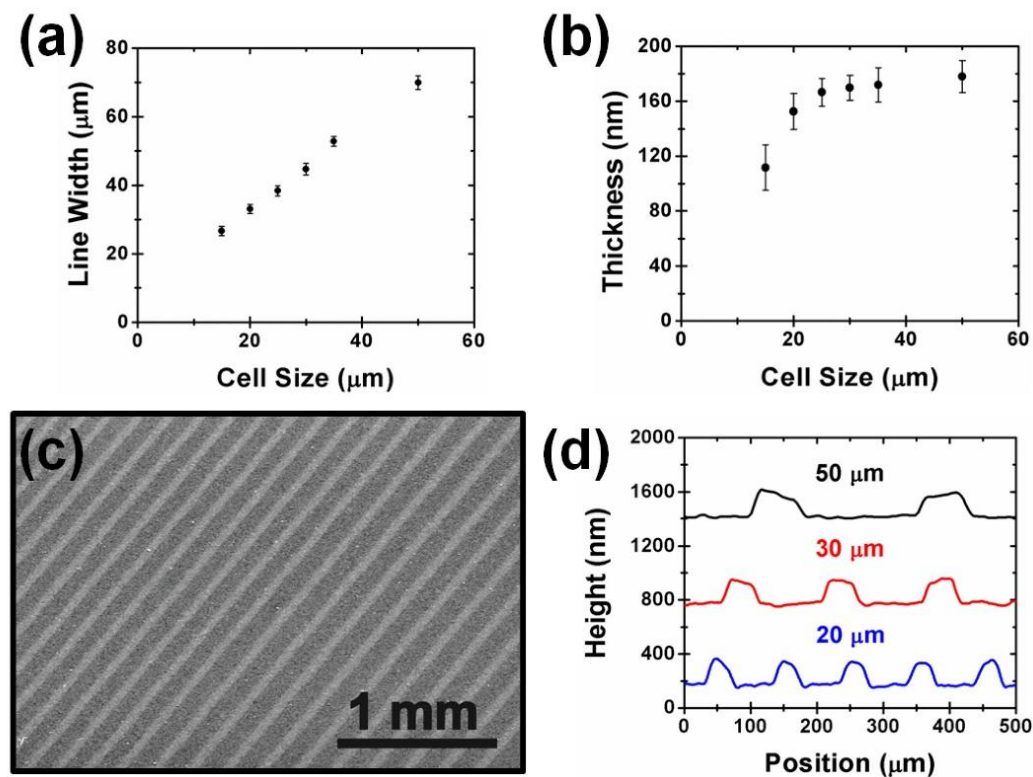


**Figure 3.5.** Characterization of gravure-printed graphene lines. (a) Line width and (b) line thickness for varying cell size. (c) Large-area scanning electron micrograph of printed lines. (d) Line height profiles measured by optical profilometry.

### 3.4. Functional Characterization of Gravure-Printed Graphene/EC

To complement the large-area fidelity of the printing process, the ink chemistry yields a dense and uniform network of graphene flakes following annealing, as the polymer stabilizer mitigates flake aggregation (Figure 3.6). To establish the electrical properties of the printed graphene lines, conductivity measurements were performed following thermal annealing at 250 °C for 30 minutes. Resistance measurements of the lines are shown in Figure 3.7a; for lines printed with cells of 20-50  $\mu\text{m}$ , ten out of ten measured lines were electrically continuous over the entire

8 mm length of the line with a standard deviation in resistance below 10%. This result indicates the continuous nature of the lines, as well as the uniformity in printing from line to line. For lines printed with a 15  $\mu\text{m}$  cell, 8 of the 10 measured lines were electrically conductive, with the same uniformity among those 8 lines as the lines printed with larger cells, which is noteworthy considering the relatively small thickness of the lines compared to the roughness of the Kapton substrate. While the lines are 100-200 nm thick prior to annealing, a vertical contraction occurs during annealing as the EC polymer stabilizer is partially decomposed. To measure the thickness evolution resulting from annealing, thicker films of the graphene/EC material were inkjet-printed onto a silicon wafer. Profilometry measurements of film thickness following different annealing conditions indicate that the graphene/EC composite contracts to  $\sim 15\%$  of the original thickness during annealing to 250  $^{\circ}\text{C}$ , as shown in Figure 3.7b. Atomic force microscopy imaging, shown in Figure 3.7c, offers a direct visualization of the resulting nanoscale thickness of the lines. The surface roughness of the substrate, measured to be  $\sim 50$  nm due primarily to the embedded particles, is large relative to the line thickness of  $\sim 15$ -30 nm. The electrical continuity of such thin lines at a macroscopic length scale, even over a surface with relatively large topographical defects, is a testament to the reliability and quality of the printing process. Overall, the electrical conductivity of the printed graphene lines is estimated to be  $\sim 10000$  S/m, based on measurements of line width, resistance, thickness prior to annealing, and film contraction during annealing. This is based on lines printed with 50  $\mu\text{m}$  cells, for which the resistance per length was  $51.9 \pm 4.4$  k $\Omega$ /mm, the width was  $69.9 \pm 2.0$   $\mu\text{m}$ , and the thickness following annealing was calculated to be  $(178 \pm 11.8$  nm) $\cdot(0.144 \pm 0.019) = 25.6 \pm 3.7$  nm, yielding a conductivity of  $10800 \pm 1800$  S/m. In addition to being highly conductive, the printed patterns exhibit robust mechanical tolerance to bending

stresses. While comprehensive flexibility tests have been previously performed on this graphene/EC material,<sup>70</sup> it is verified here that the gravure-printed lines show similar characteristics. Indeed, lines printed with both 50  $\mu\text{m}$  and 30  $\mu\text{m}$  gravure cells show no measurable loss in conductivity over 500 bending cycles at a radius of curvature of 2 mm, or an equivalent strain of 3.1%, as shown in Figure 3.7d.

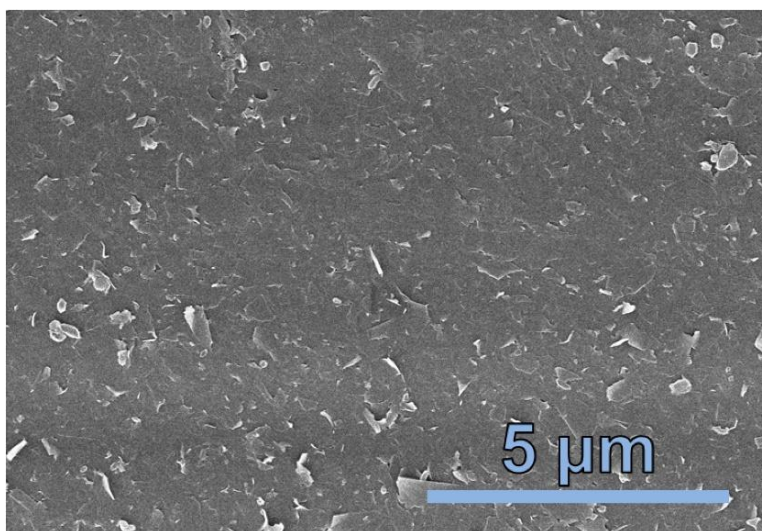


**Figure 3.6.** A scanning electron micrograph of graphene lines indicates a dense and continuous network of flakes.

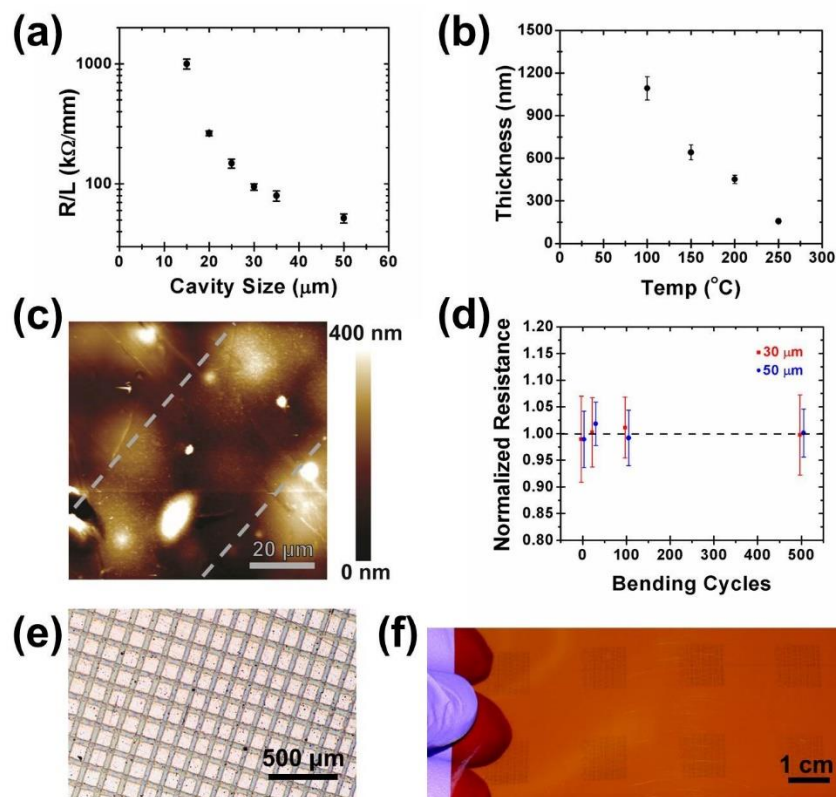


**Figure 3.7.** Characterization of gravure-printed graphene for electronics. (a) Line resistance for the varying cavity size. (b) Thickness contraction during annealing for the graphene/EC composite. (c) AFM images of a printed line, illustrating that the printed lines are considerably thinner than the substrate surface roughness. (d) Normalized resistance of printed lines over 500 bending cycles at a radius of curvature of 2 mm, or 3.1% strain. (e) Printed crossbar array. (f) Photograph of large-area patterns.

Because the essential physical processes of gravure printing are defined by filling individual cells, removing excess ink, and transferring the ink to the substrate, the inks and optimized printing parameters developed here can be readily extended to more complex patterns. For example, Figure 3.7e shows a crossbar pattern with lines printed in orthogonal directions. This pattern demonstrates the invariance of printed patterns with the printing direction, as the lines are aligned both parallel and orthogonal to the direction of printing. In addition, it demonstrates the robustness of printing even over features  $\sim 200$  nm thick on the substrate, an important prerequisite

to more complex, multi-material structures. Figure 3.7f further illustrates large-area patterns printed with graphene, thus verifying the scalability of this technique for rapid, high-volume printing applications.

### **3.5. Summary for Graphene/EC Gravure Printing**

In summary, gravure printing of large-area, high-resolution patterns of pristine graphene was demonstrated on flexible substrates through the formulation of suitable inks and the optimization of printing parameters. By adapting graphene dispersion strategies originally developed for inkjet printing, a stable, high-concentration graphene ink was developed with tunable viscosity in a chemically and environmentally benign solvent with established applicability for gravure printing. This strategy employs pristine graphene flakes, with excellent electrical conductivity and compatibility with flexible substrates. By tailoring the ink properties and printing conditions, continuous lines with resolution as fine as  $\sim 30 \mu\text{m}$  are printed over large areas with notable reliability and uniformity. The electrical conductivity of these patterns of  $\sim 10000 \text{ S/m}$  is among the highest reported for printed graphene, and is particularly impressive considering the nanoscale thickness of the patterns on a topographically rough substrate. This printing strategy thus offers the opportunity to utilize the 2D nature of graphene in a robust, large-area format. In this manner, the integration of graphene with gravure printing represents a milestone in the development of solution-processed graphene for commercially relevant, highly scalable applications in printed and flexible electronics.



## **CHAPTER FOUR**

Screen Printing of Graphene/Ethyl Cellulose



#### 4.1. Introduction to Screen Printing of Graphene

As discussed in the previous chapters, printed electronics is centered around high performance functional inks and high throughput printing methods such as inkjet, gravure, flexographic, and screen printing.<sup>165</sup> Screen printing offers a particularly versatile strategy for the integration of graphene in a robust and practical printing process. In particular, high-resolution screen printing is desired to improve the integration density and performance of electronic devices, but this requires advances in both ink design and printing methods. Here these challenges are addressed with a novel strategy for high-resolution screen printing using a silicon stencil coupled with the graphene ink processing framework that constitutes the basis of this thesis.

Screen printing is a classic mass-printing method realized by pressing an ink through a patterned stencil with a squeegee, and has been widely employed for electronics due to its versatility and compatibility with a wide variety of functional inks and substrates.<sup>166-172</sup> Although several studies have demonstrated screen printing of reduced graphene oxide,<sup>98,173,174</sup> high-resolution screen printing of pristine graphene for printed electronics has not yet been realized. This is due in part to the difficulty in producing viscous and highly loaded dispersions of pristine graphene resulting from the material's inherent tendency to aggregate. Moreover, conventional screen printing methods are restricted to a printing resolution of 50 to 150  $\mu\text{m}$  corresponding to a screen mask resolution of 40 to 120  $\mu\text{m}$ ,<sup>162,169,175,176</sup> impeding the drive for fabrication of finer patterns to facilitate higher integration density and improved device performance. The printing resolution of screen printing is highly dependent on the quality of the screen mask, which is generally prepared using a photochemically defined emulsion coated on a screen mesh. Although finer patterns of the mask are expected to improve printing resolution, the low lithography

resolution of the emulsion layer and mesh dimensions restrict the improvement in printing resolution. Thus, it is a challenge to develop a high-resolution mask that can be applied to screen printing of graphene for printed electronics.

As discussed in Chapter 1, screen printing traditionally requires high viscosity pastes. This high viscosity prevents significant spreading following printing, while shear thinning behavior allows for ink to flow more readily into high aspect ratio, high resolution openings in the screen. The challenge for screen printing graphene, then, lies in the formulation of such a suitable ink. In particular, a stable, high-concentration dispersion of graphene in suitable solvents is of critical importance. The dispersion of graphene with ethyl cellulose (EC) demonstrated in the previous chapters shows great promise in this regard, in that high concentrations of graphene are realized in chemically benign organic solvents such as ethanol and terpineol for inkjet and gravure printing.<sup>71,76</sup> Moreover, this strategy offers broad control over the dispersion viscosity, a key parameter for printing methods, and leads to high-conductivity patterns following annealing.<sup>70</sup> The ability to tune ink rheology enables pristine graphene to be integrated with rapid, low-cost, and high throughput production methods such as screen printing.

Here the precision patterning of pristine graphene by screen printing is demonstrated using a silicon stencil. The screen printing stencil is prepared from a thin silicon wafer. Silicon is compatible with photolithography processing and the silicon stencil does not have a mesh, which enables well-defined and high-resolution stencil patterns. In addition, a viscous, concentrated, pristine graphene ink is developed, and the effects of ink properties and printing parameters are studied. High-quality patterns with good electrical conductivity and excellent mechanical tolerance are produced. To demonstrate the feasibility of this approach for printed electronics, all-printed

EGTs are fabricated on flexible substrates using screen-printed graphene source and drain electrodes, and the device performance and mechanical durability are characterized.

## 4.2. Graphene/EC Ink Formulation and Screen Printing Method Development

As a first step for high-resolution screen printing of graphene, an alternative stencil design is developed based on a thinned silicon wafer. Figures 4.1-4.2 depict a schematic diagram for the preparation and use of this stencil. The silicon wafer was first thinned to impart mechanical flexibility by a simple wet etching process.<sup>177</sup> The thinned silicon wafer, with a thickness less than 120  $\mu\text{m}$ , was flexible enough to be employed for screen printing, while a wafer with a thickness less than 85  $\mu\text{m}$  has insufficient mechanical tolerance to withstand the applied force during printing. In addition, a thinner stencil facilitates easier screen printing for fine lines, because it allows the ink to travel through the stencil and transfer onto the substrate more readily. Therefore, this study used silicon wafers with a thickness of 90 ( $\pm 5$ )  $\mu\text{m}$ . As shown in Figure 4.1a, the photolithography process was then carried out to pattern openings on the thinned silicon wafers. Figure 4.3a shows the optical microscopy (OM) image of the silicon stencil showing line openings with widths ( $w_{\text{screen}}$ ) of 20, 30, and 40  $\mu\text{m}$  in the silicon stencil. The line openings were created with high fidelity by reactive ion etching. A high-resolution OM image (Figure 4.3b) reveals that the edges of the line openings are straight and the opening shapes are equivalent to the patterns in the photomask. This strategy enabled line openings as narrow as 5  $\mu\text{m}$  in the silicon stencil (Figure 4.3c).

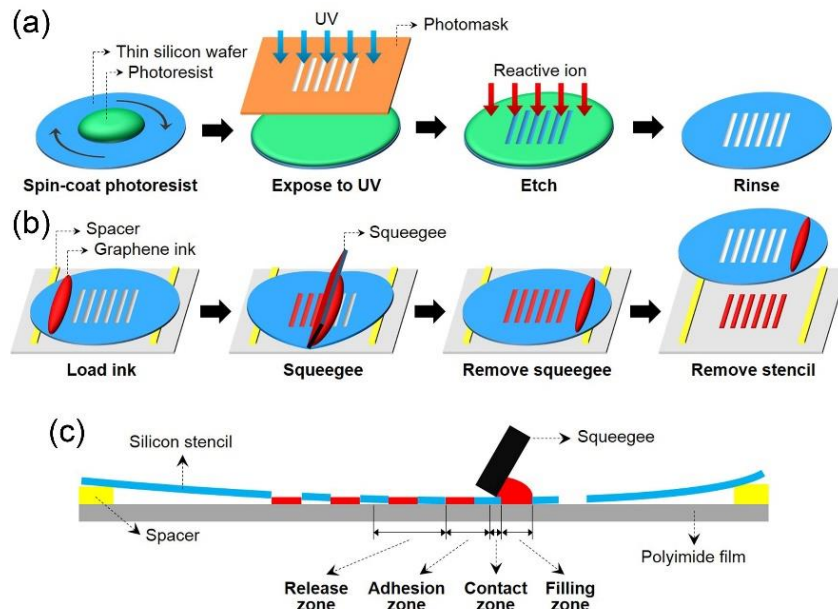


**Figure 4.1.** (a) Fabrication steps for a thin silicon stencil using conventional lithography techniques. (b) Schematic process of screen printing using the silicon stencil and a pristine graphene ink. (c) Cross-sectional illustration of the screen printing method with the flexible silicon stencil during printing.

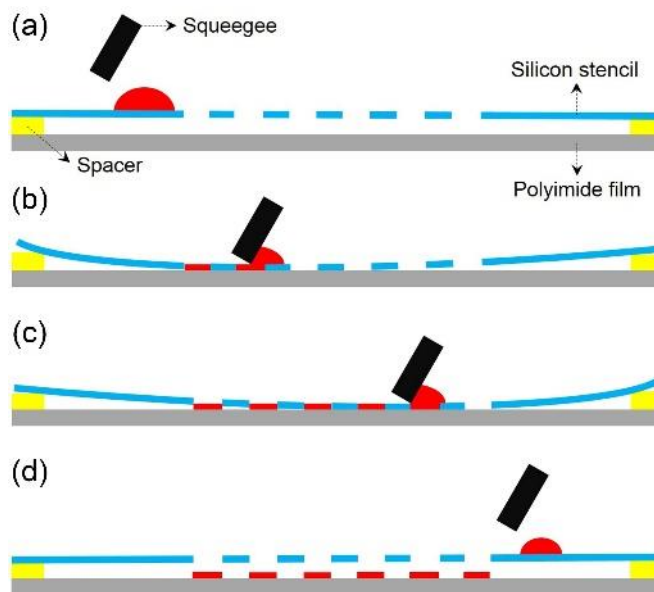


**Figure 4.2.** Schematic diagram of screen printing with a silicon stencil in a cross-sectional view. (a) The graphene ink is placed on the silicon stencil. (b) The squeegee moves the ink and presses the stencil at the same time, which makes contact between the stencil and the substrate. (c) As the squeegee passes the openings, the ink is printed on the substrate. (d) When the squeegee is removed from the stencil, the stencil separates from the substrate, leaving the ink on the substrate.

Figure 4.1b and Figure 4.2 display schematic diagrams for screen printing with the silicon stencil. The substrate was held on a vacuum plate, and spacers were inserted between the stencil and the substrate. Due to its low surface roughness, the polished face of the silicon stencil was placed down to make better contact between the stencil and the substrate during printing. The spacer was made with poly(dimethylsiloxane) (PDMS) with a thickness of ~2 mm. Use of different spacer thicknesses between 1.5 mm and 2.5 mm did not change the printing quality significantly. The somewhat adhesive surface of the PDMS spacers helps to secure the silicon stencil in place during printing. The graphene ink was then placed on top of the stencil and pushed by a squeegee. A single pass of the squeegee was sufficient to transfer the graphene pattern to the substrate. Figure 4.1c represents a schematic cross-sectional view of the stencil during printing, illustrating the equivalent mechanics of screen printing with a silicon stencil and a conventional screen. During printing, the squeegee forces the ink through the stencil while simultaneously pressing the stencil. Because the thin silicon wafer is flexible, the stencil bends, providing contact between the stencil and the substrate (contact zone). In front of the squeegee edge, the ink is moved and penetrates into the openings of the stencil (filling zone). After the squeegee edge passes the openings, the graphene ink in the openings adheres to the substrate (adhesion zone). Finally, the stencil is lifted up, leaving the ink on the substrate (release zone).

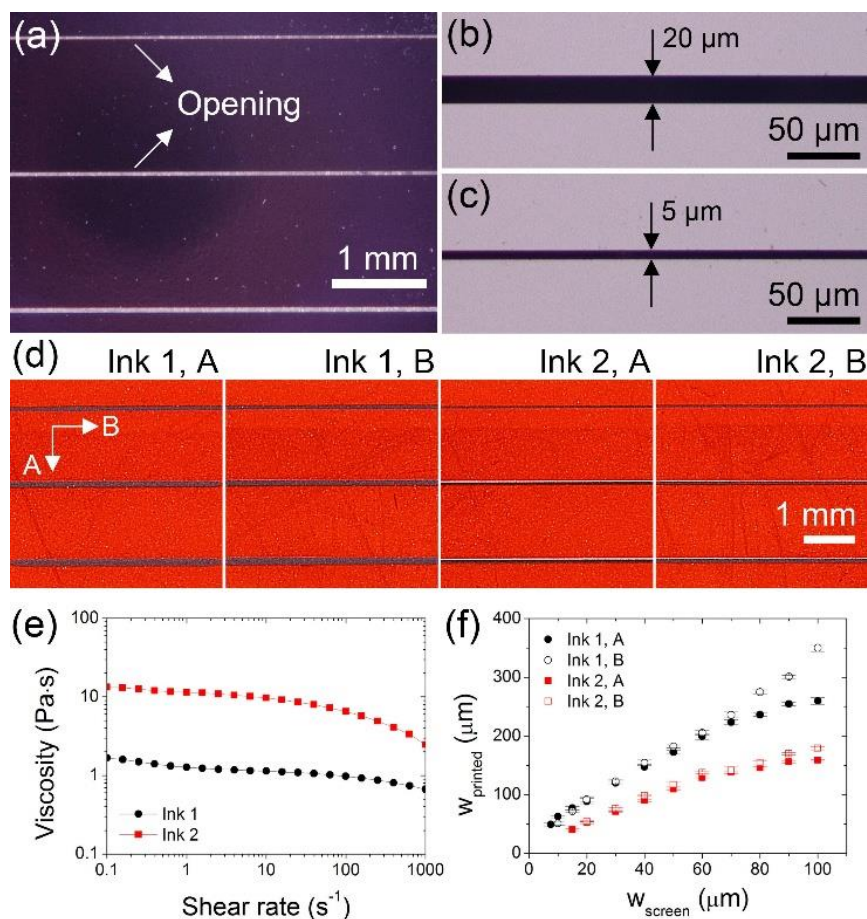


**Figure 4.3.** (a) Optical microscopy (OM) image of a thin silicon stencil showing line openings with different widths ( $w_{\text{screen}}$ ) of 20 (top), 30 (middle), and 40  $\mu\text{m}$  (bottom) in a silicon stencil. (b, c) High-resolution OM images for line openings with  $w_{\text{screen}}$  of 20 and 5  $\mu\text{m}$ , respectively. (d) OM images of graphene lines printed on polyimide films through line openings with  $w_{\text{screen}}$  of 20 (top), 30 (middle), and 40  $\mu\text{m}$  (bottom). The printing was accomplished from two inks of different viscosities (Ink 1 and 2), in two different printing directions (A and B). (e) Measured shear viscosity for Ink 1 and 2. (f) Width ( $w_{\text{printed}}$ ) of screen-printed graphene lines measured by OM on polyimide substrates with different inks and printing directions for varying  $w_{\text{screen}}$ .

In conjunction with the unique stencil design described above, pristine graphene inks were developed with properties suitable for this printing method. To prepare the graphene ink, solvent-exfoliated graphene was produced by ultrasonication of graphite in a solution of EC in ethanol. This strategy, previously reported,<sup>62</sup> offers high graphene yields ( $\sim 0.2$  mg/mL) with a short

processing time, limiting the degradation of the intrinsic structure and properties.<sup>63</sup> To isolate large graphene flakes with minimal polymer binder, a two-step centrifugation-based classification method was used. The first step at a lower centrifugation rate removed thick, unexfoliated graphite particles, retaining the supernatant. The second step at a higher rate isolated graphene flakes and EC as the sediment. This sample of graphene was redispersed with additional EC in ethanol and isolated as a solid by the flocculation procedure developed in Chapter 2. In detail, natural graphite flake (20.0 g, Asbury Graphite Mills, 3061 Grade) was dispersed in a solution of EC in ethanol (0.1% w/v dispersion, 200 mL; EC: Aldrich, viscosity 4 cP, 5% in toluene/ethanol 80:20, 48% ethoxy; ethanol: Koptec, 200 proof) in a stainless steel beaker. A probe sonication system (Fisher Scientific Sonic Dismembrator Model 500, 13 mm Branson tip) was used to sonicate the dispersion for 105 min at 50 W in an ice water bath to exfoliate graphene sheets. The resulting dispersion was centrifuged (Beckman Coulter Avanti® J-26 XPI) at 5000 rpm (~4500 g) for 15 min, and the supernatant was collected. This dispersion was further centrifuged at 7500 rpm (~10000 g) for 15 min, and the sediment was collected. The wet sediment was redispersed with ethanol (25 mL ethanol per 1.0 g sediment) and EC (100 mg EC per 2.0 g sediment; EC: Aldrich, viscosity 22 cP, 5% in toluene/ethanol 80:20, 48% ethoxy) by bath sonication for 3 h. This dispersion was passed through a 3.1  $\mu\text{m}$  glass fiber filter membrane (Acrodisc®). It was then mixed with an aqueous solution of NaCl (0.04 g/mL, Sigma-Aldrich, >99.5%) in a 16:9 weight ratio and centrifuged at 7500 rpm for 8 min, after which the supernatant was removed. To remove residual salt, the resulting graphene/EC solid was suspended in water, bath sonicated for 20 min, and collected by centrifugation at 7500 rpm for 10 min. This isolated graphene/EC composite was then dried to yield a powder. This process was repeated to produce enough material for ink production. TGA of

this powder revealed 78.3% mass retention at 400 °C, estimated to reflect the graphene solids content (temperature ramp at 10 °C/min in air).

The flakes produced by this method are primarily few-layer graphene with a typical thickness of ~2 nm and a typical area of approximately 70 nm × 70 nm, as shown in Figure 4.4. By isolating the graphene/EC composite as a powder, broad control over the final ink composition is enabled. Inks were prepared from the graphene/EC powder in terpineol, a well-established solvent for screen printing with EC as a binder.<sup>178,179</sup> Graphene/EC powder (0.5 g) and EC (0.5 g, Aldrich, 4 cP at 5 wt.% in toluene/ethanol 80:20) were dispersed in ethanol (~25 mL) and terpineol (5.0 mL, Aldrich, mixture of isomers, anhydrous) by bath sonication for ~90 min. The ethanol is used to facilitate dispersion because it maintains a low dispersion viscosity, facilitating more effective sonication, and is readily removed by applying heat. The dispersion was passed through a 3.1 µm glass fiber filter membrane (Acrodisc®). The filtered dispersion was heated on a hot plate to remove ethanol, yielding a final ink of nominally 20% w/v solids in terpineol, with a graphene:EC ratio of 2:3 by weight (Ink 1). The higher viscosity ink (Ink 2) was prepared similarly using a higher viscosity EC sample (Aldrich, 22 cP at 5 wt.% in toluene/ethanol 80:20). In this way, the two inks are characterized by nominally equivalent graphene concentration of ~80 mg/mL, much higher than alternative graphene inks developed without a polymer binder; for example, a graphene dispersion in N-methyl pyrrolidone for inkjet printing has a concentration of ~6 mg/mL.<sup>69</sup> While they have similar graphene concentrations, the viscosity of the inks varies by a factor of ~10, as shown in Figure 4.3e, with a shear viscosity of ~1 and ~10 Pa·s for Ink 1 and Ink 2, respectively, at a shear rate of 10 s<sup>-1</sup> (25 °C, measured with 25 mm, 2° cone and plate).



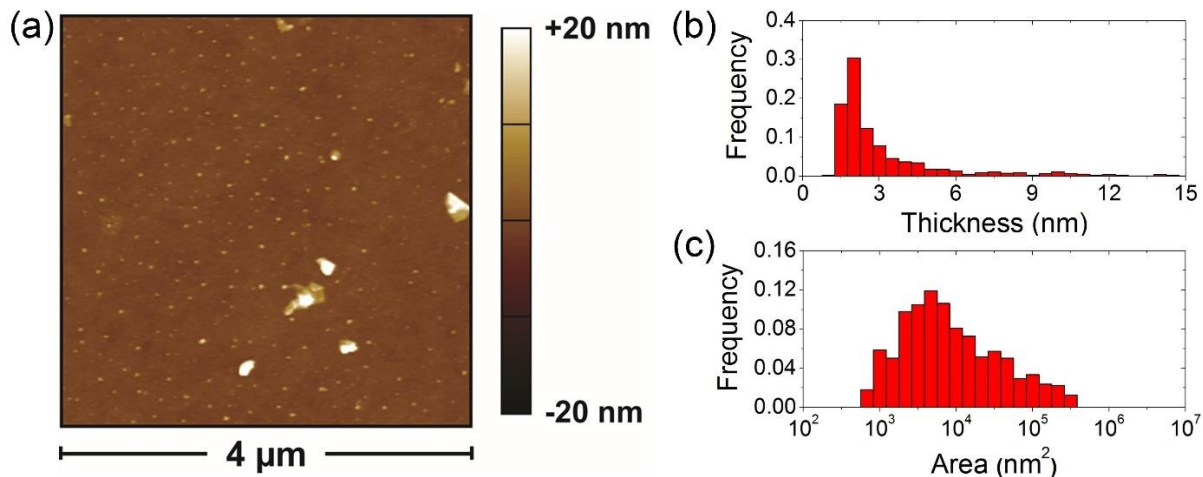


**Figure 4.4.** AFM characterization of graphene flakes. (a) Representative AFM image of graphene flakes dropcast on SiO<sub>2</sub>. Distributions of (b) flake thickness and (c) flake area for 715 particles, indicating typical flake dimensions of ~2 nm thickness and ~70 nm × 70 nm area.

### 4.3. Screen Printing Optimization and Characterization

A thorough characterization of the interplay between printing parameters and ink properties was carried out to optimize the printing of high-resolution graphene lines. To investigate the screen printing process, printing was performed in two different directions (Figure 4.3d), perpendicular (Direction A) and parallel (Direction B) to the line openings. Figure 4.3d presents the screen-printed graphene lines on polyimide using line openings with  $w_{\text{screen}}$  of 20 (top), 30 (middle), and 40 (bottom)  $\mu\text{m}$ . The OM images show precisely printed graphene lines, indicating the high-quality printing of graphene achieved using the silicon stencil. To study the transfer of ink through the stencil, a potentially limiting process for high-resolution printing, the printing capability is defined as the minimum  $w_{\text{screen}}$  for which ink is reliably transferred to the substrate. To determine the printing capability with regard to the ink viscosity and printing direction, screen printing was performed with line openings for varying  $w_{\text{screen}}$  from 5  $\mu\text{m}$  to 50  $\mu\text{m}$ . For Ink 1, the printing

capability was 7.5 and 10  $\mu\text{m}$  for printing perpendicular and parallel to the lines, respectively. For Ink 2, it was 15 and 20  $\mu\text{m}$  for printing perpendicular and parallel, respectively. This indicates that printing perpendicular to the line openings and using a lower viscosity ink are better for screen printing with fine mask patterns. It has been reported that the squeegee can deform more into the line openings perpendicular to the screen printing direction, compared to those parallel to the printing direction, which causes higher pressure to the ink underneath the squeegee in perpendicular openings than parallel openings.<sup>180</sup> This increased pressure forces the ink to contact the substrate better, leading to a higher quality print. In addition, the better printing capability with the lower viscosity ink can be attributed to the easier penetration into the stencil because it generates lower resistance to flow when the ink travels through the fine line openings.

The width of printed graphene lines ( $w_{\text{printed}}$ ) was measured for lines printed from varying  $w_{\text{screen}}$ , as shown in Figure 4.3f. It was observed that the printing direction did not affect  $w_{\text{printed}}$  significantly, whereas  $w_{\text{printed}}$  of Ink 1 was much larger than that of Ink 2 for the same  $w_{\text{screen}}$ . Larger  $w_{\text{printed}}$  with Ink 1 compared to Ink 2 can be explained by more spreading on the substrate due to the lower viscosity.<sup>168</sup> As a result, even though the printing capability ( $\geq 15 \mu\text{m}$ ) with Ink 2 was worse than that ( $\geq 7.5 \mu\text{m}$ ) with Ink 1, printed graphene lines (Figure 4.5a) as narrow as 40  $\mu\text{m}$  were achieved with Ink 2, while the narrowest lines achieved with Ink 1 were 50  $\mu\text{m}$ . Additionally, graphene lines were printed with different spacings of 30, 50, 70, and 90  $\mu\text{m}$ , as shown in Figure 4.5b, c, d, and e, respectively, which were obtained from a stencil having line openings with different spacing. They show uniform spacing between the lines, an important characteristic for application as TFT electrodes, in which the spacing between the lines defines a critical feature size, the channel length. Figure 4.5f shows the measured thickness of the screen-printed graphene

lines as a function of  $w_{\text{printed}}$ , obtained from surface profile measurements (Figure 4.6). Thicknesses for a given ink were similar for the different printing directions. On the other hand, graphene lines from Ink 2 were thicker than those printed from Ink 1 for the same  $w_{\text{printed}}$ , which implies that the higher viscosity of Ink 2 produced higher aspect ratio features (thickness/ $w_{\text{printed}}$ ) compared to Ink 1, as shown in Figure 4.7. Figure 4.5g reveals this issue for printed graphene lines through the line opening with  $w_{\text{screen}}$  of 20  $\mu\text{m}$ . Ink 2 is favorable in terms of better printing resolution and higher aspect ratio, illustrating the importance of controlling the ink rheology and producing high concentration graphene dispersions for screen printing applications. As a result, further experiments were executed with Ink 2.

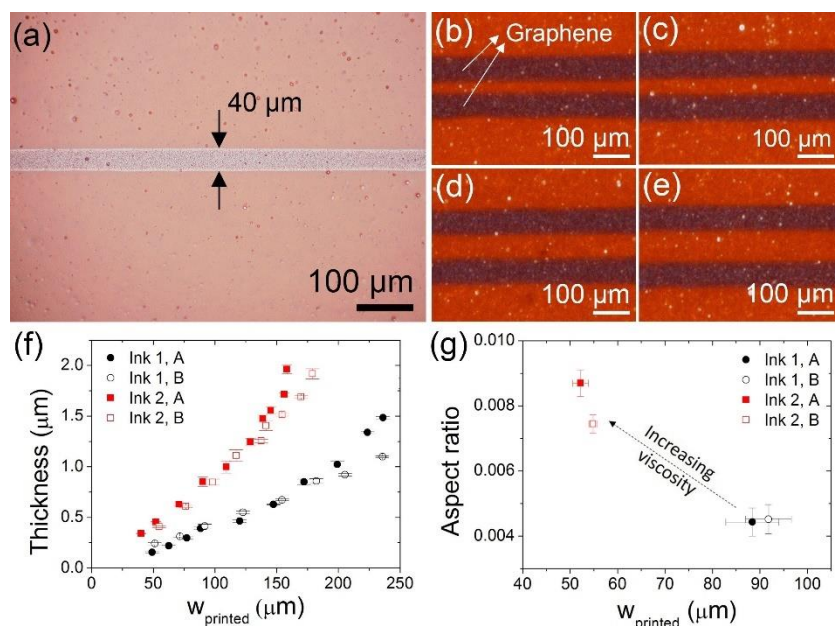


**Figure 4.5.** (a) OM images of a screen-printed graphene line with  $w_{\text{printed}}$  of 40  $\mu\text{m}$  and (b-e) graphene lines (dark double stripes) with different spacing of 30, 50, 70, and 90  $\mu\text{m}$  on polyimide films. (f) Thickness of screen-printed graphene lines for different inks and printing directions. (g) Comparison of the aspect ratio (thickness/width) and  $w_{\text{printed}}$  of the printed graphene lines through a 20  $\mu\text{m}$  wide line opening with respect to the ink viscosity and the printing direction.

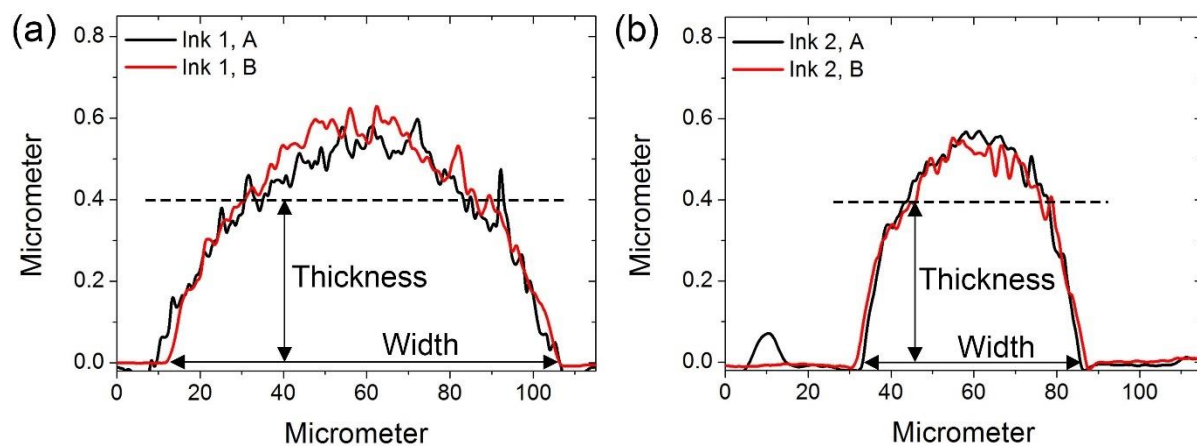


**Figure 4.6.** Surface profile of screen-printed graphene lines through 20  $\mu\text{m}$  wide line opening, from (a) Ink 1 in Direction A and B and (b) Ink 2 in Direction A and B.  $w_{\text{printed}}$  was measured from one side to the other side of printed graphene lines and thickness was obtained from average thickness between sides of printed graphene lines.

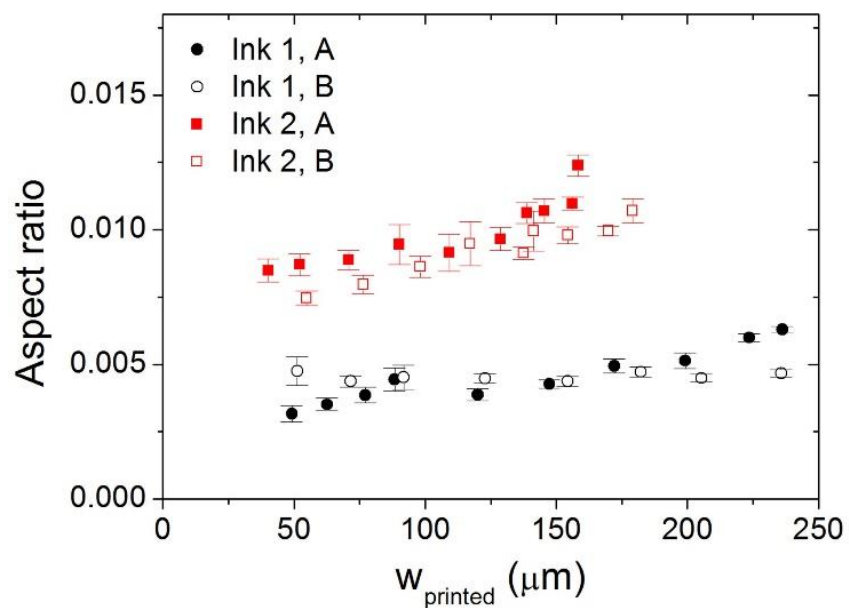


**Figure 4.7.** Aspect ratio (thickness/width) of the screen-printed graphene lines for different inks and printing directions.

#### 4.4. Functional Properties and Application of Screen-Printed Graphene/EC

In addition to the high-resolution capability of the method described above, the electrical conductivity and bending tolerance of the printed graphene lines are key attributes for applications in printed and flexible electronics. In order to characterize the electrical properties of the graphene lines, the graphene was screen-printed with a test pattern for various values of  $w_{\text{printed}}$ , as shown in Figure 4.8a. The pattern contains six contact pads for the measurement of electrical resistance at different total line lengths. Prior to measurement, they were annealed in a furnace at a temperature of 300 °C for 30 min, which led to partial decomposition of the EC polymer stabilizer to produce a dense and continuous network of graphene flakes (Figure 4.8b) for higher conductivity.<sup>70</sup> Decomposition of the EC resulted in a decrease of the pattern thickness by ~70%, as shown in Figure 4.9. Surface roughness of the annealed graphene was measured to be 32 nm by AFM. As shown in Figure 4.8c, the resistance per unit length was calculated from the linear relationship between the measured resistance and the line length, which displays a decrease of the resistance as  $w_{\text{printed}}$  increases. Based on the measured resistance and the line geometries, the conductivity was calculated to be  $1.86 \times 10^4 \pm 0.19 \times 10^4$  S/m (resistivity of  $5.37 \times 10^{-3} \pm 0.55 \times 10^{-3}$   $\Omega \cdot \text{cm}$ ), highly competitive among solution-processed graphenes.<sup>69</sup> Previous studies have demonstrated resilient mechanical properties of printed graphene lines.<sup>70,76,181</sup> To verify the mechanical bending tolerance of the screen-printed graphene on flexible substrates, bending tests were carried out for the graphene lines with different thicknesses of 137 and 637 nm, which were printed through the line openings with  $w_{\text{screen}}$  of 20 and 100  $\mu\text{m}$ . The bending test was performed at a bending radius of 4 mm, corresponding to 1.0% tensile strain. Figure 4.8d shows the relative resistances of the graphene lines over the course of the bending test, revealing a negligible change during 1000

bending cycles and thus verifying the excellent bending stability of screen-printed graphene, independent of the line thickness.

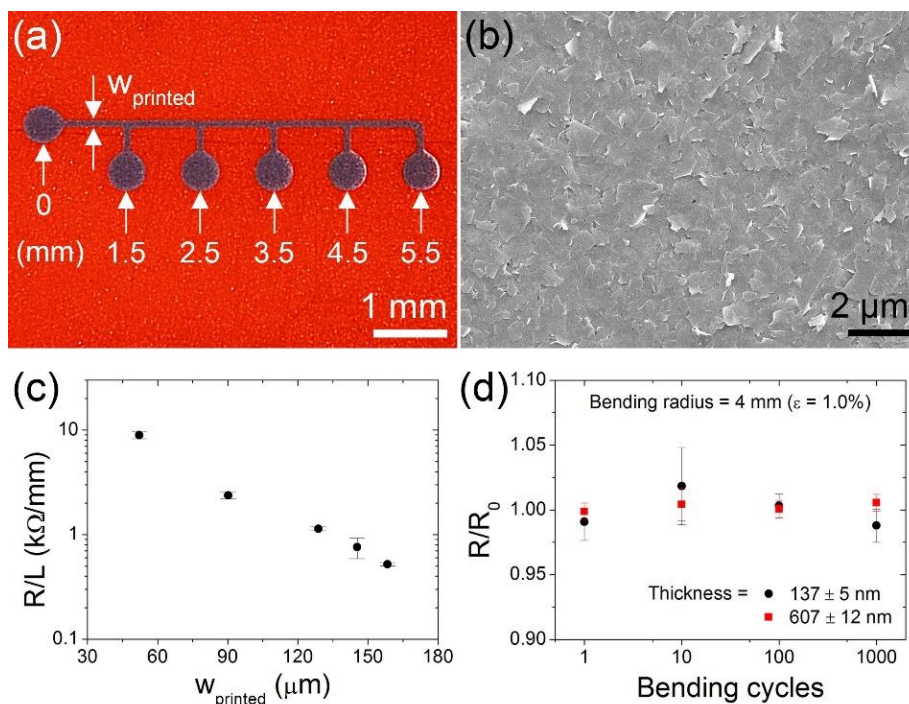


**Figure 4.8.** OM image of screen-printed graphene to measure electrical properties of the graphene lines for different lengths and  $w_{\text{printed}}$ . (b) SEM image of the graphene following annealing. (c) Resistance per unit length of the graphene as a function of  $w_{\text{printed}}$ . (d) Relative resistance of the screen-printed graphene lines on flexible substrates with two different thicknesses over 1000 bending cycles at a bending radius of 4 mm, corresponding to 1.0% tensile strain.

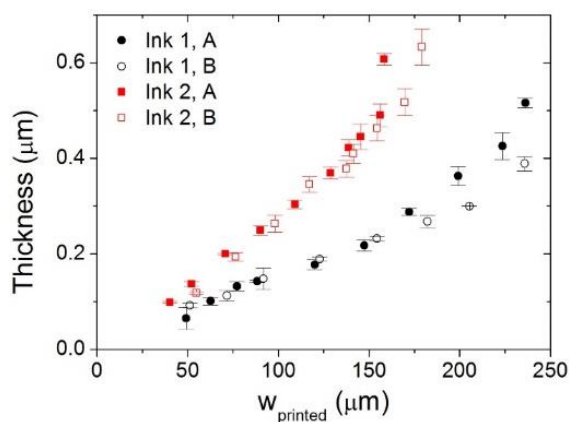


**Figure 4.9.** Thickness of the printed graphene lines after annealing at a temperature of 300 °C for 30 min.

To demonstrate a possible application of screen-printed graphene electrodes, all-printed electrolyte gated transistors (EGTs) were fabricated and characterized. EGTs are promising for flexible printed electronics; the high capacitance of the electrolyte enables low voltage operation, and the material offers broad process compatibility for printing on flexible substrates and good tolerance to thickness variations.<sup>182–184</sup> As shown in Figure 4.10a, EGTs were fabricated using screen-printed graphene for source and drain electrodes on a polyimide substrate, with a channel length (L) and width (W) of 90 and 900  $\mu\text{m}$ , respectively. Figure 4.10b shows the schematic device structure of the EGTs, in which poly(3-hexylthiophene) (P3HT), ion-gel, and poly(3,4-ethylenedioxythiophene):poly(styrene sulfonate) (PEDOT:PSS) were printed by aerosol-jet printing, for the semiconductor, gate dielectric, and gate electrode, respectively. The substrate temperature was maintained at 60°C to enhance ink drying. The semiconductor was printed with an ink containing P3HT dissolved in chloroform (1 mg/mL) and terpineol (9:1 by weight) for a thickness of 50 nm. For the dielectric, ion-gel was printed with an ink containing a triblock copolymer of poly(styrene-*b*-methyl methacrylate-*b*-styrene) (PS-PMMA-PS), ionic liquid of 1-ethyl-3-methylimidazolium bis(trifluoromethylsulfonyl)imide ([EMIM][TFSI], EMD Chemicals), and ethyl acetate at a mixing ratio of 1:9:90 (w/w/w). The gate electrode was printed with an ink containing PEDOT:PSS (PH1000, Heraeus) and ethyl acetate (9:1 by weight). The flow rates of carrier gas and sheath gas were 10 and 45 sccm for P3HT, 16 and 70 sccm for the ion-gel, and 20 and 80 sccm for PEDOT:PSS, respectively, with a 150  $\mu\text{m}$ -diameter nozzle. Finally, the sample was annealed on a hot plate with a temperature of 120°C for 30 min in a glovebox filled with nitrogen gas. The devices were measured using source meters (236 and 237, Keithley) and an electrometer (6517A, Keithley) in nitrogen atmosphere at room temperature. The gate capacitance

was measured by an impedance analyzer (4192A, Hewlett-Packard). Figures 4.10c and 4.10d present the measured transfer and output characteristics of the fabricated EGTs. The devices exhibit negligible current hysteresis between forward and reverse scans in the transfer curve, and good linear and saturation behavior at low and high drain voltage in the output curve. The charge carrier mobility ( $\mu$ ) and the threshold voltage ( $V_{th}$ ) were calculated to be  $0.21 \pm 0.02 \text{ cm}^2 \text{ V}^{-1} \text{ s}^{-1}$  and  $0.42 \pm 0.02 \text{ V}$ , respectively, from the plots of the square-root drain current ( $I_D^{1/2}$ ) as a function of the gate voltage ( $V_G$ ), according to the standard saturation regime relation:

$$I_D = \mu C_i \frac{W}{2L} (V_G - V_{TH})^2 \quad (4.1)$$

The capacitance ( $C_i$ ) of the ion-gel gate insulator was estimated to be  $86 \text{ } \mu\text{F}/\text{cm}^2$  by the capacitance-voltage characteristics, and the devices had a current on-off ratio of  $\sim 10^4$ . To investigate the mechanical flexibility of the printed EGTs with graphene source and drain electrodes, device performance during continuous bending cycles was measured, with a bending radius of 4 mm (tensile strain of 1.0%). Figure 4.10e shows minimal change in device performance in terms of  $\mu$  and  $V_{th}$  resulting from continuous bending cycles. After 1000 bending cycles,  $\mu$  and  $V_{th}$  only decreased by 1.9% and increased by 0.02 V, respectively. These results suggest that the highly flexible graphene source and drain electrodes were helpful to minimize degradation in device performance.<sup>185</sup>



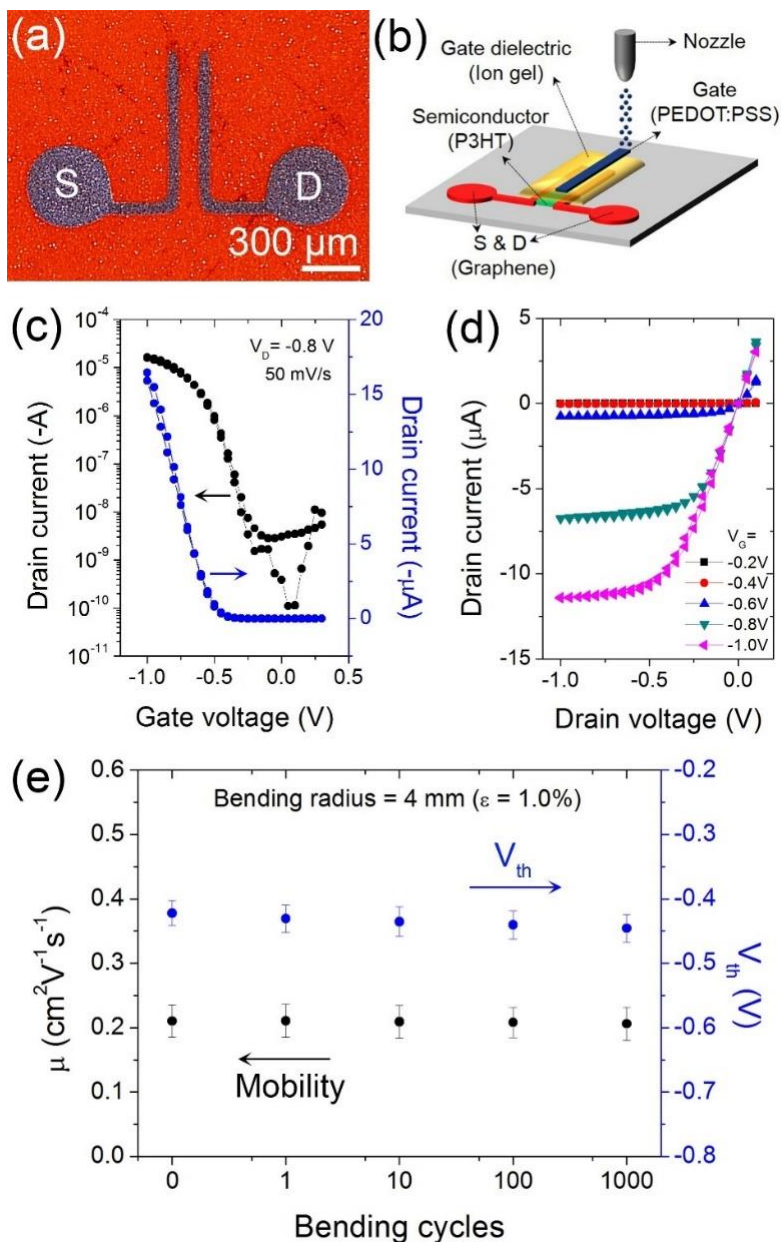


**Figure 4.10.** (a) OM image of screen-printed graphene source and drain electrodes on a polyimide substrate for EGTs ( $W/L = 900\mu\text{m}/90\mu\text{m}$ ). (b) Schematic illustration for the EGT architecture fabricated on the graphene electrodes. (c) Transfer and (d) output characteristics of the printed EGTs. The voltage sweep rate was  $50 \text{ mV s}^{-1}$ . (e) Stability of charge carrier mobility ( $\mu$ ) and threshold voltage ( $V_{th}$ ) for the EGTs during repeated bending cycles with a bending radius of 4 mm, corresponding to 1.0% strain.

#### 4.5. Summary for Graphene/EC Screen Printing

In summary, fine patterning of pristine graphene by screen printing was demonstrated using a silicon stencil and a high conductivity ink based on graphene and ethyl cellulose in terpineol. The well-defined stencil was obtained from a thin silicon wafer by a photolithography process, and was patterned with openings as fine as 5  $\mu\text{m}$  on  $\sim 90$   $\mu\text{m}$ -thick silicon wafers. The silicon stencil and ink formulation facilitated screen printing of high-quality graphene patterns, achieving a resolution as good as 40  $\mu\text{m}$ , which can be attributed to the precise line opening as well as the tailored viscosity of the graphene ink. The screen-printed graphene lines on polyimide films exhibited a good electrical conductivity of  $\sim 1.86 \times 10^4$  S/m and outstanding mechanical flexibility, suitable for electronic applications. With the high-quality and flexible graphene patterns as source and drain electrodes, all-printed EGTs on flexible substrates showed desirable transfer and output characteristics, as well as durable operation over many bending cycles. Overall, this work establishes a scalable method for the facile and practical printing of highly conductive graphene patterns for flexible and printed electronics.

## **CHAPTER FIVE**

Photonic Annealing of Graphene/Ethyl Cellulose

## 5.1. Introduction to Photonic Annealing of Graphene

The prior chapters detail the development of a graphene/EC processing framework with excellent versatility, realizing inks spanning a wide range of viscosity and tailored for inkjet, gravure, and screen printing. Following thermal annealing at 250-300 °C, these inks yield highly conductive and flexible graphene patterns. While this thermal processing requirement is compatible with select plastic substrates, such as polyimide (PI), it is not more generally applicable for thermally sensitive plastics such as polyethylene terephthalate (PET) and polyethylene naphthalate (PEN). This chapter will detail an advance in the processing of graphene/EC inks that enables the fabrication of conductive graphene/EC patterns on these substrates using a rapid and versatile process known as photonic annealing.

Photonic annealing, also known as photonic sintering/curing or intense pulsed light (IPL) annealing, is a processing method developed for printed electronics.<sup>35</sup> Thermal processing of functional inks is commonly required, such as sintering processes for silver nanoparticles, and as with graphene/EC this can impose constraints on the compatibility with certain substrates or co-printed materials. In photonic annealing, a high intensity pulsed light source, typically a xenon flash lamp, is employed to selectively heat the active materials in a very short (i.e., ~1 ms) process. Passive components such as the substrate do not absorb light, and thus experience little overall temperature change, while strongly absorbing active materials reach very high temperatures (500-1000 °C) for a short duration. In addition to effective sintering of silver nanoparticles, the short duration of this process can even be exploited for curing copper or copper oxide nanoparticle inks.<sup>33</sup> Because graphene interacts strongly with light, it is anticipated that suitable ink design and annealing parameters can achieve effective photonic annealing of graphene/EC patterns on

thermally sensitive substrates. This would overcome a key limitation in strategies for inkjet printing graphene, which are typically limited in one or more of several key qualities, namely high electrical conductivity, rapid printing and post-processing, and broad substrate compatibility.<sup>38</sup> Here, these requirements are concurrently achieved by coupling inkjet printing with IPL annealing to achieve rapid fabrication of high conductivity graphene patterns on a wide range of substrates such as PET and PEN.

## 5.2. Graphene Exfoliation and Process Overview

To realize this goal, the work described in Chapter 2 demonstrating high performance inkjet-printed graphene is leveraged,<sup>70</sup> reworking the graphene and ink production processes to enable rapid IPL annealing. Graphene is produced in gram-scale quantities by liquid phase exfoliation based on shear mixing in the presence of the polymer stabilizer, EC.<sup>62,66</sup> Graphene was exfoliated from graphite using a high shear mixer (Silverson L5M-A) with a square hole high shear screen. Ethyl cellulose (4 cP grade) was dissolved in ethanol at a concentration of 0.2-2% w/v, and flake graphite was added at 10% w/v. This mixture was shear mixed for 2 hours at 10230 rpm in an ice bath, and then centrifuged at 4000 rpm (~3000g) for 2 hours to sediment large graphite flakes. The supernatant containing graphene, EC, and ethanol was harvested by pipette. The graphene flakes produced by this method are analyzed using AFM to characterize both flake thickness and lateral area. As shown in Figure 5.1a, the graphene flakes have a typical thickness of ~2 nm and lateral area of ~100 nm × 100 nm. Histograms of the flake dimensions are shown in Figure 5.2. Note that the histograms are shown for both number-weighted (each particle weighted equally) and volume-weighted (particles weighted by relative volume) statistics. While number-

weighted distributions are common practice, weighting by volume provides more physically meaningful insight into the properties of inks and resulting thin films.

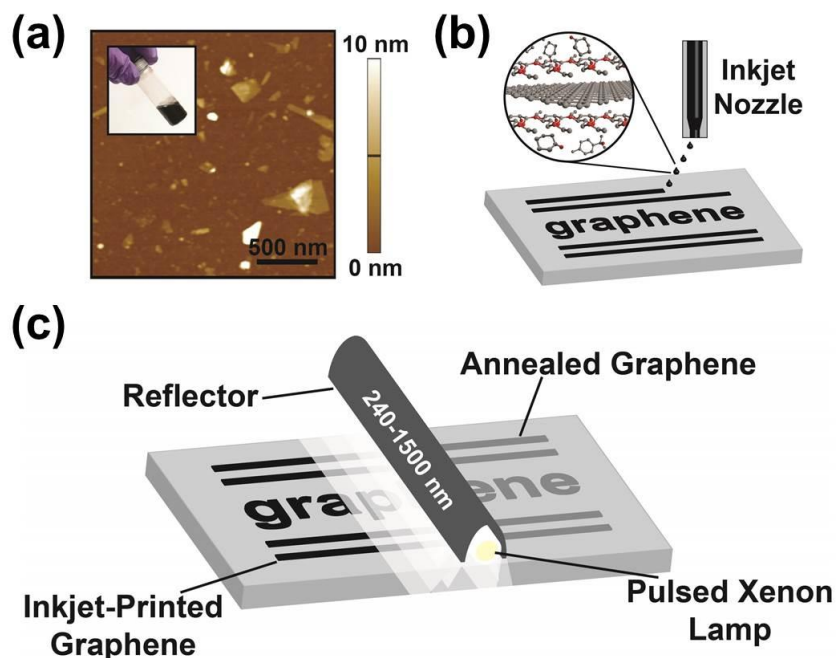


**Figure 5.1.** Inkjet printing and intense pulsed light (IPL) annealing of graphene. (a) AFM image of graphene flakes; inset: image of graphene ink vial. (b) Schematic illustration of inkjet printing of graphene. (c) Schematic illustration of IPL annealing applied to graphene patterns.

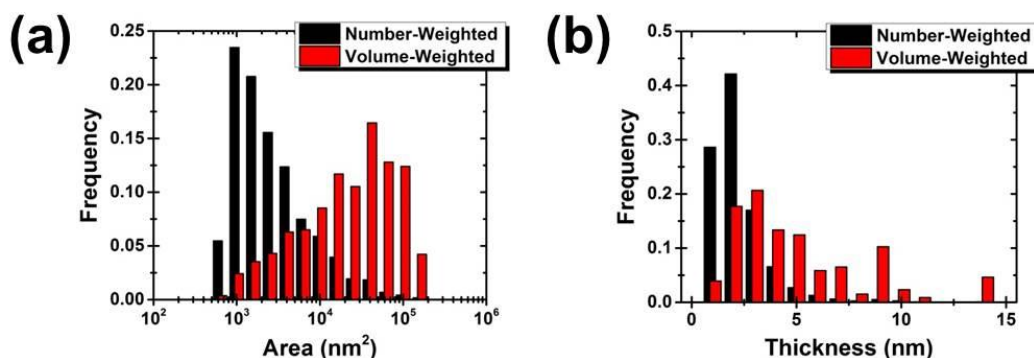


**Figure 5.2.** Characterization of solvent-exfoliated graphene comprising the inks. (a) Flake area distribution for the graphene sample, indicating both number-weighted and volume-weighted distributions. (b) Flake thickness distribution showing both number-weighted and volume-weighted histograms.

Flocculation of the graphene particles produces a graphene/EC composite powder similar to previously described methods,<sup>70</sup> from which concentrated graphene inks are prepared for inkjet printing, as illustrated in Figure 5.1b. The polymer stabilizer enhances the ink stability and printing performance, but requires decomposition following printing to achieve optimal electrical properties.<sup>70,71,186</sup> While polymer decomposition has traditionally been achieved by thermal annealing, the high temperature and long duration required are incompatible with rapid processing and thermally-sensitive substrates, such as PET and PEN, motivating the use of IPL annealing, to enable rapid processing compatible with roll-to-roll manufacturing.<sup>35,187–189</sup> As illustrated in Figure 5.1c, this method uses a high-intensity pulsed xenon lamp to anneal the printed graphene patterns. Due to the large disparity in optical absorption between the graphene and the underlying substrate, photothermal heating occurs selectively in the printed film to minimize substrate damage. Through comprehensive optimization of the graphene production, ink formulation, and annealing conditions, effective IPL annealing is demonstrated for inkjet-printed graphene patterns, achieving significant and simultaneous advances in graphene ink loading, high-speed processing, and substrate versatility.

### **5.3. Effect of Graphene Film Composition on Annealing Effectiveness**

To investigate IPL annealing of inkjet-printed graphene patterns, the importance of the printed graphene film composition is studied. In particular, the graphene:polymer ratio of the printed film is expected to influence the effectiveness of IPL annealing, because photonic annealing is commonly sensitive to the content of additives in the ink formulation.<sup>189</sup> To control the graphene:EC ratio of the powders, inks, and printed films, the concentration of EC in the initial

graphene exfoliation step was varied. As shown in Figure 5.3, increasing the EC concentration led to an increase in the graphene yield, with a stronger dependence than observed for tip sonication. The graphene:EC ratio of the powder was measured by TGA (Figure 5.3b) for an initial EC concentration of 2.0-0.2% w/v. Importantly, much of the enhancement of the graphene ratio occurs during the flocculation step, as shown in Figure 5.3c. Prior to flocculation, graphene comprises 2-10% of the total solids; the graphene composition is enhanced by ~10x during the flocculation step, enabling the high graphene content powders critical for effective IPL annealing. In this way, by changing the EC concentration in the graphene exfoliation step, graphene/EC powders are obtained with a graphene composition ranging from 25 to 65% wt. as precursors for the graphene inks.

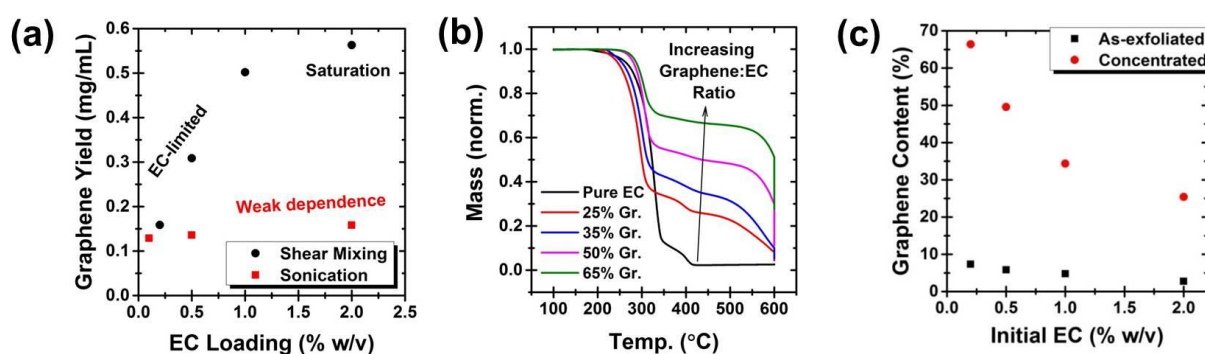


**Figure 5.3.** (a) Graphene yield as a function of EC loading for sonication and shear mixing-based exfoliation. (b) TGA curves of graphene/EC powders prepared with different initial EC concentrations, illustrating the ability to broadly tune the final graphene/EC ratio. (c) Graphene content as a percentage by weight of total solids for different batches, both prior to and following the flocculation step.

These inks are prepared by dispersion of the graphene/EC powder in a solvent system composed of 85:15 v/v cyclohexanone/terpineol, used previously for high performance inkjet printing as described in Chapter 2. This solvent system affords stable inkjet printing and uniform,



high conductivity graphene patterns with negligible evidence of coffee ring formation and good wetting/drying characteristics on a variety of substrates.<sup>70</sup> All inkjet printing for this study was accomplished with a Ceradrop X-Serie inkjet printer equipped with a 10-pL nominal drop size Dimatix cartridge (DMC-11610). Printing was performed using a custom waveform modeled after the Dimatix Model Fluid 2 waveform at 1000-2000 Hz with the inkjet nozzle plate maintained at 30 °C and the substrate held at 35 °C. Printed patterns were dried at 80 °C for 60-180 min following printing to ensure complete solvent evaporation prior to annealing. To confirm the importance of the graphene composition for IPL annealing, films containing 25 and 50% wt. graphene are printed onto glass slides and PET foils (Melinex ST579, 50  $\mu\text{m}$ ) for thermal and IPL annealing, respectively, using inks with the appropriate powders dispersed at 1% w/v in the inkjet printing solvent for a straightforward comparison. For the films containing 25% wt. graphene, the sheet resistance is shown for thermal and IPL annealing in Figure 5.4a. Although photonic annealing produces conductive films using pulse energies of 5-10  $\text{J}/\text{cm}^2$ , the conductance of these films is a factor of  $\sim 2.5$  lower than that of optimized thermally annealed films of the same composition. Corresponding data for films containing 50% wt. graphene are shown in Figure 5.4b. In this case, IPL annealing produces films with a sheet resistance within 10% of the optimized thermally annealed samples. This low sheet resistance of IPL-annealed films containing 50% wt. graphene demonstrates that IPL annealing is an effective post-processing strategy for this material system, even on temperature-sensitive substrates such as PET. In addition, comparison of the 25 and 50% wt. graphene films confirms that the effectiveness of IPL annealing depends on the graphene:polymer ratio of the printed films. Notably, a decrease in resistance is observed upon thermal annealing above a threshold temperature close to 200 °C due to decomposition of the

polymer stabilizer (Figure 5.3c). While maintaining this high temperature is incompatible with many desirable substrates, IPL annealing can exceed this threshold temperature on a timescale short enough to promote polymer decomposition with minimal substrate damage,<sup>189</sup> leading to the gradual decrease in resistance with increasing annealing energy. Unlike prior work in which GO is partially reduced using light-based methods, here the graphene is already in a non-oxidized state.<sup>62,190,191</sup> Both thermal and IPL annealing result in similar evolution of the Raman spectra, namely a reduction in the D to G band intensity ratio,  $I(D)/I(G)$ , for higher energy annealing (Figure 5.5). A reduction in  $I(D)/I(G)$  is associated with reduced defect density and increasing graphitic nature for graphene particles and films, and correlates with removal of the polymer.

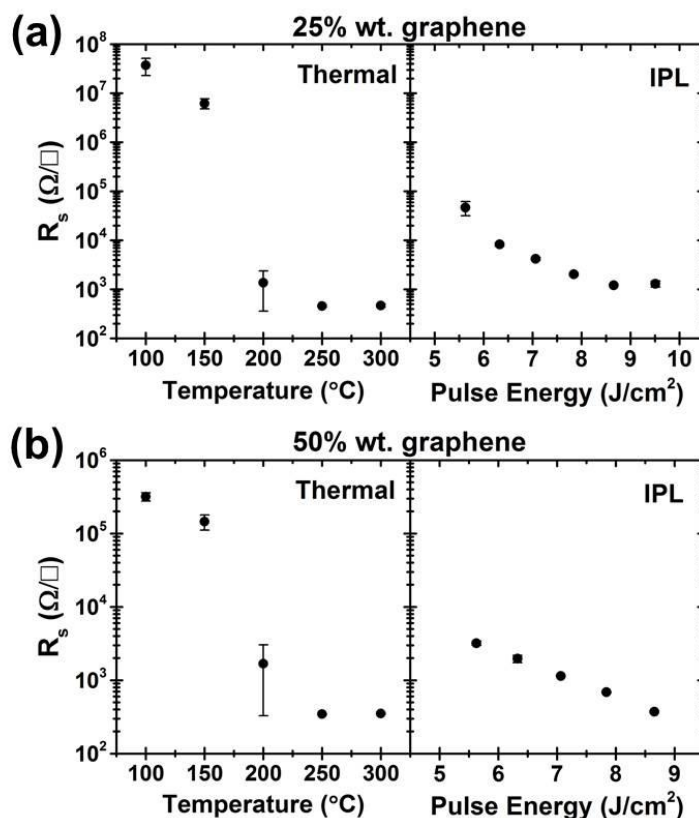


**Figure 5.4.** Dependence of annealing on graphene:polymer ratio of the films. (a) Sheet resistance as a function of processing conditions for a film containing 25% wt. graphene for thermal (left) and IPL (right) annealing. (b) Corresponding sheet resistance as a function of annealing conditions for a film containing 50% wt. graphene, showing improved effectiveness of IPL annealing.

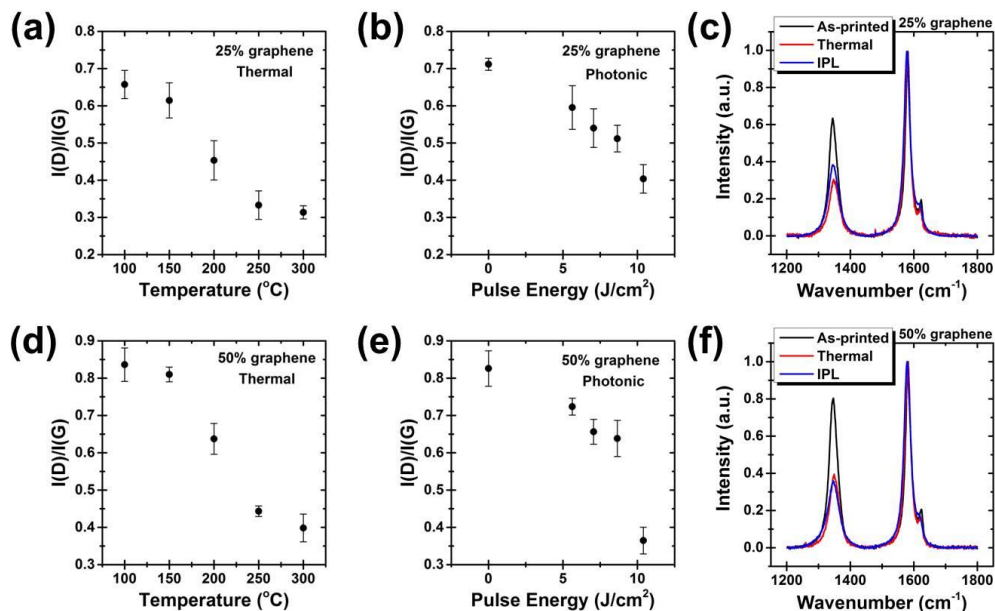


**Figure 5.5.** Raman spectroscopy of graphene films. (a,b) Evolution of the Raman D-to-G band intensity ratio for films containing 25% wt. graphene following thermal and photonic annealing, respectively. (c) Representative spectra for films containing 25% wt. graphene prior to and following annealing with the most energetic thermal and IPL annealing conditions. (d-f) Corresponding data for films containing 50% wt. graphene. Raman spectra were collected using a 532 nm laser.

#### 5.4. Process Generalization and Optimization

The realization of IPL annealing for graphene films on PET suggests that this method can be generalized to other substrates. The sheet resistance as a function of light pulse energy is shown in Figure 5.6a for films on four different substrates, namely PET, PEN, PI, and glass, confirming the versatility of this method. Consistent with previous reports, the required pulse energy depends on the particular substrate due primarily to differences in substrate thermal properties.<sup>189,192</sup> While the low thermal conductivity and limited heat capacity of PET and PEN lead to highly conductive films for low energy light pulses, the somewhat thicker PI, and much thicker glass require additional energy for comparable results. Notably, though, all substrates support graphene films

with sheet resistance comparable to that achieved through thermal annealing. To further validate the versatility of this strategy, individual lines were printed on PET, PEN, PI, glass, and HMDS-treated glass to verify the well-behaved wetting and drying properties of the ink on each substrate. To confirm that good resolution can be achieved on a range of substrates, lines were printed with a drop spacing of 20-35  $\mu\text{m}$  (Figures 5.6b and 5.7). Highly uniform lines are observed, with well-defined edges and negligible evidence of coffee ring formation, which is attributed to the ink composition, as discussed previously.<sup>70</sup> As expected, the line width decreases for increasing drop spacing, with straight and uniform lines observed in each case (Figure 5.6c). Notably, the observed line resolution on HMDS-treated glass is  $\sim 45 \mu\text{m}$  for a drop spacing of 35  $\mu\text{m}$ , confirming that this ink can produce high resolution lines when the substrate surface energy is tuned appropriately.

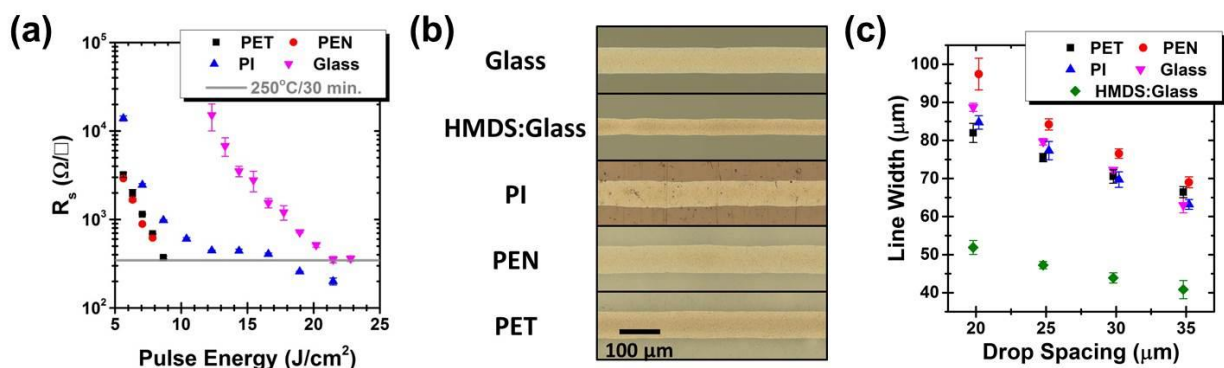


**Figure 5.6.** Versatility of IPL annealing for graphene patterns. (a) Sheet resistance of graphene films as a function of annealing voltage, for different substrates (PET, PEN, PI, and glass). (b) Optical microscopy images of lines on five different surfaces with a drop spacing of 35  $\mu\text{m}$ , showing high-fidelity, uniform pattern definition. (c) Resolution of inkjet-printed lines on the five surfaces as a function of drop spacing.

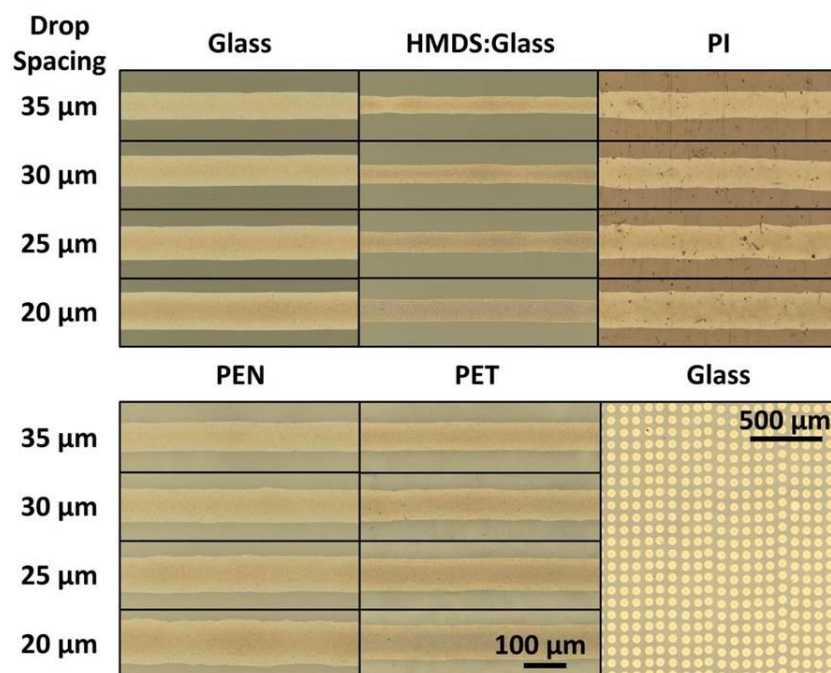


**Figure 5.7.** Characterization of inkjet-printed graphene patterns. Optical images of printed lines with different drop spacing on various substrates, including untreated glass, HMDS-treated glass, PI, PEN, and PET. (bottom right) Printed drop array on untreated glass, showing stable and reproducible jetting and wetting performance. The direction of printing is oriented vertically in this image.

### 5.5. Revisiting Inkjet Ink Formulation with Improved Process Control

While the enhanced graphene content of the ink is critical for optimal IPL annealing, it provides an additional benefit with respect to ink formulation. Specifically, graphene and other nanomaterial inks are typically characterized by a low concentration of active material.<sup>24</sup> This low nanomaterial content is a significant impediment for many practical applications, since the number of printing passes required to achieve a desired conductance, or thickness, scales inversely with the solids loading. In most cases, low concentrations are required to mitigate particle aggregation and achieve stable jetting. In contrast, EC acts as a highly effective stabilizer, allowing previously

reported graphene concentrations as high as  $\sim 3.4$  mg/mL for inkjet printing and 80 mg/mL for screen printing.<sup>70,77</sup> As evidenced by the high concentration suitable for screen printing, the graphene loading for inkjet printing is not limited by colloidal stability, but instead by ink viscosity, which is typically in the range of 8-15 mPa·s for inkjet printing.<sup>24</sup> For graphene/EC inks reported to date, the polymer component is the dominant contributor to the dispersion viscosity. Consequently, it follows that increasing the graphene content of the precursor powder offers a dual enhancement: a higher graphene concentration is achieved for the same total solids loading, and higher solids loading can be employed without exceeding the desirable viscosity range. To confirm this, a graphene ink was prepared using a 50% wt. graphene powder, with a total solids loading of 4% w/v, yielding a total graphene concentration of 20 mg/mL. Following bath sonication, the ink was filtered through a 3.1  $\mu\text{m}$  glass fiber filter. To confirm that the high graphene content facilitates inkjet printing at this high loading, an ink was prepared similarly with 15% wt. graphene powder, again at total solids loading of 4% w/v (15% wt. graphene was chosen because this corresponds to the previous report of inkjet-printed graphene using this method, in Chapter 2). The viscosity of each ink was measured at 20-40 °C, as shown in Figure 5.8. The ink containing the enriched graphene powder exhibits a viscosity of 10-15 mPa·s, within the suitable range for inkjet printing of 8-15 mPa·s.<sup>24</sup> In contrast, the ink containing the standard 15% wt. graphene powder exhibits a higher viscosity, confirming that the high polymer content imposes an upper limit on the ink loading due to the ink viscosity. Moreover, the previous ink based on 15% wt. graphene powder exhibited a similar viscosity at 2.4% w/v solids loading, with a total graphene concentration of  $\sim 3.4$  mg/mL. In this manner, by controlling the solids loading and graphene:polymer ratio

independently, a graphene ink is formulated for inkjet printing that is  $\sim 6\times$  more concentrated than previously demonstrated.

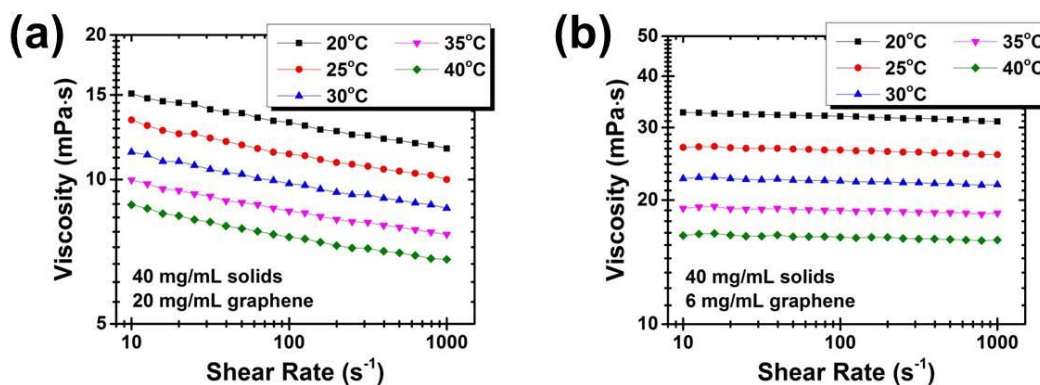


**Figure 5.8.** Rheological properties of graphene inks. (a) Viscosity as a function of shear rate for high graphene content inks at temperatures relevant for inkjet printing. (b) Corresponding viscosity vs. shear rate plots for an ink with the same solids content, but lower graphene:EC ratio, showing a viscosity too high for optimal inkjet printing.

The high graphene concentration translates into thicker films for a given number of printing passes, ultimately reducing printing time. As shown in Figure 5.9a, the film thickness scales linearly with printing passes, with each additional pass adding  $468 \pm 5$  nm in thickness prior to annealing, or  $190 \pm 6$  nm in thickness following thermal annealing. This reduction in thickness is associated with decomposition of the polymer stabilizer and densification of the graphene network, consistent with previous reports.<sup>76</sup> As shown in Figure 5.9b, the sheet resistance decreases inversely with the number of printing passes, consistent with constant bulk conductivity. The conductivity for thermally annealed samples is measured to be  $25600 \pm 900$  S/m, even after a single printing pass. While the conductivity of IPL-annealed samples cannot be reliably measured due to changes in surface topography, the sheet resistance for IPL-annealed films is comparable to that of thermally annealed films, and decreases analogously for thicker films. It is therefore likely

that IPL annealing will be effective for graphene/EC films deposited by other printing methods, such as gravure and screen printing,<sup>76,77</sup> because the primary difference between films deposited by these methods is the film thickness.

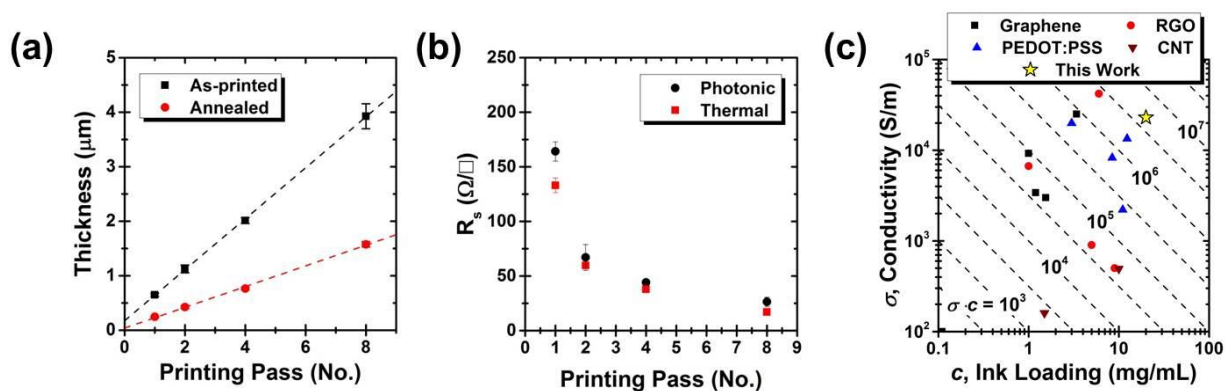


**Figure 5.9.** Characterization of high concentration graphene inks. (a) Thickness as a function of printing passes for graphene/ethyl cellulose films as-printed and following thermal annealing. Dashed lines indicate the least squares linear fit to the thickness data, indicating a thickness per pass of 190 nm following thermal annealing. (b) Sheet resistance of graphene films at various thicknesses following thermal and IPL annealing, illustrating the suitability of IPL annealing over a broad range of film thickness. (c) Map of ink concentration and conductivity for reported non-metal conductive inkjet-printable inks, including inks based on graphene, RGO, CNTs, and PEDOT:PSS. The product of conductivity ( $\sigma$ ) and concentration ( $c$ ) is an indicator of the conductance achieved per printing pass, a key figure of merit for inkjet-printed conductors. Isolines for this metric are drawn as dashed lines to aid the eye.

Altogether, these results represent a significant advance in the development of graphene inks for flexible printed electronics. IPL annealing allows rapid post-processing of graphene patterns, compatible with high-throughput roll-to-roll processing on a range of substrates. The combination of unprecedented graphene loading and high conductivity achieved for this ink offers a new route for high performance, printed electronics with clear advantages over competing graphene inks as well as other non-metal conductors, e.g., reduced graphene oxide (RGO), carbon nanotubes (CNTs), and poly(3,4-ethylenedioxythiophene) polystyrene sulfonate (PEDOT:PSS).



As previously suggested, a key figure of merit for practical applications is the conductance achieved per printing pass, which scales with the product of ink concentration and film conductivity. A range of competing conductive inkjet-printable inks is mapped out on axes of ink concentration and conductivity in Figure 5.9c, taken from the recent literature for graphene,<sup>68–71,186</sup> PEDOT:PSS,<sup>37,193–195</sup> RGO,<sup>89,92,95</sup> and CNTs.<sup>196,197</sup> The dashed lines represent isolines of the product of conductivity and ink loading. Details of each data point in Figure 5.9c are given in Table 5.1. It is important to note that the effect of film density is omitted from this comparison due to the lack of information regarding density in thin films of nanomaterials. The expected conductance per pass will scale inversely with the film density, such that low density materials will exhibit a higher conductance per pass than this analysis would suggest. This is most notable for CNTs, in which the film density can be orders of magnitude below the bulk density due to inefficient packing of CNTs in a random-network film. To confirm that the conclusions remain viable, the reported sheet resistance as a function of printing passes for competitive inks is discussed below.

Material	Conductivity, $\sigma$ (S/m)	Concentration, $c$ (mg/mL)	Ref.
This work (graphene)	25,600	20	79
Graphene	100	0.11	68
Graphene	3,400**	1.2	71
Graphene	25,000	3.4	70
Graphene	3,000	1.55	69
Graphene	9,240	1	186
PEDOT:PSS	8,250	8.5	193
PEDOT:PSS	13,400	12.4	194
PEDOT:PSS	19,900*	3	195
PEDOT:PSS	2,200	11.1	37

RGO	42,000	6	95
RGO	500	9	89
RGO	900	5	89
RGO	6,700	1	92
CNT	220*	0.15	196
CNT	526*	10	197

**Table 5.1.** Comparison of non-metal ink characteristics from the recent literature (plotted in Figure 5.9c).

\*Calculated from reported sheet resistance and thickness data; \*\*taken from Ref. 69.

After 8 printing passes, the graphene ink presented here achieves a sheet resistance of  $26.4 \pm 4.4 \Omega/\square$  following IPL annealing and  $17.1 \pm 0.5 \Omega/\square$  following thermal annealing. Su, et al. achieve a high conductivity using weakly-oxidized graphene oxide with subsequent reduction, but with a lower ink concentration, thus requiring 30 passes to reach  $25 \Omega/\square$ .<sup>95</sup> Ha, et al. use a high conductivity grade of PEDOT:PSS, achieving a sheet resistance of  $45.88 \pm 1.96 \Omega/\square$  after 8 passes.<sup>195</sup> With a highly concentrated carbon nanotube ink, Shimoni, et al. achieve a sheet resistance of  $156 \Omega/\square$  following 6 printing passes for a deliberately nonuniform film.<sup>198</sup> Aiming for a uniform CNT film, Kwon, et al. realize a sheet resistance of  $760 \Omega/\square$  following 12 printing passes.<sup>196</sup> The high concentration graphene ink presented here exhibits both high solids loading (20 mg/mL) and excellent conductivity ( $25600 \pm 900 \text{ S/m}$ ), with the product exceeding the value not only for competing graphene inks but also alternative inkjet-printed, non-metal conductors. Moreover, graphene presents additional desirable attributes, including robust chemical and environmental stability, reliable printability, and a well-defined chemistry without the need for harsh post-processing.

## 5.6. Film Morphology and Mechanical Properties

These excellent electrical properties, coupled with the intrinsic flexibility of graphene, motivate the application of graphene inks in flexible electronic circuitry. It is therefore important to characterize the morphology and mechanical properties of IPL-annealed graphene films. While mechanical testing has been extensively performed for related graphene/EC inks following thermal annealing,<sup>70</sup> the fundamentally different conditions of IPL annealing can lead to distinct properties. Indeed, the morphology of films processed by IPL annealing exhibits unique characteristics compared to thermal annealing, and is dependent on the annealing conditions. Figure 5.10 illustrates the morphology of films processed by different IPL annealing energies, as well as thermal annealing. At high pulse energies, some features appear including bubbles and microscale tears. Notably, though, these features do not preclude the realization of high electrical conductivity. A similar effect has been previously observed for metal nanoparticles sintered by IPL annealing, and is attributed to the extreme temperatures and heat gradients induced by the process.<sup>199</sup> In particular, the rapid polymer decomposition and generation of volatile products during IPL annealing could lead to local stresses, resulting in the observed unique morphological features. In addition, although it is performed in ambient conditions, the rapid nature of IPL annealing can prevent oxidative processes, an effect widely exploited for processing copper-based inks.<sup>33</sup> Because oxygen is typically involved in thermal decomposition of EC, this effect could alter the fundamental nature of the annealing process.

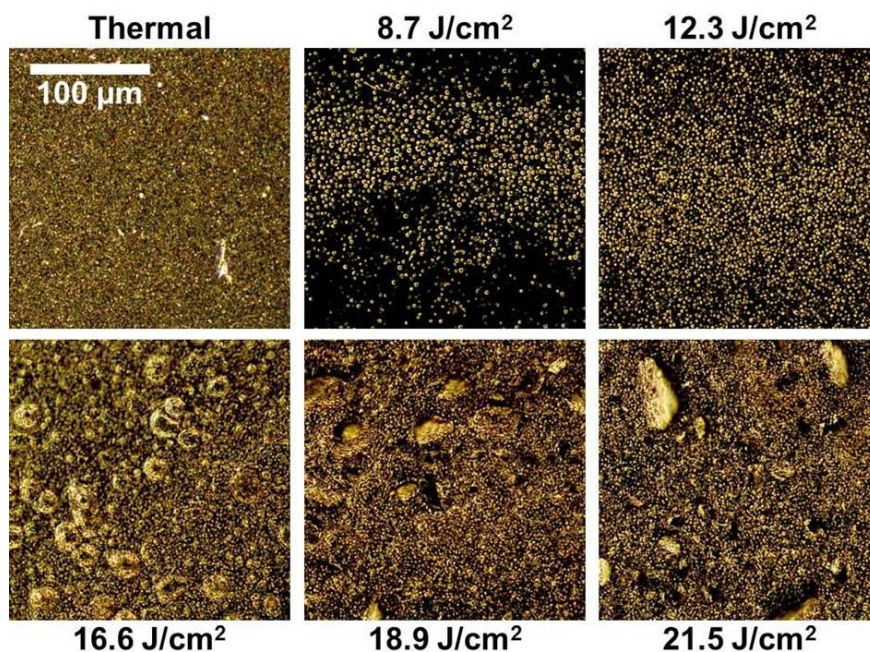


**Figure 5.10.** Film morphology changes as a function of annealing conditions, showing dark field optical microscopy images of films on PI following thermal and IPL annealing. As the pulse energy is increased, bubbles and other defects begin to form.

The evolution of film morphology also depends to some degree on the graphene film thickness. Figure 5.11 shows films on PI annealed with a pulse energy of 18.9 J/cm<sup>2</sup> for 1, 2, 4, and 8 printing passes. It is evident that the characteristic feature size increases with the film thickness. Moreover, these thicker films impose different requirements on the necessary photonic annealing energy for effective curing. Figure 5.12a shows the sheet resistance of 1, 2, 4, and 8 layer films following a single pulse with different applied energies. In addition, multiple pulses are shown to be effective for thicker films, as shown in Figure 5.12b. While there is little observed difference between a single light pulse and five pulses for a single printed layer, the 8-layer samples exhibit considerably better electrical properties following five light pulses.

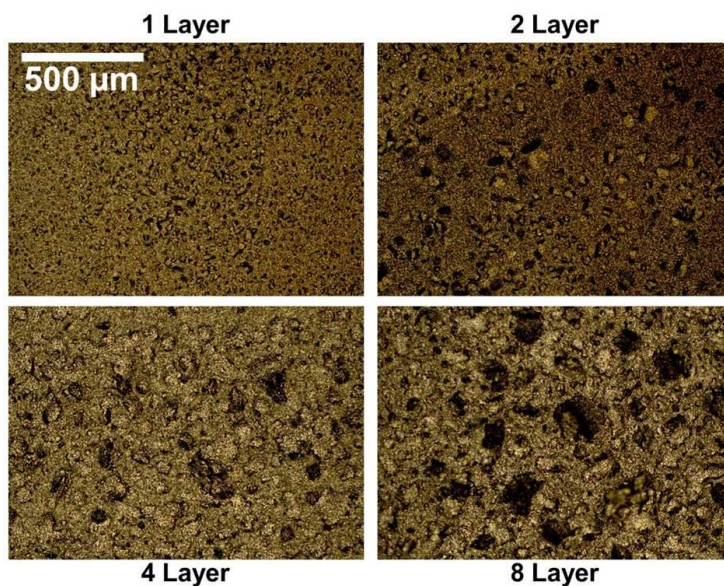


**Figure 5.11.** Film morphology as a function of film thickness for IPL annealing at  $18.9 \text{ J/cm}^2$ . Thicker films exhibit features with a larger length-scale than thin films.

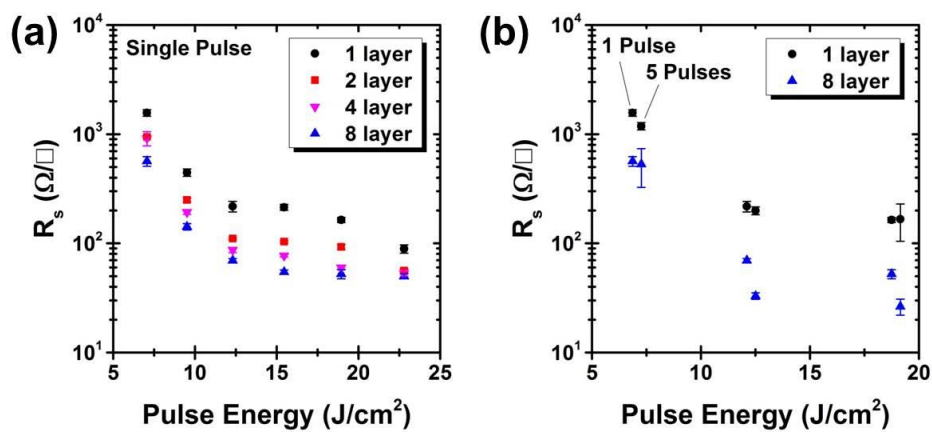


**Figure 5.12.** Effectiveness of IPL annealing for films of different thicknesses. (a) Sheet resistance as a function of IPL annealing energy for films of varying thicknesses using a single light pulse. (b) Effect of multiple light pulses for films with one and eight printed layers, showing sheet resistance for a single 1-ms pulse and five 1-ms pulses spaced by 5 s.

Inkjet printing of graphene offers promise for large-area flexible electronic circuitry (Figure 5.13a), but the rough nature of photonicallly annealed films could limit mechanical tolerance. To investigate the mechanical behavior of IPL-annealed graphene patterns, and thus confirm their suitability for flexible interconnects, several bending tests are performed. Specifically, graphene is inkjet printed onto PEN and processed by IPL annealing at two different pulse energies to produce conductive patterns. The electrical resistance of these stripes is measured over 1000 bending cycles to radii of curvature of 8.1 and 1.3 mm, as shown in Figure 5.13b-c. For the large radius of curvature, there is little discernible evolution of the line resistance. For the small bending radius test, the lower pulse energy produces lines with no deterioration upon bending, while the higher energy light pulse yielded lines with modest deterioration, exhibiting  $\sim 10\%$  increase in resistance after 1000 bending cycles.

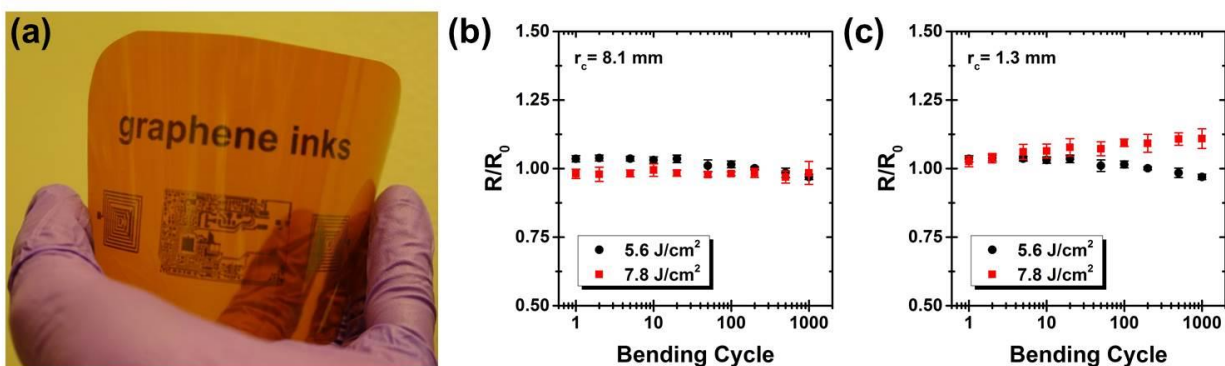


**Figure 5.13.** (a) Large-area inkjet-printed graphene patterns on PI. (b,c) Resistance measured over cyclic bending cycles of graphene lines on PEN following IPL annealing at 5.6 and 7.8 J/cm<sup>2</sup>, with bending radii of curvature of 8.1 and 1.3 mm, respectively (tensile strain of 0.0031 and 0.019, respectively).

### **5.7. Summary for Graphene/EC Photonic Annealing**

In summary, graphene is an attractive material for printed electronics, offering a chemically stable, mechanically flexible, and electrically conductive alternative to conventional metal nanoparticle and conductive polymer inks. The ink formulation, printing method, and rapid IPL annealing approach reported here overcomes several limitations of graphene inks to date, and is well suited for rapid, roll-to-roll fabrication of graphene patterns on a diverse range of substrates. Furthermore, advances in ink formulation are leveraged to produce highly concentrated inkjet-printable graphene inks, with a graphene concentration of 20 mg/mL. Overall, the high solids concentration, combined with the excellent conductivity of  $\sim 25000$  S/m achieved after a single printing pass, establishes this graphene ink as a leading candidate for printed, flexible electronics.

## **CHAPTER SIX**

Graphene Inks with a Nitrocellulose Dispersant



## 6.1. Nitrocellulose as an Alternative Graphene Dispersant

A key feature of the graphene inks that are the focus of this thesis is their use of a polymer dispersant. This stabilizing polymer offers excellent processing characteristics, including solvent compatibility, rheology tunability, and uniform film formation. Following printing, the polymer is partially decomposed by either thermal or photonic annealing, resulting in high conductivity and flexible patterns. Importantly, these graphene films are in fact a composite of graphene flakes and polymer residue, which likely consists of some form of amorphous carbon. This residue is suggested to provide improved electrical properties for the films, but its function as an electrical and mechanical linker between graphene flakes is not well understood.

This chapter will detail research to better understand the role of the polymer residue, and thereby obtain greater control over the graphene film properties. In particular, EC residue does not possess significant extended covalent bonding, resulting in a network of graphene flakes with limited cohesive strength and suboptimal tolerance to demanding environments. As a result, graphene inks that concurrently offer high electrical conductivity, mechanical durability, and environmental stability have not yet been demonstrated.

Here it is shown that the stabilizing polymer nitrocellulose (NC) addresses this deficiency by providing extended amorphous carbon residue following thermal treatment that leads to mechanically and environmentally robust films with superlative electrical performance. In particular, the use of NC is demonstrated to stabilize graphene produced by high-shear mixing, a scalable, liquid-phase exfoliation technique. Using comparable methods to those developed for graphene/EC, the exfoliated graphene dispersion is processed into a powder containing graphene and NC. This provides the foundation for a versatile platform for ink formulation that can span a

broad range of ink viscosities for different methods, including spray coating, inkjet printing, and blade coating. The thermal decomposition of the nitrocellulose binder is subsequently characterized by TGA, in situ Raman spectroscopy, in situ Fourier transform infrared (FTIR) spectroscopy, and X-ray photoelectron spectroscopy (XPS), confirming that amorphous carbon residue remains in the film following thermal annealing at 350 °C. The presence of this residue is then correlated with functional properties, including electrical conductivity as high as  $\sim 40000$  S/m, along with robust mechanical durability and environmental stability as assessed by a Scotch™ tape test, an 85/85 damp heat test,<sup>200</sup> and a water sonication test. This stability is shown to be markedly superior to previously established graphene inks, and marks a significant milestone in graphene ink development for a wide range of applications.

## 6.2. Graphene Exfoliation and Ink Development

A schematic illustration of the graphene/NC ink is shown in Figure 6.1a. Pristine graphene is exfoliated in a scalable manner by shear mixing graphite in a solution of NC and acetone.<sup>66</sup> As-received damped NC powder (Scientific Polymer, Cat. #714, 68% wt. NC damped with isopropanol) is dissolved in acetone at a NC concentration of 10 mg/mL (note that nitrocellulose with high nitrogen content is highly reactive, and thus care should be taken in handling the material to mitigate risks). Graphite flakes at a concentration of 150 mg/mL are added to the NC solution and shear mixed for 4 hours at 10230 rpm, with an ice bath employed to cool the mixture. Unexfoliated graphite flakes are removed by centrifugation in two steps, first at 5000 rpm for 15 minutes, then 6000 rpm for 20 minutes, yielding a stable dispersion of few-layer graphene with a concentration as high as  $\sim 1$  mg/mL (Figure 6.2). The graphene platelets have a typical thickness

of  $\sim 2$  nm and lateral area of  $\sim 200 \times 200$  nm as determined by AFM (Figure 6.1b-c), which are suitable for high-resolution printing methods. Salt water is added to the dispersion ( $\sim 1:3$  weight ratio of  $0.04 \text{ g mL}^{-1} \text{ NaCl}_{(\text{aq})}$  to dispersion) to induce flocculation of the graphene/NC composite, which is subsequently isolated by centrifugation at 7500 rpm for 6 minutes. This solid is washed with deionized water, collected by vacuum filtration ( $0.45 \text{ }\mu\text{m}$  filter paper), and dried to yield a fine black powder of graphene and NC. Producing a powder intermediate simplifies the ink formulation process because the powder can be directly dispersed in a suitable solvent system. This approach in turn allows for precise control of ink properties such as concentration, viscosity, surface tension, and drying kinetics to suit a range of liquid-phase deposition methods. Importantly, the viscosity of graphene/NC inks can be tuned over at least 4 orders of magnitude from a common graphene/NC precursor (Figure 6.1d). Fluid inks and thick pastes are demonstrated for spray coating and blade coating, respectively, which are well-suited for the preparation of large-area, uniform films. Moreover, this wide range of attainable viscosities spans values typically targeted for mature printing methods such as stencil, screen, gravure, flexographic, aerosol-jet, and inkjet printing.<sup>201</sup> For spray coating, graphene/NC powder is dispersed in a solvent system of 80:20 acetone/ethyl lactate at a concentration of 5 mg/mL. Spray coating is carried out with a gravity feed spray gun (TCP Global F3-SET, 1.0 mm nozzle), with a standoff distance of 15 cm and a pressure of  $\sim 200$  kPa. The substrate is fixed on a hotplate at  $100 \text{ }^\circ\text{C}$  during spray coating. For blade coating, the high viscosity paste is prepared with nominally 10% w/v graphene/NC in ethyl lactate. Graphene/NC is dispersed in ethyl lactate with excess acetone ( $\sim 2:1$  acetone/ethyl lactate v/v) to aid dispersion by bath sonication. The excess acetone is then removed upon heating to yield the graphene/NC paste.

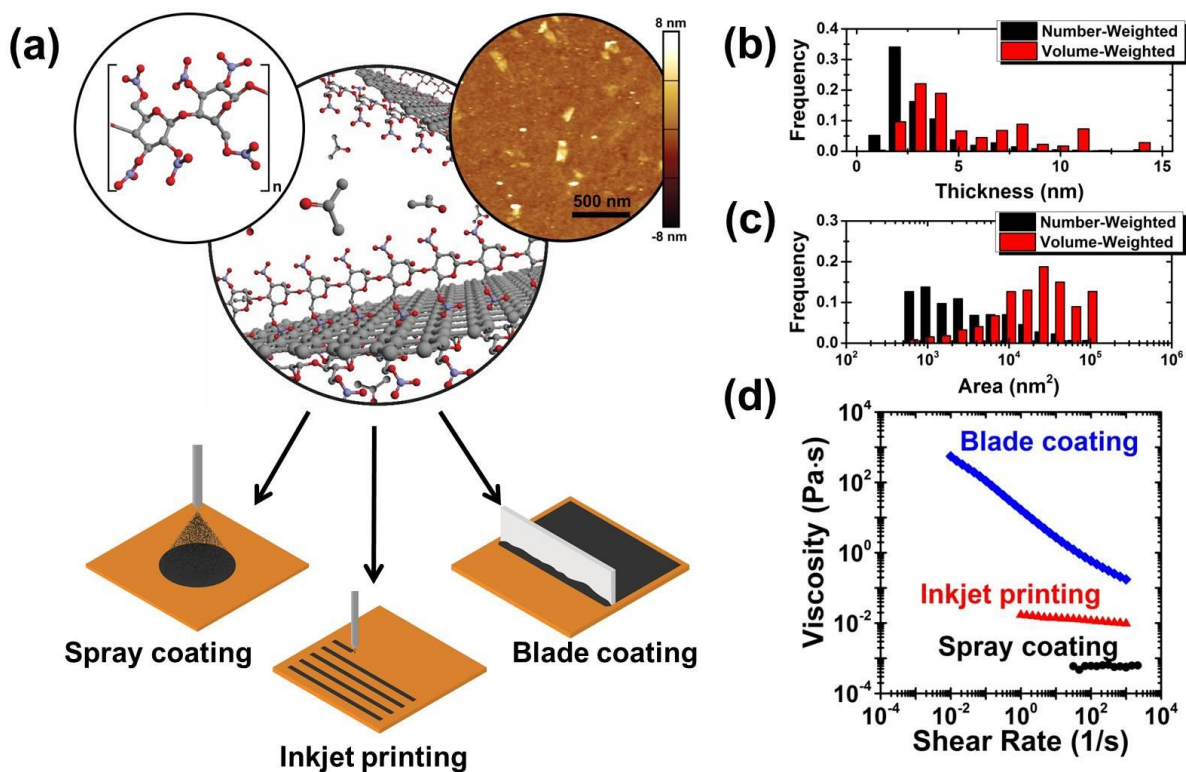


**Figure 6.1.** Process overview and ink characterization. (a) Schematic illustration of the preparation and utilization of nitrocellulose-based graphene inks, including the NC chemical structure (top left) and representative AFM image of graphene flakes (top right). (b,c) Graphene flake thickness and area distributions, respectively, showing both number-weighted and volume-weighted statistics from AFM measurements (number of flakes > 600). (d) Shear viscosity of graphene inks tailored to blade coating, inkjet printing, and spray coating.

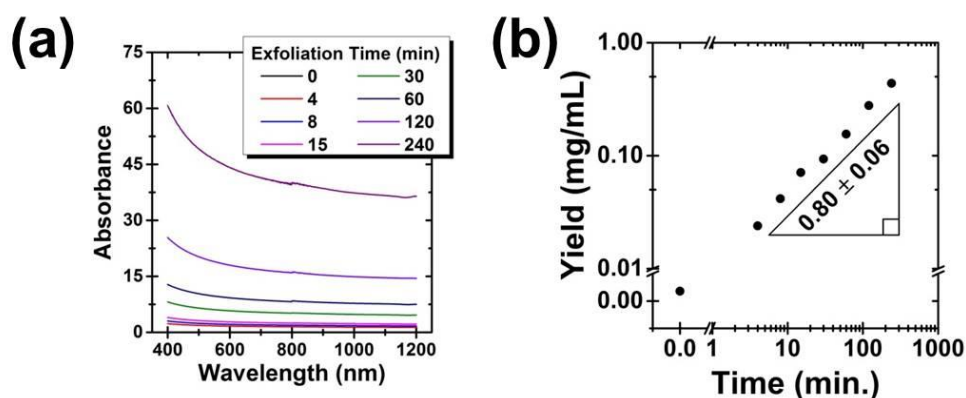


**Figure 6.2.** Liquid-phase exfoliation of graphene/NC by high shear mixing. (a) UV-Vis spectra following different exfoliation times, collected on diluted samples and rescaled. (b) Calculated graphene concentration as a function of exfoliation time, following a power-law relation.

For prototyping and high-resolution additive manufacturing, inkjet printing is a particularly attractive technique since it offers non-contact, digital patterning.<sup>202</sup> However, drop-on-demand inkjet printing requires precisely engineered inks with well-controlled properties including viscosity, surface tension, drying kinetics, and particle size.<sup>17</sup> To prepare an ink suitable for inkjet printing, the graphene/NC powder is directly dispersed in a solvent system of 75:15:10 ethyl lactate/octyl acetate/ethylene glycol diacetate by bath sonication, with a solids loading of 2.3% w/v (~10 mg/mL graphene). This ink is designed to have a shear viscosity of ~10 mPa·s, with low-volatility solvent components included to prevent particle drying at the cartridge nozzle plate and to tune ink wetting and drying properties.<sup>23</sup> During printing, the substrate and cartridge nozzle plate are held at 35 °C and 32 °C, respectively. A piezoelectric actuator drives the formation of spherical droplets (Figure 6.3a), which spread to a diameter of ~70 μm on an untreated glass substrate. The reliability of this printing process is illustrated in Figure 6.3b, with repeatable drop formation and drying achieved over large areas. In addition, the drying properties of the ink are tailored to mitigate coffee ring formation, yielding highly uniform printed features (Figure 6.3c).<sup>21</sup> As shown in Figure 6.3d, droplets coalesce to form stable and consistent lines, demonstrating the suitability of graphene/NC for high-fidelity inkjet printing of electronic components.

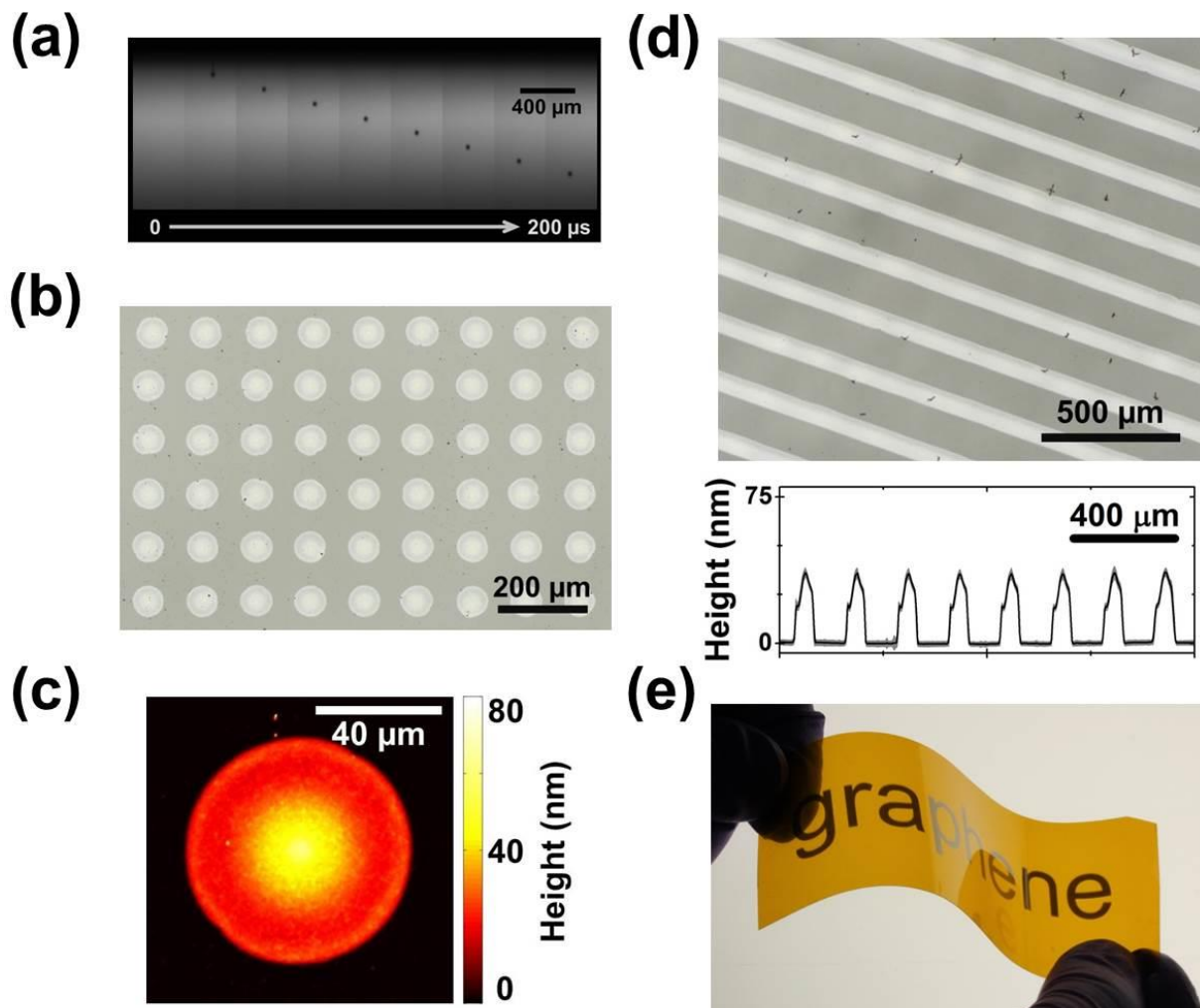


**Figure 6.3.** Inkjet printing of the graphene/NC ink. (a) Drop formation sequence using a piezoelectric inkjet printer. (b) Printed drop array on glass showing high reproducibility and uniformity. (c) Height profile of an individual printed drop, showing suppression of coffee ring formation. (d) Printed line array, showing smooth coalescence of drops to form connected lines, along with inset height profile. (e) Photograph of flexible inkjet-printed graphene/NC patterns over a large area.

### 6.3. Chemical and Structural Analysis

The versatile processing of graphene achieved using NC as a stabilizer is indicative of the ability of NC to uniformly coat graphene flakes. Because this insulating polymer will impede

charge transport between graphene flakes, graphene/NC films must be heat-treated to decompose the binder for electronics applications. This process has important implications for the functional properties of the resulting film since residue from the polymer can mediate the electrical and mechanical connections between flakes. To investigate the chemical changes to the graphene films following annealing, TGA, Raman spectroscopy, FTIR spectroscopy, and XPS are employed. TGA is carried out in an air atmosphere with a 5 °C/min. temperature ramp. In situ Raman spectroscopy during annealing of the graphene/NC films is performed using a Renishaw Raman microscope with a Linkam TS1500 stage in a controlled environment. Spray-coated films on silicon substrates are loaded into the heating stage and spectra collected at ~25 °C intervals using 532 nm excitation. The temperature-dependent frequency of the Si peak is used to calibrate the substrate temperature. In situ IR absorption spectra are collected using an FTIR spectrometer with the sample positioned on a heating stage.

As shown in Figure 6.4a, TGA reveals two primary peaks in the mass derivative curve corresponding to nitrocellulose (~200 °C) and graphene (~640 °C). The low decomposition temperature of NC has been previously exploited for annealing of metallic nanomaterials with limited thermal budget, including silver nanoparticles and copper nanowires.<sup>203,204</sup> Smaller signals associated with NC residue (~240 °C) and a secondary graphene peak (~580 °C) are also observed. From these results, it is estimated that ~25% wt. of the polymer remains following the primary decomposition, and some of this residue persists in the film up to at least ~375 °C. In contrast, for pure NC, shown in the bottom panel of Figure 6.4a, only ~9% wt. of the nitrocellulose remains as residue, which then persists up to ~450 °C. This difference suggests that the interaction of the NC and graphene alters the decomposition characteristics of the polymer. It is likely that graphene

restricts the escape of volatile decomposition products, through physical or chemical interactions, as has been observed for polymer decomposition in the presence of  $sp^2$ -bonded carbon nanomaterials.<sup>205</sup> Moreover, the nitrogen content from the polymer can influence the structure of the resulting residue, providing possible crosslinking observed during carbonization of carbon fibers.<sup>206</sup> Because the presence of polymer residue in the film following annealing to 200-375 °C is expected to have implications on the resulting functional properties, the chemical nature of this polymer residue is further investigated using in situ Raman spectroscopy, FTIR, and XPS.

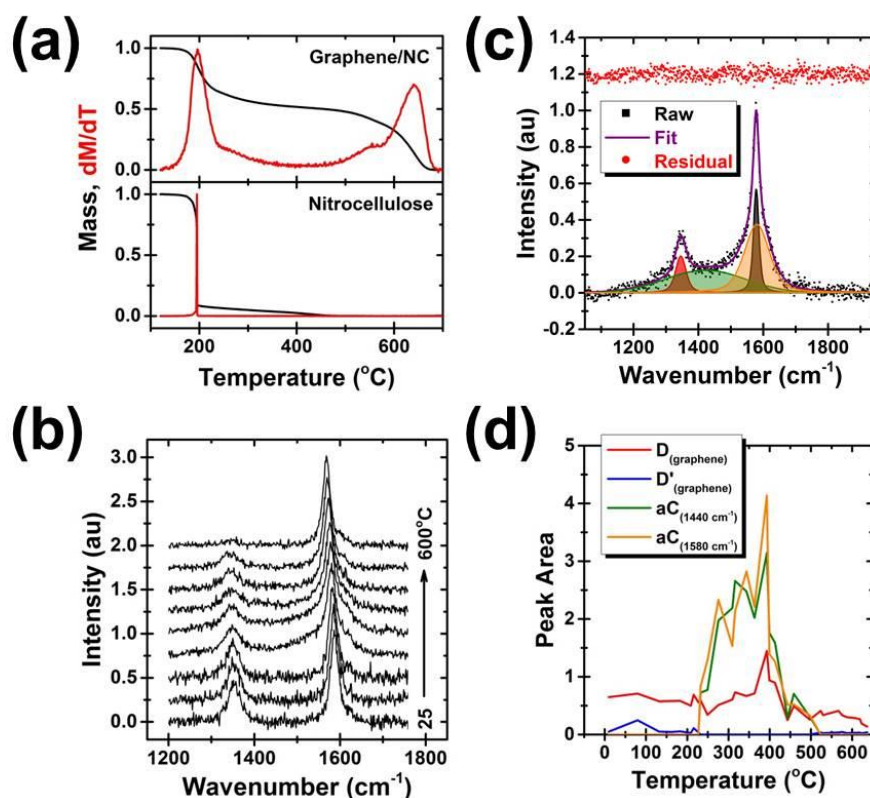


**Figure 6.4.** TGA and in situ Raman characterization of graphene/NC. (a) TGA curves showing mass and mass derivative for graphene/NC (top) and pure nitrocellulose (bottom), indicating primary nitrocellulose decomposition at 200 °C with noticeable residue. (b) Raman spectra of graphene/NC films during in situ heating in an oxidizing environment, taken at ~75 °C increments. (c) Representative Raman spectrum with peak fitting taken at 350 °C, revealing the presence of peaks in addition to the original graphene. (d) Peak area relative to the G band, plotted as a function of temperature during in situ heating.



In situ Raman spectroscopy is a powerful technique for characterizing carbon nanomaterials and has been used recently to monitor structural changes and defect evolution in graphene and carbon nanotubes.<sup>68,207–209</sup> Here in situ Raman spectroscopy is utilized to assess the evolution of graphene/NC films during thermal annealing in an oxidizing environment. As shown in Figure 6.4b, several general characteristics emerge from this analysis. The quality of a graphene sample is typically estimated from the ratio of intensities of the defect-related peak (D peak) to the peak occurring from in-plane vibrations of the carbon atoms (G peak), with a lower D/G ratio signifying fewer defects.<sup>207</sup> The in situ data reveal that annealing is accompanied by a reduction in the D/G intensity ratio, along with a minor reduction in the 2D peak intensity, consistent with a reduction in defect density (Figure 6.4b, Figure 6.5). In addition, distinct Raman peaks emerge following heating above 200 °C, including broad peaks centered near the D and G bands of graphene, as shown in Figure 6.4c, which can be attributed to the formation of amorphous carbon with high sp<sup>2</sup>-bonding character from NC decomposition.<sup>210,211</sup> This Raman feature is notably absent for graphene inks processed with ethyl cellulose (Figure 6.6),<sup>79</sup> indicating the unique nature of the polymer residue for graphene/NC and motivating further investigation of its characteristics. To study how the amorphous carbon signal evolves as a function of annealing, Figure 6.4d shows the peak areas normalized to the graphene G peak. The signature of amorphous carbon residue is present at annealing temperatures between 200 °C and 450 °C, which is broadly consistent with the observation of polymer residue at these temperatures in the TGA curve (Figure 6.4a).

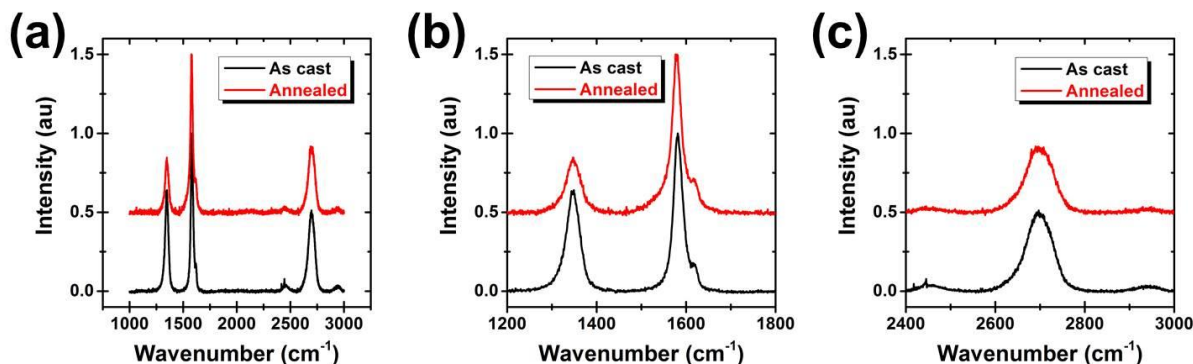


**Figure 6.5.** Raman spectra for graphene/NC films as cast and following annealing, including (a) the full measured range and zoomed in regions showing (b) D and G peaks and (c) the 2D peak. Annealing is accompanied by a reduction in the D/G intensity ratio, a slight decrease in the 2D peak, and the emergence of a distinct peak near the G band, associated with the polymer residue.

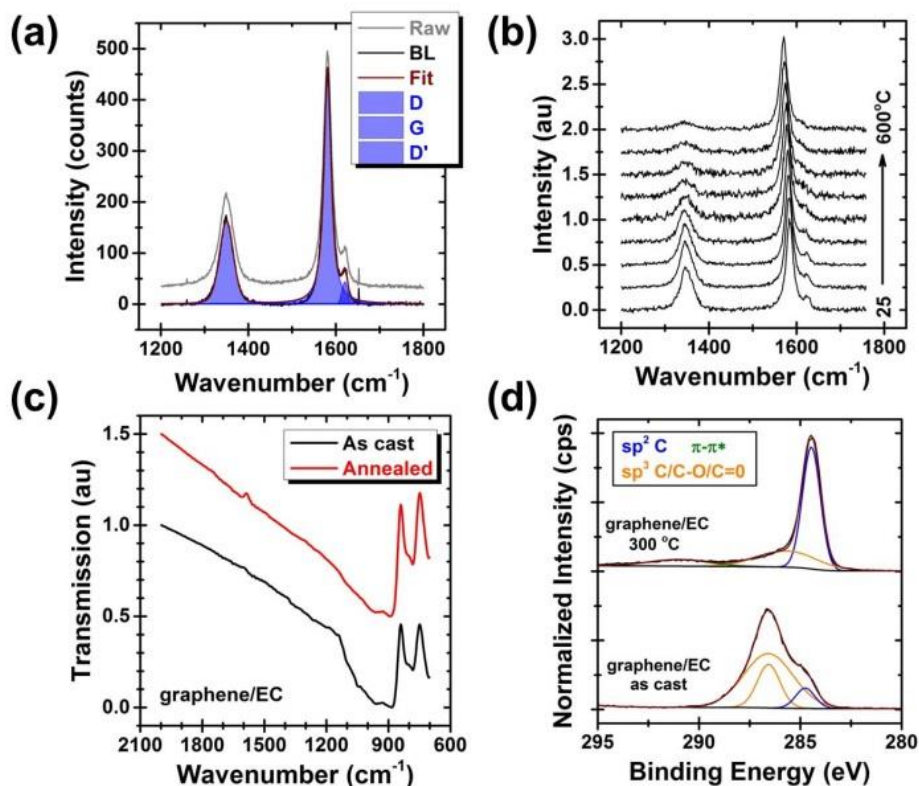


**Figure 6.6.** Chemical characterization of graphene/EC films. (a) Raman spectrum following thermal annealing with peak fitting, showing no evidence of amorphous carbon residue. (b) In situ Raman spectroscopy of graphene/EC films during thermal annealing. (c,d) FTIR spectra and XPS C1s spectra, respectively, for graphene/EC films as cast and following thermal annealing.

While Raman spectroscopy provides strong evidence for the presence of amorphous carbon residue, it does not provide significant insight into the chemical structures produced upon annealing. In situ FTIR spectroscopy is therefore performed to analyze the film chemistry during thermal annealing. As shown in Figure 6.7a, several prominent changes occur in the IR spectra collected from the graphene/NC film during heating to 300 °C. In particular, peaks at 1670  $\text{cm}^{-1}$  and 1290  $\text{cm}^{-1}$  associated with the nitrate functionality lose intensity beginning above 125 °C, and are not measurable above 200 °C (Figure 6.7b). This observation is consistent with previous literature indicating denitration of the nitrocellulose as the first stage of decomposition.<sup>212,213</sup> Furthermore, ex situ FTIR spectroscopy shows several prominent peaks in the range 1300-1600  $\text{cm}^{-1}$ , indicating covalent bonding character (Figure 6.7c). In particular, bands at 1340-1410  $\text{cm}^{-1}$  and 1550-1600  $\text{cm}^{-1}$  are consistent with the skeletal C-C modes of high  $\text{sp}^2$ -content amorphous carbon.<sup>214</sup> This bonding is likely to reinforce the mechanical properties of the film, and is not observed for graphene processed with EC (Figure 6.6c). In this way, the graphene and polymer residue can form an effective brick-and-mortar composite structure.

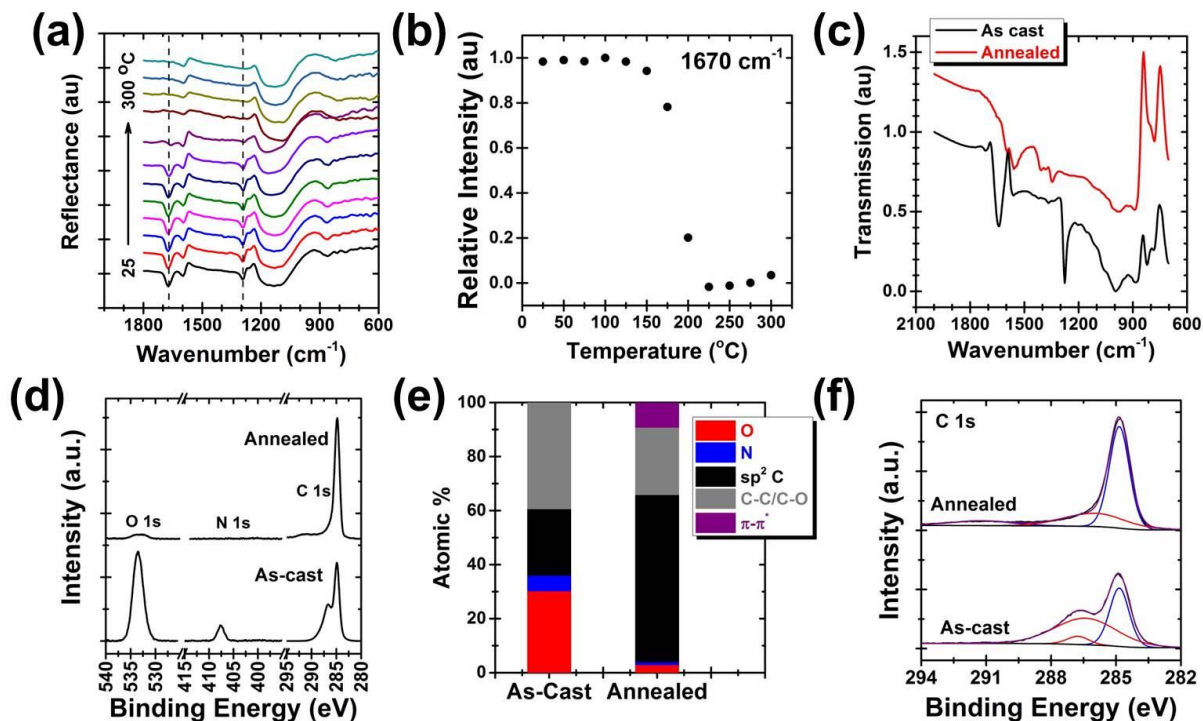


**Figure 6.7.** IR and XPS characterization of graphene/NC. (a) IR reflectance spectra collected from graphene/NC during in situ heating with 25 °C increments, showing characteristic changes resulting from polymer decomposition. (b) Intensity of a characteristic nitrate group peak at 1670 cm<sup>-1</sup> as a function of temperature. (c) Ex situ FTIR spectra before and after annealing at 350 °C. (d) XPS spectra of as-cast and annealed graphene/NC films showing the three constituent elements. (e) Atomic composition of as-cast and annealed graphene/NC films as determined by XPS. (f) High-resolution XPS spectra for as-cast and annealed graphene/NC showing the changes in the C1s peaks.

To further characterize the chemical composition of the graphene/NC film, XPS is performed on as-cast and thermally annealed films. The as-cast graphene/NC film exhibits XPS features consistent with NC, including high O and N content, in which the N1s peak at 408 eV indicates the presence of nitrate groups (Figure 6.7d). Similarly, the C1s portion of the spectrum is consistent with primarily NC, including evidence for significant ether linkages. Following annealing, the elemental composition changes substantially. Specifically, the O1s peak intensity is reduced, reflecting an O atomic composition of 3%, while only a minor N1s peak at 401 eV is

observed, indicative of decomposition of the nitrate groups with a small amount of N residue remaining (Figure 6.7e). This N content could facilitate cross-linking of the residual amorphous carbon for improved mechanical properties.<sup>215</sup> Moreover, the C1s spectrum undergoes a significant shift, with high  $sp^2$  C content and relatively low C-C/C-O character (Figure 6.7f). There remains a clear peak associated with  $sp^3$  C-C/C-O centered at 286.0 eV, even following annealing at 350 °C, indicative of persistent effects from the NC that can affect film properties. This observation is consistent with the TGA, Raman, and FTIR results, which show evidence of NC residue following thermal treatment.

Overall, TGA, Raman, FTIR, and XPS analysis of the graphene/NC films as a function of thermal annealing indicates the presence of NC residue consisting of amorphous carbon with noticeable C-O bonding character, marking a distinct difference from films processed with EC as the polymer stabilizer (Figure 6.8). Following this thorough characterization of the chemistry and morphology of graphene films derived from these graphene/NC inks, the impact of these fundamental characteristics on functional properties is examined, particularly the effect on electrical conductivity, mechanical flexibility and durability, and environmental stability.

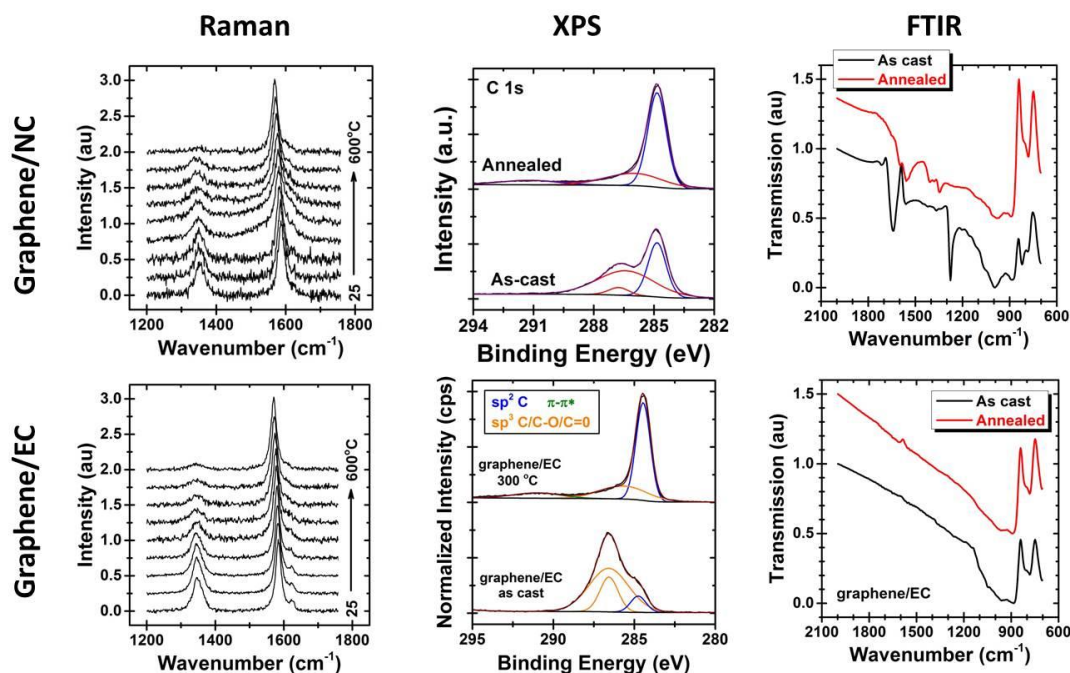


**Figure 6.8.** Direct comparison of chemical characterization for graphene/NC and graphene/EC films, including in situ Raman spectroscopy, XPS, and FTIR spectroscopy.

#### 6.4. Characterization of Functional Properties

Many applications of printed and flexible electronics require conductive elements with high electrical performance and robust stability to both environmental and mechanical stresses. Here, graphene processed with NC is shown to offer excellent properties in this regard. The film microstructure is expected to impact these properties. A dense, well-connected network of graphene flakes is known to offer superior mechanical and electrical properties.<sup>216,217</sup> SEM reveals a compact microstructure for the graphene/NC films following annealing, indicating a dense film with a high degree of flake alignment in the plane of the film (Figure 6.9a). This alignment favors improved flake-flake overlap and thus efficient charge transport. As discussed above, thermal annealing alters the composition of the graphene film, consistent with NC decomposition with

residual amorphous carbon. As a result, the electrical conductivity depends strongly on the thermal annealing conditions (Figure 6.9b). The NC is largely decomposed following annealing at 200 °C, leading to graphene films with an electrical conductivity of  $\sim 10000$  S/m. As the annealing temperature is increased, the graphene films exhibit a steadily increasing conductivity up to a peak value of  $40500 \pm 4400$  S/m following 350 °C annealing, among the highest electrical conductivity achieved for pristine graphene inks.<sup>69,73,79</sup>

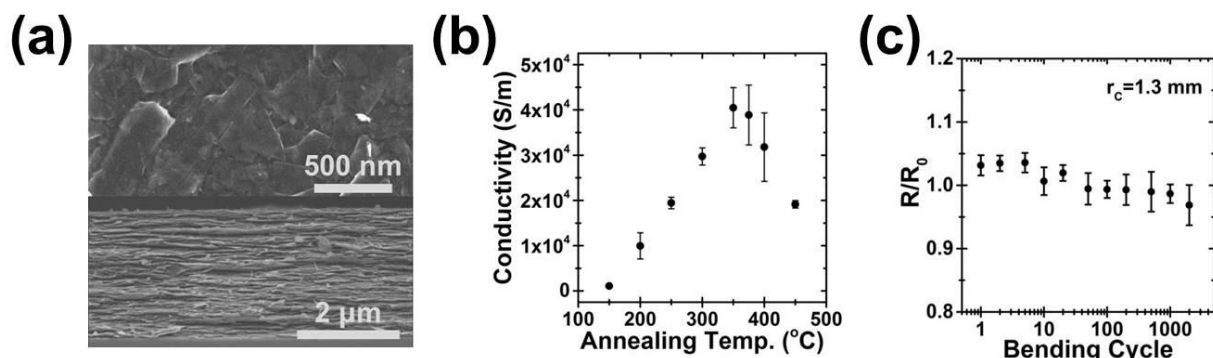


**Figure 6.9.** Morphology and electrical characterization of graphene films. (a) Plan-view (top) and cross-section (bottom) SEM images of a graphene film, showing a dense, compact microstructure with significant flake alignment. (b) Conductivity of graphene/NC films following annealing in air over the range 150-450 °C. (c) Relative resistance of graphene/NC lines following cyclic bending tests at a radius of curvature of 1.3 mm (bending strain  $\sim 4.8\%$ ).

In addition to excellent electrical performance, printed graphene patterns require mechanical durability to withstand the rigors of flexible, portable consumer electronics. To test the mechanical flexibility of graphene processed with NC, patterns were fabricated on PI substrates. The electrical resistance of the resulting graphene lines exhibits negligible change (Figure 6.9c) over 2000 bending cycles to a radius of curvature of 1.3 mm (tensile strain of  $\sim 4.8\%$ ), with a minor decrease in resistance consistent with previous reports,<sup>79</sup> verifying the utility of this material for devices in which a high tolerance to flexing is necessary.

While bending stability confirms that the material can deform without failure, it does not necessarily imply strong adhesion to the substrate or cohesive strength. A Scotch™ tape test is therefore performed to assess the substrate adhesion and film cohesion performance of the graphene patterns. Figure 6.10 shows a schematic illustration of this test in which a piece of tape is applied to the graphene pattern and removed in a controlled manner, after which the tape and sample are inspected for evidence of film damage. This test is performed on annealed graphene/NC and graphene/EC films for comparison.<sup>38,79</sup> The optical results of the test are shown in Figure 6.11a. While the graphene/EC patterns leave visible residue on the tape, this is not the case for graphene/NC. Electrical measurements corroborate this result, as shown in Figure 6.11b. Specifically, the graphene/EC patterns exhibit an increased resistance by ~10-20% following the tape test, while graphene/NC patterns exhibit negligible change. These results suggest that the differences in the polymer residue in each case play a critical role in determining the film mechanical properties, especially since this residue mediates coupling between the constituent graphene flakes. This interesting result merits a more direct and in-depth analysis of the mechanical properties including adhesive strength as a focus of future work.

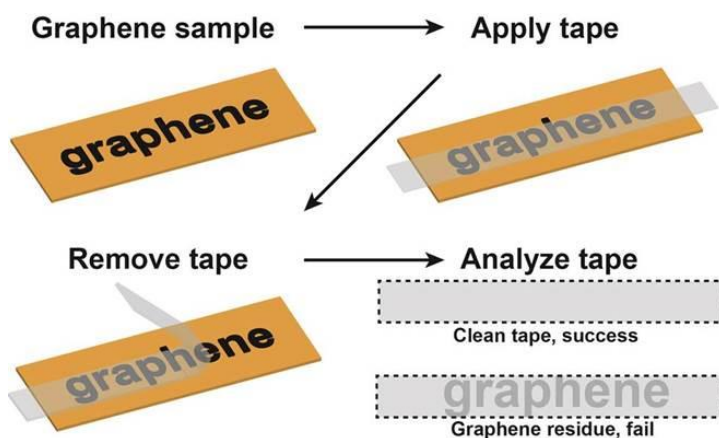


**Figure 6.10.** Schematic of the Scotch™ tape test applied to graphene films with EC and NC.



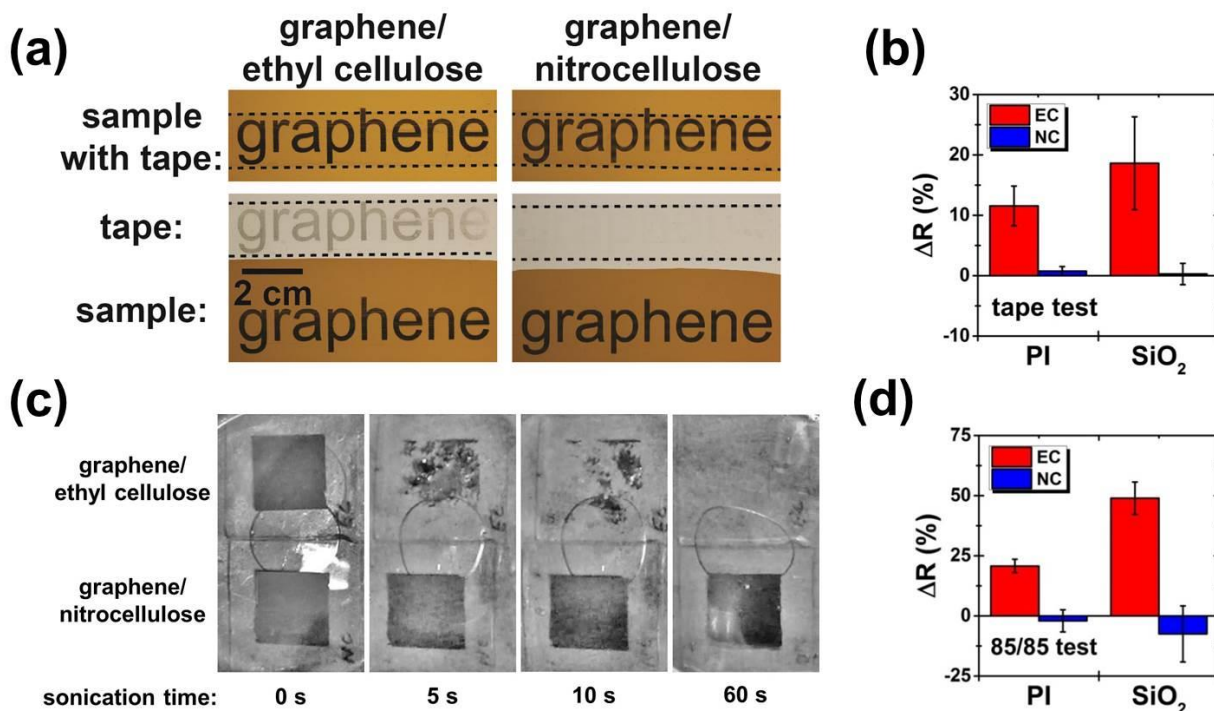


**Figure 6.11.** Mechanical and environmental stability of graphene processed with NC. (a) Images during (top) and after (bottom) the Scotch™ tape test for graphene patterns printed on polyimide. The dashed black lines indicate the outline of the tape, while the text ‘graphene’ is printed with graphene/EC (left) and graphene/NC (right). (b) Change in electrical resistance for graphene/EC and graphene/NC films following the Scotch™ tape test, with PI and glass substrates. (c) Series of images showing the water sonication test results for graphene/EC and graphene/NC. (d) Change in electrical resistance following the damp heat test, 312 h at 85 °C and 85% relative humidity, for graphene/EC and graphene/NC films on PI and glass.

A complementary test of the adhesion and mechanical properties of the graphene films is performed using ultrasonication in water. In this experiment, annealed graphene/EC and graphene/NC films on glass are immersed in water in an ultrasonic bath. As shown in Figure 6.11c, the graphene/EC film delaminates and disintegrates within ~10 seconds under the harsh conditions of the ultrasonic bath. The graphene/NC film, on the other hand, shows excellent resilience for over 1 minute, with negligible film delamination or breakage (Figure 6.12). Similar graphene/NC films on polyimide exhibit no failure for up to 10 minutes in the ultrasonic bath, suggesting that

this difference is based on adhesion at the film-substrate interface, and the driving capillary forces for water to penetrate between the film and substrate.

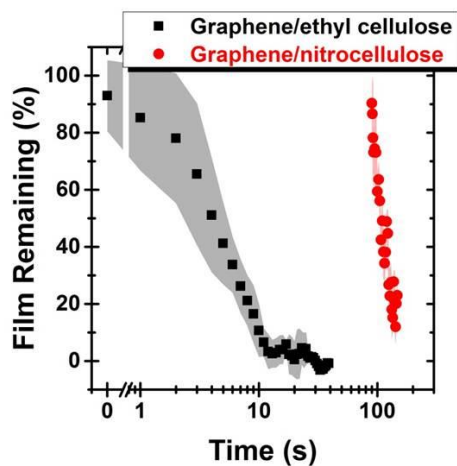


**Figure 6.12.** Water sonication test results for graphene/EC and graphene/NC, showing percentage of film remaining as a function of time during ultrasonication in deionized water. The graphene films are coated onto a glass slide and annealed prior to the test.

The stark difference in properties upon ultrasonication in water suggests that the nitrocellulose-based graphene patterns may also exhibit resistance to water exposure under less extreme conditions, such as high humidity. Resistance to humidity degradation carries significant implications for a diverse range of practical applications for which printed electronics components and devices must operate reliably in demanding environmental conditions. A damp heat test was conducted to assess the performance of graphene patterns exposed to 85 °C and 85% relative humidity for 312 hours. As shown in Figure 6.11d, graphene processed with NC and annealed shows no systematic change in electrical performance following this high temperature and high humidity exposure. In contrast, the resistance of graphene/EC patterns increases by 21% and 49% on polyimide and glass substrates, respectively. This result is important for applications in harsh environments, a key application area for graphene inks because it presents an advantage over more

reactive or unstable conductors, such as thermally sensitive conducting polymers and corrosion-susceptible metals.

### **6.5. Summary for Graphene/NC Ink Development**

In conclusion, a promising nitrocellulose-based platform is demonstrated for solution-processed graphene with excellent versatility and functional properties. This strategy combines scalable, low-cost production of graphene with tunable ink formulation for a range of liquid-phase coating and patterning techniques, enhancing the opportunities for broad integration in practical applications. Moreover, the resulting graphene patterns exhibit a suite of desirable properties such as electrical conductivity of  $\sim 40000$  S/m that is among the highest for solution-processed carbon nanomaterials. In addition, thermal decomposition of NC results in robust amorphous carbons with high  $sp^2$ -bonding character, yielding graphene patterns resilient to a range of mechanical and environmental stresses including cyclic bending, Scotch™ tape testing, and damp heat aging. The concurrent realization of these properties in a scalable and adaptable process represents a significant advance for the incorporation of graphene inks in flexible printed electronics.

## **CHAPTER SEVEN**

Combustion-Assisted Photonic Annealing of Graphene Inks

## 7.1. Introduction to Combustion-Assisted Photonic Annealing

The development of graphene/nitrocellulose (NC) inks detailed in the previous chapter offers a promising opportunity for process integration. NC offers unique thermochemical properties, including a highly exothermic and rapid decomposition, which establishes this material as a mild explosive. These characteristics are particularly well-suited for the process conditions of photonic annealing, as discussed in Chapter 5. Moreover, this strategy to integrate a reactive binder with photonic annealing offers an opportunity for more general application in printed electronics.

A key obstacle to the widespread adoption of printed electronics is the development of functional liquid inks with compatible printing and process integration. For many functional inks, traditional thermal processing limits process speed and compatibility with temperature-sensitive materials. As a result, pulsed photonic annealing has been demonstrated for rapid processing on thermally sensitive substrates, with straightforward integration in roll-to-roll processing.<sup>33-35,79,84,187,189</sup> While the initial results on photonic annealing of printable graphene inks, detailed in Chapter 5, have been promising, optimal utilization of this technique requires complementary ink properties tailored to the annealing method. Toward that end, in this chapter a graphene ink is designed for pulsed light annealing based on the polymer binder NC, which exhibits rapid and exothermic decomposition. This approach enables highly conductive and porous graphene patterns with broad process compatibility and excellent performance metrics, while also establishing a compelling ink design strategy for broader application in photonic annealing.

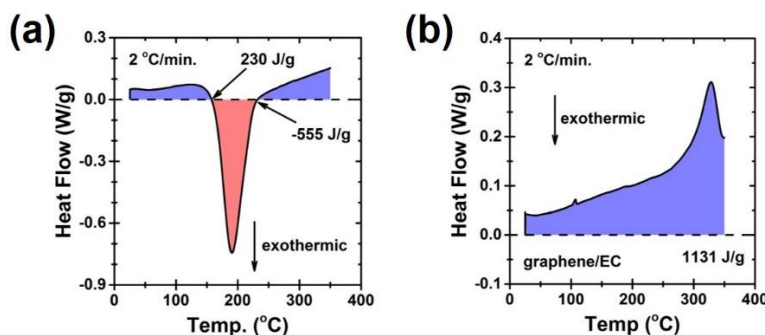
The design of graphene inks for photonic annealing draws inspiration from literature precedent in the fields of thin film metal oxide electronics and ceramic synthesis. In this context, combustion processing of metal oxide TFTs has been demonstrated by careful selection of

exothermic precursors that lower the energy barrier for annealing and densification, ultimately yielding excellent performance with reduced processing temperature.<sup>218</sup> In ceramic synthesis, the technique of self-propagating high-temperature synthesis similarly uses a locally-initiated combustion wave to process material in a rapid and efficient manner.<sup>219,220</sup> Since the decomposition of reactive precursors leads to gas evolution, this approach is particularly effective for producing porous, high surface-area morphologies.<sup>221</sup> To use photonic annealing to initiate combustion reactions in graphene inks, a reactive binder is required that undergoes rapid, exothermic decomposition. NC is a promising candidate, as it has been shown in the previous chapter to effectively disperse graphene, providing stable inks with graphene concentrations up to 10% w/v.<sup>74</sup> In addition, the oxidizing nitrate groups of NC afford high chemical reactivity that favors exothermic decomposition with rapid kinetics that are consistent with photonic annealing.<sup>203,204,212,213</sup> Due to these characteristics, NC acts as a built-in energy source to fuel a propagating reaction, with positive implications for process generality. Moreover, the evolution of volatile gaseous species upon NC decomposition leads to a highly porous microstructure, offering advantages for applications such as energy storage, catalysis, and sensing.<sup>222</sup>

## **7.2. Proof-of-Concept Combustion-Assisted Photonic Annealing**

The composite graphene/NC powder is produced by high shear mixing, centrifugation, and flocculation steps as reported in the previous chapter.<sup>74</sup> This procedure yields a powder containing ~35 wt. % graphene flakes with a typical thickness of ~2 nm and lateral size of ~300 nm. For the suggested propagating reaction to occur, the energy released upon NC decomposition must be sufficiently greater than the energy required to initiate the decomposition reaction. Differential

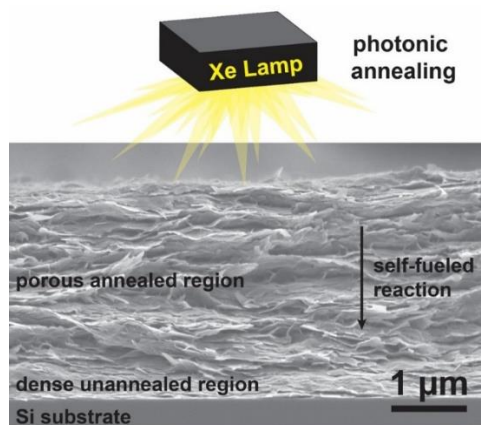
scanning calorimetry (DSC) results shown in Figure 7.1a indicate that NC decomposes exothermically at  $\sim 200$  °C, releasing  $\sim 3\times$  more energy than the amount required to heat the material to the decomposition temperature, which suggests that the NC combustion will likely propagate once locally initiated. In contrast, a control sample of graphene/ EC, a common dispersant for graphene inks,<sup>38</sup> exhibits endothermic decomposition characteristics (Figure 7.1b).



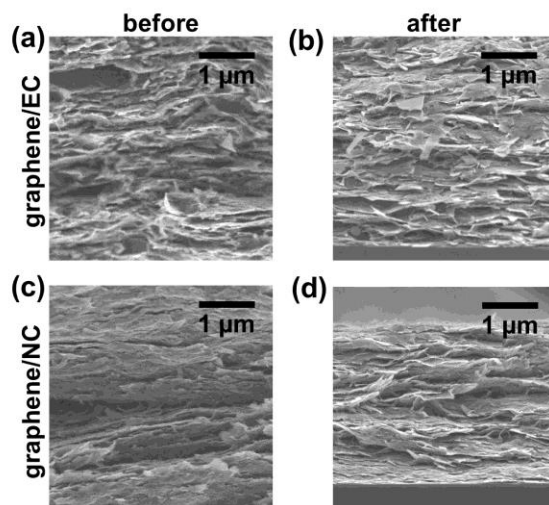
**Figure 7.1.** (a) Differential scanning calorimetry of graphene/NC showing large exothermic reaction of nitrocellulose at  $\sim 200$  °C. (b) Corresponding data for graphene/EC showing endothermic decomposition for ethyl cellulose. Measurement is taken under nitrogen to more closely mimic rapid photonic annealing.

The differences in reaction kinetics and thermodynamics between NC and EC are further demonstrated by a photonic annealing test on a silicon substrate. Importantly, photonic annealing is traditionally limited to substrates that act as poor heat sinks, such as paper and plastic. Substrates with higher thermal mass and thermal conductivity, such as silicon, extract heat out of the active film rapidly to quench the process, limiting its applicability.<sup>34,189</sup> However, the high exothermicity of NC combustion enables photonic annealing on silicon, while the rapid release of volatile decomposition products leads to a porous microstructure, as shown in the cross-section SEM image in Figure 7.2. Although the bottom portion of the film ( $<1$   $\mu\text{m}$ ) appears to remain unannealed, with a dense, polymer-rich structure, the remainder of the film (top  $\sim 3$   $\mu\text{m}$ ) shows

evidence of photonic annealing. This morphology is notably not observed for comparable films of graphene/EC (Figure 7.3).



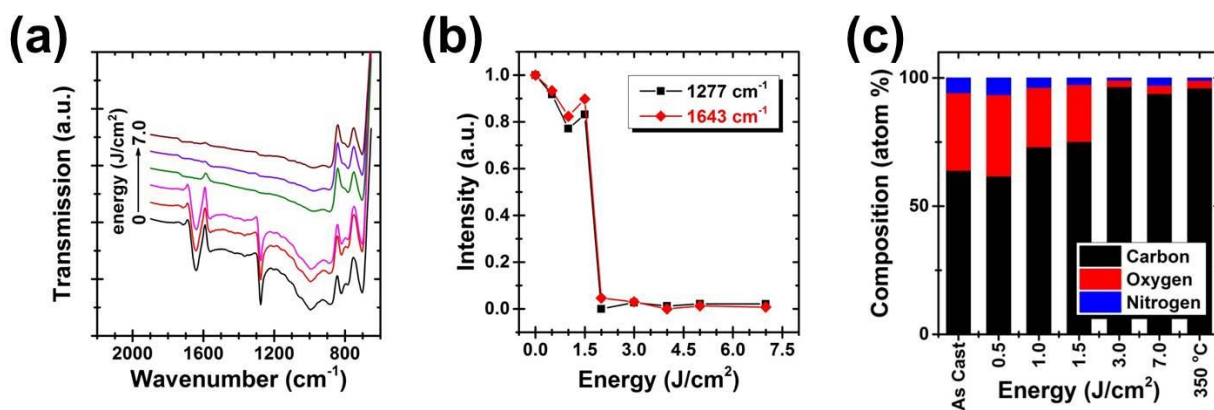
**Figure 7.2.** Schematic illustration and cross sectional SEM image showing assisted photonic annealing, with a self-fueled reaction yielding a porous graphene microstructure. Photonic annealing on a Si substrate is not typically possible due to the substrate's effective heat sink properties, but the reactive binder enables annealing through nearly the entire film, resulting in a porous microstructure.



**Figure 7.3.** Microstructural characterization of graphene films. (a,b) Cross sectional SEM images of graphene/EC films before and after exposure to pulsed light annealing, respectively, showing little change in microstructure suggesting ineffective annealing. (c,d) Corresponding images for graphene/NC films, showing evolution from a dense, polymer-rich microstructure to a porous, annealed film.

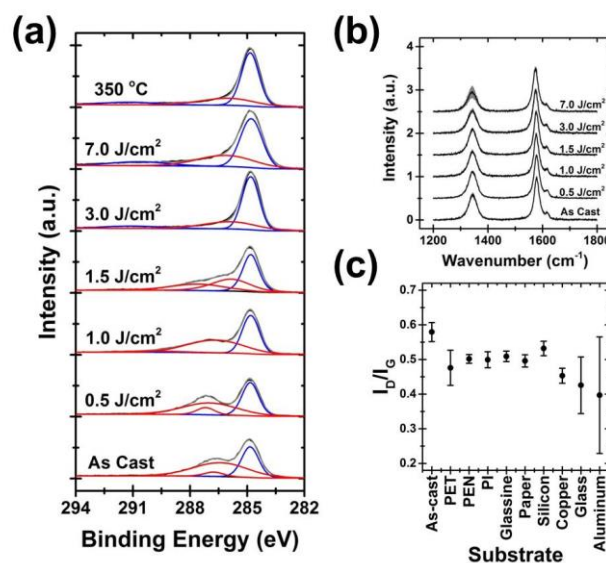


To better understand and characterize the nature of the annealing process and resulting properties, comprehensive chemical and electrical characterization was performed. For example, FTIR spectroscopy, shown in Figure 7.4a, indicates the presence of nitrate peaks from the NC at  $1277\text{ cm}^{-1}$  and  $1643\text{ cm}^{-1}$  preceding photonic annealing. At low photonic annealing energies, these peaks show little change. However, above a threshold pulse energy, the NC peaks are no longer observable, suggesting an abrupt transition between the as-cast and annealed states (Figure 7.4b). These results are consistent with a self-fueled reaction, which leads to complete annealing of the graphene/NC film following initiation. For all photonic annealing experiments, annealing was performed using a Xenon Sinteron 2010 with a spiral lamp geometry. Pulse energies of  $0\text{--}7\text{ J/cm}^2$  were estimated based on calibration data from the manufacturer. The sample was placed  $25\text{ mm}$  from the lamp, and annealing was performed with a single light pulse. For thermal annealing reference samples, the optimized annealing conditions ( $350\text{ }^{\circ}\text{C}$  for 30 minutes) were used as determined in the previous chapter.<sup>74</sup>



**Figure 7.4.** Chemical characterization of photonic annealed graphene/NC films. (a) FTIR spectra for graphene/NC films following different annealing conditions. (b) Evolution of FTIR peak intensity with pulse energy showing a sharp threshold for annealing. (c) Elemental composition determined by XPS for the films.

Similar characteristics are also observed with XPS (Figure 7.4c), which is used to track elemental composition. At low pulse energies, the films show similar composition to the as-cast film, with an abrupt transition to fully annealed films after a threshold pulse energy is exceeded. Figure 7.5a shows XPS C1s data for graphene/NC films as cast, thermally annealed to 350 °C, and photonic annealed with varying pulse energies. The as-cast film shows the presence of C-O functionality associated with the ether linkages of cellulose derivatives at peaks above 386 eV, along with  $sp^2$  C-C associated with the graphene flakes ( $\sim 285$  eV). Following photonic annealing, the spectra show minimal evolution for pulse energies below 1.5 J/cm<sup>2</sup>. A discrete change in the spectra is observed at higher energy annealing, resulting in a C1s spectrum largely consistent with thermal annealing at 350 °C. This discrete transition in the film composition supports the notion of a propagating reaction. In particular, once enough energy is added to initiate the exothermic decomposition of NC, the reaction propagates through the film to result in complete annealing.



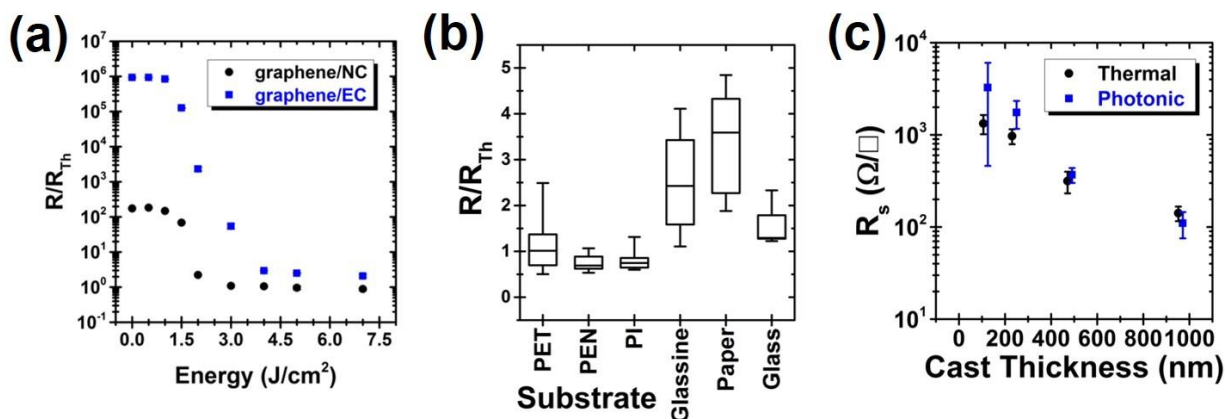
**Figure 7.5.** Chemical characterization of graphene/NC annealing. (a) XPS C1s spectra for graphene/NC films following different post-treatment conditions. (b) Representative Raman spectra for different annealing conditions. (c)  $I_D/I_G$  ratio following annealing on various substrates, showing a consistent reduction following photonic annealing for different substrates.

Figure 7.5b shows representative Raman spectra for graphene/NC films before and after photonic annealing. These spectra show the characteristic D, G, and D' peaks for graphene, with a slight reduction in the  $I_D/I_G$  ratio from 0.58 to 0.50 upon annealing, which is consistent with a decrease in  $sp^3$  bonding character in the film.<sup>79</sup> This reduction is observed for films on a wide range of substrates, including PET, PEN, PI and glassine paper (Figure 7.5c). Moreover, due to the built-in energy of NC, this change is even observed on substrates that act as effective heat sinks, such as silicon, copper, and aluminum. Altogether, this chemical characterization suggests a sharp threshold for annealing after which the propagating, self-sustaining nature of the reaction leads to nearly complete decomposition with minimal evidence of residual NC.

### 7.3. Functional Characterization of Photonic Annealed Graphene/NC

Electrical characterization of the graphene films is provided in Figure 7.6. As the annealing energy is increased, a sharp drop in sheet resistance is observed (Figure 7.6a) in a manner consistent with the preceding chemical characterization. In contrast, polymer binders with endothermic decomposition can be partially annealed by low energy pulses, which manifests itself as a gradual decrease in sheet resistance as a function of annealing energy. Despite its increased porosity, the graphene/NC films maintain a low sheet resistance similar to thermally annealed films, thus presenting a desirable combination of high surface area and efficient charge transport. Furthermore, photonic annealing with NC allows the formation of conductive graphene films on a variety of substrates as shown in Figure 7.6b. These results show that photonic annealing is effective for graphene/NC films on PET and PEN, substrates incompatible with temperatures  $>200$  °C,<sup>189</sup> along with low-cost, paper-based substrates such as glassine and standard office paper.<sup>87</sup>

The somewhat higher ( $\sim 2\text{-}4\times$ ) sheet resistance measured on these paper-based substrates is likely a result of the increased surface roughness relative to the thermally annealed control on low-roughness glass. Nevertheless, the realization of conductive graphene films on paper-based substrates offers compelling prospects for printed electronics since the low-cost, sustainable production, and recyclability of paper make it an attractive substrate for large-volume, disposable devices.<sup>223</sup>



**Figure 7.6.** Electrical characterization of photonic annealed graphene/NC films. (a) Sheet resistance relative to thermally annealed samples for graphene/NC and graphene/EC, showing an abrupt threshold for nitrocellulose decomposition and minimum resistance on par with thermal annealing. (b) Normalized sheet resistance relative to thermal annealing for graphene/NC films on various substrates. (c) Sheet resistance for graphene/NC films as a function of thickness following thermal and photonic annealing. Note that the thickness corresponds to thickness prior to annealing (photonic annealing leads to thicker films with the same amount of material due to porosity).

Photonic annealing of graphene/NC generalizes effectively across a range of film thicknesses. Figure 7.6c shows that the sheet resistances of thermally and photonic annealed films agree well as a function of thickness up to micron-thick films. Photonic annealing micron-thick graphene films without the combustion chemistry approach is often less effective than thermal annealing, because energy applied by photonic annealing is absorbed primarily near the

surface and dissipates through the film.<sup>34,79,84,189</sup> The resulting thermal gradients lead to uneven annealing of the sample, requiring multiple annealing cycles and introducing potentially damaging mechanical stresses. The high energy content and even distribution of NC, however, enables complete annealing with a single light pulse.

Photonic annealing has attracted considerable interest for additive manufacturing beyond the scope of printed electronics.<sup>135</sup> However, the effectiveness of this technique has historically been strongly dependent on the thermal properties of the substrate.<sup>34,189</sup> While the field of printed electronics is largely concerned with applications on thin, thermally-insulating substrates (e.g., plastic and paper), many other additive manufacturing applications involve substrates that act as effective heat sinks, including materials with high thermal conductivity and thermal mass. In this scenario, the rapid dissipation of heat from the functional film can severely limit the efficacy of photonic annealing, with the required power scaling with the square root of the substrate thermal conductivity. For example, photonic annealing on silicon is expected to require ~25 times more power than annealing on PET, which exceeds the limits of many photonic annealing systems.<sup>34</sup> On the other hand, the exothermicity of NC overcomes this limitation, as demonstrated by successful photonic annealing on a silicon wafer (Figure 7.2). To further support this feature of graphene/NC, photonic annealing was performed on substrates ranging from paper to copper foil. In all cases, Raman spectroscopy indicated a reduction in the  $I_D/I_G$  ratio following photonic annealing (Figure 7.5c), indicative of effective photonic annealing even on substrates with high thermal conductivity, such as aluminum foil.

#### 7.4. Application of Porous Graphene Thin Films for Printed Microsupercapacitors

The combination of high surface area and efficient charge transport for photonically annealed graphene/NC films is desirable for many applications including energy storage, catalysis, and sensing.<sup>222,224</sup> In particular, microsupercapacitors (MSCs) are an emerging energy storage platform for printed electronics. These devices store charge at the interface of electrodes and a liquid or gel electrolyte, offering high power density, excellent cycling lifetime, and straightforward fabrication.<sup>225</sup> The planar architecture of MSCs also facilitates integration of energy storage and other circuit components on a single substrate, providing benefits for portable, wearable electronics with on-chip power management. To illustrate the utility of graphene/NC for MSCs, a graphene/NC ink was developed for direct ink writing (DIW), which is a digital, liquid-phase printing method that allows for low-cost, additive fabrication of complex patterns.<sup>226</sup> The excellent dispersion stability, solvent compatibility, and tunable rheology of graphene/NC allows for the straightforward preparation of a DIW printable graphene/NC ink. Graphene/NC powder is directly dispersed in ethyl lactate at a concentration of 8% w/v using bath sonication. This ink is used to fabricate graphene/NC interdigitated patterns by DIW (Figure 7.7a) for application as MSC electrodes, using a HyRel System 30M 3D printer with a 200  $\mu\text{m}$  diameter extrusion tip.

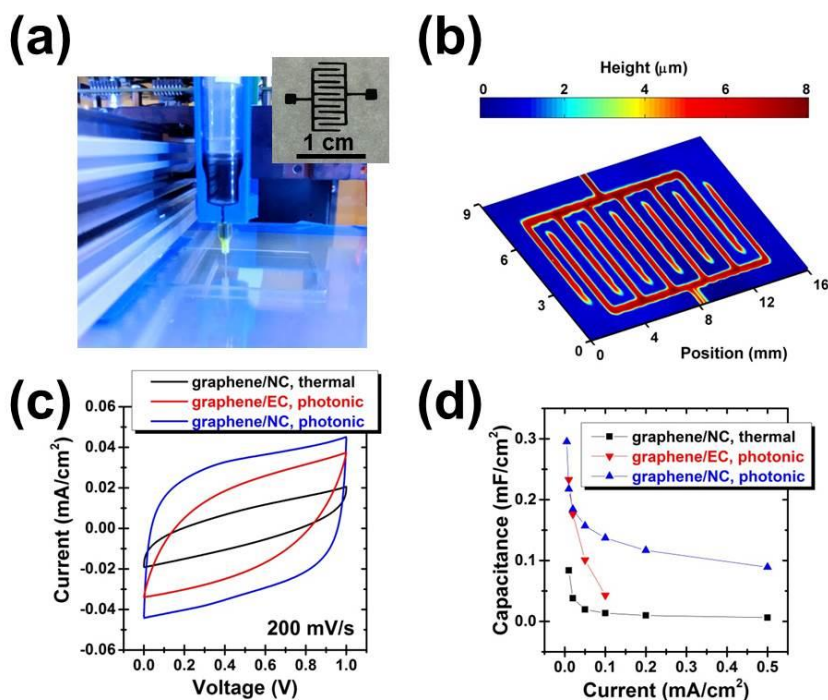


**Figure 7.7.** Printed graphene/NC microsupercapacitors. (a) Photograph of the extrusion printing head during device fabrication, with inset photograph of printed interdigitated electrodes. (b) Optical profilometry data showing the height map of the device active area. (c) Cyclic voltammetry for devices following thermal and photonic annealing. (d) Device capacitance as a function of current for MSCs from galvanostatic charge/discharge cycling.

Graphene/NC MSCs were DIW printed and processed by thermal or photonic annealing, along with control devices of graphene/EC for comparison. An optical profilometry height map of a representative printed graphene/NC pattern is shown in Figure 7.7b. The consistent height and trace width confirms the reliability of the DIW printing process, while the thickness of the pattern can be readily controlled by varying the number of printed layers (Figure 7.8a). Electrochemical measurements were performed following application of a gel electrolyte containing 1.0 g phosphoric acid, 1.0 g PVA ( $M_w = 50000$ , Aldrich), 3.0 g IPA, and 6.0 g water, similar to that reported previously.<sup>82</sup> The samples were then dried overnight and tested by cyclic voltammetry

(CV) and galvanostatic charge/discharge measurements using a CHI 760D potentiostat. CV curves are shown in Figure 7.7c, exhibiting a rectangular shape and an increased current for photonic annealed graphene/NC devices. These MSCs show higher current than thermally annealed devices, resulting from the porous morphology and increased active surface area realized by photonic annealing. The graphene/EC devices, however, exhibit a less rectangular CV profile, due to higher series resistance resulting from the limited efficacy of photonic annealing for thick graphene/EC films.

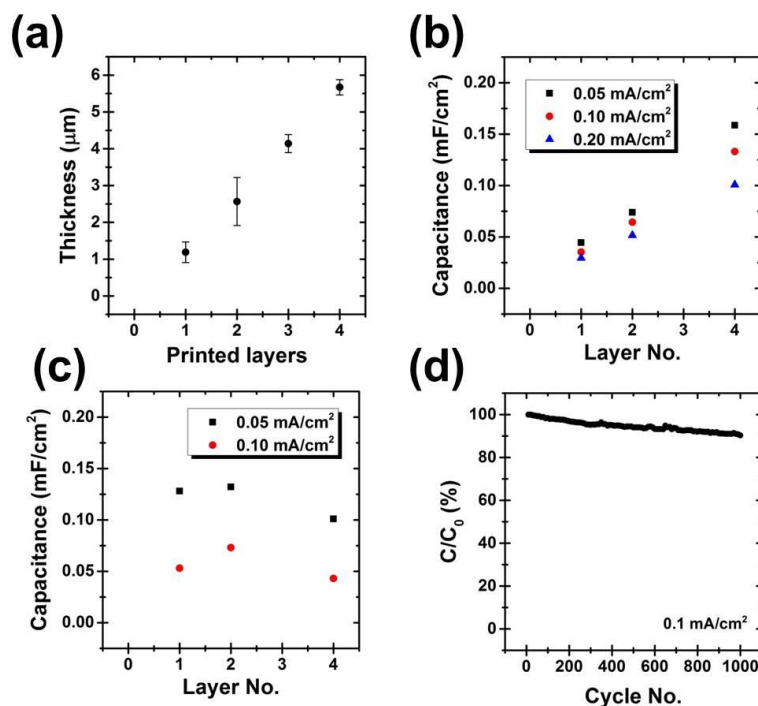


**Figure 7.8.** Characterization of graphene MSCs. (a) Thickness and (b) capacitance of printed graphene/NC MSCs as a function of printed layer number, showing a consistent linear increase in both values. (c) Capacitance for graphene/EC MSCs with different thicknesses, showing saturation of the performance. (d) Capacitance retention of graphene/NC MSC over 1000 cycles.

Galvanostatic charge/discharge cycling was performed to measure the capacitance and rate capability of the photonic annealed graphene/NC MSCs (Figure 7.7d). Notably, at a moderate



current density of  $0.1 \text{ mA/cm}^2$ , the photonic annealed graphene/NC MSC on glassine exhibits a capacitance of  $0.14 \text{ mF/cm}^2$ , which is 10x greater than the capacitance of the thermally annealed device and an improvement of 3x relative to the graphene/EC case and similar printed, graphene-based MSCs in the literature.<sup>71,81,82</sup> Moreover, the performance is found to scale linearly with device thickness, which is a characteristic not observed for graphene/EC due to the reduced efficacy of photonic annealing for thick films containing the EC binder (Figure 7.8b-c). In addition, the glassine-based photonic annealed graphene/NC MSC possesses high cycling stability, with >90% capacitance retention following 1000 cycles (Figure 7.8d).

### **7.5. Summary for Graphene/NC Photonic Annealing**

In summary, rapid photonic annealing of graphene/NC films results in a unique combination of processing attributes and functional properties. In particular, the exothermic NC binder acts as a built-in energy source to assist the annealing reaction, resulting in improved process integration and generality. The rapid volatilization of the NC binder further leads to a porous microstructure with efficient charge transport and high surface area, providing desirable advantages for applications such as energy storage, sensing, and catalysis. Combining these features with the versatile liquid-phase processing platform for graphene inks, direct ink writing of printed solid-state graphene microsupercapacitors was demonstrated with excellent performance on flexible substrates such as glassine paper. While particularly useful for graphene inks, the attributes of NC as a synergistic binder for photonic annealing can likely be applied more generally to other material systems of interest to additive manufacturing.

## **CHAPTER EIGHT**

Chemically Stable Electrodes for Printed InGaZnO  
Transistors

## 8.1. Introduction to Printed InGaZnO Transistors

While Chapters 2-7 detailed processing advances for graphene inks, this chapter transitions to selected applications for this class of inks. In particular, the stability of graphene is critical for many applications that also require good electrical conductivity. One such application is for transistor electrodes with chemically or electrochemically sensitive materials. This chapter discusses the favorable integration of graphene as a stable source/drain electrode materials for inkjet-printed InGaZnO (indium-gallium-zinc-oxide, or IGZO) thin film transistors (TFTs), leveraging the robust chemical and thermal stability of graphene to achieve excellent long-term and environmental stability.

Amorphous oxide semiconductors have been a focal point of recent advances in inorganic materials for large-area electronics.<sup>26,227,228</sup> These materials offer a route for low-cost, low-temperature processing with large-area uniformity and exceptionally smooth interfaces without the drawback of grain boundaries and carrier concentration control that can be present in polycrystalline materials.<sup>228</sup> Amorphous IGZO is particularly prominent in display applications due to its impressive electronic properties, environmental and bias-stress stability, and processability.<sup>229</sup> In addition, the introduction of sol-gel techniques to fabricate IGZO from liquid inks offers the opportunity to incorporate this material in low-cost printed electronics applications.<sup>230-233</sup> Considerable progress has been realized in low-temperature, solution-based processing of IGZO,<sup>146,218,234-237</sup> combustion processing,<sup>218</sup> for example, has afforded high quality oxide materials with enhanced materials compatibility and relevance to display applications.<sup>238,239</sup> This strategy has shown versatile application with oxide dielectrics and contacts, as well as hybrid materials for flexible applications.<sup>240,241</sup> However, the extension of this knowledge to printed

devices has been hindered by challenges of interface engineering and materials compatibility for more complex architectures. Standard source/drain electrode materials for IGZO, such as aluminum, molybdenum, and titanium/gold, are incompatible with high-resolution, liquid-phase printing methods. Conducting metal oxides, such as antimony tin oxide and indium tin oxide (ITO), are challenging to process at low temperatures from solution by conventional sol-gel techniques with adequate electrical conductivity.<sup>146,242–244</sup>

In contrast, silver is the most prevalent inkjet-printed conductor, with silver nanoparticle or molecular precursor inks widely used due to their resistance to oxidation, low temperature sintering compatibility, and high electrical conductivity.<sup>24</sup> Consequently, to develop printed source/drain electrodes for IGZO TFTs, the suitability of a commercial silver nanoparticle ink is first assessed. It is found that inkjet-printable conductive silver-based inks form poor electrical contact to IGZO due to deleterious interfacial chemical interactions. These limitations motivate the investigation of an alternative electrode material to enable fully printed IGZO TFTs. Towards this end, composite and hybrid electrodes containing carbon nanomaterials have been recently employed for TFTs based on semiconducting oxides, resulting in desirable electronic and chemical properties.<sup>245–248</sup> In particular, the robust chemical and environmental stability of graphene has been exploited to mitigate undesirable chemical and electrochemical interactions at the electrode-channel interface.<sup>245</sup> Moreover, graphene/EC inks suitable for a range of printing methods have been demonstrated in the prior chapters, with electrical conductivities as high as  $\sim 2.5 \times 10^4$  S/m and excellent mechanical flexibility.<sup>38,70,76,77,79</sup> Following a comprehensive exploration of device geometries, graphene contacts embedded between consecutive IGZO printing passes yield favorable transistor operational characteristics. Finally, these graphene-contacted IGZO TFTs

possess robust stability in long-term aging and high-temperature exposure, validating the potential of this approach for a range of printed electronics applications that are currently inaccessible to conventional organic electronics.

## **8.2. Demonstration of Stable Graphene Electrodes for InGaZnO**

To investigate printed source/drain contacts for IGZO TFTs, devices are first fabricated using a commercial silver nanoparticle ink due to its widespread use as a printed conductor. Figure 8.1a illustrates the process flow for the fabrication of IGZO TFTs with silver electrodes. IGZO films are printed on Si/SiO<sub>2</sub> wafers following the established procedure,<sup>237</sup> with a maximum processing temperature of 300 °C. Silver source/drain electrodes are then printed and annealed at 150-250 °C to complete the device. Electrical measurements, shown in Figure 8.1b, reveal that these TFTs have poor, unstable electrical operation, as evidenced by the low and irregular source-drain current.

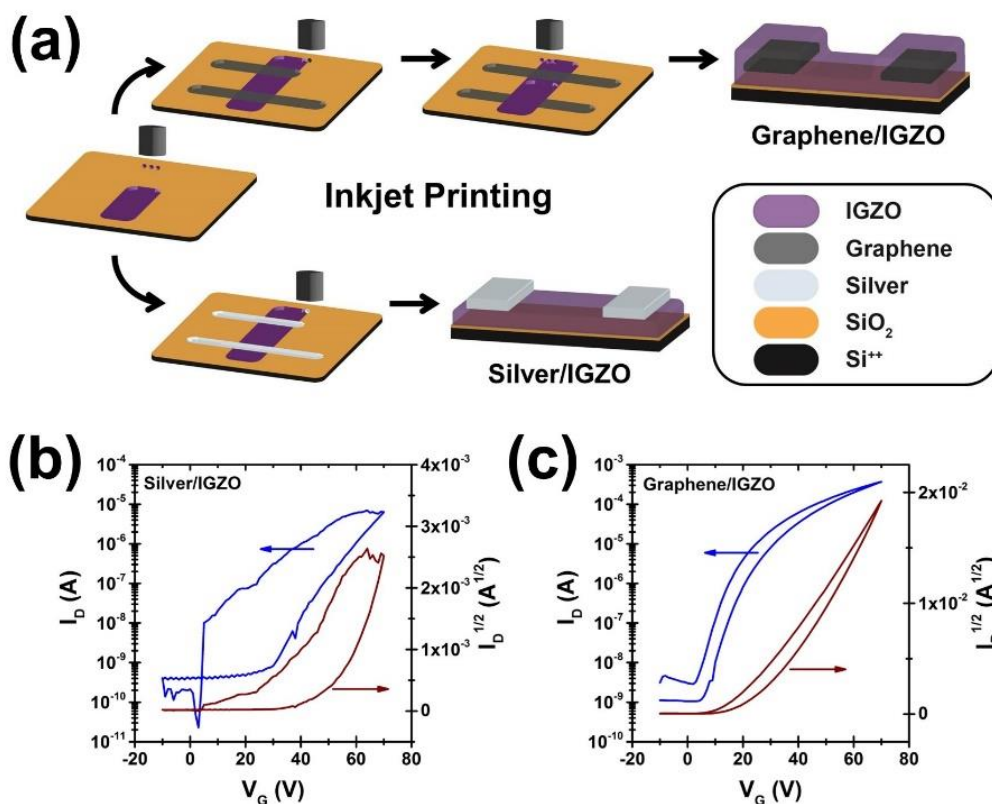


**Figure 8.1.** Process flow and comparison of IGZO TFTs with silver and graphene contacts. (a) Schematic illustration of the fabrication of inkjet-printed IGZO TFTs with silver and graphene source/drain electrodes. (b,c) Representative saturation transfer characteristics for IGZO TFTs with silver and graphene contacts, respectively (channel length  $\sim 200 \mu\text{m}$ ).

To provide insight into the underlying chemistry and physics, and to verify that more optimal processing conditions will not mitigate these issues, silver/IGZO TFTs were fabricated with varying annealing temperatures for the silver electrodes. The silver nanoparticle ink requires annealing at 150 °C for highly conductive films, so this was selected as the minimum temperature condition. As shown in Figure 8.2, devices annealed at 150 °C exhibit poor electron mobility of  $< 0.1 \text{ cm}^2/\text{V}\cdot\text{s}$ . As the annealing temperature is increased, the performance improves slightly to a peak mobility of  $\sim 0.3 \text{ cm}^2/\text{V}\cdot\text{s}$  for 200 °C processing, although the device-to-device variation

remains high. At higher temperatures, the performance again decreases, likely due to silver migration and oxide formation at the contact interface. Although silver could conceivably migrate into the oxide gate dielectric as well, with a relatively thick (300 nm) dielectric, increased gate leakage is not observed (Figure 8.2c). These results are consistent with previous work describing sputtered and evaporated silver contacts for IGZO TFTs.<sup>249,250</sup>

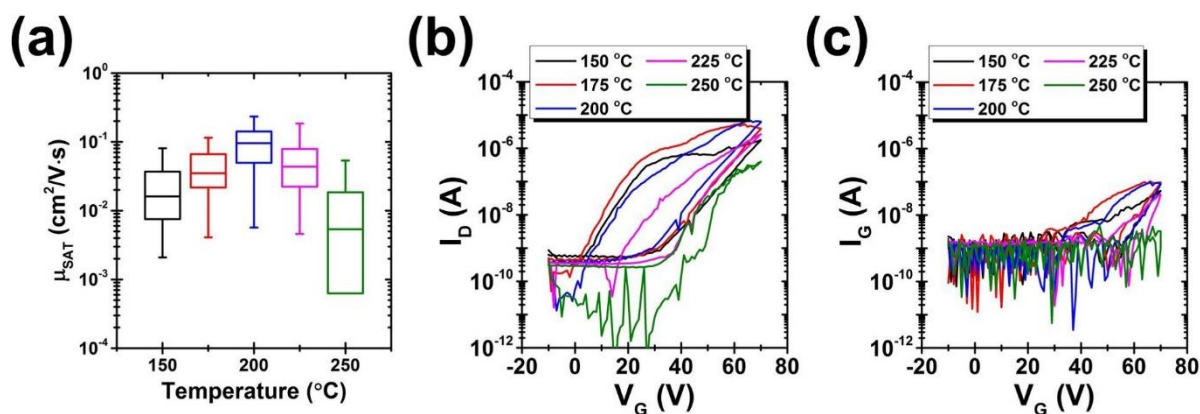


**Figure 8.2.** Annealing optimization for IGZO TFTs with silver contacts. (a) Box plots of mobility for IGZO with silver contacts fabricated with processing temperatures from 150-250  $^{\circ}\text{C}$  ( $n = 31$ , 5 min annealing in ambient at the specified temperature in each case). (b,c) Representative transfer curves and corresponding gate leakage, respectively, for IGZO TFTs with silver contacts.

To provide a more chemically-inert contact for the oxide semiconductor, IGZO TFTs were inkjet-printed with graphene electrodes, as illustrated schematically in Figure 8.1a. Graphene offers excellent thermal and chemical stability, and is not expected to chemically interact with the IGZO channel upon annealing or application of electrical bias. Unlike the corresponding TFTs with printed silver contacts, IGZO TFTs with graphene contacts exhibit stable and high-performance electrical operation, as shown in Figure 8.1c. This initial result demonstrates the viability of graphene as a printed source/drain electrode material for IGZO TFTs, and motivates further investigation of device structures and resulting properties.

### 8.3. Study and Optimization of Device Geometry

With this promising proof-of-concept of graphene as a suitable electrode material for IGZO TFTs, it is important to next assess the role of device architecture in achieving effective charge injection and low contact resistance. Since the contact geometry can have a significant effect on TFT performance through various mechanisms such as morphological, compositional, and electrostatic effects,<sup>146,242,251–253</sup> top-contact (TC) and bottom-contact (BC) devices were fabricated and tested. Representative output curves for TC and BC TFTs are shown in Figures 8.3a-b, respectively. While the TC device supports much higher current at saturation, it also exhibits a more pronounced nonlinearity in the output curve at low drain bias (Figure 8.4), which suggests the presence of an injection barrier. This presents an impediment to proper operation, particularly for applications in which operation in the linear regime is desired. The BC device shows superior linearity in the output curves at low drain bias (Figure 8.4), but with significantly reduced currents at saturation, which is indicative of higher contact resistance or lower charge carrier mobility.

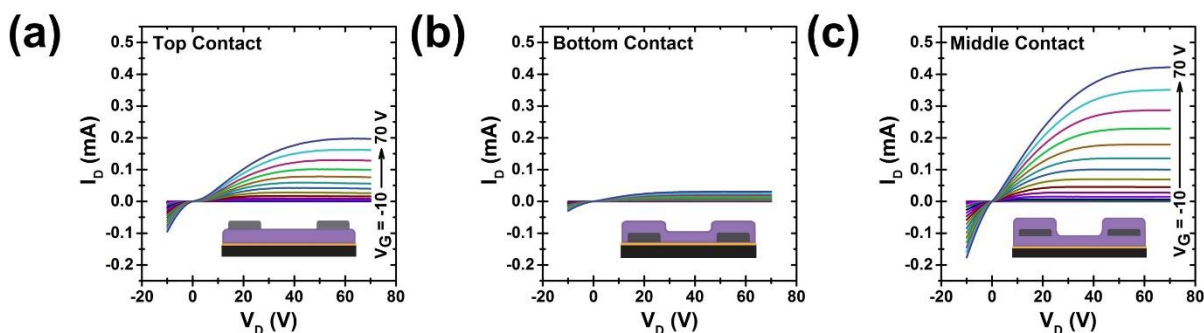


**Figure 8.3.** Effect of device architecture on IGZO TFTs with graphene contacts. (a-c) Representative output characteristics of IGZO TFTs with graphene source/drain electrodes in a top contact, bottom contact, and middle contact configuration, respectively (channel length  $\sim 200$   $\mu\text{m}$ ). Inset diagrams illustrate cross-sections of the device structure in each case.



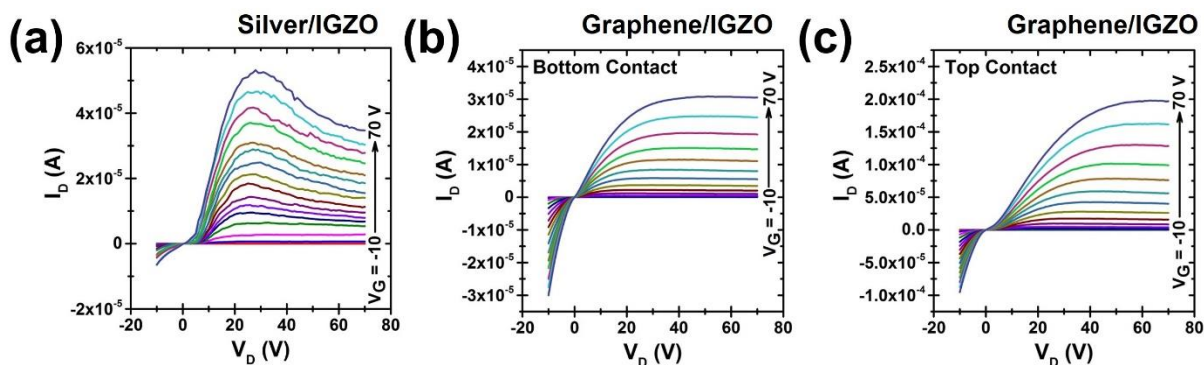


**Figure 8.4.** Representative output curves for non-optimal IGZO devices. (a) Output characteristics for an IGZO TFT with silver source/drain contacts, following optimal annealing at 200 °C. (b,c) Output characteristics for IGZO TFTs with graphene bottom and top contacts, respectively. Note the low drain current for the case of (b), and the nonlinearity at low bias for (c).

The increased current of the TC TFT is likely due to superior IGZO film quality, since IGZO can form dense, uniform films when printed on smooth, pristine SiO<sub>2</sub> substrates. In contrast, the BC device is printed on a substrate patterned with rough electrodes (~28 nm roughness, Figure 8.5), which is likely to disrupt the IGZO film growth near the contacts. This roughness is particularly problematic considering the total thickness of the IGZO film is ~15 nm (Figure 8.6). The difference in output curve linearity at low bias may be due to a number of factors related to the chemical/physical interface between the contacts and the channel, as well as electronic effects.<sup>251–253</sup> In light of these differences, TFTs were also printed with the graphene source/drain electrodes in the center of the IGZO film, as illustrated schematically in Figure 8.1a. This geometry provides high-quality IGZO films printed prior to the contacts, while maintaining the favorable characteristics of the graphene/IGZO interface offered by the BC geometry. A representative output curve for this geometry, referred to as a middle-contact (MC) device, is shown in Figure 8.3c. This device exhibits a high current at saturation, with nearly linear I-V characteristics at low

drain bias. In this manner, the MC device geometry successfully integrates the desirable characteristics of both TC and BC device structures.

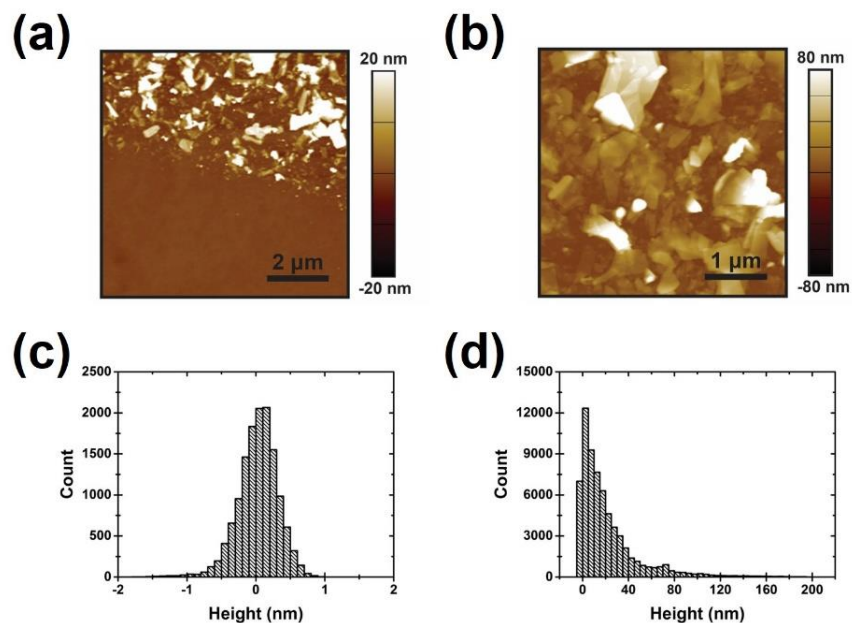


**Figure 8.5.** Atomic force microscopy characterization of an IGZO TFT with graphene contacts. (a,b) AFM topography images at the channel-electrode interface and at the center of the electrode, respectively. (c,d) Height histograms for regions on the IGZO film and on the graphene electrode, respectively.

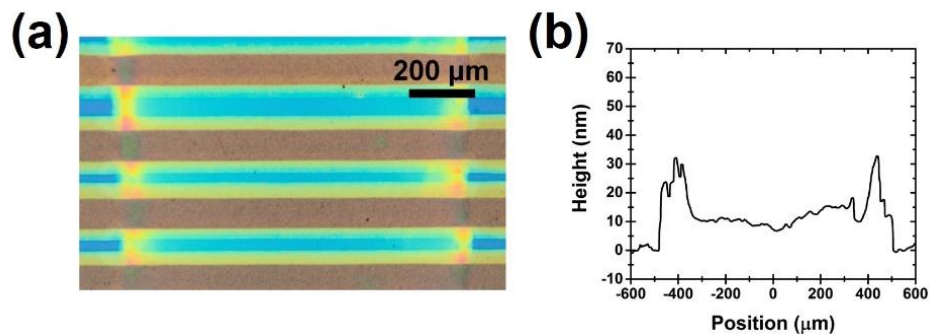


**Figure 8.6.** (a) Optical microscopy image of IGZO TFTs with graphene contacts inkjet-printed on Si/SiO<sub>2</sub>. (b) Thickness profile across an inkjet-printed IGZO film following five printing passes, showing an average thickness of 15 nm.

#### 8.4. Detailed Transistor and Contact Characterization

While the discussion thus far has been limited to single representative devices, quantitative electrical characterization of a large sampling of devices provides more compelling statistical support for the suitability of graphene electrodes for IGZO TFTs. A representative transfer curve for a MC TFT is shown in Figure 8.1c, which reveals excellent transistor behavior with high on/off current ratio ( $I_{ON}/I_{OFF}$ ) and a turn-on voltage well-aligned for complementary circuit integration.<sup>254</sup> The saturation mobility ( $\mu_{SAT}$ ) and threshold voltage ( $V_{TH}$ ) are extracted from the transfer characteristics. The mobility for MC TFTs (number of devices,  $n = 122$ ) with varying channel lengths is plotted as a function of channel length in Figure 8.7, along with corresponding data for TC and BC geometries. For devices with long channel lengths, the mobility saturates at a high value of  $\sim 6 \text{ cm}^2/\text{V}\cdot\text{s}$ . In addition to high mobility, these devices display a high on/off current ratio of  $\sim 10^5$  and a low, positive threshold voltage (Table 8.1, Figure 8.8). Altogether, the mobility, on/off current ratio, and threshold voltage of these devices show promise for a range of circuit applications.

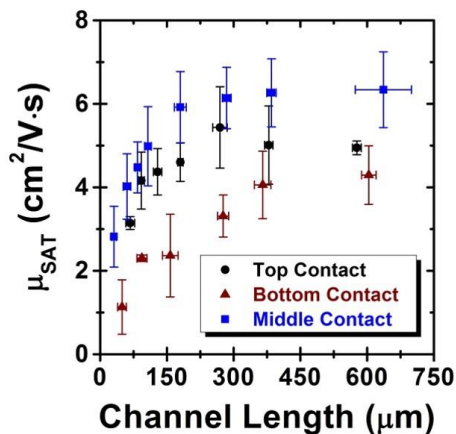


**Figure 8.7.** Measured mobility ( $\mu_{SAT}$ ) for top, bottom, and middle contact devices as a function of channel length ( $n = 40, 25, 122$  for TC, BC, and MC, respectively).

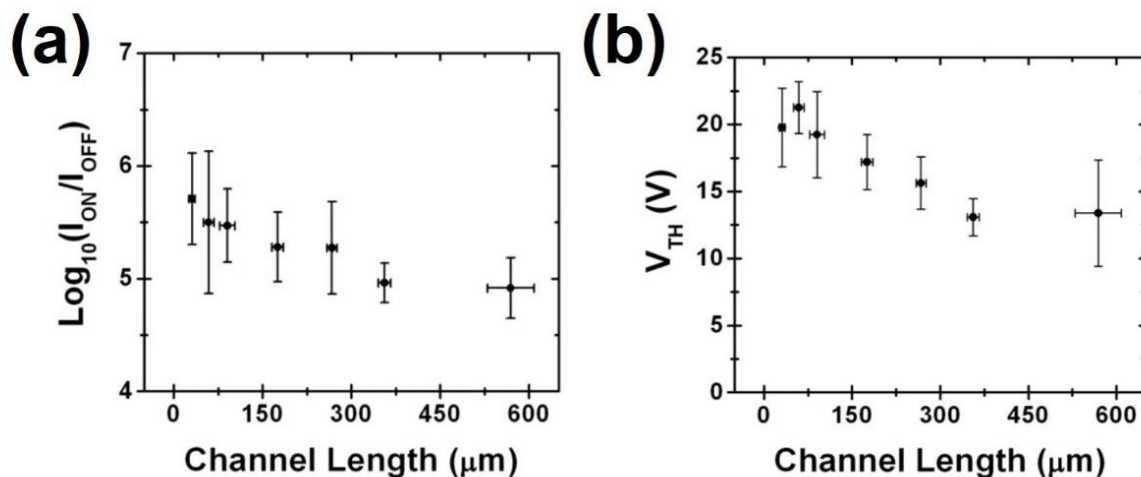


**Figure 8.8.** Electrical characteristics of MC IGZO TFTs with graphene contacts. (a,b) Current on/off ratio ( $I_{\text{ON}}/I_{\text{OFF}}$ ) and threshold voltage ( $V_{\text{TH}}$ ), respectively, plotted against channel length ( $n = 122$ ).

Geometry	L (μm)	$\mu_{\text{SAT}}$ (cm <sup>2</sup> /V·s)	$\text{Log}_{10}(I_{\text{ON}}/I_{\text{OFF}})$	$V_{\text{TH}}$ (V)	SS (V/dec)
BC	~150	2.16 (1.03)*	5.02 (0.27)	25.6 (2.2)	4.87 (0.41)
	~250	3.31 (0.50)	5.10 (0.16)	22.2 (2.4)	5.12 (0.96)
TC	~150	4.32 (0.16)	5.55 (0.54)	16.1 (3.0)	2.49 (0.72)
	~250	5.42 (0.64)	5.55 (0.57)	18.4 (3.6)	2.74 (0.57)
MC	~150	6.38 (0.19)	4.92 (0.29)	7.2 (0.8)	4.28 (1.19)
	~250	6.42 (0.41)	4.99 (0.65)	7.9 (1.1)	4.57 (0.95)

\*All data indicate average (and standard deviation) for four devices. SS = subthreshold swing  
**Table 8.1.** Device metrics for IGZO TFTs having different contact geometries.

As shown in Figure 8.7, for TFTs with short channel lengths, the mobility increases with channel length. This channel length dependence suggests that the contact resistance has a non-negligible contribution to the overall resistance, a relation described by

$$R_T = \frac{\partial V_{DS}}{\partial I_{DS}} = r_{ch}L + R_C \quad (8.1)$$

in which  $R_T$  denotes the total resistance,  $I_{DS}$  and  $V_{DS}$  are the source-drain current and voltage, respectively,  $r_{ch}L$  is the channel resistance, and  $R_C$  is the contact resistance accounting for both contacts. The contact resistance is assessed for MC graphene/IGZO TFTs using the transmission line method.<sup>255</sup> Specifically, output characteristics are collected for devices with a range of channel lengths, and the total resistance at a particular gate bias ( $V_G$ ) is determined by the slope in the linear region of the curve. To account for variations in threshold voltage, the total resistance values are plotted for fixed channel bias conditions (i.e., fixed  $V_G - V_{TH}$ ), which is accomplished by collecting output curves at 5 V increments in  $V_G$ , calculating the total resistance in each case, and interpolating to determine the resistance at a given value of  $V_G - V_{TH}$ . A linear fit to the total resistance as a function of the channel length describes the data well, as shown in Figure 8.9a, with a positive intercept corresponding to the contact resistance. From these measurements, the contact resistance is found to decrease with increasing gate bias, as shown in Figure 8.9b, reaching a low value of  $2.9 \pm 0.2 \text{ k}\Omega \cdot \text{cm}$  for  $V_G - V_{TH}$  of 50 V. This result is comparable to IGZO TFTs having sputtered ITO contacts using a similar combustion-processing approach ( $2.79\text{-}10.1 \text{ k}\Omega \cdot \text{cm}$  at  $\sim 50\text{-}60 \text{ V}_G - V_{TH}$ ),<sup>146</sup> and indicates the suitability of graphene as a contact despite its dissimilar chemical and structural nature.

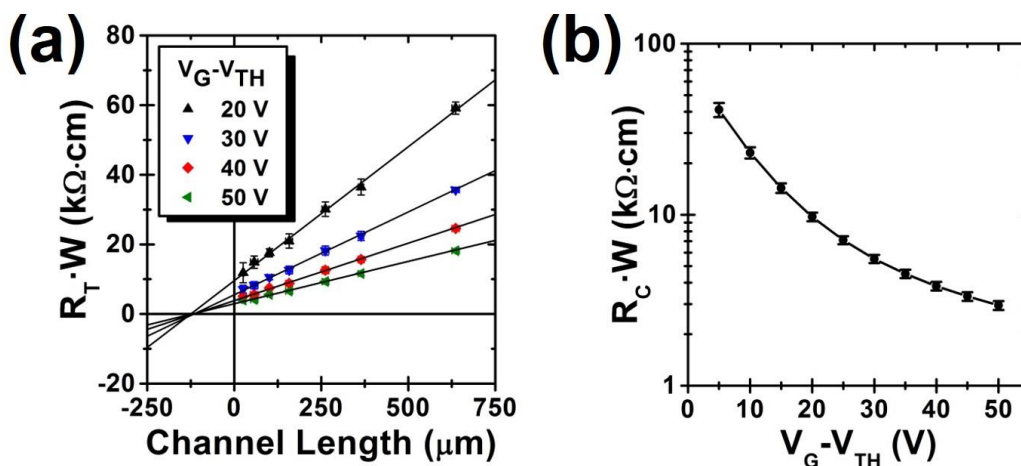


**Figure 8.9.** Electrical characterization of IGZO TFTs with graphene middle contacts. (a) Measured mobility for devices as a function of channel length ( $n = 122$ ). (b) Total resistance plotted against channel length, which allows for the extraction of contact resistance by the transmission line method. (c) Contact resistance plotted as a function of gate voltage.

Figure 8.10 shows corresponding contact resistance measurements for TC and BC devices. Although the TC devices show a similar contact resistance to MC devices, it is important to note that these devices exhibit nonlinearity in the output curves. To calculate total resistance in this case, the lowest-resistance region of the output curves are used. The BC TFTs exhibit a higher contact resistance, consistent with the slow increase in measured mobility with increasing channel length (Figure 8.7). The contact resistance of these devices is one contribution to the decreased mobility measured for TFTs with shorter channel lengths.

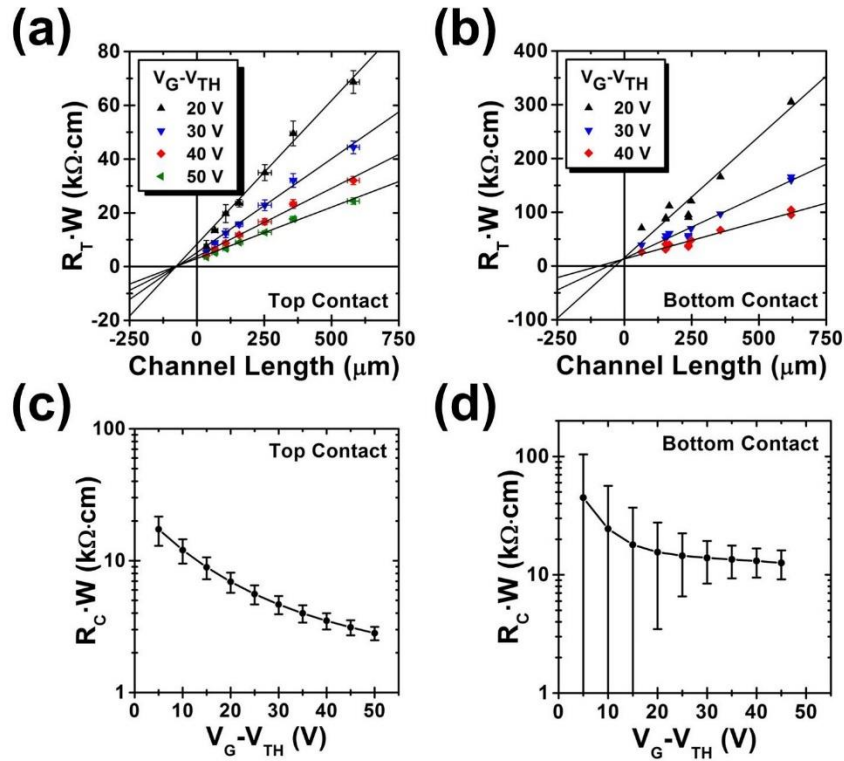


**Figure 8.10.** Contact resistance measurements for IGZO TFTs with graphene contacts. (a,b) Total resistance plotted against channel length for top contact and bottom contact devices, respectively. (c,d) Contact resistance plotted against gate bias for top contact and bottom contact devices, respectively.

With the contact resistance measurements for IGZO TFTs with different contact geometries, it is possible to calculate mobility corrected for the contact resistance. The measured total resistance is used to calculate channel resistance using the relation above (Equation 8.1). The corrected mobility is calculated as

$$\mu_{corr} = \frac{1}{C_i W} \frac{\partial \left( \frac{1}{r_{ch}} \right)}{\partial V_G} \quad (8.2)$$

in which  $C_i$  is the gate capacitance,  $W$  is the channel width, and  $V_G$  is the gate voltage. This analysis was applied to IGZO TFTs with the three different contact geometries, and the corrected mobility

for BC, TC, and MC devices was calculated to be  $3.51 \pm 1.29$ ,  $5.68 \pm 0.89$ , and  $9.61 \pm 1.27$   $\text{cm}^2/\text{V}\cdot\text{s}$ , respectively.

In addition to the contact resistance, a channel length-dependent hysteretic effect can contribute to the observed variation of mobility with channel length. As shown in Figure 8.1c, modest hysteretic behavior is evident in the transfer characteristics of the IGZO TFTs with graphene contacts. While this is small relative to that observed for IGZO TFTs with silver contacts, it affects the electrical measurements of devices. It should be noted that all reported data is obtained using the forward sweep of the transfer curve. In Figure 8.11, more thorough details are presented regarding the hysteretic behavior for the MC IGZO devices (number of devices,  $n = 122$ ). Figure 8.11a shows the threshold voltage hysteresis calculated from the forward and reverse sweeps of the transfer curve, indicating greater hysteresis for shorter channel length devices. Figure 8.11b shows the corresponding data for the calculated mobility, indicating similar channel length dependence and a higher mobility calculated from the reverse sweep. Figure 8.11c shows the average calculated mobility from the transconductance of the forward and reverse voltage sweeps as a function of channel length. Compared to Figure 8.7, the channel length dependence is greatly reduced when the forward and reverse sweeps are averaged. While this does not represent a true mobility, it suggests that hysteretic effects are one source of the decrease in measured mobility for TFTs with shorter channel lengths.



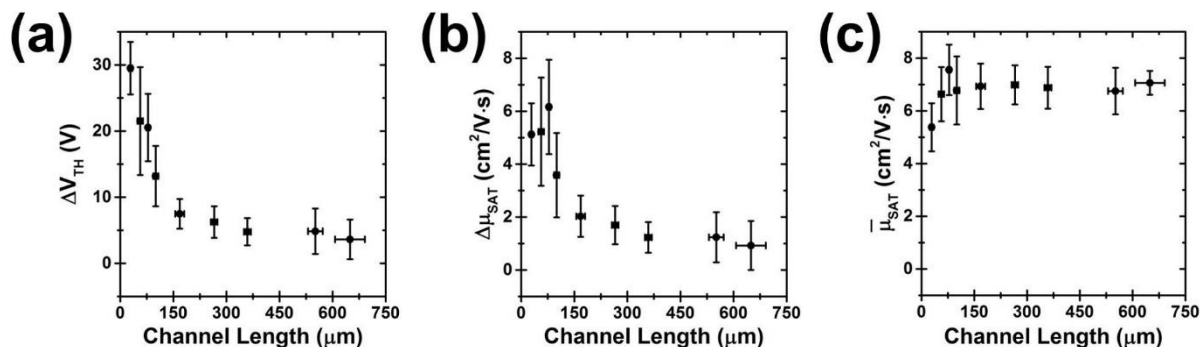


**Figure 8.11.** Characterization of hysteresis for MC IGZO TFTs with graphene contacts. (a) Threshold voltage hysteresis from the forward and reverse sweeps of the transfer characteristics. (b) Difference in calculated mobility based on the forward and reverse voltage sweeps. (c) Calculated mobility plotted against channel length using the average mobility calculated from the forward and reverse voltage sweeps. Number of devices,  $n = 122$ .

### 8.5. Stability Assessment for Inkjet-Printed InGaZnO Transistors

Both graphene and IGZO are characterized by excellent environmental stability relative to traditional materials for printed electronics, particularly organic molecules and polymers. As such, the combination of graphene and IGZO may enable opportunities for functional devices in extreme environments. To assess this possibility, the thermal and long-term ambient stability of MC graphene/IGZO TFTs is characterized. In particular, inkjet-printed TFTs were stored in dark ambient conditions for 365 days, with the electronic properties measured at nine points during this period. Representative transfer curve data from one device with a channel length of 150 μm is shown in Figure 8.12. While the threshold voltage shows an initial shift, it remains at a low, positive value for the remaining time, with small fluctuations likely due to environmental factors such as humidity and no systematic shifts.

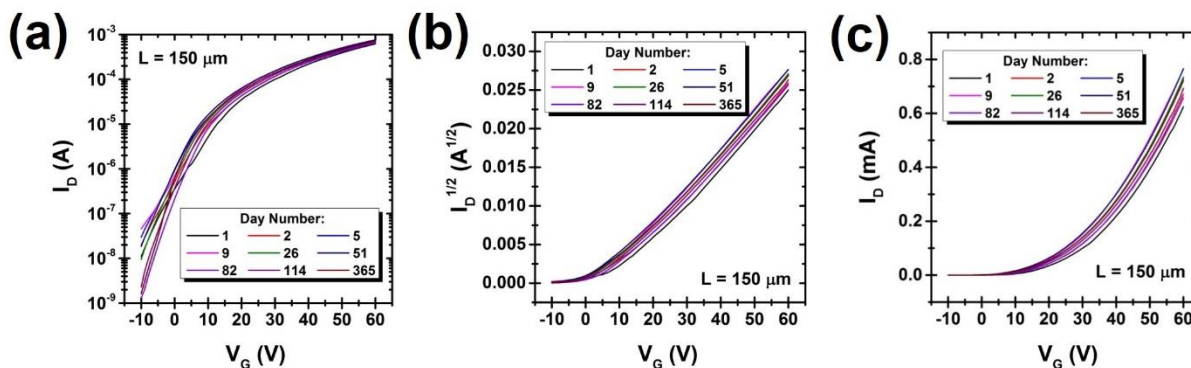


**Figure 8.12.** Electrical performance of MC graphene/IGZO TFTs during aging in ambient conditions. (a-c) Transfer characteristics for a single device measured nine times over the course of 365 days, with different axes scaling.

More extensive statistical characterization is shown in Figure 8.13. It is evident that the present devices maintain a high, stable saturation mobility of  $\sim 6 \text{ cm}^2/\text{V}\cdot\text{s}$  throughout this period, with no evidence of systematic degradation (Figure 8.13a). The current on/off ratio, shown in Figure 8.13b, is also consistent with a typical value of  $\sim 10^5$ , while the threshold voltage stabilizes at a positive value suitable for complementary operation. This robust stability is highly advantageous for applications requiring an exposed semiconducting channel, such as sensors, and mitigates the need for expensive, high quality encapsulation.

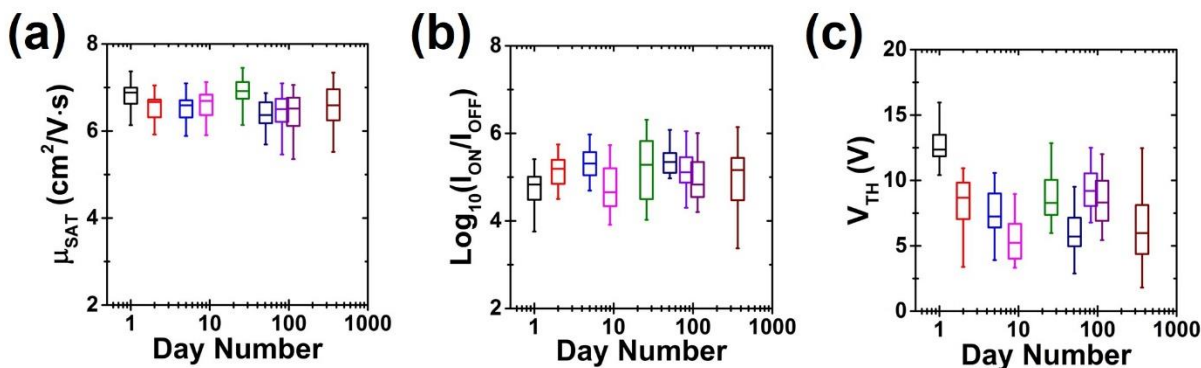


**Figure 8.13.** Stability of graphene/IGZO TFTs against ambient aging. (a) Mobility, (b)  $I_{\text{ON}}/I_{\text{OFF}}$ , and (c)  $V_{\text{TH}}$ , measured at various times over 365 days ( $n = 22$ ).

An additional attraction of the present materials combination is the high thermal tolerance of both graphene and IGZO. During fabrication, these devices are exposed to 300 °C in air, suggesting stability at this temperature. To verify this thermal stability, 30 graphene/IGZO TFTs were exposed to increasing temperatures in air, with the electrical performance measured. As shown in Figure 8.14a, for temperatures up to the fabrication temperature of 300 °C, no significant degradation is observed in the saturation mobility. Moreover, with heat treatment up to 400 °C, an enhancement in device performance is observed. Similarly, the current on/off ratio, shown in Figure 8.14b, exhibits no systematic degradation following this thermal stress. As in the case for long-term aging, the threshold voltage stabilizes at a positive value suitable for complementary operation, as shown in Figure 8.14c. This thermal stability is greater than that observed for typical printed organic electronics, and enables applications in extreme environments not possible with traditional organic electronic materials. In addition, this robust tolerance relaxes process constraints for the more versatile integration of IGZO with advanced materials and traditional semiconductors, offering potential routes toward novel heterostructures.<sup>256</sup>

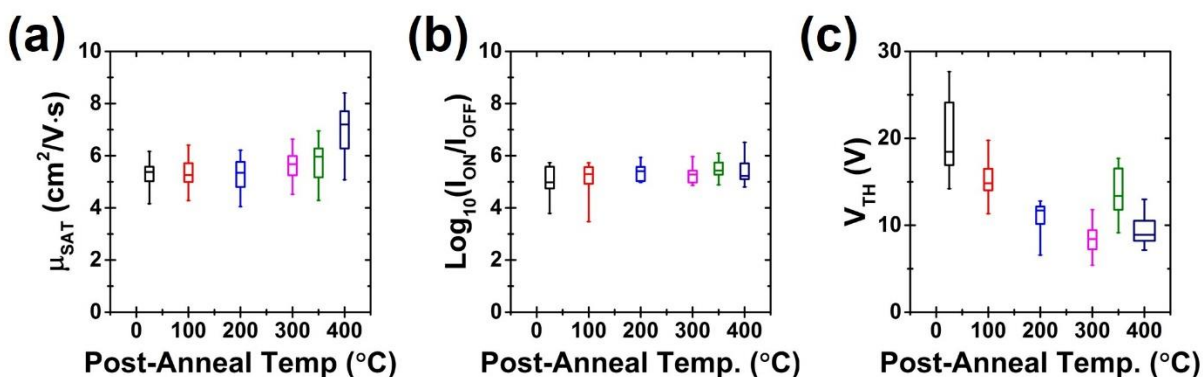


**Figure 8.14.** Stability of graphene/IGZO TFTs against high temperatures. (a) Mobility, (b)  $I_{ON}/I_{OFF}$ , and (c)  $V_{TH}$ , measured following post-fabrication thermal treatment to 100-400 °C in air ( $n = 30$ ).

As one example of a more complex structure, graphene/IGZO TFTs were fabricated with silver interconnects to model a practical circuit (Figure 8.15). Although graphene presents a superior contact material to IGZO compared to silver, silver remains a desirable material for printed interconnects and wires due to its excellent electrical conductivity. Therefore, a suitable device format would include IGZO TFTs with graphene contacts connected to the larger circuit with silver interconnects. To confirm that the graphene presents a stable interface with silver, as well as a suitable barrier between silver and IGZO, TFTs were fabricated using contacts composed of both silver and graphene concurrently. As shown in Figure 8.15, a layer of silver was inserted into standard MC graphene/IGZO TFTs. Because the contact-channel interface is at the leading edge of the graphene contact, which is not covered with silver, a second layer of graphene on top of the silver was unnecessary. An optical micrograph of the devices is shown in Figure 8.15b. The devices exhibit performance metrics nominally identical to MC devices without silver (Figure 8.15c), confirming the robustness of the graphene barrier separating the silver and IGZO and offering a promising route toward practical implementation.

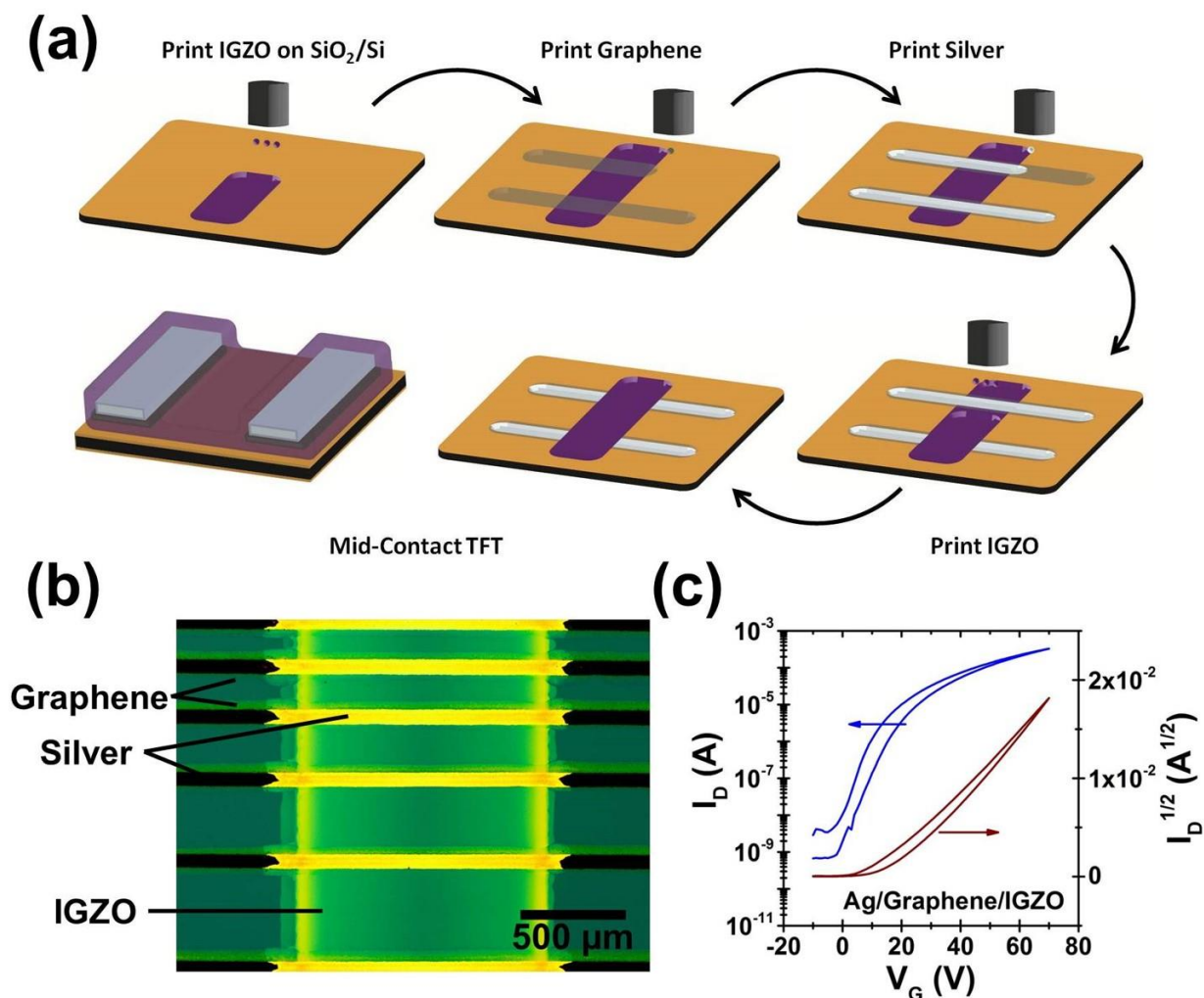


**Figure 8.15.** Connection of graphene/IGZO TFTs with silver interconnects. (a) Schematic illustration showing TFT fabrication process with silver inserted into standard MC graphene/IGZO TFTs. (b) Optical micrograph showing the printed devices, with the different materials indicated. (c) Representative transfer curve for the TFTs.

## 8.6. Summary of Graphene Electrodes for Chemically Stable InGaZnO Electrodes

In summary, this chapter describes the use of graphene source/drain electrodes for high-performance inkjet-printed IGZO TFTs. The combination of graphene with combustion-processed

IGZO enables the fabrication of printed TFTs with a maximum processing temperature of 300 °C. By exploring various contact geometries, the limitations of traditional top-contact and bottom-contact structures were revealed, and a unique middle-contact device architecture was introduced that exhibits several advantages for these devices, combining the desirable properties of both TC and BC geometries. With mobilities exceeding 6 cm<sup>2</sup>/V·s, current on/off ratios greater than 10<sup>5</sup>, and favorable threshold voltages, these devices provide a promising foundation for integration into more complex circuits. Moreover, their excellent thermal stability eases constraints for integration with different materials, in addition to expanding the scope of possible applications in extreme environments. This robustness is reinforced by their outstanding long-term ambient stability, with no systematic degradation observed in devices measured over a full year. In this manner, graphene not only facilitates the development of printed IGZO devices, but also provides additional benefits over standard contact materials. Overall, the successful integration of graphene and IGZO in a printed format represents a significant advance in fabricating printed electronics based on high-performance, stable inorganic components.

## **CHAPTER NINE**

Stable Graphene Contacts for Liquid Metal

## 9.1. Introduction to Stable Graphene Contacts for Liquid Metal

Chapter 8 demonstrated the benefit of graphene inks for the fabrication of stable electrodes to InGaZnO transistors. In this capacity, silver electrodes lead to poor and unstable performance due to migration of silver ions into the oxide semiconductor, while graphene's inert nature allows for a stable contact interface. In the present chapter, this characteristic of graphene will again be exploited to enable stable interfaces with another high performance printed material, namely liquid metal.

Gallium-based liquid metal alloys are a unique class of advanced materials with the potential to offer unprecedented opportunities in stretchable and reconfigurable electronics.<sup>257,258</sup> As a room temperature liquid, eutectic gallium-indium (eGaIn) presents mechanical properties unmatched by conventional electronic materials. By leveraging these exceptional characteristics, researchers have recently demonstrated advances ranging from reconfigurable liquid metal switches and responsive sensors to robust and stretchable interconnects.<sup>259–262</sup> Moreover, the fluid nature of eGaIn enables broad process compatibility with additive printing methods, with demonstrations of direct write, inkjet, transfer, and 3D printing.<sup>263–266</sup> As such, the development of liquid metals for applications in printed, stretchable, and reconfigurable electronics is a critical area of research with broad scientific and practical interest.

Despite their promise, the development of liquid metal electronics must overcome several challenges for widespread application. In a recent overview, Dickey identified stable electrical contacts as a critical challenge for the integration of eGaIn in electronic circuits and systems.<sup>257</sup> Gallium alloys rapidly with conventional metals, leading to unstable or mechanically sensitive interfaces and preventing the reliable integration of eGaIn functionality with conventional



electronics. In a recent dramatic demonstration of this effect, Dickey and coworkers exploited the aggressive alloying of eGaIn with silver to direct the motion of liquid metal droplets across a surface.<sup>267</sup> To enable broader application of eGaIn with conventional circuits, this problem must be addressed.

Similar to their application for InGaZnO TFTs, printable graphene inks offer a reliable and high performance strategy to form electrical connections to eGaIn. In contrast to conventional metals,  $sp^2$ -bonded carbon materials are stable to alloy formation with the liquid metal.<sup>268,269</sup> A thin (~100 nm) film of graphene printed between conventional silver leads and eGaIn effectively passivates the interface, preventing alloy formation as a physical barrier. Moreover, the graphene interfacial contacts offer excellent durability, with thermal stability to 300 °C and robust tolerance to mechanical bending.

## **9.2. Process Integration of Graphene with Liquid Metal**

To demonstrate the utility of graphene as a conductive interface layer, circuits are printed with silver, graphene, and liquid metal. For the control sample, eGaIn lines are printed directly on top of silver traces (Figure 9.1a,b). This configuration exhibits clear alloying between the silver and eGaIn, as expected from prior reports. To establish the ability of graphene to stabilize this interface, a similar sample is fabricated with a thin film (~100 nm) of graphene printed between the silver and eGaIn. In this configuration, no alloy formation is observed (Figure 9.1a,c). These samples are further analyzed by optical profilometry to confirm the stability of the graphene interface (Figure 9.2).

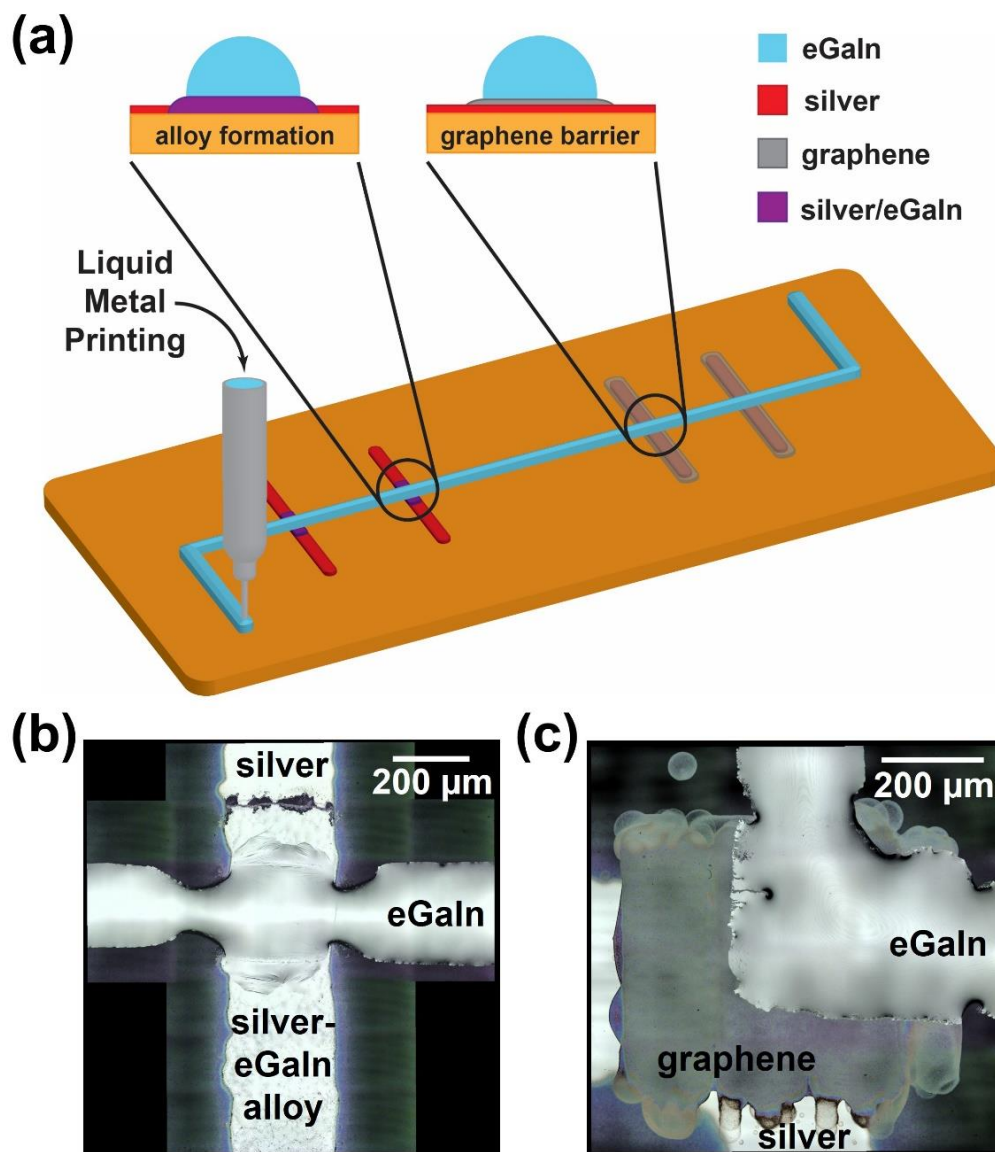


**Figure 9.1.** Proof of concept demonstration of graphene as a stable interfacial material for eGaIn. (a) Schematic of test setup, showing eGaIn printed over exposed and graphene-covered silver lines, with alloy formation occurring for the eGaIn-silver interface. (b) Optical microscopy image showing formation of the silver-eGaIn alloy resulting in large defects. (c) Optical microscopy image showing a graphene-passivated junction with a silver-graphene-eGaIn configuration, with no alloy formation evident.

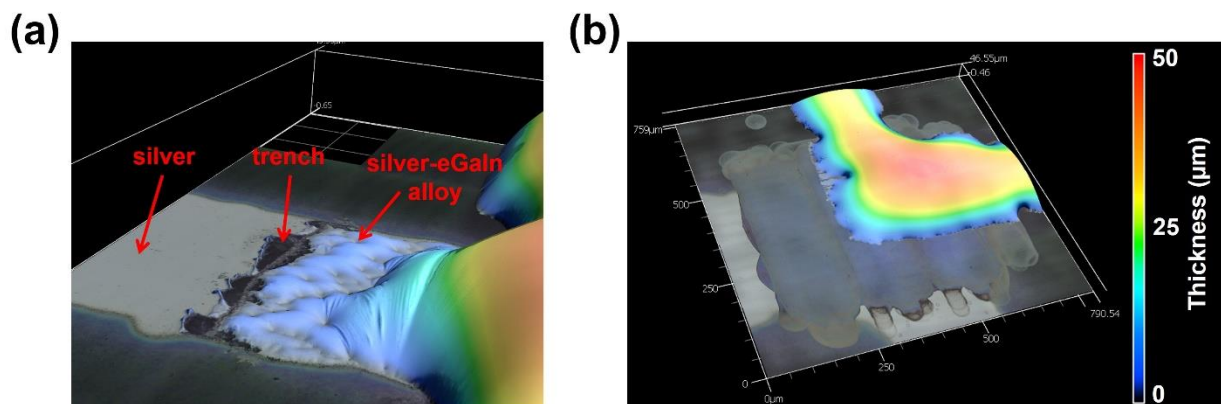


**Figure 9.2.** Optical profilometry images of the samples shown in Figure 9.1b-c, confirming the alloy formation and severe instability of the silver-eGaN junction (a) and passivated junction with graphene (b).

Because graphene offers substantial benefit for electrical connections in printed liquid metal electronics, the development of reliable and controlled processing methods to integrate these materials is desired. In particular, the high surface energy of eGaN and rapid formation of a surface oxide endow it with unconventional rheological behavior compared to traditional printed materials. Reliable direct-write printing of eGaN therefore requires engineering of the substrate surface properties to ensure adequate and stable adhesion of the  $\text{GaO}_x$ . This challenge is illustrated in Figure 9.3a, which shows optical microscopy images of eGaN printed across a glass-graphene film boundary to demonstrate the contrasting behavior between the two surfaces. When deposited directly onto as-printed graphene or films following oxidative surface treatment, the liquid metal traces show insufficient adhesion for stable pattern formation and break apart. By tuning the annealing process for the graphene, by annealing between 250 and 350 °C to partially decompose the polymer dispersant of the ink, reliable wetting and adhesion of the liquid metal is achieved (Figure 9.3a). Moreover, the wetting properties of the eGaN on the graphene surface can be

tailored within this suitable range. To further investigate this, the aspect ratio of eGaIn lines printed on glass and graphene is analyzed (Figure 9.3b). The aspect ratio, defined as thickness/width, is an indicator of the wetting behavior of the eGaIn. It is evident that the wetting improves following higher temperature heat treatment. This is correlated with previous work in Chapter 6 showing the decomposition and structural change of the graphene ink binder residue over this temperature range,<sup>74</sup> and suggests that some residual polymer decomposition products are desirable to maintain proper printing of the liquid metal. Overall, the line aspect ratio can be controllably tuned from 0.87 to 0.66 for annealing at 250 and 350 °C, respectively.

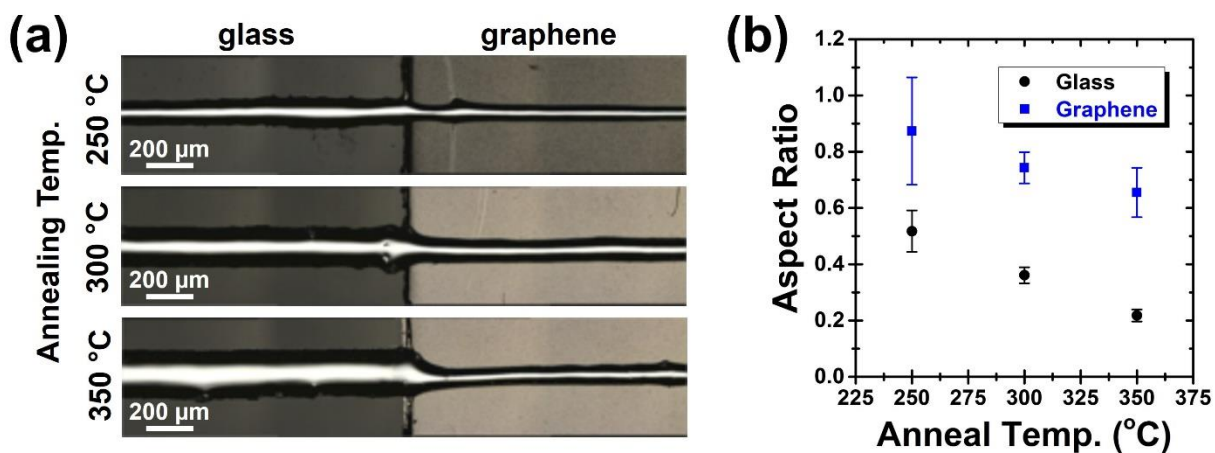


**Figure 9.3.** Process development for the integration of eGaIn with graphene. (a) Optical microscopy images showing printed tracks of eGaIn (horizontal lines) across a bare glass-graphene film boundary (left: glass; right: graphene), resulting in changes in line morphology. Following annealing of the graphene films at 250-350 °C, stable wetting of the eGaIn was achieved to print continuous lines. (b) Summary of aspect ratio for printed eGaIn lines on glass and graphene, showing a systematic trend of decreasing aspect ratio, associated with improved wetting, for graphene films annealed at higher temperatures.

### 9.3. Electrical Characteristics and Stability of Graphene Interfaces

Having established suitable conditions for process integration of graphene and eGaIn, the electrical properties of the interface are characterized for practical applications. Contact resistance offers a useful metric for assessing the electrical junction. The contact resistance for the graphene/eGaIn junction is calculated by the transmission line method, shown in Figure 9.4a.<sup>255</sup> This method is also used to measure contact resistance for different material sets, namely silver-graphene and silver-graphene-eGaIn, as shown in Figure 9.4b. The individual silver-graphene and graphene-eGaIn junctions exhibit contact resistances of  $4.13 \pm 0.32$  and  $8.79 \pm 0.31 \text{ } \Omega \cdot \text{mm}$ , respectively. A large contribution of the contact resistance in these cases is likely a result of current crowding due to the mismatch in electrical conductivity between the materials. As a result, the junction resistance was also measured for the three-material sample containing a silver-graphene-eGaIn junction, in which the graphene prevents alloy formation between the silver and eGaIn. In this configuration, current crowding effects no longer dominate because silver and eGaIn have similar conductivity, while the graphene functions only as a thin ( $\sim 100 \text{ nm}$ ), conductive interfacial barrier. In this configuration, the measured junction resistance is substantially lower at  $0.263 \pm 0.041 \text{ } \Omega \cdot \text{mm}$ , suitable for a range of practical applications.

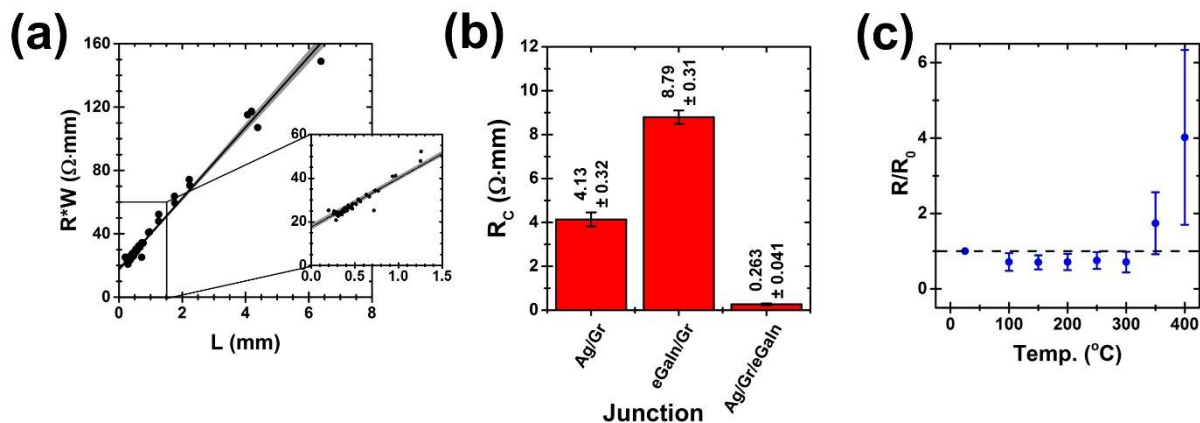


**Figure 9.4.** Electrical characterization of graphene interfaces. (a) Contact resistance measurement for a graphene-eGaIn junction using the transmission line method. (b) Summary of contact resistances for three junction configurations, namely silver-graphene, eGaIn-graphene, and silver-graphene-eGaIn. The reduced contact resistance in the silver-graphene-eGaIn configuration is likely a result of current crowding for the individual silver-graphene and graphene-eGaIn junctions. (c) Normalized electrical resistance of silver-graphene-eGaIn junctions following thermal treatment, showing stable performance up to at least 300  $^\circ\text{C}$ .

As discussed above, the stability of the graphene barrier is critical for long-term operation of the liquid metal components. To test stability under stressful conditions, the silver-graphene-eGaIn junctions were exposed to progressively higher temperatures up to 400  $^\circ\text{C}$ . As shown in Figure 9.4c, the samples exhibit excellent stability to thermal exposure as high as 300  $^\circ\text{C}$ . Following exposure to 350 and 400  $^\circ\text{C}$ , an increase in resistance is observed, along with evidence for alloy formation between the silver and eGaIn. This temperature corresponds to the annealing temperature of the graphene films prior to eGaIn deposition, and suggests that volatilization and release of polymer residue from the graphene may underlie the observed degradation by causing local build-up of stresses and eventual failure. Nevertheless, stability to 300  $^\circ\text{C}$  is highly advantageous for many potential applications, and opens a broad window for processing, including

the possibility for integration with other materials that may require high temperature deposition or curing.

The graphene-stabilized liquid metal contacts exhibit excellent electrical properties and thermal stability. For many desirable applications of liquid metals, such as flexible circuits, mechanical durability is also critically important. To assess this, silver-graphene-eGaIn structures were printed on polyimide and the resistance was tested under cyclic bending around a well-defined radius of curvature. As shown in Figure 9.5a, only a slight increase in resistance of ~5% was measured over 250 bending cycles, evidence for the mechanical integrity of the contact. Moreover, this resistance increase is primarily associated with the silver-graphene components, with the resistance of the liquid metal contact increasing only ~2%. This is investigated further by testing a sample configuration without silver, containing only the graphene-eGaIn junction positioned directly over the center of bending. Figure 9.5b shows the measurement resistance during bending, as measured through eGaIn lines connected by graphene. During bending to a high angle, a slight increase in resistance is measured. This is consistent with an increased resistance through the eGaIn lines resulting from deformation upon bending. Importantly, this small change is reversible, supporting the claim that this resistance increase is likely due to the liquid metal itself, and not broader systematic degradation. This is verified with a cyclic bending test over 100 cycles, shown in Figure 9.5c, which shows negligible change in resistance. This confirms the suitability of this materials system for application in flexible electronics, a key focus of liquid metal development.

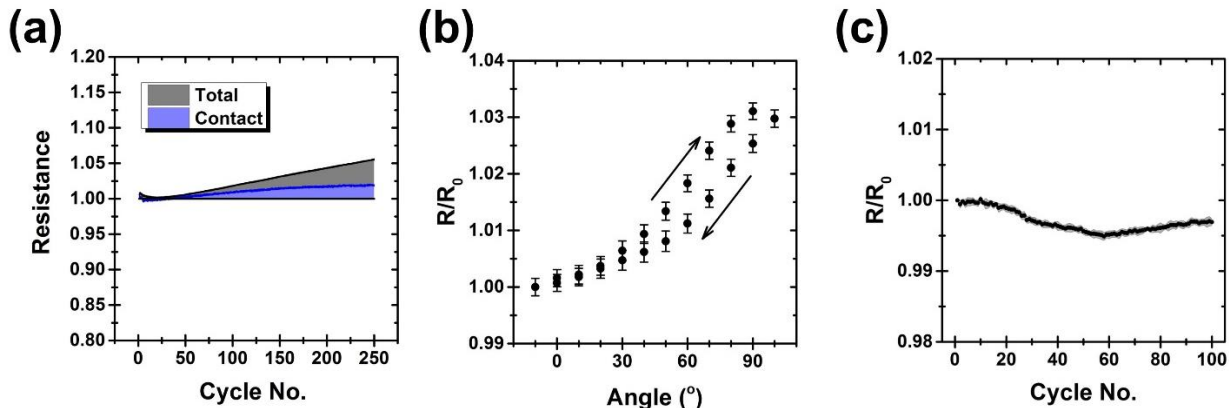


**Figure 9.5.** Mechanical testing of graphene contacts for liquid metal. (a) Normalized resistance of silver-graphene-eGaIn structures over 250 bending cycles, with the resistance change subdivided into contact resistance associated with the eGaIn and total resistance including the silver-graphene lines. (b) Normalized resistance of graphene-eGaIn junction as a function of bending angle, showing a small and reversible change in resistance likely due to deformation of the eGaIn patterns. (c) Normalized resistance of graphene-eGaIn junctions over 100 bending cycles, showing stable performance.

#### 9.4. Summary of Stable Graphene Electrodes for Liquid Metal Electronics

In summary, printable graphene inks have been demonstrated as a high-performance, reliable interfacial material to enable stable electrical connections between conventional and liquid metals. In this context, the thin nature, dense film formation, high electrical conductivity, and robust chemical, thermal, and mechanical stability of graphene offer key benefits, while the broad process compatibility with liquid-phase printing methods suggests promise for more widespread use for both research and practical applications. A thin (~100 nm) film of printed graphene was shown to effectively suppress alloy formation between eGaIn and silver, while maintaining good electrical performance and excellent thermal and mechanical durability. Overall, this offers a promising solution to a well-established challenge in the development of liquid metal electronics for a variety of target applications.



## **CHAPTER TEN**

Interfacing Graphene with Organic Semiconductors and  
Electrolytes

## 10.1. Introduction to Graphene Interfaces with Organic and Electrolytic Materials

While the preceding chapters focused on the use of graphene for stable interfaces with inorganic ceramics and metals, this chapter will present a brief snapshot of applications with organic and electrolytic materials. The first demonstration will examine how the unique structure of graphene, namely the  $sp^2$  carbon lattice with extended  $\pi$ -bonding, can offer favorable interfaces with small molecule organic semiconductors. In this case, a graphene film templates the deposition and crystal formation of the fullerene  $C_{60}$ , leading to improved performance in electronic devices.<sup>270</sup> Polymer semiconductors are also highly desired for printed electronics, such as the benchmark polymer P3HT. The second demonstration utilizes highly stable and flexible graphene electrodes for electrolyte-gated transistors (EGTs) with P3HT. Compatibility with photonic annealing enables device integration on paper-based substrates,<sup>87</sup> and high resolution patterning allows for improvements in performance and device density. In this context, the stability of the graphene surface to the electrolytic gate dielectric is critical, and control devices with clean silver electrodes instead of graphene exhibit unstable performance. This electrochemical stability is also leveraged for the third demonstration here, the fabrication of graphene microsupercapacitors (MSCs) with an acidic electrolyte.<sup>82</sup> In this capacity, the graphene offers a stable, high surface area material for advanced energy storage. Because these studies use the graphene inks developed in this research, but do not constitute the core focus of this thesis, the discussion in each case will include only a brief, high-level overview. Altogether, these examples demonstrate the broad applicability of graphene inks, leveraging their unique combination of high conductivity, chemical stability, mechanical flexibility, and two-dimensional structure. While the work presented in this chapter builds on the prior material development in this thesis, this work was primarily done

external to the central thesis research, through collaborative efforts with excellent researchers both at Northwestern and at other universities. For each section, the primary contributions will be explicitly acknowledged, and a high-level overview will be presented with reference to individual works containing more extensive details.

## 10.2. Templating C<sub>60</sub> Devices with a Graphene Ink Interlayer

Due to its atomic-scale structure, graphene offers unique properties for interfacing with organic materials.<sup>271</sup> In particular, organic semiconductors have a  $\pi$ -conjugated electronic structure which facilitates delocalized charge transport. Because graphene shares this feature, it can interact with these materials differently than conventional metals.<sup>272</sup> One example of this is the use of graphene for templating the deposition and growth of small-molecule organic semiconductors.<sup>273</sup> It has been demonstrated that graphene can alter the preferred crystalline packing orientation, for example, in the growth of pentacene.<sup>274</sup> However, most studies observing this effect use high quality, single-layer CVD graphene.<sup>275</sup> To explore whether solution-processed graphene influences the structure and performance of the molecular semiconductor C<sub>60</sub>, thin film deposition experiments and device measurements were performed. Figure 10.1 summarizes the results. When grown on bare ITO, C<sub>60</sub> exhibits very small grain size, as shown by grazing-incidence X-ray diffraction (GIXD) and SEM (Figure 10.1a-b). However, when deposited on a graphene thin film, particularly when deposition takes place at 150 °C, the C<sub>60</sub> forms a highly crystalline film with large grains (Figure 10.1c-d) and a preferred orientation of the FCC C<sub>60</sub> lattice with respect to the graphene film surface. The impact of this morphology difference on charge transport properties is explored through the fabrication and testing of electron-only devices, based on the structure shown

in Figure 10.1e. Devices with a graphene interlayer to template the  $C_{60}$  growth exhibited considerably higher current density, as shown in Figure 10.1f. This suggests the benefits of graphene, even in a solution-processed film, for interfacing favorably with organic semiconductors and offering unique characteristics for a printed conductor. This work was done primarily at the University of Massachusetts, Amherst in collaboration with Leonardo Gonzalez Arellano, Hyunbok Lee, Edmund Burnett, Prof. James Watkins, and Prof. Alejandro Briseno.

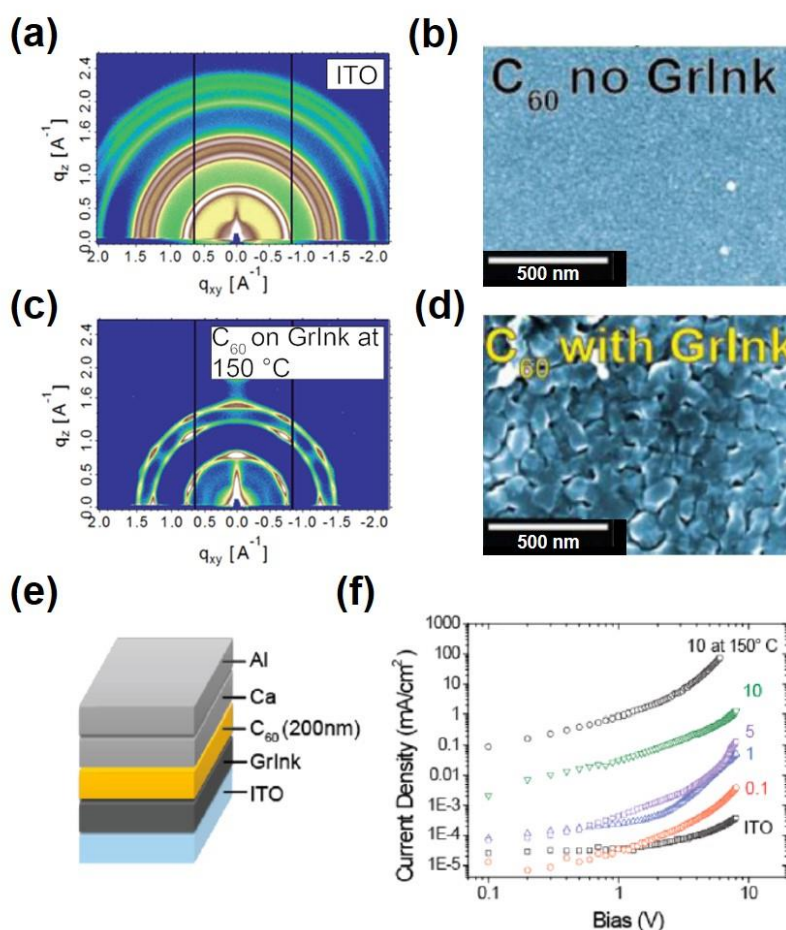


**Figure 10.1.** Templating  $C_{60}$  deposition with a graphene film. (a,b) GIXD data and SEM image, respectively, for a  $C_{60}$  film deposited on ITO. (c,d) Corresponding data for a  $C_{60}$  film deposited on graphene at 150 °C, showing improved crystallinity. (e) Schematic of device design and (f) electrical characterization, showing greatly improved current density for films deposited on graphene (the inset labels indicate the graphene ink concentration, and correlate with film thickness).

### 10.3. Graphene Electrodes for Printed, Flexible Electrolyte-Gated Transistors

Having established favorable interfaces to organic semiconductors, it is useful to explore the application of graphene electrodes more broadly for organic transistors. Many flexible electronics devices are based on semiconducting polymers, such as the benchmark p-type polymer poly(3-hexylthiophene), or P3HT.<sup>276</sup> Transistors require source/drain electrodes that interface well with the semiconducting material. Due to factors such as stability and work function, gold is commonly used in this capacity.<sup>277,278</sup> To investigate a low-cost, flexible alternative to gold, the graphene inks developed here were employed as source/drain electrodes in organic transistors, using multiple strategies for integration. By leveraging the compatibility of graphene inks with screen printing and photonic annealing, printed EGTs based on P3HT and graphene electrodes were fabricated on glassine paper substrates, as shown in Figure 10.2.<sup>87</sup> The high mechanical tolerance of the graphene lines, along with process compatibility, allowed not only fabrication on glassine, a type of supercalendered paper, but also operation following discrete folding of the patterns (Figure 10.2a-c). This durability was leveraged to demonstrate printed EGTs on paper, which showed good performance even following repeated folding (Figure 10.2d-f). This work was performed primarily at the University of Minnesota, with key contributions from Dr. Woo Jin Hyun, Geoffrey A. Rojas, Prof. Lorraine F. Francis, and Prof. C. Daniel Frisbie.

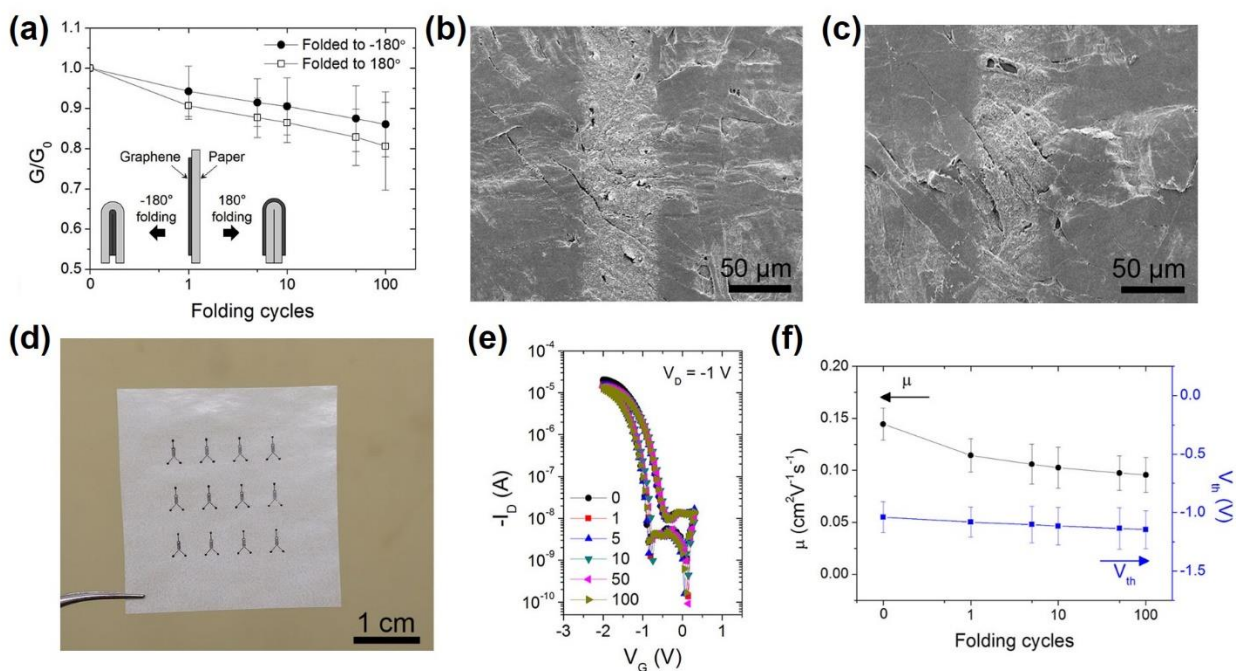


**Figure 10.2.** Foldable organic transistors on paper using graphene electrodes. (a) Change in conductance of graphene lines as a function of folding cycles, showing retention of performance following extreme mechanical deformation. (b,c) SEM images of graphene lines on glassine paper before and after folding, respectively. (d) Photograph of printed graphene electrodes on paper for EGT fabrication. (e) Transfer curves and (f) mobility and threshold voltage for transistors over 100 folding cycles.

As discussed in Section 1.6.2, there is significant benefit to scaling down device dimensions, in terms of both performance and packing density. To develop strategies for printing high-resolution graphene patterns, a precision transfer printing method was developed which decouples the annealing of functional materials from the thermal tolerance of the target substrate.<sup>129</sup> In particular, a silicon mold was patterned by photolithography, and coated with Cytop, an amorphous fluoropolymer. An engineered graphene ink could selectively dewet the surface of the mold while filling trenches, with feature sizes ranging from  $3.2$  to  $2000\ \mu\text{m}$  wide. By annealing the graphene in the silicon mold at temperatures as high as  $250\ ^\circ\text{C}$ , the graphene could then be transfer printed to a PET substrate using a UV-curable adhesive. This technique was

used to fabricate graphene lines on PET with line width as small as  $3.2\ \mu\text{m}$  and a pitch of  $6\ \mu\text{m}$  (Figure 10.3a). Such high-resolution graphene patterns were used for source/drain contacts in EGTs (Figure 10.3b-c). While clean silver electrodes showed unstable performance for transistor operation, the electrochemically stable graphene electrodes showed stable, high performance operation and excellent flexibility (Figure 10.3d-e). This marks an advance in high resolution patterning of graphene inks, and offers excellent control and unique opportunities for further experiments. This work was performed at the University of Minnesota, with key contributions from Dr. Donghoon Song, Dr. Ankit Mahajan, Prof. Lorraine F. Francis, and Prof. C. Daniel Frisbie.

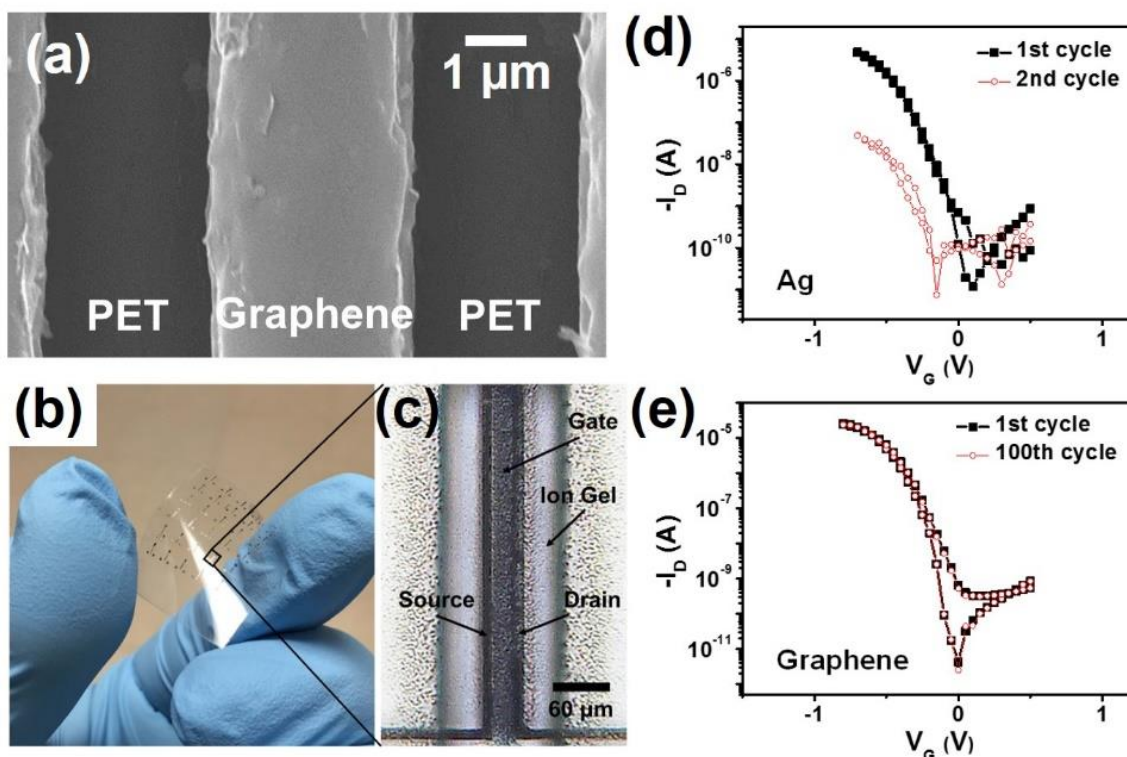


**Figure 10.3.** High resolution graphene printing for organic transistors. (a) SEM image showing a  $3.2\ \mu\text{m}$  wide graphene line on PET, with a pitch of  $6\ \mu\text{m}$ . (b) Macroscopic photograph and (c) microscope image of fabricated EGTs using graphene electrodes. (d,e) Transistor performance for devices based on clean silver electrodes and graphene electrodes, showing superior stability with graphene.

#### 10.4. Printed, Flexible Graphene Microsupercapacitors

The electrochemical stability of graphene that is critical for electrodes in EGTs can also be leveraged for energy storage applications. In particular, supercapacitors store energy in built-up charge at the interface between solid electrodes and a liquid or gel electrolyte.<sup>224</sup> Supercapacitor electrodes therefore require electrochemical stability, electrical conductivity, and a high surface area for favorable performance. Graphene excels in these metrics, and is therefore widely studied for electrochemical energy storage.<sup>279</sup> Solid-state supercapacitors employing an acid gel electrolyte were fabricated using graphene/EC inks, resulting in high volumetric energy density.<sup>82</sup> The high conductivity of the graphene enables its use as both the electrode and current collector, simplifying the device design and fabrication process. Moreover, the printable nature of graphene/EC was exploited to inkjet print MSCs, as shown in Figure 10.4, which operate as a supercapacitor but employ a coplanar, interdigitated electrode structure well-suited for on-chip integration. These devices showed proper electric double layer capacitor performance (Figure 10.4b), with high capacitance and stability upon extended cycling and bending (Figure 10.4c-f). Graphene therefore presents a promising material for applications in printed energy storage devices.<sup>280</sup> This work, performed at Northwestern University, requires acknowledgement of the key contributions of Dr. Lei Li.



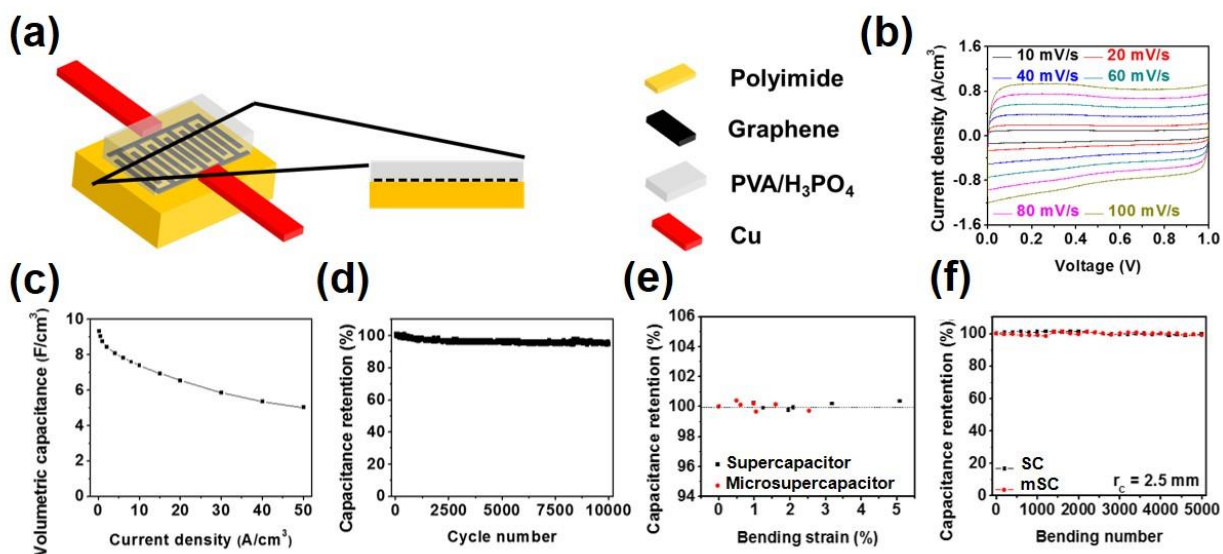


**Figure 10.4.** Printed graphene microsupercapacitors. (a) Schematic structure of a printed graphene MSC on polyimide. (b) Cyclic voltammetry data for the MSC at various scan rates, showing suitable operation as an electrolytic double layer capacitor. (c) Capacitance as a function of current density, collected from galvanostatic charge/discharge measurements. (d-f) Stability of device performance upon extended cycling, operation while under strain, and repeated bending, respectively. Red data points in (e) and (f) correspond to a MSC, while black points correspond to a sandwich-structure supercapacitor.

## 10.5. Summary of Graphene Applications with Organic and Electrolytic Materials

In summary, the favorable integration of graphene was demonstrated with a wide range of organic and electrolytic materials, exploiting the robust stability of this material for key applications. First, a thin graphene film was demonstrated to template the crystal growth of C<sub>60</sub> for high performance electronic devices. The beneficial interfacial properties of graphene with organic  $\pi$ -bonded systems were extended to organic transistors based on P3HT. By leveraging the broad process compatibility of graphene inks, electrolyte-gated transistors on glassine paper substrates were fabricated, with demonstrated operation even after repeated folding cycles. The electrochemical stability of graphene was shown to be critical for such EGTs, in that clean silver

electrodes exhibit degradation under the corrosive operating conditions. Higher-resolution devices were fabricated on PET using a novel transfer printing method, which was developed for the graphene inks to allow thermal annealing prior to transfer. Graphene lines as narrow as 3.2  $\mu\text{m}$  were demonstrated, with a pitch as small as 6  $\mu\text{m}$ , allowing improvements in device performance and transistor density. Finally, the electrochemical stability of graphene was leveraged for energy storage applications, particularly printed graphene MSCs. With stable and promising performance, these devices demonstrate the benefits of graphene's electrical conductivity, electrochemical stability, flexibility and high surface area for advanced energy storage. This suite of properties offers advantages for electrochemical energy storage beyond supercapacitors, including as an additive for lithium-ion batteries,<sup>281</sup> suggesting the broad applicability of this material.

## **CHAPTER ELEVEN**

Opportunities for Future Research

### **11.1. Introduction to Future Work**

The research presented to this point has resulted in a versatile and promising processing platform for graphene inks, and offers opportunities for future work. Three different dimensions of possible future work will be highlighted here. First, the translation of methods and knowledge from graphene to alternative nanomaterials, particularly 2D nanomaterials such as MoS<sub>2</sub> and hBN, would accelerate the development of mutually-compatible inks with complementary electronic functionality. Second, extending the graphene/EC processing framework beyond printed electronics, to more traditional polymer-processing methods, would offer interesting opportunities for process integration and tailoring microstructure. Finally, the broad control over graphene processing with EC, and the unique nature of the composite system, offers a strong foundation for fundamental studies in electrical properties, mechanical behavior, rheology, and surface/interface control, which could provide deeper scientific and theoretical insight into similar material systems, while also presenting practical benefits for select applications.

### **11.2. Translating Concepts to Other Nanomaterials**

Ethyl cellulose, and cellulose derivatives more broadly, present excellent characteristics for processing graphene inks. These materials have been applied to alternative materials beyond graphene, including multi-walled carbon nanotubes (MWCNTs) and silver nanoparticles (Figure 11.1). Due to the common dispersant system, accelerated development of these inks is enabled, along with the straightforward preparation of stable and homogeneous composite inks. While the materials mentioned thus far are conductors, extending this concept to materials with more diverse electronic functionality offers opportunities for select applications, both entailing standalone

materials and composite systems. Two clear targets for this work are  $\text{MoS}_2$  and  $\text{hBN}$ ,<sup>101</sup> and preliminary work has been performed to demonstrate the generality of the EC-based processing protocol (Figure 11.2). Moreover, beyond these posterchild materials there remains a broad range of 2D chalcogenides,<sup>107</sup> oxides,<sup>120</sup> IV-VI compounds,<sup>118</sup> carbides,<sup>117,119</sup> and more that may prove impactful. The ability to translate processing methods developed for graphene to alternative materials would accelerate their development by incorporating them into an established framework and open opportunities for material integration.

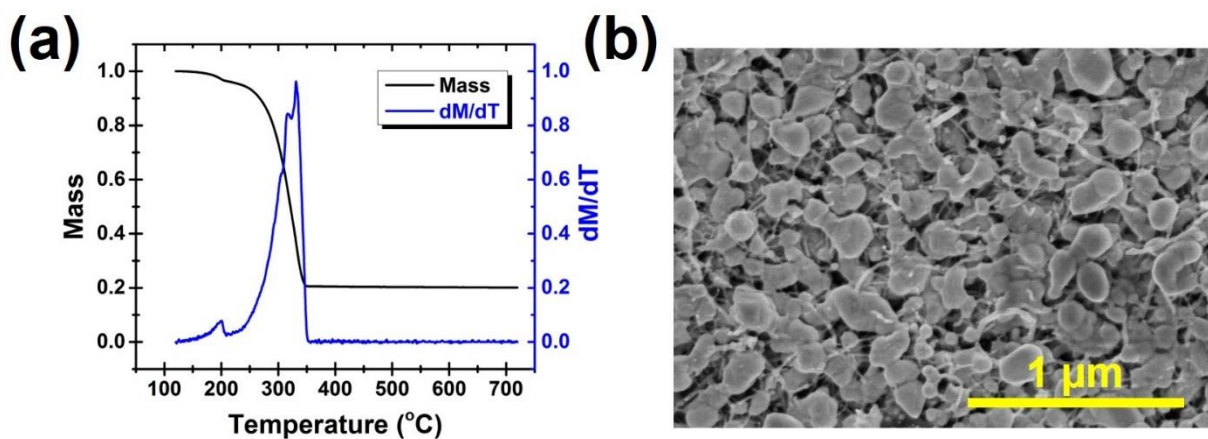


**Figure 11.1.** Processing conductive nanomaterials with ethyl cellulose. (a) Thermal gravimetric analysis data for a silver nanoparticle/EC composite, showing ~20% wt. silver nanoparticles with minimal EC residue. (b) SEM image of a composite silver nanoparticle/MWCNT film following annealing, showing homogeneous dispersion of the materials enabled by a common polymer dispersant, EC.

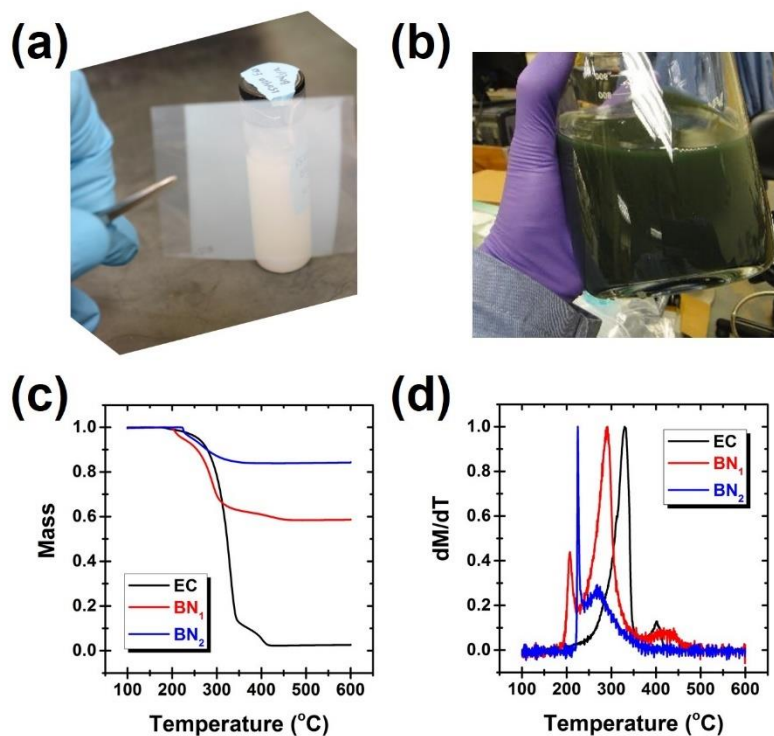


**Figure 11.2.** Extending processing methods to post-graphene 2D nanomaterials. (a) Photograph of a spray coated thin film of hBN held in front of the ink vial. (b) Photograph of an exfoliated MoS<sub>2</sub> dispersion with EC. (c,d) TGA data for hBN/EC powders, including the mass curve and mass derivative, respectively.

One thing to note is that, in preliminary work with post-graphene 2D nanomaterials, the exfoliation yield of thin flakes is substantially lower. In practice, this leads to relaxed centrifugation conditions and a retention of thicker flakes in the sample to improve yield. While this provides reasonable quantities of material for ink development and experiments, the thicker distribution of particles likely has some downstream tradeoffs, for example in ink colloidal stability, film packing/uniformity and exposed surface area. As a result, improvements in the exfoliation process, such as pre-processing steps to facilitate exfoliation of thinner, high aspect ratio flakes, would likely have substantial downstream benefits in processing and applications.

Beyond leveraging the same class of polymers for 2D crystals such as hBN and MoS<sub>2</sub> inks, another research area drawing inspiration from graphene is in the use of synergistic ink binders or additives. A key of EC is its multiple functions, as dispersant, rheology modifier, binder, and, following partial decomposition, modifier of the mechanical and electrical connections between flakes in thin films. However, the carbonaceous residue that is highly effective for conductive graphene films is not necessarily desirable for hBN and MoS<sub>2</sub> films offering complementary functionality. As a result, this final purpose of EC, namely the synergistic residue, could be more effectively fulfilled with different ink additives. For hBN processing, for example, boron oxide (B<sub>2</sub>O<sub>3</sub>) can act as a sintering aide at high temperatures, potentially strengthening hBN structures following high temperature treatment.<sup>282</sup> For MoS<sub>2</sub>, several chemical precursors have been introduced for synthesis of MoS<sub>2</sub>. One example is ammonium tetrathiomolybdate, (NH<sub>4</sub>)<sub>2</sub>MoS<sub>4</sub>.<sup>283</sup> Following thermal treatment at 600 °C or higher, this salt undergoes a series of reactions to produce MoS<sub>2</sub>. Such high temperatures could potentially be achieved by photonic annealing, and a composite film of clean MoS<sub>2</sub> flakes with (NH<sub>4</sub>)<sub>2</sub>MoS<sub>4</sub> could absorb light strongly.<sup>284</sup> Moreover, in such a composite system the amount of MoS<sub>2</sub> growth from the precursor salt would need to be minimal, only enough to bridge flakes, and would be templated by the surrounding crystalline MoS<sub>2</sub>. Compared to the reported case where this salt is used to grow MoS<sub>2</sub> from scratch over a large area, this would present considerably relaxed process and performance requirements.

### 11.3. Expanded Processing Beyond Printed Electronics

Throughout this thesis, the unique benefits of processing graphene with EC and related polymers has been leveraged for printed electronics. In this capacity, the excellent solution-

processing characteristics of polymers are exploited to utilize the functional properties of graphene. This general framework can be extended beyond printed electronics and graphene inks. There is a rich variety of polymer processing methods that could potentially be leveraged for graphene, offering processing advantages for unique forms and microstructures that maintain the functional benefits of graphene. Polymer processing of graphene would not be merely a straightforward extension of traditional methods, due to the unique rheology imposed by graphene flakes in high concentration, and this framework would also lead to applications distinct from traditional polymers.

A variety of polymer processing methods could in principle be modified for graphene/polymer composites. For tailoring the microstructure of graphene films/materials, phase inversion techniques could be developed that leverage the well-defined solubility of the associated polymer.<sup>285,286</sup> Phase inversion commonly exploits changes in temperature or solvent environment to drive a system into an unstable phase space, in which phase segregation spontaneously occurs (Figure 11.3).<sup>287,288</sup> This can lead to controlled void formation and microstructure tuning, and is a widely used technique industrially with an extensive history and body of knowledge.<sup>289</sup> Integrating novel materials, such as graphene and post-graphene 2D nanomaterials, with established methods such as this provides clear merit and opportunities for fundamental work.<sup>290</sup> Another class of methods for controlling microstructure is the family of foam fabrication methods. Similar to phase inversion, these methods have an extensive history with significant practical interest, and would present an interesting platform to understand the effects of graphene during such processes and the resulting functional properties.



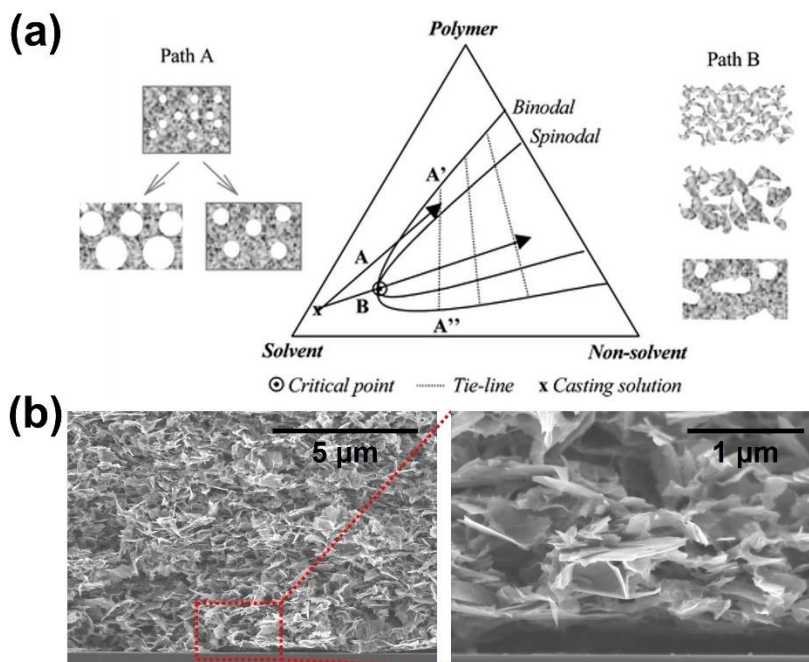


**Figure 11.3.** Phase inversion for morphology control. (a) Schematic explanation of the phase inversion process based on a ternary phase diagram, adapted from Ref. 287. (b) SEM images of graphene/EC films cast using a phase inversion process to induce porosity.

An additional set of polymer processing methods that could potentially leverage highly-loaded graphene composites involves melt processing. Ethyl cellulose is a thermoplastic material, and at fairly low graphene content graphene/EC composites have shown a tendency to melt. Controlling this process could allow the integration of graphene in traditional melt processing methods, such as fused deposition modeling (FDM), a common variant of 3D printing. Similarly, laser printing, or xerographic printing, commonly utilizes powders with a thermoplastic polymer for 2D patterning, and could present an interesting target for the integration of graphene, provided control over surface charging could be obtained by tailoring the graphene/EC ratio.

Fiber spinning also presents opportunities for integration of graphene in several forms. Wet spinning leverages a phase inversion process to produce fibers with controlled microstructure.<sup>291</sup>

Draw spinning of solvent-based inks,<sup>292</sup> electrospinning,<sup>293–295</sup> solution blow spinning,<sup>296,297</sup> or potentially melt spinning could also be utilized. Solution blow spinning is a particularly promising method for laboratory experiments, in that it requires only low cost equipment, offers a simplified process for streamlined optimization and straightforward scale-up, and does not entail potential hazards such as high temperatures or voltages.<sup>298–300</sup> While graphene oxide has been demonstrated for some of these techniques due to its prevalence and ease of manufacture/processing,<sup>301–304</sup> if these methods could be developed for graphene/EC inks they could presumably translate to hBN, MoS<sub>2</sub> or additional materials, offering greater novelty and scientific value.

For the more versatile development of graphene/polymer composites for polymer processing, a key factor is the molecular weight of the polymer. This will control the polymer-like character of the composite for process integration. Therefore, more fundamental investigation and materials development for graphene composites with different molecular weights is recommended as a supporting component for these future studies.

#### **11.4. Fundamental Investigation Utilizing Versatile Process Control**

A third broad thrust for future work involves more careful, fundamental characterization. The graphene/EC system has unique characteristics, in that it has a graphene loading significantly higher than traditional composites but remains well dispersed. The broad process control, including particle size, graphene:EC ratio, and EC molecular weight, would allow for careful studies of fundamental science in similar systems. This could include electrical and mechanical properties (ie, percolation, decoupling electrical effects of the matrix and particles), along with processing characteristics (ie, rheology, glass transition point). Importantly, while almost all work

to date has focused on the graphene, there has been little direct study of the effect of graphene on the polymer. Adsorption on the graphene surface, and confinement between graphene flakes, presumably impacts the mechanical response and thermochemical properties of the polymer. As alluded to above, in depth rheological characterization of graphene/EC dispersions or melts would be instrumental to controllable process development. The rich variety of rheological methods could also offer a valuable tool for characterizing interactions between graphene and EC.

In depth mechanical characterization of graphene using this processing framework would also offer practical benefits. In particular, the interesting result of adding NC to graphene inks has been discussed in detail in Chapter 6.<sup>74</sup> The mechanical characterization in this study was largely limited to the Scotch™ tape test, but more direct and quantitative characterization of mechanical properties is highly desired, such as nanoindentation testing or measurements on freestanding films. Understanding the mechanical response is critical for rational integration in practical applications, within printed electronics and especially for free-standing or microstructured forms beyond printed electronics. Some examples include cantilevers, such as MEMS-based microcantilever sensors,<sup>305</sup> and durability of porous films and foams. If broader use of the research in this thesis is expected, it is recommended that such detailed fundamental characterization is carried out, both for scientific and practical interest.

Another area that has had limited characterization to date and merits further study is the interface of graphene with biological materials. Graphene offers advantages for applications in bio-integrated electronics, such as stability in biological media, nontoxicity in certain forms, and flexibility.<sup>306,307</sup> Because of these, and the strengthening push towards bioelectronics, understanding the interaction of graphene patterns using the framework described here with

biological materials and environments would be valuable. Practical applications to guide this investigation could include biosensors,<sup>308</sup> neural electrodes,<sup>309,310</sup> and on-skin biomedical monitoring. Moreover, interest in broader applications of the graphene/EC system would benefit from detailed characterization of associated hazards.

A final topic for more fundamental study with practical outcomes is controlled doping of solution-processed graphene films. As a semimetal, graphene can in principle be doped to tailor electronic properties. There have been extensive studies regarding this for single-layer graphene, including micromechanically exfoliated and CVD-grown samples.<sup>311</sup> For solution-processed materials, heteroatom doping of RGO has been demonstrated many times, for energy storage and sensing, among other applications.<sup>312</sup> Systematic studies of doping in printed graphene films based on the graphene inks presented here would be useful for tailoring electronic interfaces with other materials, a common feature of the demonstrated practical applications in Chapters 8-10. One speculative note which could offer generality to other applications comes from the study of graphene contacts for InGaZnO presented in Chapter 8. In this application, qualitatively different performance was observed for top-contact and bottom-contact devices.<sup>313</sup> One potential explanation for this is the plasma treatment of graphene electrodes during bottom-contact device fabrication. In particular, exposure to nitrogen or oxygen plasma could possibly shift the work function of graphene to align more or less favorably with the InGaZnO.<sup>314,315</sup> If this could be carefully studied and controlled, i.e., by a simple plasma treatment with a controlled atmosphere, power, and duration, it could benefit applications of graphene as an engineered interfacial material more broadly.

### **11.5. Summary of Future Work**

The research presented in this thesis offers many opportunities for meaningful follow-up work of both academic and practical interest. Several promising routes for further investigation have been outline briefly here, and are organized into three broad categories: translating the materials, methods, and concepts developed here to alternative materials; leveraging the processing platform for graphene inks to integrate graphene more broadly in polymer processing frameworks; and studying more fundamental characteristics of the system to fine-tune and understand properties – electronic and biological interfaces, as well as mechanical and rheological effects – in order to more rationally incorporate graphene, and other materials based on this platform, into a variety of multifunctional applications. Overall, the research constituting this thesis has generated more questions than answers, and leaves many promising routes for future work built on the knowledge, materials, and methods discussed here.

## **CHAPTER TWELVE**

Summary and Outlook

## 12.1. Summary of Thesis Research

The research discussed in this thesis describes a compelling platform for graphene ink development for integration in printed electronics. By using a class of cellulosic polymers as multifunctional graphene dispersants, a combination of process versatility, simplified ink formulation, and competitive performance metrics is realized. This represents an advance in the field of graphene inks, and materials and methods developed and demonstrated during this research have been adopted more broadly in the community in recent years.

Printed electronics represents a compelling manufacturing framework for high-throughput or custom fabrication of advanced electronic devices with novel functionality and cost-performance tradeoffs compared to traditional silicon electronics. By leveraging additive, liquid-phase patterning methods, this strategy enables large-area, flexible devices with broad materials compatibility. A key bottleneck in the advancement of printed electronics is the development of a diverse palette of functional liquid inks based on high performance materials, particularly nanomaterials offering suitable colloidal stability. Graphene is a promising material for a range of printed electronics applications, offering good electrical conductivity, flexibility, and robust mechanical, chemical, and environmental stability. However, the design of suitable graphene-based inks combining dispersion stability, versatility in ink formulation, precision patterning, and competitive performance metrics presents a significant technical challenge at the core of this thesis.

Chapter 1 outlines the general field of printed electronics, with the necessary background information and context to frame the research, including a specific focus on graphene inks. A diverse suite of printing methods is presented for patterning of functional materials, motivating the

technical capability to tailor inks to different methods for generality. This requires broad control over ink fluid properties and solvent systems, particularly the ink rheology, capillarity, and evaporation kinetics, along with excellent colloidal stability. By exploiting the favorable solution-phase processing characteristics of polymers, graphene inks can be developed with suitable control over ink formulation, and a promising class of such inks is the focus of this work. Chapters 2-7 detail the basic processing and material advances underlying this research, Chapters 8-10 explore applications of the graphene inks, and Chapter 11 discusses future work building off this foundation.

Chapter 2 outlines the basic processing framework for graphene inks stabilized by ethyl cellulose (EC). This chapter details the general experimental procedure used in this research for graphene production, based on exfoliation, centrifugation, and flocculation. It also establishes the baseline properties of the graphene/EC system regarding thermal annealing, conductivity, and morphology, providing important context for the subsequent work.

Chapters 3 and 4 extend the graphene/EC ink formulation framework to gravure and screen printing, respectively. The combination of excellent colloidal stability, tunable viscosity, and bottom-up ink development allow straightforward translation of the materials and methods in Chapter 2 to these higher throughput printing methods, an important advance towards generality and commercial applications. Notably, neither of these methods had been demonstrated with pristine graphene inks prior to this work.

In Chapter 5, the thermal annealing requirement of the graphene/EC inks is addressed. Annealing at 250-300 °C allows application of the graphene inks on select plastic substrates, such as polyimide, but restricts integration with thermally sensitive materials such as PET and PEN.



Photonic annealing is demonstrated for rapid annealing of the graphene/EC inks on a wide range of substrates, including PET and PEN, offering broader process compatibility and promise for high throughput, roll-to-roll manufacturing.

Chapters 6 and 7 explore the translation of the graphene processing framework to an alternative cellulose derivative, nitrocellulose (NC). Chapter 6 details the modified graphene production and ink formulation procedures, along with unique and intriguing properties resulting from thermal annealing. In particular, charring of the NC leaves amorphous carbon residue in the graphene film, which serves to improve mechanical connectivity for enhanced durability. In Chapter 7, the application of photonic annealing to the graphene/NC system is discussed, for which the rapid and exothermic decomposition of NC leads to unique process and performance characteristics.

Chapters 8-10 explore several applications of the graphene inks in which the unique properties of graphene offer a key functional benefit. In particular, the robust stability of graphene leads to promising performance as a conductive interfacial material, with compatibility across different classes of materials. Chapter 8 describes the use of stable graphene contacts for printed InGaZnO TFTs. By replacing chemically reactive silver electrodes with graphene, proper transistor performance is achieved, along with excellent stability to extreme temperatures and aging. Chapter 9 describes the rational use of graphene as a passivating interfacial material in liquid metal electronics. Gallium-based liquid metals alloy aggressively with other metals, leading to unreliable and unstable electrical connections when interfacing liquid metal electronics with conventional circuits. A thin film of graphene at the interface between liquid and conventional metals prevents alloy formation while offering suitable electrical properties and robust mechanical

and environmental stability. Chapter 10 describes several uses of graphene in organic and electrolytic systems. These include templating the growth of molecular semiconductors; replacing gold for printed source/drain electrodes of organic transistors for foldable, paper-based circuits or high resolution devices; and microsupercapacitor electrodes for printed, flexible energy storage systems. Overall, the various uses of graphene presented here span a wide range of materials systems, and demonstrate the versatility of this material and promise for practical applications.

Chapter 11 outlines possible future work building off the foundation of this thesis research. This is organized into three broad thrusts. First, the materials and strategies developed here for graphene can be translated to alternative nanomaterial inks. Hexagonal boron nitride and molybdenum disulfide are highlighted, as preliminary work shows promise for these systems. In addition to the straightforward extension of cellulosic polymers and liquid-phase processing methods, this thrust includes broader concepts for synergistic binders, in which ink additives can be tailored to improve performance metrics. The second direction is the extension of the graphene/polymer system beyond printed electronics. In particular, the homogeneous dispersion of a very high loading of graphene in a thermoplastic polymer presents a unique system, and exploiting the dispersion capability of the polymer for processing methods beyond printed electronics offers numerous possibilities. The final potential research thrust encompasses a more careful and systematic study of fundamental characteristics of this system. If cellulose derivatives are likely to be applied more broadly for nanomaterial ink development, it serves to better understanding the basic factors influencing electrical, mechanical, biological, and rheological properties. In each case, the excellent process control enables careful studies, which could benefit application development and offer fundamental insight for nanomaterial inks more broadly.

## 12.2. Outlook for Practical Applications

The platform for graphene ink development resulting from this research exhibits reasonable potential for practical applications. Several specific application areas have been addressed explicitly in this thesis, while ongoing or collaborative work beyond the scope of this thesis has spanned applications in electronics, sensors, batteries,<sup>281</sup> supercapacitors,<sup>82,280</sup> photovoltaics, and thermoelectrics, a testament to the versatility of graphene as a functional material. For translating this technology beyond the academic lab, the graphene production method based on high shear mixing is readily scaled up, and the raw materials are inexpensive and abundant. Moreover, the versatility of the system is promising for tailoring inks and further refining the formulation. To explore the potential demand for graphene inks, graphene/EC inks have been distributed through Sigma Aldrich for several years.<sup>316-318</sup> Sustained demand for these inks, despite their high initial price, supports confidence in the potential for commercial opportunities. As an initial step, a scaled-up graphene production system has been designed and assembled to better understand the scaling and optimization of exfoliation based on shear mixing. This system, pictured in Figure 12.1, allows graphene production with the ethanol/EC system in a 20 L batch volume, a factor of 100x greater than the original graphene batch volume at the onset of this work. Promising preliminary results support ongoing research using graphene/EC, and provide key knowledge to guide further scale-up and price reduction targets for possible commercial applications. While the ultimate translation of this research beyond the laboratory will require clear market demand and sustained effort, the research presented in this thesis offers a strong foundation.

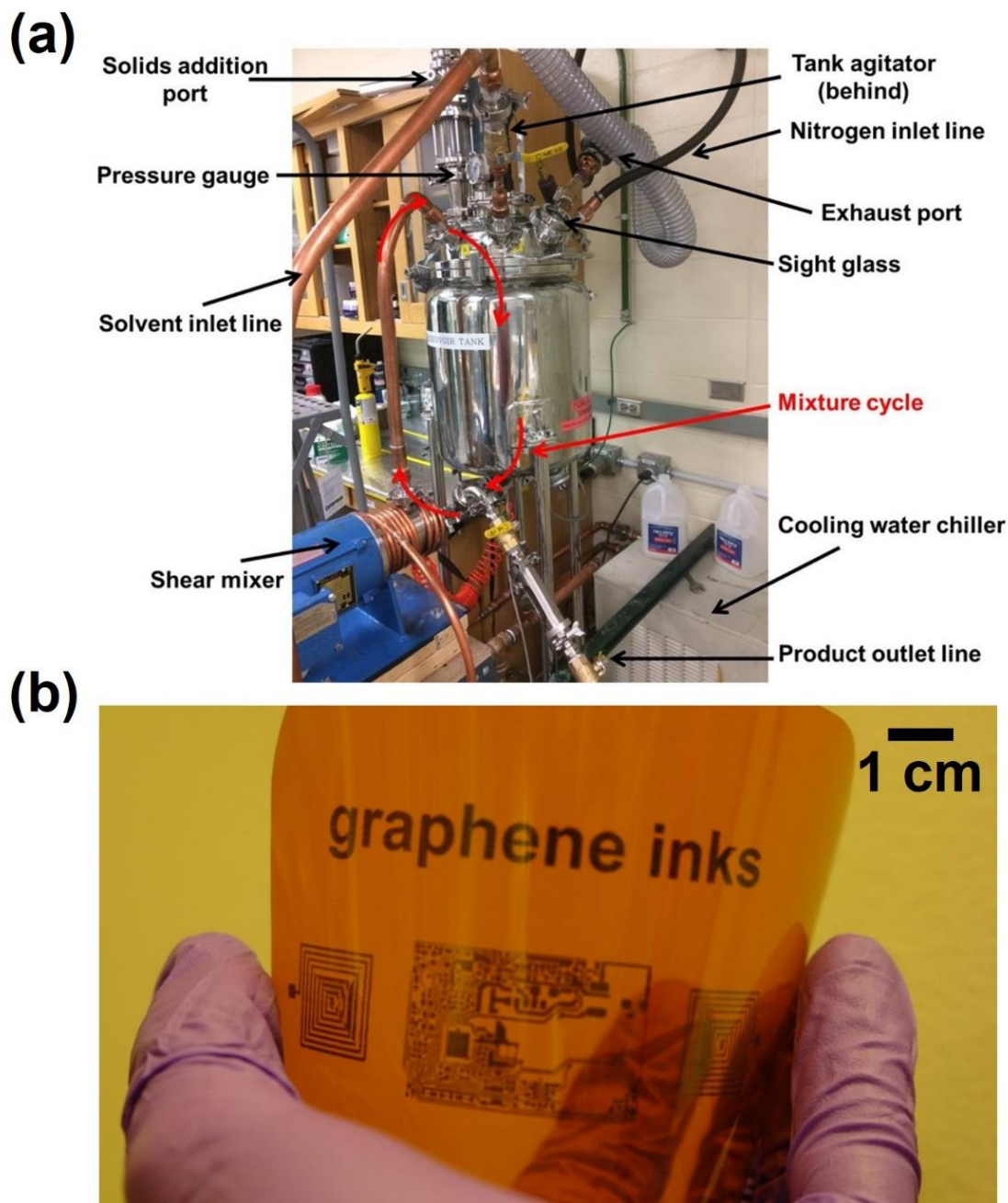


**Figure 12.1.** Scaling production of graphene inks for large-area flexible electronics. (a) Photograph of a closed-loop system for graphene exfoliation based on high shear mixing. (b) Photograph of large area inkjet-printed graphene patterns.

## REFERENCES

- (1) Arias, A. C.; MacKenzie, J. D.; McCulloch, I.; Rivnay, J.; Salleo, A. Materials and Applications for Large Area Electronics: Solution-Based Approaches. *Chem. Rev.* **2010**, *110*, 3–24.
- (2) Lupo, D.; Clemens, W.; Breitung, S.; Hecker, K. Applications of Organic and Printed Electronics. In *Applications of Organic and Printed Electronics: A Technology-Enabled Revolution*; Cantatore, E., Ed.; Springer US: Boston, MA, 2013; pp. 1–26.
- (3) Nathan, A.; Ahnood, A.; Cole, M. T.; Suzuki, Y.; Hiralal, P.; Bonaccorso, F.; Hasan, T.; Garcia-Gancedo, L.; Dyadyusha, A.; Haque, S.; *et al.* Flexible Electronics: The Next Ubiquitous Platform. *Proc. IEEE* **2012**, *100*, 1486–1517.
- (4) Azzellino, G.; Grimoldi, A.; Binda, M.; Caironi, M.; Natali, D.; Sampietro, M. Fully Inkjet-Printed Organic Photodetectors with High Quantum Yield. *Adv. Mater.* **2013**, *25*, 6829–6833.
- (5) Jang, J.; Ha, J.; Cho, J. Fabrication of Water-Dispersible Polyaniline-Poly(4-Styrenesulfonate) Nanoparticles for Inkjet-Printed Chemical-Sensor Applications. *Adv. Mater.* **2007**, *19*, 1772–1775.
- (6) Sokolov, A. N.; Roberts, M. E.; Bao, Z. Fabrication of Low-Cost Electronic Biosensors. *Mater. Today* **2009**, *12*, 12–20.
- (7) Ng, T. N.; Schwartz, D. E.; Lavery, L. L.; Whiting, G. L.; Russo, B.; Krusor, B.; Veres, J.; Bröms, P.; Herlogsson, L.; Alam, N.; *et al.* Scalable Printed Electronics: An Organic Decoder Addressing Ferroelectric Non-Volatile Memory. *Sci. Rep.* **2012**, *2*, 585.
- (8) Subramanian, V.; Fréchet, J. M. J.; Chang, P. C.; Member, S.; Huang, D. C.; Lee, J. B.; Molesa, S. E.; Murphy, A. R.; Redinger, D. R.; Volkman, S. K. Progress Toward Development of All-Printed RFID Tags: Materials, Processes, and Devices. *Proc. IEEE* **2005**, *93*, 1330–1338.
- (9) Wood, V.; Panzer, M. J.; Chen, J.; Bradley, M. S.; Halpert, J. E.; Bawendi, M. G.; Bulović, V. Inkjet-Printed Quantum Dot-Polymer Composites for Full-Color AC-Driven Displays. *Adv. Mater.* **2009**, *21*, 2151–2155.
- (10) Rogers, J.; Bao, Z.; Baldwin, K.; Dodabalapur, A.; Crone, B.; Raju, V. R.; Kuck, V.; Katz, H.; Amundson, K.; Ewing, J.; *et al.* Paper-like Electronic Displays: Large-Area Rubber-Stamped Plastic Sheets of Electronics and Microencapsulated Electrophoretic Inks. *Proc. Natl. Acad. Sci. U. S. A.* **2001**, *98*, 4835–4840.

- (11) Hoth, C. N.; Choulis, S. A.; Schilinsky, P.; Brabec, C. J. High Photovoltaic Performance of Inkjet Printed Polymer:Fullerene Blends. *Adv. Mater.* **2007**, *19*, 3973–3978.
- (12) Gaikwad, A. M.; Whiting, G. L.; Steingart, D. A.; Arias, A. C. Highly Flexible, Printed Alkaline Batteries Based on Mesh-Embedded Electrodes. *Adv. Mater.* **2011**, *23*, 3251–3255.
- (13) Zhan, Y.; Mei, Y.; Zheng, L. Materials Capability and Device Performance in Flexible Electronics for the Internet of Things. *J. Mater. Chem. C* **2014**, *2*, 1220–1232.
- (14) Fukuda, K.; Someya, T. Recent Progress in the Development of Printed Thin-Film Transistors and Circuits with High-Resolution Printing Technology. *Adv. Mater.* **2016**, DOI: 10.1002/adma.201602736.
- (15) Frisbie, C. D. Roll-to-Roll, High Speed Printing of Multi-Functional, Distributed Sensor Networks for Enhancing the Brain-Machine Interface, **2011**.
- (16) Jang, D.; Kim, D.; Moon, J. Influence of Fluid Physical Properties on Ink-Jet Printability. *Langmuir* **2009**, *25*, 2629–2635.
- (17) Derby, B. Inkjet Printing of Functional and Structural Materials: Fluid Property Requirements, Feature Stability, and Resolution. *Annu. Rev. Mater. Res.* **2010**, *40*, 395–414.
- (18) Lee, A.; Sudau, K.; Ahn, K. H.; Lee, S. J.; Willenbacher, N. Optimization of Experimental Parameters to Suppress Nozzle Clogging in Inkjet Printing. *Ind. Eng. Chem. Res.* **2012**, *51*, 13195–13204.
- (19) Stringer, J.; Derby, B. Formation and Stability of Lines Produced by Inkjet Printing. *Langmuir* **2010**, *26*, 10365–10372.
- (20) Duineveld, P. C. The Stability of Ink-Jet Printed Lines of Liquid with Zero Receding Contact Angle on a Homogeneous Substrate. *J. Fluid Mech.* **2003**, *477*, 175–200.
- (21) de Gans, B.-J.; Schubert, U. S. Inkjet Printing of Well-Defined Polymer Dots and Arrays. *Langmuir* **2004**, *20*, 7789–7793.
- (22) Soltman, D.; Subramanian, V. Inkjet-Printed Line Morphologies and Temperature Control of the Coffee Ring Effect. *Langmuir* **2008**, *24*, 2224–2231.
- (23) Tekin, E.; de Gans, B.-J.; Schubert, U. S. Ink-Jet Printing of Polymers - from Single Dots to Thin Film Libraries. *J. Mater. Chem.* **2004**, *14*, 2627.

- (24) Kamyshny, A.; Magdassi, S. Conductive Nanomaterials for Printed Electronics. *Small* **2014**, *10*, 3515–3535.
- (25) Ortiz, P.; Facchetti, A.; Marks, T. J. High- $\kappa$  Organic, Inorganic, and Hybrid Dielectrics for Low-Voltage Organic Field-Effect Transistors. *Chem. Rev.* **2010**, *110*, 205–239.
- (26) Yu, X.; Marks, T. J.; Facchetti, A. Metal Oxides for Optoelectronic Applications. *Nat. Mater.* **2016**, *15*, 383–396.
- (27) Chen, K.; Gao, W.; Emaminejad, S.; Kiriya, D.; Ota, H.; Nyein, H. Y. Y.; Takei, K.; Javey, A. Printed Carbon Nanotube Electronics and Sensor Systems. *Adv. Mater.* **2016**, *28*, 4397–4414.
- (28) Rouhi, N.; Jain, D.; Burke, P. J. High-Performance Semiconducting Nanotube Inks: Progress and Prospects. *ACS Nano* **2011**, *5*, 8471–8487.
- (29) Perelaer, J.; Smith, P. J.; Mager, D.; Soltman, D.; Volkman, S. K.; Subramanian, V.; Korvink, J. G.; Schubert, U. S. Printed Electronics: The Challenges Involved in Printing Devices, Interconnects, and Contacts Based on Inorganic Materials. *J. Mater. Chem.* **2010**, *20*, 8446.
- (30) Walker, S. B.; Lewis, J. A. Reactive Silver Inks for Patterning High-Conductivity Features at Mild Temperatures. *J. Am. Chem. Soc.* **2012**, *134*, 1419–1421.
- (31) Khan, Y.; Pavinatto, F. J.; Lin, M. C.; Liao, A.; Swisher, S. L.; Mann, K.; Subramanian, V.; Maharbiz, M. M.; Arias, A. C. Inkjet-Printed Flexible Gold Electrode Arrays for Bioelectronic Interfaces. *Adv. Funct. Mater.* **2016**, *26*, 1004–1013.
- (32) Kang, H.; Sowade, E.; Baumann, R. R. Direct Intense Pulsed Light Sintering of Inkjet-Printed Copper Oxide Layers within Six Milliseconds. *ACS Appl. Mater. Interfaces* **2014**, *6*, 1682–1687.
- (33) Kim, H.-S.; Dhage, S. R.; Shim, D.-E.; Hahn, H. T. Intense Pulsed Light Sintering of Copper Nanoink for Printed Electronics. *Appl. Phys. A* **2009**, *97*, 791–798.
- (34) Schroder, K. A. Mechanisms of Photonic Curing<sup>TM</sup>: Processing High Temperature Films on Low Temperature Substrates. *Technical Proceedings of the 2011 NSTI Nanotechnology Conference and Trade Show* **2011**, *2*, 220–223.
- (35) Schroder, K. A.; McCool, S. C.; Furlan, W. F. Broadcast Photonic Curing of Metallic Nanoparticle Films. *Technical Proceedings of the 2006 NSTI Nanotechnology Conference and Trade Show* **2006**, *3*, 198–201.

- (36) Crispin, X.; Jakobsson, F. L. E.; Crispin, A.; Grim, P. C. M.; Andersson, P.; Volodin, A.; van Haesendonck, C.; Van der Auweraer, M.; Salaneck, W. R.; Berggren, M. The Origin of the High Conductivity of Poly(3,4-ethylenedioxythiophene)–Poly(styrenesulfonate) (PEDOT–PSS) Plastic Electrodes. *Chem. Mater.* **2006**, *18*, 4354–4360.
- (37) Hu, B.; Li, D.; Ala, O.; Manandhar, P.; Fan, Q.; Kasilingam, D.; Calvert, P. D. Textile-Based Flexible Electroluminescent Devices. *Adv. Funct. Mater.* **2011**, *21*, 305–311.
- (38) Secor, E. B.; Hersam, M. C. Emerging Carbon and Post-Carbon Nanomaterial Inks for Printed Electronics. *J. Phys. Chem. Lett.* **2015**, *6*, 620–626.
- (39) Yang, W.; Wang, C. Graphene and the Related Conductive Inks for Flexible Electronics. *J. Mater. Chem. C* **2016**, *4*, 7193–7207.
- (40) Novoselov, K. S.; Geim, A. K.; Morozov, S. V.; Jiang, D.; Zhang, Y.; Dubonos, S. V.; Grigorieva, I. V.; Firsov, A. A. Electric Field Effect in Atomically Thin Carbon Films. *Science* **2004**, *306*, 666–669.
- (41) Novoselov, K. S.; Fal'ko, V. I.; Colombo, L.; Gellert, P. R.; Schwab, M. G.; Kim, K. A Roadmap for Graphene. *Nature* **2012**, *490*, 192–200.
- (42) Castro Neto, A. H.; Peres, N. M. R.; Novoselov, K. S.; Geim, A. K. The Electronic Properties of Graphene. *Rev. Mod. Phys.* **2009**, *81*, 109–162.
- (43) Balandin, A. A.; Ghosh, S.; Bao, W.; Calizo, I.; Teweldebrhan, D.; Miao, F.; Lau, C. N. Superior Thermal Conductivity of Single-Layer Graphene. *Nano Lett.* **2008**, *8*, 902–907.
- (44) Lee, C.; Wei, X.; Kysar, J. W.; Hone, J. Measurement of the Elastic Properties and Intrinsic Strength of Monolayer Graphene. *Science* **2008**, *321*, 385–388.
- (45) Schwierz, F. Graphene Transistors. *Nat. Nanotechnol.* **2010**, *5*, 487–496.
- (46) Stoller, M. D.; Park, S.; Zhu, Y.; An, J.; Ruoff, R. S. Graphene-Based Ultracapacitors. *Nano Lett.* **2008**, *8*, 3498–3502.
- (47) Schedin, F.; Geim, A. K.; Morozov, S. V.; Hill, E. W.; Blake, P.; Katsnelson, M. I.; Novoselov, K. S. Detection of Individual Gas Molecules Adsorbed on Graphene. *Nat. Mater.* **2007**, *6*, 652–655.
- (48) Stankovich, S.; Dikin, D. A.; Dommett, G. H. B.; Kohlhaas, K. M.; Zimney, E. J.; Stach, E. A.; Piner, R. D.; Nguyen, S. T.; Ruoff, R. S. Graphene-Based Composite Materials. *Nature* **2006**, *442*, 282–286.



- (49) Emtsev, K. V.; Bostwick, A.; Horn, K.; Jobst, J.; Kellogg, G. L.; Ley, L.; McChesney, J. L.; Ohta, T.; Reshanov, S. A.; Röhrl, J.; *et al.* Towards Wafer-Size Graphene Layers by Atmospheric Pressure Graphitization of Silicon Carbide. *Nat. Mater.* **2009**, *8*, 203–207.
- (50) Li, X.; Cai, W.; An, J.; Kim, S.; Nah, J.; Yang, D.; Piner, R.; Velamakanni, A.; Jung, I.; Tutuc, E.; *et al.* Large-Area Synthesis of High-Quality and Uniform Graphene Films on Copper Foils. *Science* **2009**, *324*, 1312–1314.
- (51) Choucair, M.; Thordarson, P.; Stride, J. A. Gram-Scale Production of Graphene Based on Solvothermal Synthesis and Sonication. *Nat. Nanotechnol.* **2009**, *4*, 30–33.
- (52) Hernandez, Y.; Nicolosi, V.; Lotya, M.; Blighe, F. M.; Sun, Z.; De, S.; McGovern, I. T.; Holland, B.; Byrne, M.; Gun'ko, Y. K.; *et al.* High-Yield Production of Graphene by Liquid-Phase Exfoliation of Graphite. *Nat. Nanotechnol.* **2008**, *3*, 563–568.
- (53) Stankovich, S.; Dikin, D. A.; Piner, R. D.; Kohlhaas, K. A.; Kleinhammes, A.; Jia, Y.; Wu, Y.; Nguyen, S. T.; Ruoff, R. S. Synthesis of Graphene-Based Nanosheets via Chemical Reduction of Exfoliated Graphite Oxide. *Carbon* **2007**, *45*, 1558–1565.
- (54) Ciesielski, A.; Samorì, P. Graphene via Sonication Assisted Liquid-Phase Exfoliation. *Chem. Soc. Rev.* **2014**, *43*, 381–398.
- (55) Gómez-Navarro, C.; Weitz, R. T.; Bittner, A. M.; Scolari, M.; Mews, A.; Burghard, M.; Kern, K. Electronic Transport Properties of Individual Chemically Reduced Graphene Oxide Sheets. *Nano Lett.* **2007**, *7*, 3499–3503.
- (56) Mao, S.; Pu, H.; Chen, J. Graphene Oxide and Its Reduction: Modeling and Experimental Progress. *RSC Adv.* **2012**, *2*, 2643.
- (57) Hernandez, Y.; Lotya, M.; Rickard, D.; Bergin, S. D.; Coleman, J. N. Measurement of Multicomponent Solubility Parameters for Graphene Facilitates Solvent Discovery. *Langmuir* **2010**, *26*, 3208–3213.
- (58) Khan, U.; O'Neill, A.; Porwal, H.; May, P.; Nawaz, K.; Coleman, J. N. Size Selection of Dispersed, Exfoliated Graphene Flakes by Controlled Centrifugation. *Carbon* **2012**, *50*, 470–475.
- (59) Khan, U.; Porwal, H.; O'Neill, A.; Nawaz, K.; May, P.; Coleman, J. N. Solvent-Exfoliated Graphene at Extremely High Concentration. *Langmuir* **2011**, *27*, 9077–9082.

- (60) Lotya, M.; Hernandez, Y.; King, P. J.; Smith, R. J.; Nicolosi, V.; Karlsson, L. S.; Blighe, F. M.; De, S.; Wang, Z.; McGovern, I. T.; *et al.* Liquid Phase Production of Graphene by Exfoliation of Graphite in Surfactant/Water Solutions. *J. Am. Chem. Soc.* **2009**, *131*, 3611–3620.
- (61) Green, A. A.; Hersam, M. C. Solution Phase Production of Graphene with Controlled Thickness via Density Differentiation. *Nano Lett.* **2009**, *9*, 4031–4036.
- (62) Liang, Y. T.; Hersam, M. C. Highly Concentrated Graphene Solutions via Polymer Enhanced Solvent Exfoliation and Iterative Solvent Exchange. *J. Am. Chem. Soc.* **2010**, *132*, 17661–17663.
- (63) Bracamonte, M. V.; Lacconi, G. I.; Urreta, S. E.; Torres, L. E. F. F. On the Nature of Defects in Liquid-Phase Exfoliated Graphene. *J. Phys. Chem. C* **2014**, *118*, 15455–15459.
- (64) Knieke, C.; Berger, A.; Voigt, M.; Taylor, R. N. K.; Röhl, J.; Peukert, W. Scalable Production of Graphene Sheets by Mechanical Delamination. *Carbon* **2010**, *48*, 3196–3204.
- (65) Su, C.-Y.; Lu, A.-Y.; Xu, Y.; Chen, F.-R.; Khlobystov, A. N.; Li, L.-J. High-Quality Thin Graphene Films from Fast Electrochemical Exfoliation. *ACS Nano* **2011**, *5*, 2332–2339.
- (66) Paton, K. R.; Varrla, E.; Backes, C.; Smith, R. J.; Khan, U.; O'Neill, A.; Boland, C.; Lotya, M.; Istrate, O. M.; King, P.; *et al.* Scalable Production of Large Quantities of Defect-Free Few-Layer Graphene by Shear Exfoliation in Liquids. *Nat. Mater.* **2014**, *13*, 624–630.
- (67) Karagiannidis, P. G.; Hodge, S. A.; Lombardi, L.; Tomarchio, F.; Decorde, N.; Milana, S.; Goykhman, I.; Su, Y.; Mesite, S. V.; Johnstone, D. N.; *et al.* Microfluidization of Graphite and Formulation of Graphene-Based Conductive Inks. *ACS Nano* **2017**, *11*, 2742–2755.
- (68) Torrisi, F.; Hasan, T.; Wu, W.; Sun, Z.; Lombardo, A.; Kulmala, T. S.; Hsieh, G.-W.; Jung, S.; Bonaccorso, F.; Paul, P. J.; *et al.* Inkjet-Printed Graphene Electronics. *ACS Nano* **2012**, *6*, 2992–3006.
- (69) Finn, D.; Lotya, M.; Cunningham, G.; Smith, R.; McCloskey, D.; Donegan, J.; Coleman, J. N. Inkjet Deposition of Liquid-Exfoliated Graphene and MoS<sub>2</sub> Nanosheets for Printed Device Applications. *J. Mater. Chem. C* **2014**, *2*, 925–932.
- (70) Secor, E. B.; Prabhurashi, P. L.; Puntambekar, K.; Geier, M. L.; Hersam, M. C. Inkjet Printing of High Conductivity, Flexible Graphene Patterns. *J. Phys. Chem. Lett.* **2013**, *4*, 1347–1351.

- (71) Li, J.; Ye, F.; Vaziri, S.; Muhammed, M.; Lemme, M. C.; Östling, M. Efficient Inkjet Printing of Graphene. *Adv. Mater.* **2013**, *25*, 3985–3992.
- (72) Gao, Y.; Shi, W.; Wang, W.; Leng, Y.; Zhao, Y. Inkjet Printing Patterns of Highly Conductive Pristine Graphene on Flexible Substrates. *Ind. Eng. Chem. Res.* **2014**, *53*, 16777–16784.
- (73) Majee, S.; Song, M.; Zhang, S.-L.; Zhang, Z.-B. Scalable Inkjet Printing of Shear-Exfoliated Graphene Transparent Conductive Films. *Carbon* **2016**, *102*, 51–57.
- (74) Secor, E. B.; Gao, T. Z.; Islam, A. E.; Rao, R.; Wallace, S. G.; Zhu, J.; Putz, K. W.; Maruyama, B.; Hersam, M. C. Enhanced Conductivity, Adhesion, and Environmental Stability of Printed Graphene Inks with Nitrocellulose. *Chem. Mater.* **2017**, *29*, 2332–2340.
- (75) Majee, S.; Liu, C.; Wu, B.; Zhang, S.-L.; Zhang, Z.-B. Ink-Jet Printed Highly Conductive Pristine Graphene Patterns Achieved with Water-Based Ink and Aqueous Doping Processing. *Carbon* **2017**, *114*, 77–83.
- (76) Secor, E. B.; Lim, S.; Zhang, H.; Frisbie, C. D.; Francis, L. F.; Hersam, M. C. Gravure Printing of Graphene for Large-Area Flexible Electronics. *Adv. Mater.* **2014**, *26*, 4533–4538.
- (77) Hyun, W. J.; Secor, E. B.; Hersam, M. C.; Frisbie, C. D.; Francis, L. F. High-Resolution Patterning of Graphene by Screen Printing with a Silicon Stencil for Highly Flexible Printed Electronics. *Adv. Mater.* **2015**, *27*, 109–115.
- (78) Jabari, E.; Toyserkani, E. Micro-Scale Aerosol-Jet Printing of Graphene Interconnects. *Carbon* **2015**, *91*, 321–329.
- (79) Secor, E. B.; Ahn, B. Y.; Gao, T. Z.; Lewis, J. A.; Hersam, M. C. Rapid and Versatile Photonic Annealing of Graphene Inks for Flexible Printed Electronics. *Adv. Mater.* **2015**, *27*, 6683–6688.
- (80) McManus, D.; Vranic, S.; Withers, F.; Sanchez-Romaguera, V.; Macucci, M.; Yang, H.; Sorrentino, R.; Parvez, K.; Son, S.-K.; Iannaccone, G.; *et al.* Water-Based and Biocompatible 2D Crystal Inks for All-Inkjet-Printed Heterostructures. *Nat. Nanotechnol.* **2017**, DOI: 10.1038/nnano.2016.281.
- (81) Li, J.; Mishukova, V.; Östling, M. All-Solid-State Micro-Supercapacitors Based on Inkjet Printed Graphene Electrodes. *Appl. Phys. Lett.* **2016**, *109*, 123901.

- (82) Li, L.; Secor, E. B.; Chen, K.; Zhu, J.; Liu, X.; Gao, T. Z.; Seo, J. T.; Zhao, Y.; Hersam, M. C. High-Performance Solid-State Supercapacitors and Microsupercapacitors Derived from Printable Graphene Inks. *Adv. Energy Mater.* **2016**, *6*, 1600909.
- (83) Arapov, K.; Rubingh, E.; Abbel, R.; Laven, J.; De With, G.; Friedrich, H. Conductive Screen Printing Inks by Gelation of Graphene Dispersions. *Adv. Funct. Mater.* **2016**, *26*, 586–593.
- (84) Arapov, K.; Bex, G.; Hendriks, R.; Rubingh, E.; Abbel, R.; de With, G.; Friedrich, H. Conductivity Enhancement of Binder-Based Graphene Inks by Photonic Annealing and Subsequent Compression Rolling. *Adv. Eng. Mater.* **2016**, *18*, 1234–1239.
- (85) Arapov, K.; Jaakkola, K.; Ermolov, V.; Bex, G.; Rubingh, E.; Haque, S.; Sandberg, H.; Abbel, R.; de With, G.; Friedrich, H. Graphene Screen-Printed Radio-Frequency Identification Devices on Flexible Substrates. *Phys. Status Solidi - Rapid Res. Lett.* **2016**, *10*, 812–818.
- (86) Huang, X.; Leng, T.; Zhu, M.; Zhang, X.; Chen, J.; Chang, K.; Aqeeli, M.; Geim, A. K.; Novoselov, K. S.; Hu, Z. Highly Flexible and Conductive Printed Graphene for Wireless Wearable Communications Applications. *Sci. Rep.* **2015**, *5*, 18298.
- (87) Hyun, W. J.; Secor, E. B.; Rojas, G. A.; Hersam, M. C.; Francis, L. F.; Frisbie, C. D. All-Printed, Foldable Organic Thin-Film Transistors on Glassine Paper. *Adv. Mater.* **2015**, *27*, 7058–7064.
- (88) Dua, V.; Surwade, S. P.; Ammu, S.; Agnihotra, S. R.; Jain, S.; Roberts, K. E.; Park, S.; Ruoff, R. S.; Manohar, S. K. All-Organic Vapor Sensor Using Inkjet-Printed Reduced Graphene Oxide. *Angew. Chemie* **2010**, *49*, 2154–2157.
- (89) Huang, L.; Huang, Y.; Liang, J.; Wan, X.; Chen, Y. Graphene-Based Conducting Inks for Direct Inkjet Printing of Flexible Conductive Patterns and Their Applications in Electric Circuits and Chemical Sensors. *Nano Res.* **2011**, *4*, 675–684.
- (90) Le, L. T.; Ervin, M. H.; Qiu, H.; Fuchs, B. E.; Lee, W. Y. Graphene Supercapacitor Electrodes Fabricated by Inkjet Printing and Thermal Reduction of Graphene Oxide. *Electrochem. Commun.* **2011**, *13*, 355–358.
- (91) Kong, D.; Le, L. T.; Li, Y.; Zunino, J. L.; Lee, W. Temperature-Dependent Electrical Properties of Graphene Inkjet-Printed on Flexible Materials. *Langmuir* **2012**, *28*, 13467–13472.
- (92) Shin, K.-Y.; Hong, J.-Y.; Jang, J. Flexible and Transparent Graphene Films as Acoustic Actuator Electrodes Using Inkjet Printing. *Chem. Commun.* **2011**, *47*, 8527–8529.

- (93) Shin, K.-Y.; Hong, J.-Y.; Jang, J. Micropatterning of Graphene Sheets by Inkjet Printing and Its Wideband Dipole-Antenna Application. *Adv. Mater.* **2011**, *23*, 2113–2118.
- (94) Lim, S.; Kang, B.; Kwak, D.; Lee, W. H.; Lim, J. A.; Cho, K. Inkjet-Printed Reduced Graphene Oxide/Poly(Vinyl Alcohol) Composite Electrodes for Flexible Transparent Organic Field-Effect Transistors. *J. Phys. Chem. C* **2012**, *116*, 7520–7525.
- (95) Su, Y.; Du, J.; Sun, D.; Liu, C.; Cheng, H. Reduced Graphene Oxide with a Highly Restored  $\pi$ -Conjugated Structure for Inkjet Printing and Its Use in All-Carbon Transistors. *Nano Res.* **2013**, *6*, 842–852.
- (96) Huang, L.; Wang, Z.-P.; Pu, J.-L.; Shen, L.; Zhang, J.-K. Graphene Pattern by Gravure Printing for Wireless Strain Sensor. In *2013 Seventh International Conference on Sensing Technology (ICST)*; IEEE, **2013**, 387–389.
- (97) Huang, L.; Wang, Z.; Zhang, J.; Pu, J.; Lin, Y.; Xu, S.; Shen, L.; Chen, Q.; Shi, W. Fully Printed, Rapid-Response Sensors Based on Chemically Modified Graphene for Detecting NO<sub>2</sub> at Room Temperature. *ACS Appl. Mater. Interfaces* **2014**, *6*, 7426–7433.
- (98) Qian, M.; Feng, T.; Ding, H.; Lin, L.; Li, H.; Chen, Y.; Sun, Z. Electron Field Emission from Screen-Printed Graphene Films. *Nanotechnology* **2009**, *20*, 425702.
- (99) Tölle, F. J.; Fabritius, M.; Mühlaupt, R. Emulsifier-Free Graphene Dispersions with High Graphene Content for Printed Electronics and Freestanding Graphene Films. *Adv. Funct. Mater.* **2012**, *22*, 1136–1144.
- (100) Nathan-Walleser, T.; Lazar, I.-M.; Fabritius, M.; Tölle, F. J.; Xia, Q.; Bruchmann, B.; Venkataraman, S. S.; Schwab, M. G.; Mühlaupt, R. 3D Micro-Extrusion of Graphene-Based Active Electrodes: Towards High-Rate AC Line Filtering Performance Electrochemical Capacitors. *Adv. Funct. Mater.* **2014**, *24*, 4706–4716.
- (101) Coleman, J. N.; Lotya, M.; O'Neill, A.; Bergin, S. D.; King, P. J.; Khan, U.; Young, K.; Gaucher, A.; De, S.; Smith, R. J.; *et al.* Two-Dimensional Nanosheets Produced by Liquid Exfoliation of Layered Materials. *Science* **2011**, *331*, 568–571.
- (102) Jo, I.; Pettes, M. T.; Kim, J.; Watanabe, K.; Taniguchi, T.; Yao, Z.; Shi, L. Thermal Conductivity and Phonon Transport in Suspended Few-Layer Hexagonal Boron Nitride. *Nano Lett.* **2013**, *13*, 550–554.
- (103) Joseph, A. M.; Nagendra, B.; Bhoje Gowd, E.; Surendran, K. P. Screen-Printable Electronic Ink of Ultrathin Boron Nitride Nanosheets. *ACS Omega* **2016**, *1*, 1220–1228.

- (104) Zhu, J.; Kang, J.; Kang, J.; Jariwala, D.; Wood, J. D.; Seo, J. W. T.; Chen, K. S.; Marks, T. J.; Hersam, M. C. Solution-Processed Dielectrics Based on Thickness-Sorted Two-Dimensional Hexagonal Boron Nitride Nanosheets. *Nano Lett.* **2015**, *15*, 7029–7036.
- (105) Zheng, J.-C.; Zhang, L.; Kretinin, A. V; Morozov, S. V; Wang, Y. B.; Wang, T.; Li, X.; Ren, F.; Zhang, J.; Lu, C.-Y.; *et al.* High Thermal Conductivity of Hexagonal Boron Nitride Laminates. *2D Mater.* **2016**, *3*, 11004.
- (106) Bhimanapati, G. R.; Lin, Z.; Meunier, V.; Jung, Y.; Cha, J.; Das, S.; Xiao, D.; Son, Y.; Strano, M. S.; Cooper, V. R.; *et al.* Recent Advances in Two-Dimensional Materials beyond Graphene. *ACS Nano* **2015**, *9*, 11509–11539.
- (107) Chhowalla, M.; Shin, H. S.; Eda, G.; Li, L.-J.; Loh, K. P.; Zhang, H. The Chemistry of Two-Dimensional Layered Transition Metal Dichalcogenide Nanosheets. *Nat. Chem.* **2013**, *5*, 263–275.
- (108) Li, J.; Naiini, M. M.; Vaziri, S.; Lemme, M. C.; Östling, M. Inkjet Printing of MoS<sub>2</sub>. *Adv. Funct. Mater.* **2014**, *24*, 6524–6531.
- (109) Yang, H.; Withers, F.; Gebremedhn, E.; Lewis, E.; Britnell, L.; Felten, A.; Palermo, V.; Haigh, S.; Beljonne, D.; Casiraghi, C. Dielectric Nanosheets Made by Liquid-Phase Exfoliation in Water and Their Use in Graphene-Based Electronics. *2D Mater.* **2014**, *1*, 11012.
- (110) Withers, F.; Yang, H.; Britnell, L.; Rooney, A. P.; Lewis, E.; Felten, A.; Woods, C. R.; Romaguera, V. S.; Georgiou, T.; Eckmann, A.; *et al.* Heterostructures Produced from Nanosheet-Based Inks. *Nano Lett.* **2014**, *14*, 3987–3992.
- (111) Yu, X.; Pre, M. S.; Sivula, K. Multi Flake Thin Film Electronic Devices of Solution Processed 2D MoS<sub>2</sub> Enabled by Sonopolymer Assisted Exfoliation and Surface Modification. *Chem. Mater.* **2014**, *26*, 5892–5899.
- (112) Zhou, K.-G.; Mao, N.-N.; Wang, H.-X.; Peng, Y.; Zhang, H.-L. A Mixed-Solvent Strategy for Efficient Exfoliation of Inorganic Graphene Analogues. *Angew. Chemie* **2011**, *50*, 10839–10842.
- (113) Capasso, A.; Del Rio Castillo, A. E.; Sun, H.; Ansaldo, A.; Pellegrini, V.; Bonaccorso, F. Ink-Jet Printing of Graphene for Flexible Electronics: An Environmentally-Friendly Approach. *Solid State Commun.* **2015**, *224*, 53–63.

- (114) Byun, S.; Kim, J. H.; Song, S. H.; Lee, M.; Park, J. J.; Lee, G.; Hong, S. H.; Lee, D. Ordered, Scalable Heterostructure Comprising Boron Nitride and Graphene for High-Performance Flexible Supercapacitors. *Chem. Mater.* **2016**, *28*, 7750–7756.
- (115) Kang, Y.; Jiang, Z.; Ma, T.; Chu, Z.; Li, G. Hybrids of Reduced Graphene Oxide and Hexagonal Boron Nitride: Lightweight Absorbers with Tunable and Highly Efficient Microwave Attenuation Properties. *ACS Appl. Mater. Interfaces* **2016**, *8*, 32468–32476.
- (116) Kelly, A. G.; Hallam, T.; Backes, C.; Harvey, A.; Esmaily, A. S.; Godwin, I.; Coelho, J.; Nicolosi, V.; Lauth, J.; Kulkarni, A.; *et al.* All-Printed Thin-Film Transistors from Networks of Liquid-Exfoliated Nanosheets. *Science* **2017**, *356*, 69–73.
- (117) Ghidui, M.; Lukatskaya, M. R.; Zhao, M.-Q.; Gogotsi, Y.; Barsoum, M. W. Conductive Two-Dimensional Titanium Carbide “Clay” with High Volumetric Capacitance. *Nature* **2014**, *516*, 78–81.
- (118) Lin, Z.; Chen, Y.; Yin, A.; He, Q.; Huang, X.; Xu, Y.; Liu, Y.; Zhong, X.; Huang, Y.; Duan, X. Solution Processable Colloidal Nanoplates as Building Blocks for High-Performance Electronic Thin Films on Flexible Substrates. *Nano Lett.* **2014**, *14*, 6547–6553.
- (119) Maleski, K.; Mochalin, V. N.; Gogotsi, Y. Dispersions of Two-Dimensional Titanium Carbide MXene in Organic Solvents. *Chem. Mater.* **2017**, *29*, 1632–1640.
- (120) Alsaif, M. M. Y. A.; Chrimes, A. F.; Daeneke, T.; Balendhran, S.; Bellisario, D. O.; Son, Y.; Field, M. R.; Zhang, W.; Nili, H.; Nguyen, E. P.; *et al.* High-Performance Field Effect Transistors Using Electronic Inks of 2D Molybdenum Oxide Nanoflakes. *Adv. Funct. Mater.* **2016**, *26*, 91–100.
- (121) An, B. W.; Kim, K.; Kim, M.; Kim, S. Y.; Hur, S. H.; Park, J. U. Direct Printing of Reduced Graphene Oxide on Planar or Highly Curved Surfaces with High Resolutions Using Electrohydrodynamics. *Small* **2015**, *11*, 2263–2268.
- (122) Onses, M. S.; Sutanto, E.; Ferreira, P. M.; Alleyne, A. G.; Rogers, J. A. Mechanisms, Capabilities, and Applications of High-Resolution Electrohydrodynamic Jet Printing. *Small* **2015**, *11*, 4237–4266.
- (123) Kitsomboonloha, R.; Morris, S. J. S.; Rong, X.; Subramanian, V. Femtoliter-Scale Patterning by High-Speed, Highly Scaled Inverse Gravure Printing. *Langmuir* **2012**, *28*, 16711–16723.

- (124) Hariprasad, D. S.; Grau, G.; Schunk, P. R.; Tjiptowidjojo, K. A Computational Model for Doctoring Fluid Films in Gravure Printing. *J. Appl. Phys.* **2016**, *119*, 135303.
- (125) Zhang, H.; Ramm, A.; Lim, S.; Xie, W.; Ahn, B. Y.; Xu, W. C.; Mahajan, A.; Suszynski, W. J.; Kim, C.; Lewis, J. A.; *et al.* Wettability Contrast Gravure Printing. *Adv. Mater.* **2015**, *27*, 7420–7425.
- (126) Tseng, H. Scaling of Inkjet-Printed Transistors Using Novel Printing Techniques, University of California, Berkeley, **2011**.
- (127) Subramanian, V.; Cen, J.; de la Fuente Vornbrock, A.; Grau, G.; Kang, H.; Kitsomboonloha, R.; Soltman, D.; Tseng, H.-Y. High-Speed Printing of Transistors: From Inks to Devices. *Proc. IEEE* **2015**, *103*, 567–582.
- (128) Eckstein, R.; Alt, M.; Roedlmeier, T.; Scharfer, P.; Lemmer, U.; Hernandez-Sosa, G. Digitally Printed Dewetting Patterns for Self-Organized Microelectronics. *Adv. Mater.* **2016**, *28*, 7708–7715.
- (129) Mahajan, A. New Approaches for Printed Electronics Manufacturing, University of Minnesota, **2015**.
- (130) Mahajan, A.; Hyun, W. J.; Walker, S. B.; Lewis, J. A.; Francis, L. F.; Frisbie, C. D. High-Resolution, High-Aspect Ratio Conductive Wires Embedded in Plastic Substrates. *ACS Appl. Mater. Interfaces* **2015**, *7*, 1841–1847.
- (131) Mahajan, A.; Hyun, W. J.; Walker, S. B.; Rojas, G. A.; Choi, J. H.; Lewis, J. A.; Francis, L. F.; Frisbie, C. D. A Self-Aligned Strategy for Printed Electronics: Exploiting Capillary Flow on Microstructured Plastic Surfaces. *Adv. Electron. Mater.* **2015**, *1*, 1500137.
- (132) Hyun, W. J.; Bidoky, F. Z.; Walker, S. B.; Lewis, J. A.; Francis, L. F.; Frisbie, C. D. Printed, Self-Aligned Side-Gate Organic Transistors with a Sub-5  $\mu\text{m}$  Gate-Channel Distance on Imprinted Plastic Substrates. *Adv. Electron. Mater.* **2016**, *2*, 1600293.
- (133) Adams, J. J.; Duoss, E. B.; Malkowski, T. F.; Motala, M. J.; Ahn, B. Y.; Nuzzo, R. G.; Bernhard, J. T.; Lewis, J. A. Conformal Printing of Electrically Small Antennas on Three-Dimensional Surfaces. *Adv. Mater.* **2011**, *23*, 1335–1340.
- (134) Seifert, T.; Sowade, E.; Roscher, F.; Wiemer, M.; Gessner, T.; Baumann, R. R. Additive Manufacturing Technologies Compared: Morphology of Deposits of Silver Ink Using Inkjet and Aerosol Jet Printing. *Ind. Eng. Chem. Res.* **2015**, *54*, 769–779.



- (135) Sarobol, P.; Cook, A.; Clem, P. G.; Keicher, D.; Hirschfeld, D.; Hall, A. C.; Bell, N. S. Additive Manufacturing of Hybrid Circuits. *Annu. Rev. Mater. Res.* **2016**, *46*, 41–62.
- (136) Khan, Y.; Garg, M.; Gui, Q.; Schadt, M.; Gaikwad, A.; Han, D.; Yamamoto, N. A. D.; Hart, P.; Welte, R.; Wilson, W.; *et al.* Flexible Hybrid Electronics: Direct Interfacing of Soft and Hard Electronics for Wearable Health Monitoring. *Adv. Funct. Mater.* **2016**, *26*, 8764–8775.
- (137) Reuss, B. R. H.; Raupp, G. B.; Gnade, B. E. Special Issue on Advanced Flexible Electronics for Sensing Applications. *Proc. IEEE* **2015**, *103*, 491–496.
- (138) Verma, N.; Hu, Y.; Huang, L.; Rieutort-Louis, W. S. A.; Robinson, J. S.; Moy, T.; Glisic, B.; Wagner, S.; Sturm, J. C. Enabling Scalable Hybrid Systems: Architectures for Exploiting Large-Area Electronics in Applications. *Proc. IEEE* **2015**, *103*, 690–712.
- (139) Hackler, D.; Sime, D. G.; Wald, S. F. Enabling Electronics with Physically Flexible ICs and Hybrid Manufacturing. *Proc. IEEE* **2015**, *103*, 633–643.
- (140) Kim, J.; Kumar, R.; Bandodkar, A. J.; Wang, J. Advanced Materials for Printed Wearable Electrochemical Devices: A Review. *Adv. Electron. Mater.* **2017**, *3*, 1600260.
- (141) Gao, M.; Li, L.; Song, Y. Inkjet Printing Wearable Electronic Devices. *J. Mater. Chem. C* **2017**, *5*, 2971.
- (142) Baby, T. T.; Rommel, M.; von Seggern, F.; Friederich, P.; Reitz, C.; Dehm, S.; Kübel, C.; Wenzel, W.; Hahn, H.; Dasgupta, S. Sub-50 nm Channel Vertical Field-Effect Transistors Using Conventional Ink-Jet Printing. *Adv. Mater.* **2017**, *29*, 1603858.
- (143) Ben-Sasson, A. J.; Azulai, D.; Gilon, H.; Facchetti, A.; Markovich, G.; Tessler, N. Self-Assembled Metallic Nanowire-Based Vertical Organic Field-Effect Transistor. *ACS Appl. Mater. Interfaces* **2015**, *7*, 2149–2152.
- (144) Singh, M.; Haverinen, H. M.; Dhagat, P.; Jabbour, G. E. Inkjet Printing-Process and Its Applications. *Adv. Mater.* **2010**, *22*, 673–685.
- (145) Yan, H.; Chen, Z.; Zheng, Y.; Newman, C.; Quinn, J. R.; Dötz, F.; Kastler, M.; Facchetti, A. A High-Mobility Electron-Transporting Polymer for Printed Transistors. *Nature* **2009**, *457*, 679–686.
- (146) Hennek, J. W.; Xia, Y.; Everaerts, K.; Hersam, M. C.; Facchetti, A.; Marks, T. J. Reduced Contact Resistance in Inkjet Printed High-Performance Amorphous Indium Gallium Zinc Oxide Transistors. *ACS Appl. Mater. Interfaces* **2012**, *4*, 1614–1619.

- (147) Hoth, C. N.; Schilinsky, P.; Choulis, S. A.; Brabec, C. J. Printing Highly Efficient Organic Solar Cells. *Nano Lett.* **2008**, *8*, 2806–2813.
- (148) Lavery, L. L.; Whiting, G. L.; Arias, A. C. All Ink-Jet Printed Polyfluorene Photosensor for High Illuminance Detection. *Org. Electron.* **2011**, *12*, 682–685.
- (149) Jeong, S.; Kim, D.; Moon, J. Ink-Jet-Printed Organic-Inorganic Hybrid Dielectrics for Organic Thin-Film Transistors. *J. Phys. Chem. C* **2008**, *112*, 5245–5249.
- (150) Lim, J. A.; Lee, W. H.; Lee, H. S.; Lee, J. H.; Park, Y. D.; Cho, K. Self-Organization of Ink-Jet-Printed Triisopropylsilylethynyl Pentacene via Evaporation-Induced Flows in a Drying Droplet. *Adv. Funct. Mater.* **2008**, *18*, 229–234.
- (151) Hu, H.; Larson, R. G. Marangoni Effect Reverses Coffee-Ring Depositions. *J. Phys. Chem. B* **2006**, *110*, 7090–7094.
- (152) Keiluweit, M.; Nico, P. S.; Johnson, M. G.; Kleber, M. Dynamic Molecular Structure of Plant Biomass-Derived Black Carbon (Biochar). *Environ. Sci. Technol.* **2010**, *44*, 1247–1253.
- (153) Pastorova, I.; Botto, R. E.; Arisz, P. W. Cellulose Char Structure: A Combined Analytical Py-GC-MS, FTIR, and NMR Study. *Carbohydr. Res.* **1994**, *262*, 27–47.
- (154) Jo, J.; Yu, J.-S.; Lee, T.-M.; Kim, D.-S. Fabrication of Printed Organic Thin-Film Transistors Using Roll Printing. *Jpn. J. Appl. Phys.* **2009**, *48*, 04C181.
- (155) Voigt, M. M.; Guite, A.; Chung, D.-Y.; Khan, R. U. a.; Campbell, A. J.; Bradley, D. D. C.; Meng, F.; Steinke, J. H. G.; Tierney, S.; McCulloch, I.; *et al.* Polymer Field-Effect Transistors Fabricated by the Sequential Gravure Printing of Polythiophene, Two Insulator Layers, and a Metal Ink Gate. *Adv. Funct. Mater.* **2010**, *20*, 239–246.
- (156) Hamsch, M.; Reuter, K.; Stanel, M.; Schmidt, G.; Kempa, H.; Fügmann, U.; Hahn, U.; Hübner, A. C. Uniformity of Fully Gravure Printed Organic Field-Effect Transistors. *Mater. Sci. Eng. B* **2010**, *170*, 93–98.
- (157) Noh, J.; Jung, K.; Kim, J.; Kim, S.; Cho, S.; Cho, G.; Abstract, A. Fully Gravure-Printed Flexible Full Adder Using SWNT-Based TFTs. *IEEE Electron Device Lett.* **2012**, *33*, 1574–1576.
- (158) Kang, H.; Kitsomboonloha, R.; Jang, J.; Subramanian, V. High-Performance Printed Transistors Realized Using Femtoliter Gravure-Printed Sub-10  $\mu\text{m}$  Metallic Nanoparticle Patterns and Highly Uniform Polymer Dielectric and Semiconductor Layers. *Adv. Mater.* **2012**, *24*, 3065–3069.

- (159) Lau, P. H.; Takei, K.; Wang, C.; Ju, Y.; Kim, J.; Yu, Z.; Takahashi, T.; Cho, G.; Javey, A. Fully Printed, High Performance Carbon Nanotube Thin-Film Transistors on Flexible Substrates. *Nano Lett.* **2013**, *13*, 3864–3869.
- (160) Kamyshny, A.; Magdassi, S. Conductive Nanomaterials for Printed Electronics. *Small* **2014**, *10*, 3515–3535.
- (161) Mattevi, C.; Eda, G.; Agnoli, S.; Miller, S.; Mkhoyan, K. A.; Celik, O.; Mastrogiovanni, D.; Granozzi, G.; Garfunkel, E.; Chhowalla, M. Evolution of Electrical, Chemical, and Structural Properties of Transparent and Conducting Chemically Derived Graphene Thin Films. *Adv. Funct. Mater.* **2009**, *19*, 2577–2583.
- (162) Pudas, M.; Hagberg, J.; Leppävuori, S. Printing Parameters and Ink Components Affecting Ultra-Fine-Line Gravure-Offset Printing for Electronics Applications. *J. Eur. Ceram. Soc.* **2004**, *24*, 2943–2950.
- (163) Lahti, M.; Leppavuori, S.; Lantto, V. Gravure-Offset-Printing Technique for the Fabrication of Solid Films. *Appl. Surf. Sci.* **1999**, *142*, 367–370.
- (164) Sung, D.; de la Fuente Vornbrock, A.; Subramanian, V. Scaling and Optimization of Gravure-Printed Silver Nanoparticle Lines for Printed Electronics. *IEEE Trans. Components Packag. Technol.* **2010**, *33*, 105–114.
- (165) Aleeva, Y.; Pignataro, B. Recent Advances in Upscalable Wet Methods and Ink Formulation for Printed Electronics. *J. Mater. Chem. C* **2012**, *2*, 6436–6453.
- (166) Bao, Z. N.; Feng, Y.; Dodabalapur, A.; Raju, V. R.; Lovinger, A. J. High-Performance Plastic Transistors Fabricated by Printing Techniques. *Chem. Mater.* **1997**, *9*, 1299.
- (167) Pardo, D.; Jabbour, G. Application of Screen Printing in the Fabrication of Organic Light-Emitting Devices. *Adv. Mater.* **2000**, *12*, 1249–1252.
- (168) Lee, T. M.; Choi, Y. J.; Nam, S. Y.; You, C. W.; Na, D. Y.; Choi, H. C.; Shin, D. Y.; Kim, K. Y.; Jung, K. I. Color Filter Patterned by Screen Printing. *Thin Solid Films* **2008**, *516*, 7875–7880.
- (169) Erath, D.; Filipovic, A.; Retzlaff, M.; Goetz, A. K.; Clement, F.; Biro, D. Advanced Screen Printing Technique for High Definition Front Side Metallization of Crystalline Silicon Solar Cells. *Sol. Energy Mater. Sol. Cells* **2010**, *94*, 57–61.

- (170) Bae, S.; Kim, H.; Lee, Y.; Xu, X.; Park, J.-S.; Zheng, Y.; Balakrishnan, J.; Lei, T.; Ri Kim, H.; Song, Y. Il; *et al.* Roll-to-Roll Production of 30-Inch Graphene Films for Transparent Electrodes. *Nat. Nanotechnol.* **2010**, *5*, 574–578.
- (171) Zirkl, M.; Sawatdee, A.; Helbig, U.; Krause, M.; Scheipl, G.; Kraker, E.; Ersman, P. A.; Nilsson, D.; Platt, D.; Bodö, P.; *et al.* An All-Printed Ferroelectric Active Matrix Sensor Network Based on Only Five Functional Materials Forming a Touchless Control Interface. *Adv. Mater.* **2011**, *23*, 2069–2074.
- (172) Moonen, P. F.; Yakimets, I.; Huskens, J. Fabrication of Transistors on Flexible Substrates: From Mass-Printing to High-Resolution Alternative Lithography Strategies. *Adv. Mater.* **2012**, *24*, 5526–5541.
- (173) Zhang, D. W.; Li, X. D.; Li, H. B.; Chen, S.; Sun, Z.; Yin, X. J.; Huang, S. M. Graphene-Based Counter Electrode for Dye-Sensitized Solar Cells. *Carbon* **2011**, *49*, 5382–5388.
- (174) Ping, J.; Wu, J.; Wang, Y.; Ying, Y. Simultaneous Determination of Ascorbic Acid, Dopamine and Uric Acid Using High-Performance Screen-Printed Graphene Electrode. *Biosens. Bioelectron.* **2012**, *34*, 70–76.
- (175) Reese, C.; Roberts, M.; Ling, M.; Bao, Z. Organic Thin Film Transistors. *Mater. Today* **2004**, *7*, 20–27.
- (176) Soukup, R.; Hamacek, A.; Reboun, J. Organic Based Sensors: Novel Screen Printing Technique for Sensing Layers Deposition. In *2012 35th International Spring Seminar on Electronics Technology* **2012**, 19–24.
- (177) Kovacs, G. T. A.; Maluf, N. I.; Petersen, K. E. Bulk Micromachining of Silicon. *Proc. IEEE* **1998**, *86*, 1536–1551.
- (178) Phair, J. W. Rheological Analysis of Concentrated Zirconia Pastes with Ethyl Cellulose for Screen Printing SOFC Electrolyte Films. *J. Am. Ceram. Soc.* **2008**, *91*, 2130–2137.
- (179) Dürr, M.; Schmid, A.; Obermaier, M.; Rosselli, S.; Yasuda, A.; Nelles, G. Low-Temperature Fabrication of Dye-Sensitized Solar Cells by Transfer of Composite Porous Layers. *Nat. Mater.* **2005**, *4*, 607–611.
- (180) Mannan, S. H.; Ekere, N. N.; Ismail, I.; Lo, E. K. Squeegee Deformation Study in the Stencil Printing of Solder Pastes. *IEEE Trans. Components Packag. Manuf. Technol. Part A* **1994**, *17*, 470–476.

- (181) Hyun, W. J.; Park, O. O.; Chin, B. D. Foldable Graphene Electronic Circuits Based on Paper Substrates. *Adv. Mater.* **2013**, *25*, 4729–4734.
- (182) Herlogsson, L.; Crispin, X.; Tierney, S.; Berggren, M. Polyelectrolyte-Gated Organic Complementary Circuits Operating at Low Power and Voltage. *Adv. Mater.* **2011**, *23*, 4684–4689.
- (183) Kim, S. H.; Hong, K.; Xie, W.; Lee, K. H.; Zhang, S.; Lodge, T. P.; Frisbie, C. D. Electrolyte-Gated Transistors for Organic and Printed Electronics. *Adv. Mater.* **2013**, *25*, 1822–1846.
- (184) Cho, J. H.; Lee, J.; Xia, Y.; Kim, B.; He, Y.; Renn, M. J.; Lodge, T. P.; Frisbie, C. D. Printable Ion-Gel Gate Dielectrics for Low-Voltage Polymer Thin-Film Transistors on Plastic. *Nat. Mater.* **2008**, *7*, 900–906.
- (185) Joo, S.; Baldwin, D. F. Adhesion Mechanisms of Nanoparticle Silver to Substrate Materials: Identification. *Nanotechnology* **2010**, *21*, 55204.
- (186) Gao, Y.; Shi, W.; Wang, W.; Leng, Y.; Zhao, Y. Inkjet Printing Patterns of Highly Conductive Pristine Graphene on Flexible Substrates. *Ind. Eng. Chem. Res.* **2014**, *53*, 16777–16784.
- (187) Perelaer, J.; Abbel, R.; Wünscher, S.; Jani, R.; van Lammeren, T.; Schubert, U. S. Roll-to-Roll Compatible Sintering of Inkjet Printed Features by Photonic and Microwave Exposure: From Non-Conductive Ink to 40% Bulk Silver Conductivity in Less than 15 Seconds. *Adv. Mater.* **2012**, *24*, 2620–2625.
- (188) Angmo, D.; Larsen-Olsen, T. T.; Jørgensen, M.; Søndergaard, R. R.; Krebs, F. C. Roll-to-Roll Inkjet Printing and Photonic Sintering of Electrodes for ITO Free Polymer Solar Cell Modules and Facile Product Integration. *Adv. Energy Mater.* **2013**, *3*, 172–175.
- (189) Wunscher, S.; Abbel, R.; Perelaer, J.; Schubert, U. S. Progress of Alternative Sintering Approaches of Inkjet-Printed Metal Inks and Their Application for Manufacturing of Flexible Electronic Devices. *J. Mater. Chem. C* **2014**, *2*, 10232–10261.
- (190) Cote, L. J.; Cruz-Silva, R.; Huang, J. Flash Reduction and Patterning of Graphite Oxide and its Polymer Composite. *J. Am. Chem. Soc.* **2009**, *131*, 11027–11032.
- (191) Park, S.-H.; Kim, H.-S. Environmentally Benign and Facile Reduction of Graphene Oxide by Flash Light Irradiation. *Nanotechnology* **2015**, *26*, 205601.

- (192) Jiu, J.; Sugahara, T.; Nogi, M.; Araki, T.; Suganuma, K.; Uchida, H.; Shinozaki, K. High-Intensity Pulse Light Sintering of Silver Nanowire Transparent Films on Polymer Substrates: The Effect of the Thermal Properties of Substrates on the Performance of Silver Films. *Nanoscale* **2013**, *5*, 11820–11828.
- (193) Xiong, Z.; Liu, C. Optimization of Inkjet Printed PEDOT:PSS Thin Films through Annealing Processes. *Org. Electron.* **2012**, *13*, 1532–1540.
- (194) Wilson, P.; Lekakou, C.; Watts, J. F. In-Plane Conduction Characterisation and Charge Transport Model of DMSO Co-Doped, Inkjet Printed Poly(3,4-Ethylenedioxythiophene): Polystyrene Sulfonate (PEDOT:PSS). *Org. Electron.* **2013**, *14*, 3277–3285.
- (195) Ha, J.; Park, J.; Ha, J.; Kim, D.; Chung, S.; Lee, C.; Hong, Y. Selectively Modulated Inkjet Printing of Highly Conductive and Transparent Foldable Polymer Electrodes for Flexible Polymer Light-Emitting Diode Applications. *Org. Electron.* **2015**, *19*, 147–156.
- (196) Kwon, O. S.; Kim, H.; Ko, H.; Lee, J.; Lee, B.; Jung, C. H.; Choi, J. H.; Shin, K. Fabrication and Characterization of Inkjet-Printed Carbon Nanotube Electrode Patterns on Paper. *Carbon* **2013**, *58*, 116–127.
- (197) Azoubel, S.; Shemesh, S.; Magdassi, S. Flexible Electroluminescent Device with Inkjet-Printed Carbon Nanotube Electrodes. *Nanotechnology* **2012**, *23*, 344003.
- (198) Shimoni, A.; Azoubel, S.; Magdassi, S. Inkjet Printing of Flexible High-Performance Carbon Nanotube Transparent Conductive Films by “Coffee Ring Effect.” *Nanoscale* **2014**, *6*, 1–6.
- (199) Lee, D. J.; Park, S. H.; Jang, S.; Kim, H. S.; Oh, J. H.; Song, Y. W. Pulsed Light Sintering Characteristics of Inkjet-Printed Nanosilver Films on a Polymer Substrate. *J. Micromechanics Microengineering* **2011**, *21*, 125023.
- (200) Sutter, F.; Fernandez-García, A.; Wette, J.; Heller, P. Comparison and Evaluation of Accelerated Aging Tests for Reflectors. *Energy Procedia* **2013**, *49*, 1718–1727.
- (201) Søndergaard, R. R.; Hösel, M.; Krebs, F. C. Roll-to-Roll Fabrication of Large Area Functional Organic Materials. *J. Polym. Sci. Part B Polym. Phys.* **2013**, *51*, 16–34.
- (202) Calvert, P. Inkjet Printing for Materials and Devices. *Chem. Mater.* **2001**, *13*, 3299–3305.

- (203) Nguyen, B. T.; Gautrot, J. E.; Nguyen, M. T.; Zhu, X. X. Nitrocellulose-Stabilized Silver Nanoparticles as Low Conversion Temperature Precursors Useful for Inkjet Printed Electronics. *J. Mater. Chem.* **2007**, *17*, 1725.
- (204) Rathmell, A. R.; Wiley, B. J. The Synthesis and Coating of Long, Thin Copper Nanowires to Make Flexible, Transparent Conducting Films on Plastic Substrates. *Adv. Mater.* **2011**, *23*, 4798–4803.
- (205) Chae, H. G.; Minus, M. L.; Rasheed, A.; Kumar, S. Stabilization and Carbonization of Gel Spun Polyacrylonitrile/Single Wall Carbon Nanotube Composite Fibers. *Polymer* **2007**, *48*, 3781–3789.
- (206) Huang, X. Fabrication and Properties of Carbon Fibers. *Materials* **2009**, *2*, 2369–2403.
- (207) Ferrari, A. C.; Basko, D. M. Raman Spectroscopy as a Versatile Tool for Studying the Properties of Graphene. *Nat. Nanotechnol.* **2013**, *8*, 235–246.
- (208) Islam, A. E.; Kim, S. S.; Rao, R.; Ngo, Y.; Jiang, J.; Nikolaev, P.; Naik, R.; Pachter, R.; Boeckl, J.; Maruyama, B. Photo-Thermal Oxidation of Single Layer Graphene. *RSC Adv.* **2016**, *6*, 42545–42553.
- (209) Rao, R.; Islam, A. E.; Pierce, N.; Nikolaev, P.; Maruyama, B. Chiral Angle-Dependent Defect Evolution in CVD-Grown Single-Walled Carbon Nanotubes. *Carbon* **2015**, *95*, 287–291.
- (210) Ferrari, A. C. Raman Spectroscopy of Graphene and Graphite: Disorder, Electron-Phonon Coupling, Doping and Nonadiabatic Effects. *Solid State Commun.* **2007**, *143*, 47–57.
- (211) Ferrari, A.; Robertson, J. Interpretation of Raman Spectra of Disordered and Amorphous Carbon. *Phys. Rev. B* **2000**, *61*, 14095–14107.
- (212) Jutier, J. J.; Harrison, Y.; Premont, S.; Prud'homme, R. E. A Nonisothermal Fourier Transform Infrared Degradation Study of Nitrocellulose Derived from Wood and Cotton. *J. Appl. Polym. Sci.* **1987**, *33*, 1359–1375.
- (213) Brill, T. B.; Gongwer, P. E. Thermal Decomposition of Energetic Materials 69. Analysis of the Kinetics of Nitrocellulose at 50 °C–500 °C. *Propellants, Explos. Pyrotech.* **1997**, *22*, 38–44.
- (214) Ferrari, A. C.; Rodil, S. E.; Robertson, J. Interpretation of Infrared and Raman Spectra of Amorphous Carbon Nitrides. *Phys. Rev. B* **2003**, *12*, 905–910.

- (215) Beyler, C. L.; Hirschler, M. M. Thermal Decomposition of Polymers. In *SPFE Handbook of Fire Protection Engineering*; Quincy, Mass.: National Fire Protection Association; Bethesda, Md.: Society of Fire Protection Engineers, **2002**, 110–131.
- (216) Arapov, K.; Bex, G.; Hendriks, R.; Rubingh, E.; Abbel, R.; de With, G.; Friedrich, H. Conductivity Enhancement of Binder-Based Graphene Inks by Photonic Annealing and Subsequent Compression Rolling. *Adv. Eng. Mater.* **2016**, *18*, 1234–1239.
- (217) Malekpour, H.; Chang, K.-H.; Chen, J.-C.; Lu, C.-Y.; Nika, D. L.; Novoselov, K. S.; Balandin, A. A. Thermal Conductivity of Graphene Laminate. *Nano Lett.* **2014**, *14*, 5155–5161.
- (218) Kim, M.-G.; Kanatzidis, M. G.; Facchetti, A.; Marks, T. J. Low-Temperature Fabrication of High-Performance Metal Oxide Thin-Film Electronics via Combustion Processing. *Nat. Mater.* **2011**, *10*, 382–388.
- (219) Merzhanov, A. G. History and Recent Developments in SHS. *Ceram. Int.* **1995**, *21*, 371–379.
- (220) Su, X.; Fu, F.; Yan, Y.; Zheng, G.; Liang, T.; Zhang, Q.; Cheng, X.; Yang, D.; Chi, H.; Tang, X.; *et al.* Self-Propagating High-Temperature Synthesis for Compound Thermoelectrics and New Criterion for Combustion Processing. *Nat. Commun.* **2014**, *5*, 4908.
- (221) Li, F.; Ran, J.; Jaroniec, M.; Qiao, S. Z. Solution Combustion Synthesis of Metal Oxide Nanomaterials for Energy Storage and Conversion. *Nanoscale* **2015**, *7*, 17590–17610.
- (222) Han, S.; Wu, D.; Li, S.; Zhang, F.; Feng, X. Porous Graphene Materials for Advanced Electrochemical Energy Storage and Conversion Devices. *Adv. Mater.* **2014**, *26*, 849–864.
- (223) Tobjörk, D.; Österbacka, R. Paper Electronics. *Adv. Mater.* **2011**, *23*, 1935–1961.
- (224) Zhai, Y.; Dou, Y.; Zhao, D.; Fulvio, P. F.; Mayes, R. T.; Dai, S. Carbon Materials for Chemical Capacitive Energy Storage. *Adv. Mater.* **2011**, *23*, 4828–4850.
- (225) Kyeremateng, N. A.; Brousse, T.; Pech, D. Microsupercapacitors as Miniaturized Energy-Storage Components for On-Chip Electronics. *Nat. Nanotechnol.* **2017**, *12*, 7–15.
- (226) Lewis, J. A. Direct-Write Assembly of Ceramics from Colloidal Inks. *Curr. Opin. Solid State Mater. Sci.* **2002**, *6*, 245–250.
- (227) Nomura, K.; Ohta, H.; Takagi, A.; Kamiya, T.; Hirano, M.; Hosono, H. Room-Temperature Fabrication of Transparent Flexible Thin-Film Transistors Using Amorphous Oxide Semiconductors. *Nature* **2004**, *432*, 488–492.



- (228) Fortunato, E.; Barquinha, P.; Martins, R. Oxide Semiconductor Thin-Film Transistors: A Review of Recent Advances. *Adv. Mater.* **2012**, *24*, 2945–2986.
- (229) Kamiya, T.; Nomura, K.; Hosono, H. Present Status of Amorphous In–Ga–Zn–O Thin-Film Transistors. *Sci. Technol. Adv. Mater.* **2010**, *11*, 44305.
- (230) Lee, D. H.; Chang, Y. J.; Herman, G. S.; Chang, C. H. A General Route to Printable High-Mobility Transparent Amorphous Oxide Semiconductors. *Adv. Mater.* **2007**, *19*, 843–847.
- (231) Thomas, S. R.; Pattanasattayavong, P.; Anthopoulos, T. D. Solution-Processable Metal Oxide Semiconductors for Thin-Film Transistor Applications. *Chem. Soc. Rev.* **2013**, *42*, 6910–6923.
- (232) Kim, D.; Koo, C. Y.; Song, K.; Jeong, Y.; Moon, J. Compositional Influence on Sol-Gel-Derived Amorphous Oxide Semiconductor Thin Film Transistors. *Appl. Phys. Lett.* **2009**, *95*, 103501.
- (233) Street, R. A.; Ng, T. N.; Lujan, R. A.; Son, I.; Smith, M.; Kim, S.; Lee, T.; Moon, Y.; Cho, S. Sol-Gel Solution-Deposited InGaZnO Thin Film Transistors. *ACS Appl. Mater. Interfaces* **2014**, *6*, 4428–4437.
- (234) Banger, K. K.; Yamashita, Y.; Mori, K.; Peterson, R. L.; Leedham, T.; Rickard, J.; Sirringhaus, H. Low-Temperature, High-Performance Solution-Processed Metal Oxide Thin-Film Transistors Formed by a “Sol–Gel on Chip” Process. *Nat. Mater.* **2011**, *10*, 45–50.
- (235) Kim, Y.-H.; Heo, J.-S.; Kim, T.-H.; Park, S.; Yoon, M.-H.; Kim, J.; Oh, M. S.; Yi, G.-R.; Noh, Y.-Y.; Park, S. K. Flexible Metal-Oxide Devices Made by Room-Temperature Photochemical Activation of Sol-Gel Films. *Nature* **2012**, *489*, 128–132.
- (236) Hennek, J. W.; Smith, J.; Yan, A.; Kim, M.-G.; Zhao, W.; Druvid, V. P.; Facchetti, A.; Marks, T. J. Oxygen “Getter” Effects on Microstructure and Carrier Transport in Low Temperature Combustion-Processed a-InXZnO (X = Ga, Sc, Y, La) Transistors. *J. Am. Chem. Soc.* **2013**, *135*, 10729–10741.
- (237) Everaerts, K.; Zeng, L.; Hennek, J. W.; Camacho, D. I.; Jariwala, D.; Bedzyk, M. J.; Hersam, M. C.; Marks, T. J. Printed Indium Gallium Zinc Oxide Transistors. Self-Assembled Nanodielectric Effects on Low-Temperature Combustion Growth and Carrier Mobility. *ACS Appl. Mater. Interfaces* **2013**, *5*, 11884–11893.

- (238) Yu, X.; Smith, J.; Zhou, N.; Zeng, L.; Guo, P.; Xia, Y.; Alvarez, A.; Aghion, S.; Lin, H.; Yu, J.; *et al.* Spray-Combustion Synthesis: Efficient Solution Route to High-Performance Oxide Transistors. *Proc. Natl. Acad. Sci. U. S. A.* **2015**, *112*, 3217–3222.
- (239) Hsieh, H. H.; Yu, X.; Xia, Y.; Sheets, C. W.; Hsiao, C. C.; Marks, T. J.; Facchetti, A. Novel Approaches for Fabricating High-Performance Low-Temperature Solution-Processed Metal Oxide Transistors. *SID Symp. Dig. Tech. Pap.* **2014**, *45*, 427–430.
- (240) Wang, B.; Yu, X.; Guo, P.; Huang, W.; Zeng, L.; Zhou, N.; Chi, L.; Bedzyk, M. J.; Chang, R. P. H.; Marks, T. J.; *et al.* Solution-Processed All-Oxide Transparent High-Performance Transistors Fabricated by Spray-Combustion Synthesis. *Adv. Electron. Mater.* **2016**, *2*, 1500427.
- (241) Yu, X.; Zeng, L.; Zhou, N.; Guo, P.; Shi, F.; Buchholz, D. B.; Ma, Q.; Yu, J.; Dravid, V. P.; Chang, R. P. H.; *et al.* Ultra-Flexible, “Invisible” Thin-Film Transistors Enabled by Amorphous Metal Oxide/Polymer Channel Layer Blends. *Adv. Mater.* **2015**, *27*, 2390–2399.
- (242) Barquinha, P.; Vilà, A. M.; Gonçalves, G.; Pereira, L.; Martins, R.; Morante, J. R.; Fortunato, E. Gallium-Indium-Zinc-Oxide-Based Thin-Film Transistors: Influence of the Source/Drain Material. *IEEE Trans. Electron Devices* **2008**, *55*, 954–960.
- (243) Wang, Y.; Sun, X. W.; Liu, S. W.; Kyaw, A. K. K.; Zhao, J. L. Oxide Thin Film Transistors with Ink-Jet Printed In-Ga-Zn Oxide Channel Layer and ITO/IZO Source/drain Contacts. In *Proceedings of the IEEE International Nanoelectronics Conference*; IEEE, **2013**, 168–171.
- (244) Kiani, A.; Hasko, D. G.; Milne, W. I.; Flewitt, A. J. Analysis of Amorphous Indium-Gallium-Zinc-Oxide Thin-Film Transistor Contact Metal Using Pilling-Bedworth Theory and a Variable Capacitance Diode Model. *Appl. Phys. Lett.* **2013**, *102*, 152102.
- (245) Lee, J. E.; Sharma, B. K.; Lee, S.-K.; Jeon, H.; Hee Hong, B.; Lee, H.-J.; Ahn, J.-H. Thermal Stability of Metal Ohmic Contacts in Indium Gallium Zinc Oxide Transistors Using a Graphene Barrier Layer. *Appl. Phys. Lett.* **2013**, *102*, 113112.
- (246) Luo, D.; Xu, H.; Zhao, M.; Li, M.; Xu, M.; Zou, J.; Tao, H.; Wang, L.; Peng, J. Influence of Source and Drain Contacts on the Properties of Indium-Gallium-Zinc-Oxide Thin-Film Transistors Based on Amorphous Carbon Nanofilm as Barrier Layer. *ACS Appl. Mater. Interfaces* **2015**, *7*, 3633–3640.
- (247) Lee, M. S.; Lee, K.; Kim, S. Y.; Lee, H.; Park, J.; Choi, K. H.; Kim, H. K.; Kim, D. G.; Lee, D. Y.; Nam, S.; *et al.* High-Performance, Transparent, and Stretchable Electrodes Using Graphene-Metal Nanowire Hybrid Structures. *Nano Lett.* **2013**, *13*, 2814–2821.

- (248) Lee, S. J.; Lee, T. II; Park, J. H.; Oh, I.-K.; Kim, H.; Kim, J. H.; Kim, C.-H.; Chae, G. S.; Baik, H. K.; Myoung, J.-M. Lowering Contact Resistance by SWCNT–Al Bilayer Electrodes in Solution Processable Metal-Oxide Thin Film Transistor. *J. Mater. Chem. C* **2015**, *3*, 1403–1407.
- (249) Wu, Q.; Xu, L.; Xu, J.; Xie, H.; Dong, C. Amorphous InGaZnO Thin Film Transistors with Sputtered Silver Source/Drain and Gate Electrodes. *Mater. Sci. Semicond. Process.* **2016**, *48*, 23–26.
- (250) Ueoka, Y.; Ishikawa, Y.; Bermundo, J. P.; Yamazaki, H.; Urakawa, S.; Osada, Y.; Horita, M.; Uraoka, Y. Effect of Contact Material on Amorphous InGaZnO Thin-Film Transistor Characteristics. *Jpn. J. Appl. Phys.* **2014**, *53*, 03CC04.
- (251) Gwinner, M. C.; Jakubka, F.; Gannott, F.; Sirringhaus, H.; Zaumseil, J. Enhanced Ambipolar Charge Injection with Semiconducting Polymer/Carbon Nanotube Thin Films for Light-Emitting Transistors. *ACS Nano* **2012**, *6*, 539–548.
- (252) Pegg, L. J.; Hatton, R. A. Nanoscale Geometric Electric Field Enhancement in Organic Photovoltaics. *ACS Nano* **2012**, *6*, 4722–4730.
- (253) Wang, L.; Meric, I.; Huang, P. Y.; Gao, Q.; Gao, Y.; Tran, H.; Taniguchi, T.; Watanabe, K.; Campos, L. M.; Muller, D. A.; *et al.* One-Dimensional Electrical Contact to a Two-Dimensional Material. *Science* **2013**, *342*, 614–617.
- (254) Geier, M. L.; Prabhumirashi, P. L.; McMorrow, J. J.; Xu, W.; Seo, J.-W. T.; Everaerts, K.; Kim, C. H.; Marks, T. J.; Hersam, M. C. Subnanowatt Carbon Nanotube Complementary Logic Enabled by Threshold Voltage Control. *Nano Lett.* **2013**, *13*, 4810–4814.
- (255) Reeves, G. K.; Harrison, H. B. Obtaining the Specific Contact Resistance from Transmission Line Model Measurements. *IEEE Electron Device Lett.* **1982**, *3*, 111–113.
- (256) Jariwala, D.; Sangwan, V. K.; Seo, J. W. T.; Xu, W.; Smith, J.; Kim, C. H.; Lauhon, L. J.; Marks, T. J.; Hersam, M. C. Large-Area, Low-Voltage, Antiambipolar Heterojunctions from Solution-Processed Semiconductors. *Nano Lett.* **2015**, *15*, 416–421.
- (257) Dickey, M. D. Stretchable and Soft Electronics Using Liquid Metals. *Adv. Mater.* **2017**, 1606425.
- (258) Dickey, M. D. Emerging Applications of Liquid Metals Featuring Surface Oxides. *ACS Appl. Mater. Interfaces* **2014**, *6*, 18369–18379.

- (259) Bilodeau, R. A.; Zemlyanov, D. Y.; Kramer, R. K. Liquid Metal Switches for Environmentally Responsive Electronics. *Adv. Mater. Interfaces* **2017**, *4*, 1600913.
- (260) Diebold, A. V.; Watson, A. M.; Holcomb, S.; Tabor, C.; Mast, D.; Dickey, M. D.; Heikenfeld, J. Electrowetting-Actuated Liquid Metal for RF Applications. *J. Micromechanics Microengineering* **2017**, *27*, 25010.
- (261) Kim, S.; Lee, J.; Choi, B. Stretching and Twisting Sensing with Liquid-Metal Strain Gauges Printed on Silicone Elastomers. *IEEE Sens. J.* **2015**, *15*, 6077–6078.
- (262) Zhu, S.; So, J. H.; Mays, R.; Desai, S.; Barnes, W. R.; Pourdeyhimi, B.; Dickey, M. D. Ultrastretchable Fibers with Metallic Conductivity Using a Liquid Metal Alloy Core. *Adv. Funct. Mater.* **2013**, *23*, 2308–2314.
- (263) Boley, J. W.; White, E. L.; Chiu, G. T. C.; Kramer, R. K. Direct Writing of Gallium-Indium Alloy for Stretchable Electronics. *Adv. Funct. Mater.* **2014**, *24*, 3501–3507.
- (264) Gozen, B. A.; Tabatabai, A.; Ozdoganlar, O. B.; Majidi, C. High-Density Soft-Matter Electronics with Micron-Scale Line Width. *Adv. Mater.* **2014**, *26*, 5211–5216.
- (265) Mohammed, M. G.; Kramer, R. All-Printed Flexible and Stretchable Electronics. *Adv. Mater.* **2017**, *29*, 1604965.
- (266) Ladd, C.; So, J. H.; Muth, J.; Dickey, M. D. 3D Printing of Free Standing Liquid Metal Microstructures. *Adv. Mater.* **2013**, *25*, 5081–5085.
- (267) Mohammed, M.; Sundaresan, R.; Dickey, M. D. Self-Running Liquid Metal Drops That Delaminate Metal Films at Record Velocities. *ACS Appl. Mater. Interfaces* **2015**, *7*, 23163–23171.
- (268) Hu, L.; Wang, L.; Ding, Y.; Zhan, S.; Liu, J. Manipulation of Liquid Metals on a Graphite Surface. *Adv. Mater.* **2016**, *28*, 9210–9217.
- (269) Ordonez, R. C.; Ha Yashi, C. K.; Torres, C. M.; Hafner, N.; Adleman, J. R.; Acosta, N. M.; Melcher, J.; Kamin, N. M.; Garmire, D. Conformal Liquid-Metal Electrodes for Flexible Graphene Device Interconnects. *IEEE Trans. Electron Devices* **2016**, *63*, 4018–4023.
- (270) Gonzalez Arellano, D. L.; Lee, H.; Secor, E. B.; Burnett, E. K.; Hersam, M. C.; Watkins, J. J.; Briseno, A. L. Graphene Ink as a Conductive Templating Interlayer for Enhanced Charge Transport of C<sub>60</sub>-Based Devices. *ACS Appl. Mater. Interfaces* **2016**, *8*, 29594–29599.
- (271) Wang, Q. H.; Hersam, M. C. Room-Temperature Molecular-Resolution Characterization of Self-Assembled Organic Monolayers on Epitaxial Graphene. *Nat. Chem.* **2009**, *1*, 206–211.

- (272) Cho, J.; Smerdon, J.; Gao, L.; Süzer, O.; Guest, J. R.; Guisinger, N. P. Structural and Electronic Decoupling of C<sub>60</sub> from Epitaxial Graphene on SiC. *Nano Lett.* **2012**, *12*, 3018–3024.
- (273) Zhang, Y.; Diao, Y.; Lee, H.; Mirabito, T. J.; Johnson, R. W.; Puodziukynaite, E.; John, J.; Carter, K. R.; Emrick, T.; Mannsfeld, S. C. B.; *et al.* Intrinsic and Extrinsic Parameters for Controlling the Growth of Organic Single-Crystalline Nanopillars in Photovoltaics. *Nano Lett.* **2014**, *14*, 5547–5554.
- (274) Nguyen, N. N.; Jo, S. B.; Lee, S. K.; Sin, D. H.; Kang, B.; Kim, H. H.; Lee, H.; Cho, K. Atomically Thin Epitaxial Template for Organic Crystal Growth Using Graphene with Controlled Surface Wettability. *Nano Lett.* **2015**, *15*, 2474–2484.
- (275) Kim, K.; Lee, T. H.; Santos, E. J. G.; Pil, A.; Jo, S.; Salleo, A.; Nishi, Y.; Bao, Z. Structural and Electrical Investigation of C<sub>60</sub>-Graphene Vertical Heterostructures. *ACS Nano* **2015**, *9*, 5922–5928.
- (276) Clemens, W.; Fix, W.; Ficker, J.; Knobloch, A.; Ullmann, A. From Polymer Transistors toward Printed Electronics. *J. Mater. Res.* **2004**, *19*, 1963–1973.
- (277) Noh, Y.-Y.; Zhao, N.; Caironi, M.; Sirringhaus, H. Downscaling of Self-Aligned, All-Printed Polymer Thin-Film Transistors. *Nat. Nanotechnol.* **2007**, *2*, 784–789.
- (278) Wu, Y.; Li, Y.; Ong, B. S.; Liu, P.; Gardner, S.; Chiang, B. High-Performance Organic Thin-Film Transistors with Solution-Printed Gold Contacts. *Adv. Mater.* **2005**, *17*, 184–187.
- (279) Huang, Y.; Liang, J.; Chen, Y. An Overview of the Applications of Graphene-Based Materials in Supercapacitors. *Small* **2012**, *8*, 1805–1834.
- (280) Hyun, W. J.; Secor, E. B.; Kim, C.-H.; Hersam, M. C.; Francis, L. F.; Frisbie, C. D. Scalable, Self-Aligned Printing of Flexible Graphene Micro-Supercapacitors. *Adv. Energy Mater.* **2017**, 1700285.
- (281) Chen, K. S.; Xu, R.; Luu, N. S.; Secor, E. B.; Hamamoto, K.; Li, Q.; Kim, S.; Sangwan, V. K.; Balla, I.; Guiney, L. M.; *et al.* Comprehensive Enhancement of Nanostructured Lithium-Ion Battery Cathode Materials via Conformal Graphene Dispersion. *Nano Lett.* **2017**, *17*, 2539–2546.
- (282) Hagio, T.; Yoshida, H. Sintering and Crystallization of Ground Hexagonal Boron Nitride Powders. *J. Mater. Sci. Lett.* **2000**, *13*, 653–655.
- (283) Zeng, X.; Hirwa, H.; Ortel, M.; Nerl, H.; Nicolosi, V.; Wagner, V. Growth of Large Size Two-Dimensional MoS<sub>2</sub> Flakes in Aqueous Solution. *Nanoscale* **2017**, *9*, 6575–6580.

- (284) Lee, S. K.; Chu, D.; Song, D. Y.; Pak, S. W.; Kim, E. K. Electrical and Photovoltaic Properties of Residue-Free MoS<sub>2</sub> Thin Films by Liquid Exfoliation Method. *Nanotechnology* **2017**, *28*, 195703.
- (285) Yang, X.; Chen, Y.; Wang, M.; Zhang, H.; Li, X. Phase Inversion: A Universal Method to Create High- Performance Porous Electrodes for Nanoparticle-Based Energy Storage Devices. *Adv. Funct. Mater.* **2016**, *26*, 8427–8434.
- (286) Blake, A. J. From 2D to 3D: On the Development of Flexible and Conformal Li-Ion Batteries via Additive Manufacturing, Wright State University, 2013.
- (287) Vandezande, P.; Gevers, E. M.; Vankelecom, I. F. J. Solvent Resistant Nanofiltration: Separating on a Molecular Level. *Chem. Soc. Rev.* **2008**, *37*, 365–405.
- (288) Ren, J.; Wang, R. Preparation of Polymeric Membranes. In *Handbook of Environmental Engineering, Membrane and Desalination Technologies*; Wang, L. K., Ed.; Springer Science, **2011**; Vol. 13, pp. 47–100.
- (289) Pierce, H. F. Nitrocellulose Membranes of Graded Permeability. *J. Biol. Chem.* **1927**, *75*, 795–815.
- (290) Liu, Z.; Li, Z.; Xu, Z.; Xia, Z.; Hu, X.; Kou, L.; Peng, L.; Wei, Y.; Gao, C. Wet-Spun Continuous Graphene Films. *Chem. Mater.* **2014**, *26*, 6786–6795.
- (291) Behabtu, N.; Young, C. C.; Tsentalovich, D. E.; Kleinerman, O.; Wang, X.; Ma, A. W. K.; Bengio, E. A.; Waarbeek, R. F.; Jong, J. J. De; Hoogerwerf, R. E.; *et al.* Fibers of Carbon Nanotubes with Ultrahigh Conductivity. *Science* **2013**, *3*, 182–187.
- (292) Bai, X.; Liao, S.; Huang, Y.; Song, J.; Liu, Z.; Fang, M.; Xu, C.; Cui, Y.; Wu, H. Continuous Draw Spinning of Extra-Long Silver Submicron Fibers with Micrometer Patterning Capability. *Nano Lett.* **2017**, *17*, 1883–1891.
- (293) Lim, Y.; Pyo, J. Preparation of Cellulose-Based Nanofibers Using Electrospinning. In *Nanofibers*; Kumar, A., Ed.; InTech, **2010**; pp. 179–188.
- (294) Wu, X.; Wang, L.; Yu, H.; Huang, Y. Effect of Solvent on Morphology of Electrospinning Ethyl Cellulose Fibers. *J. Appl. Polym. Sci.* **2005**, *97*, 1292–12976.
- (295) Wang, X.; He, G.; Liu, H.; Zheng, G.; Sun, D. Fabrication and Morphological Control of Electrospun Ethyl Cellulose Nanofibers. In *IEEE NEMS2013*; **2013**; pp. 324–327.

- (296) Daristotle, J. L.; Behrens, A. M.; Sandler, A. D.; Ko, P. A Review of the Fundamental Principles and Applications of Solution Blow Spinning. *ACS Appl. Mater. Interfaces* **2016**, *8*, 34951–34963.
- (297) Medeiros, E. S.; Glenn, G. M.; Klamczynski, A. P.; Orts, W. J.; Mattoso, L. H. C. Solution Blow Spinning: A New Method to Produce Micro- and Nanofibers from Polymer Solutions. *J. Appl. Polym. Sci.* **2009**, *113*, 2322–2330.
- (298) Wang, H.; Liao, S.; Bai, X.; Liu, Z.; Fang, M.; Liu, T.; Wang, N.; Wu, H. Highly Flexible Indium Tin Oxide Nanofiber Transparent Electrodes by Blow Spinning. *ACS Appl. Mater. Interfaces* **2016**, *8*, 32661–32666.
- (299) Khalid, B.; Bai, X.; Wei, H.; Huang, Y.; Wu, H.; Cui, Y. Direct Blow-Spinning of Nanofibers on a Window Screen for Highly Efficient PM 2.5 Removal. *Nano Lett.* **2017**, *17*, 1140–1148.
- (300) Huang, Y.; Bai, X.; Zhou, M.; Liao, S.; Yu, Z.; Wang, Y.; Wu, H. Large-Scale Spinning of Silver Nanofibers as Flexible and Reliable Conductors. *Nano Lett.* **2016**, *16*, 5846–5851.
- (301) Yu, D.; Goh, K.; Wang, H.; Wei, L.; Jiang, W.; Zhang, Q.; Dai, L.; Chen, Y. Scalable Synthesis of Hierarchically Structured Carbon Nanotube – Graphene Fibres for Capacitive Energy Storage. *Nat. Nanotechnol.* **2014**, *9*, 555-562.
- (302) Wang, R.; Xu, Z.; Zhuang, J.; Liu, Z.; Peng, L.; Li, Z.; Liu, Y. Highly Stretchable Graphene Fibers with Ultrafast Electrothermal Response for Low-Voltage Wearable Heaters. *Adv. Electron. Mater.* **2017**, *3*, 1600425.
- (303) Li, Z.; Xu, Z.; Liu, Y.; Wang, R.; Gao, C. Multifunctional Non-Woven Fabrics of Interfused Graphene Fibres. *Nat. Commun.* **2016**, *7*, 13684.
- (304) Ma, Y.; Li, P.; Sedloff, J. W.; Zhang, X.; Zhang, H.; Liu, J. Conductive Graphene Fibers for Wire-Shaped Supercapacitors Strengthened by Unfunctionalized Few-Walled Carbon Nanotubes. *ACS Nano* **2015**, *9*, 1352–1359.
- (305) Park, E. S.; Chen, Y.; Liu, T. K.; Subramanian, V. A New Switching Device for Printed Electronics: Inkjet-Printed Microelectromechanical Relay. *Nano Lett.* **2013**, *13*, 5355–5360.
- (306) Jakus, A. E.; Secor, E. B.; Rutz, A. L.; Jordan, S. W.; Hersam, M. C. Three-Dimensional Printing of High-Content Graphene Scaffolds for Electronic and Biomedical Applications. *ACS Nano* **2015**, *9*, 4636–4648.

- (307) Rastogi, S. K.; Raghavan, G.; Yang, G.; Cohen-Karni, T. Effect of Graphene on Nonneuronal and Neuronal Cell Viability and Stress. *Nano Lett.* **2017**, *17*, 3297–3301.
- (308) Shao, Y.; Wang, J.; Wu, H.; Liu, J.; Aksay, I. A.; Lin, Y. Graphene Based Electrochemical Sensors and Biosensors: A Review. *Electroanalysis* **2010**, *22*, 1027–1036.
- (309) Zhao, S.; Liu, X.; Xu, Z.; Ren, H.; Deng, B.; Tang, M.; Lu, L.; Fu, X.; Peng, H.; Liu, Z.; *et al.* Graphene Encapsulated Copper Microwires as Highly MRI Compatible Neural Electrodes. *Nano Lett.* **2016**, *16*, 7731–7738.
- (310) Fabbro, A.; Scaini, D.; Leo, V.; Vazquez, E.; Cellot, G.; Privitera, G.; Ferrari, A. C.; Ballerini, L.; Prato, M. Graphene-Based Interfaces Do Not Alter Target Nerve Cells. *ACS Nano* **2016**, *10*, 615–623.
- (311) Guo, S.; Dong, S. Graphene Nanosheet: Synthesis, Molecular Engineering, Thin Film, Hybrids, and Energy and Analytical Applications. *Chem. Soc. Rev.* **2011**, *40*, 2644–2672.
- (312) Wang, H.; Maiyalagan, T.; Wang, X. Review on Recent Progress in Nitrogen-Doped Graphene: Synthesis, Characterization, and Its Potential Applications. *ACS Catal.* **2012**, *2*, 781–794.
- (313) Secor, E. B.; Smith, J.; Marks, T. J.; Hersam, M. C. High-Performance Inkjet-Printed Indium-Gallium-Zinc-Oxide Transistors Enabled by Embedded, Chemically Stable Graphene Electrodes. *ACS Appl. Mater. Interfaces* **2016**, *8*, 17428–17434.
- (314) Wang, Y.; Shao, Y.; Matson, D. W.; Li, J.; Lin, Y. Nitrogen-Doped Graphene and Its Biosensing. *ACS Nano* **2010**, *4*, 1790–1798.
- (315) Lin, Y.; Teng, P.; Yeh, C.; Koshino, M.; Chiu, P.; Suenaga, K. Structural and Chemical Dynamics of Pyridinic-Nitrogen Defects in Graphene. *Nano Lett.* **2015**, *15*, 7408–7413.
- (316) Hersam, M. C.; Liang, Y. T.; Secor, E. B.; Prabhumirashi, P. L.; Puntambekar, K. P.; Geier, M. L.; Ahn, B. Y.; Lewis, J. A. Methods for Preparation of Concentrated Graphene Ink Compositions and Related Composite Materials. US Patent Application, 14/756,304, **2015**.
- (317) Hersam, M. C.; Secor, E. B.; Lim, S.; Frisbie, C. D.; Francis, L. F.; Hyun, W. J. High-Resolution Patterning of Graphene by Screen and Gravure Printing for Highly Flexible Printed Electronics. US Patent Application, 14/699,822, **2015**.
- (318) Secor, E. B.; Hersam, M. C. Graphene Inks for Printed Electronics, Sigma-Aldrich Technical Documents, **2014**.



## Curriculum Vitae for Ethan B. Secor

---

### Education

- **Northwestern University, Evanston, IL**  
PhD in materials science and engineering (Expected, June 2017)  
Thesis Title: "Production, Processing, and Applications of Graphene Inks"  
GPA 4.00/4.00
- **Drake University, Des Moines, IA**  
Bachelors of science in physics (2012)  
Bachelors of science in chemistry (2012)  
GPA 4.00/4.00

### Scientific Experience

- **Graduate Researcher with Professor Mark Hersam at Northwestern (20012-present)**
  - Solution-phase exfoliation and processing of graphene
  - Formulation of graphene inks for additive printing techniques
  - Photothermal processing of graphene composite films
- **Undergraduate Researcher with Dr. Vilas Pol at Argonne National Laboratory (2012)**
  - Sonochemical modification of lithium ion battery cathode and anode materials
  - Assembly and electrochemical testing of lithium ion batteries
- **Undergraduate Researcher at Drake University (2009-2012)**
  - Numerical calculations for quantum mechanical interactions of electromagnetic radiation with molecular species (Professor Klaus Bartschat, Physics)
  - Metallorganic synthesis and characterization of  $\alpha$ -amino acids (Professor John Gitua, Chemistry)
- **Technical Aide at 3M Corporate Research Process Laboratory with Dr. Richard Jendrejack (2011)**
- **Summer REU Student at Sandia National Laboratories, Advanced Materials Laboratory with Dr. P. Randall Schunk (2010)**

### Leadership

- Mentored two undergraduate researchers for a total of 5 years
- Transferred research projects to three graduate students and post-doctoral researchers
- Managed successful collaborative research with over 10 research groups

## Skills

- **Instrumental Characterization Techniques** (AFM, SEM, XRD, XPS, EDS, TGA, GC, fluorometry, rheometry and IR, Raman and UV-Vis spectroscopy)
- **Laboratory Methods for Fabrication and Characterization** (inkjet printing, solution-based electronic device fabrication and electrical measurements)
- **Experimental Apparatus Fabrication and Assembly** (Scale-up shear mixing system design and assembly for 20 liter batch volume)
- **Programming Language Experience** (LabVIEW, FORTRAN 77/90, C/C++, Perl, Matlab and PWSCF)

## Awards and Honors

- Truman Fellowship, 2017
- Cabell Terminal Year Fellowship, 2016
- IIN Outstanding Researcher Award, 2016
- Ryan Fellowship, 2014
- National Defense Science and Engineering Graduate Fellowship, 2013
- Finalist for the Hertz Foundation Fellowship, 2012
- Barry M. Goldwater Scholarship, 2011
- Drake Physics Prize, 2008

## Publications

- [17] Hyun, W.J.; **Secor, E.B.**; Kim, C.-H.; Hersam, M.C.; Francis, L.F.; Frisbie, C.D. Scalable, Self-Aligned Printing of Flexible Graphene Micro-Supercapacitors. *Adv. Energy Mater.*, **2017**, 1700285.
- [16] **Secor, E.B.\***; Gao, T.Z.\*; Wallace, S.G.; Zhu, J.; Putz, K.W.; Hersam, M.C. Enhanced Conductivity, Adhesion, and Environmental Stability of Printed Graphene Inks with Nitrocellulose. *Chem. Mater.* **2017**, *29*, 2332-2340
- [15] Chen, K.-S.; Xu, R.; Luu, N. S.; **Secor, E. B.**; Hamamoto, K.; Li, Q.; Kim, S.; Sangwan, V. K.; Balla, I.; Guiney, L. M.; *et al.* Comprehensive Enhancement of Nanostructured Lithium-Ion Battery Cathode Materials via Conformal Graphene Dispersion. *Nano Lett.* **2017**, *17* (4), 2539-2546.
- [14] Gonzalez Arellano, D.L.; Lee, H.; **Secor, E.B.**; Burnett, E.K.; Hersam, M.C. Watkins, J.J.; Briseno, A.L. Graphene Ink as a Conductive Templating Interlayer for Enhanced Charge Transport of C<sub>60</sub>-Based Devices. *ACS Appl. Mater. Interfaces*, **2016**, *8*, 29594.
- [13] Li, L.\*; **Secor, E.B.\***; Chen, K.-S.; Zhu, J.; Liu, X.; Gao, T.Z.; Seo, J.-W.T.; Zhao, Y.; Hersam, M.C. High-Performance Solid-State Supercapacitors and Microsupercapacitors Derived from Printable Graphene Inks. *Adv. Energy Mater.*, **2016**, 1600909.

- [12] **Secor, E.B.**; Smith, J.; Marks, T.J.; Hersam, M.C. High-Performance Inkjet-Printed Indium-Gallium-Zinc-Oxide Transistors Enabled by Embedded, Chemically Stable Graphene Electrodes. *ACS Appl. Mater. Interfaces*, **2016**, *8*, 17428.
- [11] Hyun, W.J.; **Secor, E.B.**; Rojas, G.A.; Hersam, M.C.; Francis, L.F.; Frisbie, C.D. All-Printed, Foldable Organic Thin-Film Transistors on Glassine Paper. *Adv. Mater.* **2015**, *27*, 7058.
- [10] **Secor, E.B.**; Ahn, B.Y.; Gao, T.Z.; Lewis, J.A.; Hersam, M.C. Rapid and Versatile Photonic Annealing of Graphene Inks for Flexible Printed Electronics. *Adv. Mater.* **2015**, *27*, 6683.
- [9] Jakus, A.E.; **Secor, E.B.**; Rutz, A.L.; Jordan, S.W.; Hersam, M.C.; Shah, R.N. Three-Dimensional Printing of High-Content Graphene Scaffolds for Electronic and Biomedical Applications. *ACS Nano* **2015**, *9*, 4636.
- [8] **Secor, E.B.**; Hersam, M.C. Emerging Carbon and Post-Carbon Nanomaterial Inks for Printed Electronics. *J. Phys. Chem. Lett.* **2015**, *6*, 620.
- [7] Hyun, W.J.\*; **Secor, E.B.\***; Hersam, M.C.; Frisbie, C.D.; Francis, L.F. High-Resolution Patterning of Graphene by Screen Printing with a Silicon Stencil for Highly Flexible Printed Electronics. *Adv. Mater.* **2015**, *27*, 109.
- [6] **Secor, E.B.\***; Lim, S.\*; Zhang, H.; Frisbie, C.D.; Francis, L.F.; Hersam, M.C. Gravure Printing of Graphene for Large-Area Flexible Electronics. *Adv. Mater.* **2014**, *26*, 4533.
- [5] Pol, V.G.; Li, Y.; Dogan, F.; **Secor, E.**; Thackeray, M.M.; Abraham, D.P. Pulsed Sonication for Alumina Coatings on High-Capacity Oxides: Performance in Lithium-Ion Cells. *J. Power Sources* **2014**, *258*, 46-53.
- [4] **Secor, E.B.**; Prabhumirashi, P.L.; Puntambekar, K.; Geier, M.L.; Hersam, M.C. Inkjet Printing of High Conductivity, Flexible Graphene Patterns. *J. Phys. Chem. Lett.* **2013**, *4*, 1347-1351.
- [3] Guan, X.; **Secor, E.B.**; DuToit, R.C.; Bartschat, K. Diffraction Patterns in the Ionization of the Heteronuclear  $\text{HeH}^{2+}$  Ion by Attosecond X-Ray Radiation. *Phy. Rev. A* **2012**, *86*, 053425.
- [2] Guan, X.; **Secor, E.B.**; Bartschat, K.; Schneider, B.I. Double-Slit Interference Effect in Electron Emission from  $\text{H}_2^+$  Exposed to X-ray Radiation. *Phy. Rev. A* **2012**, *85*, 043419. (2012).
- [1] Guan, X.; **Secor, E.**; Bartschat, K.; Schneider, B. Multiphoton Ionization of the  $\text{H}_2^+$  Molecule in XUV Laser Pulses. *Phy. Rev. A* **2011**, *84*, 033420.

\* These authors contributed equally to this work

## Patents

- [6] US Provisional Patent Application 62/464,167, 2017: Hersam, M.C.; Secor, E.B.; Chen, K.-S. Comprehensive Enhancement of Nano-structured Cathode Materials via Graphene Dispersion for Lithium-ion Batteries.

- [5] US Provisional Patent Application 62/360,727, 2016: Hersam, M.C.; Secor, E.B.; Li, L. High-Performance Solid-State Supercapacitors and Microsupercapacitors Derived from Printable Graphene Inks.
- [4] US Provisional Patent Application 62/359,583, 2016: Hersam, M.C.; Secor, E.B.; Gao, T.Z. Enhanced Conductivity, Adhesion and Environmental Stability of Printed Graphene Inks with Nitrocellulose.
- [3] US Patent Application 15/500,339; PCT/US2015/055773, 2015: Shah, R.N.; Hersam, M.C.; Jakus, A.E.; Secor, E.B. Graphene-based Ink Compositions for Three-Dimensional Printing Applications.
- [2] US Patent Application 14/699,822, 2015: Hersam, M.C.; Secor, E.B.; Lim, S.; Frisbie, C.D.; Francis, L.F.; Hyun, W.J., High-Resolution Patterning of Graphene by Screen and Gravure Printing for Highly Flexible Printed Electronics.  
(Continuation of US Provisional Patent Application 61/985,914, 2014 and US Provisional Patent Application 62/076,233, 2014)
- [1] US Patent Application 14/756,304, 2015: Hersam, M.C.; Liang, Y.T.; Secor, E.B.; Prabhumirashi, P.L.; Puntambekar, K.P.; Geier, M.L.; Ahn, B.Y.; Lewis, J.A., Methods for Preparation of Concentrated Graphene Ink Compositions and Related Composite Materials.  
(Continuation in Part of US Patent Application 14/121,097 (2014))

## Presentations

- [9] **Secor, E.B.** Hilliard Symposium, Northwestern University, May 2017. Production, Patterning, and Application of Graphene Inks.
- [8] **Secor, E.B.;** Gao, T.Z.; Hersam, M.C. Oral presentation at the Materials Research Society Meeting, April 2017. Versatile and High-Performance Graphene Inks for Printed and Flexible Electronics.
- [7] **Secor, E.B.** Chemistry and Physics Colloquium, Drake University, March 2017. Production, Patterning, and Applications of Graphene Inks.
- [6] **Secor, E.B.** SPIE Student Seminar Series, Northwestern University, January 2017. Production, Patterning, and Applications of Graphene Inks.
- [5] **Secor, E.B.;** Hyun, W.J.; Lim, S.; Prabhumirashi, P.L.; Puntambekar, K.; Geier, M.L.; Zhang, H.; Frisbie, C.D.; Francis, L.F.; Hersam, M.C. Oral presentation at the Materials Research Society Meeting, April 2015. Versatile and High-Performance Graphene Inks for Printed and Flexible Electronics.
- [4] **Secor, E.B.** Seminar at Corporate Research Process Laboratory, 3M Company, November 2014. Development and Application of Graphene Inks.
- [3] **Secor, E.;** Guan, X.; Bartschat, K.; Schneider, B.I. Poster presentation at the American Physical Society Division of Atomic, Molecular and Optical Physics 43<sup>rd</sup> Annual

Meeting, June 2012. Double-Slit Interference in  $\text{H}_2^+$  Subjected to Ultrashort X-ray Radiation.

- [2] **Secor, E.**; Guan, X.; Bartschat, K.; Schneider, B. Oral presentation at the American Physical Society Division of Atomic, Molecular and Optical Physics 42<sup>nd</sup> Annual Meeting, June 2011. Multiphoton Ionization of the  $\text{H}_2^+$  Molecule by a Laser Pulse.
- [1] Giles, D.W.; Briese, T.E.; **Secor, E.B.**; Macosko, C.W.; Secor, R.B. Oral presentation at the 81<sup>st</sup> Annual Meeting of the Society of Rheology, October, 2009. High Shear Rate Rheometry using Narrow Gap Rotating Parallel Plates.